



POLITECNICO DI TORINO

Master Degree
in Physics of Complex Systems

Master Degree Thesis

Coherent electron transport in nanowires with spin-orbit coupling.

Supervisor

prof. Fabrizio Dolcini

Candidate

Leonid Gogin

ACADEMIC YEAR 2021-2022

Introduction

In this thesis I investigate the coherent electron transport in a nanowire with spin-orbit coupling. Spin orbit coupling is a relativistic effect resulting in a coupling between the spin of an electron and its motion in an electric field. While in atomic physics it explains the fine structure of the atomic spectrum, this effect is also relevant in various semiconductors (e.g. InSb or InAs), for spintronics applications. In particular, nanowires (NWs) with a strong Rashba spin orbit coupling (RSOC), are currently on the spotlight of the condensed matter community. Indeed the technological advances in NW gating allow to tune the RSOC. Moreover, when combined with a Zeeman magnetic field, the RSOC in NWs gives rise to one-dimensional helical electron states that are topologically protected. Inspired by these motivations, this thesis aims to model the electron transport properties of NWs with an inhomogeneous RSOC and exposed to a Zeeman magnetic field, in the low temperature mesoscopic regime, where decoherence is absent and the wavelike nature of electrons emerges. The Thesis is organized as follows.

Chapter 1 reviews the origin of the spin-orbit coupling and its effects in semiconducting materials,

Chapter 2 reviews the Scattering Matrix approach (SMA), i.e. the quantum approach used to analyze the transport properties in the quantum mesoscopic regime. The subsequent two chapters contain original research work. In particular:

Chapter 3 applies the SMA to the case of NW. In particular, motivated by the advances in gating techniques, I focus on NWs with an inhomogeneous RSOC. After performing the analytical calculation of the Boundary Matrix in each NW portion, I have written a numerical Python code to compute the Scattering matrix of the NW, whence I derived its transport properties. Specifically, I have considered two configurations of the inhomogeneous RSOC that correspond to physically interesting situations, and I have shown that the conductance can be widely tuned both electrically and magnetically.

Chapter 4 focusses on the regime where the RSOC is much bigger than the Zeeman energy. This is the case where the NWs exhibits one-dimensional helical electron states, i.e. states described by a massless Dirac equation where the helicity value (+/-1) encodes the locking between the direction of propagation and the spin orientation. In particular, I investigated the so called Dirac paradox, which emerges at the interface between two regions of opposite helicity: An electron impinging from one side can seemingly neither be transmitted nor reflected. While the Dirac paradox has been investigated in higher dimensions (e.g. in 3D topological insulators), its implementation in NWs is particularly interesting since the helical states are actual 1D channels, preventing electrons from escaping along the interface of the two regions. While purely massless Dirac models predict that the solution of the Dirac paradox does not exist or is trivial, in a NW the paradox has a non trivial solution, due to the role played by additional massive Dirac modes. Although these modes carry no current, they allow the wavefunction matching at the interface for the massless modes, and the electron transmission can be controlled electrically. These results are described in a research article that is currently under review:

L. Gogin *et. al* "*The Dirac paradox in 1+1 dimensions and its realization with spin-orbit coupled nanowires*", cond-mat arXiv:2109.07355

Contents

1 Spin-orbit interaction	5
1.1 Origin of the spin-orbit interaction	5
1.1.1 Heuristic derivation	5
1.1.2 The Dirac equation and its non-relativistic limit	6
1.1.3 The perturbative expansion method	8
1.1.4 Löwdin partitioning	11
1.1.5 Non-relativistic expansion with Löwdin partitioning	13
1.1.6 The case of an atomic central potential	15
1.2 Spin-orbit interaction in materials: Dresselhaus and Rashba couplings	16
1.2.1 $\mathbf{k} \cdot \mathbf{p}$ theory	17
1.2.2 The Kane model	20
1.3 The effects of confinement potentials	25
1.3.1 The envelope function approximation	26
1.3.2 SOC in a quantum well	28
1.4 SOC in 1D nanowires	32
1.5 Applications of the spin-orbit coupling	36
1.5.1 Datta-Das transistor	37
2 The Scattering Matrix formalism	41
2.1 The quantum mesoscopic regime	41
2.2 Scheme of a typical measurement setup	43
2.3 Landauer-Büttiker model for the setup	45
2.3.1 Modelling the leads	46
2.3.2 The Scattering Matrix of the mesoscopic system	49
2.3.3 Electrical current	54
2.3.4 Thermal current	56
2.3.5 Linear response regime	57
3 Rashba Nanowire exposed to an external magnetic field	61
3.1 Nanowire with a homogeneous RSOC	61
3.1.1 Spectrum	63
3.1.2 Eigenstates	66
3.1.3 The Rashba dominated regime: helical states	67
3.2 The case of inhomogeneous RSOC	72

3.2.1	Relabelling the states in terms of energy	74
3.2.2	Results for the conductance of the single interface problem	79
3.2.3	Generalization to multiple interfaces	90
3.2.4	Results for the conductance of the double interface problem	91
4	The Dirac paradox and its realization with nanowires	97
4.1	Dirac paradox	98
4.1.1	Massless Dirac heterojunctions	99
4.2	Dirac Heterojunctions with massless and massive modes	104
4.2.1	Derivation of the transfer matrix	106
4.2.2	Scattering states	107
4.3	Realization with spin-orbit nanowires	112
4.3.1	Transmission coefficient in the case of InSb	116
5	Conclusions	119
A	Energy relabelling of eigenfunctions	123
A.1	Propagating modes	124
A.2	Evanescant modes	127
B	Current operator in the presence of Rashba coupling.	129
C	Details about the transfer matrix.	133
	List of Figures	135
	List of Tables	137

Chapter 1

Spin-orbit interaction

1.1 Origin of the spin-orbit interaction

This section is devoted to illustrate the origin of the spin-orbit interaction, whose effects in nanowires are the focus of my thesis. In atomic physics this interaction explains the fine structure of the atomic spectra, i.e. the lifting of energy level degeneracy occurring even in the absence of a magnetic field[47]. A customary pictorial way to explain the origin of this interaction is that, due to relativistic effects, electric and magnetic fields depend on the reference frame. Thus, an electron performing its orbit in the electric field generated by the atomic nucleus feels an effective magnetic field in its reference frame. The coupling of its spin with such magnetic field results in the 'spin-orbit' interaction. At a more rigorous level, such interaction can be properly derived from the Dirac equation in non relativistic limit.[29, 37].

This section is structured as follows. We first present a heuristic derivation of the spin-orbit interaction, based on the relativistic transformation of the electromagnetic fields. Then, we present a rigorous derivation of the effect, starting from the Dirac equation and analyzing its non-relativistic limit. Specifically we present two equivalent derivations. One is based on a direct perturbative expansion[29], while the other one is based on the Löwdin partitioning approach[25], which can be considered as the generalization of the Foldy–Wouthuysen Transformation[37].

1.1.1 Heuristic derivation

A heuristic argument to justify the appearance of the spin-orbit interaction is based on the Lorentz transformation of the electromagnetic field between two inertial reference frames[47]. Let Σ be an inertial reference frame, where, at a given time t , a particle with charge q is moving with velocity \mathbf{u} . At that time, there is an instantaneous inertial reference frame Σ' , moving with that constant velocity \mathbf{u} with respect to Σ , where the particle is momentarily at rest. Decomposing in each frame the electric and magnetic

fields in direction parallel and orthogonal to \mathbf{u} one has

$$\begin{cases} \mathbf{E} = \mathbf{E}_{\parallel} + \mathbf{E}_{\perp} \\ \mathbf{B} = \mathbf{B}_{\parallel} + \mathbf{B}_{\perp} \end{cases} \quad \begin{cases} \mathbf{E}' = \mathbf{E}'_{\parallel} + \mathbf{E}'_{\perp} \\ \mathbf{B}' = \mathbf{B}'_{\parallel} + \mathbf{B}'_{\perp} \end{cases} \quad (1.1)$$

one has [74]

$$\begin{cases} \mathbf{E}'_{\parallel} = \mathbf{E}_{\parallel} \\ \mathbf{E}'_{\perp} = \gamma(\mathbf{E} + \mathbf{u} \times \mathbf{B})_{\perp} \\ \mathbf{B}'_{\parallel} = \mathbf{B}_{\parallel} \\ \mathbf{B}'_{\perp} = \gamma(\mathbf{B} - \mathbf{u} \times \frac{\mathbf{E}}{c^2})_{\perp} \end{cases} \quad (1.2)$$

where the relativistic factor $\gamma = 1/\sqrt{1 - v^2/c^2}$ is roughly equal to 1 if $|v| \ll c$. In particular, from Eqs.(1.2) we can see that, even if in Σ only an electric field \mathbf{E} is present ($\mathbf{B} = 0$), in its rest frame Σ' the particle experiences **also a magnetic field** perpendicular to its velocity

$$\mathbf{B}' = \gamma \frac{\mathbf{E}}{c} \times \frac{\mathbf{u}}{c} \simeq \frac{\mathbf{E} \times \mathbf{p}}{m_0 c^2} \quad (1.3)$$

In turn, the particle spin couples to such magnetic field \mathbf{B}' through a Zeeman coupling, giving rise to an effective term

$$H_{so}^{heuristic} = -\frac{\hbar q}{2m_0} \boldsymbol{\sigma} \cdot \mathbf{B}' = -\frac{\hbar q}{2m_0^2 c^2} \boldsymbol{\sigma} \cdot (\mathbf{E} \times \mathbf{p}) \quad (1.4)$$

where the *so*-subscript stands for 'spin-orbit', since the prototypical example of this effect occurs in an atom, where an electron experiences an effective magnetic field while performing its orbit under the electric field $\mathbf{E} = -\nabla V$ generated by the electrostatic potential V of the nucleus.

This heuristic argument reproduces surprisingly well all the ingredients of the effect and the dependence on the mass and c . However, Eq.(1.4) overestimates by a factor of 2 (i.e. by the gyromagnetic factor $g_0 \simeq 2$ [47]) the actual coupling

$$H_{so} = -\frac{\hbar q}{4m_0^2 c^2} \boldsymbol{\sigma} \cdot (\mathbf{E} \times \mathbf{p}) \quad (1.5)$$

Here below we shall thus derive Eq.(1.5) rigorously, starting from the Dirac Equation.

1.1.2 The Dirac equation and its non-relativistic limit

A free relativistic spin-1/2 particle is described by the Dirac equation[29]

$$i\hbar \frac{\partial \Psi}{\partial t} = \left(c\boldsymbol{\alpha} \cdot \hat{\mathbf{p}} + \beta m_0 c^2 \right) \Psi \quad (1.6)$$

where $\hat{\mathbf{p}} = -i\hbar\nabla$ is canonical momentum, Ψ is the 4-spinor wavefunction of the particle, and α, β is a vector of 4×4 matrices that in the case of 3+1 dimensions can be expressed as

$$\alpha = \begin{pmatrix} 0 & \boldsymbol{\sigma} \\ \boldsymbol{\sigma} & 0 \end{pmatrix} \quad \beta = \begin{pmatrix} \sigma_0 & 0 \\ 0 & -\sigma_0 \end{pmatrix} \quad (1.7)$$

where $\boldsymbol{\sigma} = (\sigma_x, \sigma_y, \sigma_z)$ are the 3 Pauli matrices and σ_0 is the 2×2 identity matrix. The Dirac equation (1.6) is fully relativistic and is characterized by the well known relativistic energy spectrum, i.e.

$$E = \sqrt{c^2\mathbf{p}^2 + m_0^2c^4} \quad (1.8)$$

The coupling with electromagnetic fields $\mathbf{E}(\mathbf{r}), \mathbf{B}(\mathbf{r})$ can be introduced through the substitution of the canonical momentum by a kinetic one, and through an energy change

$$\hat{\mathbf{p}} \mapsto \hat{\boldsymbol{\pi}} = \hat{\mathbf{p}} - q\mathbf{A} \quad (1.9)$$

$$\hat{E} \mapsto E + qV \quad (1.10)$$

where $V(\mathbf{r})$ and $\mathbf{A}(\mathbf{r})$ are the scalar and vector potentials, related to $\mathbf{E}(\mathbf{r}), \mathbf{B}(\mathbf{r})$

$$\mathbf{E}(\mathbf{r}) = -\nabla V(\mathbf{r}) \quad (1.11)$$

$$\mathbf{B}(\mathbf{r}) = \nabla \times \mathbf{A}(\mathbf{r}) \quad (1.12)$$

and q is the electrical charge. The Dirac Equation becomes

$$i\hbar \frac{\partial \Psi}{\partial t} = \hat{H}_D \Psi \quad (1.13)$$

where

$$\hat{H}_D \doteq c\boldsymbol{\alpha} \cdot (\hat{\mathbf{p}} - q\mathbf{A}) + \beta m_0 c^2 + qV \quad (1.14)$$

is the Dirac Hamiltonian. The spin-orbit effect is obtained from the non-relativistic limit of the Dirac equation (1.13). In order to analyze this limit, we observe that the full 4×1 spinor can be written as the composition of two 2×1 spinors

$$\Psi(\mathbf{r}, t) = \begin{pmatrix} \Phi_U(\mathbf{r}, t) \\ \Phi_L(\mathbf{r}, t) \end{pmatrix} \quad (1.15)$$

where Φ_U and Φ_L denote the upper and lower spinor, respectively. In this way the Dirac equation (1.13) can be rewritten as two coupled differential equations for each 2×1 spinor

$$\begin{cases} i\hbar \frac{\partial \Phi_U}{\partial t} = c\boldsymbol{\sigma} \cdot \hat{\boldsymbol{\pi}} \Phi_L + m_0 c^2 \Phi_U + qV \Phi_U \\ i\hbar \frac{\partial \Phi_L}{\partial t} = c\boldsymbol{\sigma} \cdot \hat{\boldsymbol{\pi}} \Phi_U - m_0 c^2 \Phi_L + qV \Phi_L \end{cases} \quad (1.16)$$

Looking for stationary solutions

$$\begin{pmatrix} \Phi_U(\mathbf{r}, t) \\ \Phi_L(\mathbf{r}, t) \end{pmatrix} = e^{-i\frac{E}{\hbar}t} \begin{pmatrix} \phi_U(\mathbf{r}) \\ \phi_L(\mathbf{r}) \end{pmatrix} \quad (1.17)$$

one can always write the energy E as the sum of the rest energy m_0c^2 and the deviation ε from it

$$E = m_0c^2 + \varepsilon \quad (1.18)$$

In the non relativistic limit, namely $|\mathbf{p}| \ll m_0c$, the rest energy m_0c^2 is the dominant energy scale, whereas

$$\varepsilon = \left| \sqrt{c^2\mathbf{p}^2 + m_0^2c^4} - m_0c^2 \right| \ll m_0c^2 \quad (1.19)$$

represents the non-relativistic energy. Substituting Eq.(1.18) into Eq.(1.17) and singling out the rest energy in the time-dependent phase, the full wavefunction (1.15) can be expressed as the product of a fast oscillating factor related to the rest energy and a slowly oscillating envelope

$$\begin{pmatrix} \Phi_U(\mathbf{r}, t) \\ \Phi_L(\mathbf{r}, t) \end{pmatrix} = \underbrace{e^{-i\frac{m_0c^2}{\hbar}t}}_{\text{fast oscillating}} \underbrace{e^{-i\frac{\varepsilon}{\hbar}t} \begin{pmatrix} \phi_U(\mathbf{r}) \\ \phi_L(\mathbf{r}) \end{pmatrix}}_{\text{slowly oscillating}} \quad (1.20)$$

Plugging the above relation into Eq.(1.16) one obtains a system of two coupled differential equations for slowly oscillating wavefunctions

$$\begin{cases} c\boldsymbol{\sigma} \cdot \hat{\boldsymbol{\pi}}\phi_L(\mathbf{r}) = (\varepsilon - qV(\mathbf{r}))\phi_U(\mathbf{r}) \\ c\boldsymbol{\sigma} \cdot \hat{\boldsymbol{\pi}}\phi_U(\mathbf{r}) = (2m_0c^2 + \varepsilon - qV(\mathbf{r}))\phi_L(\mathbf{r}) \end{cases} \quad (1.21)$$

This is the starting point to analyze the non-relativistic limit of the Dirac Equation. In the literature there exist two methods to show that the spin-orbit interaction arises from such non-relativistic limit. The first one is a perturbation expansion, while the second one is the so called Löwdin partitioning. Here below I shall illustrate both these approaches.

1.1.3 The perturbative expansion method

Let us start by illustrating the perturbative expansion method. The second Eq.(1.21) implies the relation

$$\phi_L(\mathbf{r}) = \frac{c}{2m_0c^2 + \varepsilon - qV(\mathbf{r})} \boldsymbol{\sigma} \cdot \hat{\boldsymbol{\pi}}\phi_U(\mathbf{r}) \quad (1.22)$$

showing that the lower spinor ϕ_L is negligible w.r.t. the upper spinor ϕ_U in non relativistic limit since $|\boldsymbol{\sigma} \cdot \hat{\boldsymbol{\pi}}| = |\hat{\boldsymbol{\pi}}| \ll m_0c^2$. Plugging Eq.(1.22) into the first Eq.(1.21), leads to

$$\boldsymbol{\sigma} \cdot \hat{\boldsymbol{\pi}} \frac{c^2}{2m_0c^2 + \varepsilon - qV(\mathbf{r})} \boldsymbol{\sigma} \cdot \hat{\boldsymbol{\pi}}\phi_U(\mathbf{r}) = (\varepsilon - qV(\mathbf{r}))\phi_U(\mathbf{r}) \quad (1.23)$$

Note that, because $V = V(\mathbf{r})$ and $\hat{\boldsymbol{\pi}} = -i\hbar\nabla - q\mathbf{A}$ contains a derivative operator, the operators $\boldsymbol{\sigma} \cdot \hat{\boldsymbol{\pi}}$ and $(\varepsilon + 2m_0c^2 - qV(\mathbf{r}))^{-1}$ do not commute.

In the non-relativistic limit one has

$$\varepsilon \ll m_0c^2 \quad |qV| \ll m_0c^2 \quad (1.24)$$

and one can perform the following perturbative expansion

$$\frac{c^2}{2m_0c^2 + \varepsilon - qV(\mathbf{r})} = \frac{1}{2m_0} \frac{1}{1 + \frac{2m_0c^2 + \varepsilon - qV(\mathbf{r})}{2m_0c^2}} = \frac{1}{2m_0} \left(1 - \frac{\varepsilon - qV(\mathbf{r})}{2m_0c^2} + \dots \right) \quad (1.25)$$

which can be regarded as an expansion in powers of $u/c \ll 1$, where u is the particle velocity, since from Eq.(1.23) one has $|\varepsilon - qV| \sim |\boldsymbol{\pi}|^2/2m_0 = \frac{1}{2}m_0u^2$.

Zero order of Eq.(1.25)

Retaining only the zero order of Eq.(1.25)

$$\frac{c^2}{2m_0c^2 + \varepsilon - qV(\mathbf{r})} \simeq \frac{1}{2m_0} \quad , \quad (1.26)$$

and replacing it into Eq.(1.23) one obtains

$$\frac{(\boldsymbol{\sigma} \cdot \hat{\boldsymbol{\pi}})^2}{2m_0} \phi_U(\mathbf{r}) = (\varepsilon - qV(\mathbf{r})) \phi_U(\mathbf{r}) \quad (1.27)$$

Recalling that $\hat{\boldsymbol{\pi}} = \hat{\mathbf{p}} - q\mathbf{A}$ and observing that

$$\begin{aligned} (\boldsymbol{\sigma} \cdot \hat{\boldsymbol{\pi}})^2 &= \hat{\boldsymbol{\pi}}^2 + i \boldsymbol{\sigma} \cdot (\hat{\boldsymbol{\pi}} \times \hat{\boldsymbol{\pi}}) = \\ &= \hat{\boldsymbol{\pi}}^2 - \hbar q \boldsymbol{\sigma} \cdot (\nabla \times \mathbf{A}) = \hat{\boldsymbol{\pi}}^2 - \hbar q \boldsymbol{\sigma} \cdot \mathbf{B} \end{aligned} \quad (1.28)$$

one finds

$$\left(\frac{\hat{\boldsymbol{\pi}}^2}{2m_0} - \frac{\hbar q}{2m_0} \mathbf{B} \cdot \boldsymbol{\sigma} + qV(\mathbf{r}) \right) \phi_U = \varepsilon \phi_U \quad (1.29)$$

This is the Schrödinger-Pauli equation for the 2×1 spinor ϕ_U that represents the upper and dominant part of the original 4×1 Dirac spinor. Note that the Zeeman coupling has the correct gyromagnetic factor $g_0 = 2$ [37].

First order of Eq.(1.25)

Retaining also the first order in the expansion Eq.(1.25), which corresponds to a *second* order in $|u|/c$,

$$\frac{c^2}{2m_0c^2 + \varepsilon - qV(\mathbf{r})} \simeq \frac{1}{2m_0} \left(1 - \underbrace{\frac{\varepsilon - qV(\mathbf{r})}{2m_0c^2}}_{\mathcal{O}(|u|/c)^2} \right) \quad , \quad (1.30)$$

Eq.(1.23) becomes

$$\left(\frac{\boldsymbol{\sigma} \cdot \hat{\boldsymbol{\pi}}}{2m_0} \left(1 - \frac{\varepsilon - qV(\mathbf{r})}{2m_0c^2} \right) \boldsymbol{\sigma} \cdot \hat{\boldsymbol{\pi}} \right) \phi_U(\mathbf{r}) = (\varepsilon - qV(\mathbf{r})) \phi_U(\mathbf{r}) \quad (1.31)$$

which can formally be written as

$$\hat{H}_U \phi_U = \varepsilon \phi_U \quad (1.32)$$

with

$$\hat{H}_U = \frac{\boldsymbol{\sigma} \cdot \hat{\boldsymbol{\pi}}}{2m_0} \left(1 - \frac{\varepsilon - qV(\mathbf{r})}{2m_0 c^2} \right) \boldsymbol{\sigma} \cdot \hat{\boldsymbol{\pi}} + qV(\mathbf{r}) \quad (1.33)$$

Notably, Eq.(1.32) cannot be considered as an eigenvalue equation for ϕ_U , for three reasons. First, because the eigenvalue ε also appears in the Hamiltonian \hat{H}_U itself. Second, by expanding the operator \hat{H}_U to $\mathcal{O}(|\hat{\boldsymbol{\pi}}|/2m_0c)^2 = \mathcal{O}(|u|/c)^2$, it can be shown that it contains a non-Hermitean term $i\hbar\mathbf{E} \cdot \hat{\mathbf{p}}$. Third, because, differently from the zero order case, the spinor ϕ_U is not normalized to this order.

Let us start by discussing the last issue. From the relation (1.22) between ϕ_L and ϕ_U , we observe that the normalization of the 4×1 spinor (1.15)[25, 29]

$$\int d\mathbf{r} \Psi^\dagger \Psi = \int d\mathbf{r} (\phi_U^\dagger \phi_U + \phi_L^\dagger \phi_L) = 1 \quad (1.34)$$

implies that, to order $\mathcal{O}(|\boldsymbol{\pi}|/2m_0c)^2 = \mathcal{O}(|u|/c)^2$,

$$\int d\mathbf{r} \phi_U^\dagger \left(1 + \frac{(\boldsymbol{\sigma} \cdot \hat{\boldsymbol{\pi}})^2}{4m_0^2 c^2} \right) \phi_U \simeq 1 \quad (1.35)$$

This relation shows that, differently from the zero order case Eq.(1.26), to order $\mathcal{O}(|u|/c)^2$ the upper spinor ϕ_U itself is not normalized, since a fraction of the probability density is ascribed to the lower spinor $\phi_L^\dagger \phi_L$ contribution[25]. In order to deal with a normalized 2×1 spinor, one thus introduces a renormalized spinor

$$\varphi \doteq \Omega \phi_U \quad \leftrightarrow \quad \phi_U = \Omega^{-1} \varphi \quad (1.36)$$

where the operator $\Omega = 1 + \frac{(\boldsymbol{\sigma} \cdot \hat{\boldsymbol{\pi}})^2}{8m_0^2 c^2}$ compensates for the probability density leak of ϕ_U , in order for the 2×1 spinor φ to be normalized up to $\mathcal{O}(|\boldsymbol{\pi}|/2m_0c)^2$, in view of Eq.(1.35). By multiplying both sides of Eq.(1.32) by $\Omega^{-1} \simeq 1 - \frac{(\boldsymbol{\sigma} \cdot \hat{\boldsymbol{\pi}})^2}{8m_0^2 c^2}$ [29]

$$\Omega^{-1} H_A \Omega^{-1} \varphi = \varepsilon \Omega^{-2} \varphi \quad (1.37)$$

and by consistently retaining only terms to order $\mathcal{O}(|\hat{\boldsymbol{\pi}}|/2m_0c)^2 = \mathcal{O}(|u|/c)^2$, one obtains the equation for the normalized eigenfunction φ [29]

$$\left(\frac{(\boldsymbol{\sigma} \cdot \hat{\boldsymbol{\pi}})^2}{2m_0} + qV(\mathbf{r}) + \frac{q}{4m_0^2 c^2} \boldsymbol{\sigma} \cdot \hat{\boldsymbol{\pi}} V(\mathbf{r}) \boldsymbol{\sigma} \cdot \hat{\boldsymbol{\pi}} - \frac{q}{8m_0^2 c^2} \left\{ (\boldsymbol{\sigma} \cdot \hat{\boldsymbol{\pi}})^2, V(\mathbf{r}) \right\} \right) \varphi = \varepsilon \varphi \quad (1.38)$$

Note that the kinetic momentum $\hat{\boldsymbol{\pi}}$ and $V(\mathbf{r})$ do not commute. Eq.(1.38) can be rewritten in a more insightful form by exploiting the following general equation

$$\left\{ \hat{A}^2, \hat{B} \right\} - 2\hat{A}\hat{B}\hat{A} = \left[\hat{A}, \left[\hat{A}, \hat{B} \right] \right] \quad (1.39)$$

to the operators $\hat{A} = \boldsymbol{\sigma} \cdot \hat{\boldsymbol{\pi}}$ and $\hat{B} = V(\mathbf{r})$, and the following relations

$$[\hat{\boldsymbol{\pi}}, qV] = iq\hbar\mathbf{E} \quad (1.40)$$

$$[\hat{\pi}_i, E_i] = -i\hbar\partial_i E_i \quad (1.41)$$

$$(\boldsymbol{\sigma} \cdot \mathbf{a})(\boldsymbol{\sigma} \cdot \mathbf{b}) = \mathbf{a} \cdot \mathbf{b} + i\boldsymbol{\sigma} \cdot (\mathbf{a} \times \mathbf{b}) \quad (1.42)$$

where \mathbf{a} , \mathbf{b} are two generic vectors, and the definitions (1.11)-(1.12) and $\hat{\boldsymbol{\pi}} = -i\hbar\nabla - q\mathbf{A}$ have been used. With help of the above relations, Eq.(1.38) can be rewritten as[29]

$$\left(\frac{(\hat{\mathbf{p}} - q\mathbf{A})^2}{2m_0} - \frac{\hbar q}{2m_0} \mathbf{B} \cdot \boldsymbol{\sigma} + qV(\mathbf{r}) - \frac{q\hbar}{4m_0^2 c^2} \boldsymbol{\sigma} \cdot \mathbf{E} \times (\hat{\mathbf{p}} - q\mathbf{A}) - \frac{q\hbar^2}{8m_0^2 c^2} \nabla \cdot \mathbf{E} \right) \varphi = \varepsilon\varphi \quad (1.43)$$

Notably, Eq.(1.43) is now a proper eigenvalue problem for the normalized eigenfunction φ , with a Hermitean Hamiltonian. While the first three terms can be easily identified with already familiar contributions, namely the kinetic energy, Zeeman splitting and external scalar potential, the last two terms correspond to the new corrections. In particular,

$$H_D = -\frac{e\hbar^2}{8m_0^2 c^2} \nabla \cdot \mathbf{E} \quad (1.44)$$

is called the the Darwin term and can be interpreted as a smearing of the atomic potential due to the quantum fluctuations of electron position as result of creation and annihilation of electron-positron pair. In the case of Coulomb potential the Darwin term is non-vanishing only at the origin. It thus involves only the s -state and then can be neglected for atoms with high atomic number[24, 47]. The other term

$$H_{SO} = -\frac{q\hbar}{4m_0^2 c^2} \boldsymbol{\sigma} \cdot (\mathbf{E} \times \hat{\boldsymbol{\pi}}) \quad (1.45)$$

is the *spin-orbit interaction*. By comparing with the heuristically derived expression (1.4), we see that Eq.(1.45) now has the correct gyromagnetic factor.

1.1.4 Löwdin partitioning

An alternative derivation of the spin-orbit interaction from the non relativistic limit of the Dirac equation can be carried out with the Foldy–Wouthuysen transformation, that is a unitary transformation allowing to decouple small spinor component ϕ_L and dominant one ϕ_U [37]. The transformation can be found in closed form in the case of free particle, while in the presence of electromagnetic field the unitary transformation only could be approximated with power expansion of $1/(m_0c)$. Here we shall describe a more systematic approach, known as the Löwdin partitioning, which can be considered as generalization of Foldy–Wouthuysen transformation and that enables us to include the electromagnetic field as well. The Löwdin partitioning is a quasi-degenerate perturbation theory that leads to an approximated diagonalization of time independent block Hamiltonians[25]. It aims

to construct a unitary transformation such that the resulting transformed Hamiltonian would be block diagonal. With respect to Foldy–Wouthuysen transformation, the Löwdin partitioning is valid for larger sets of possibly degenerate states. Consider the Hamiltonian decomposition

$$H = H_0 + H' \quad (1.46)$$

where H_0 is an unperturbed Hamiltonian whose energy eigenvalues E_n and corresponding eigenstates $|\psi_n\rangle$ are known. The idea is that the unperturbed eigenstates can be divided into 2 subsets $\{|\psi_n\rangle\} = \{|\psi_m\rangle : m \in A\} \cup \{|\psi_l\rangle : l \in B\}$, and H' is a weak perturbation that couple states from subset A and B . The coupling Hamiltonian H' can be written as

$$H' = H_1 + H_2 \quad (1.47)$$

where H_1 is the block diagonal part i.e. $\langle\psi_m|H_1|\psi_n\rangle \neq 0$ if $n, m \in A$ or $n, m \in B$ and H_2 is the off-diagonal part, i.e. $\langle\psi_m|H_2|\psi_n\rangle \neq 0$ if $n \in A, m \in B$ or vice versa $m \in A, n \in B$. The two subsets of states of the full Hamiltonian can be decoupled if one can construct, exactly or approximately, a unitary transformation $U = e^{-S}$ such that

$$\tilde{H} = e^S H e^{-S} \quad (1.48)$$

is block diagonal up to given order of perturbation H' i.e. $\langle\psi_m|\tilde{H}|\psi_n\rangle = \mathcal{O}((H')^\delta)$ if $m \in A$ and $n \in B$. It can be observed that in order to guarantee the unitarity of the transformation, the operator S must be anti-Hermitian $S^\dagger = -S$. Furthermore S is expected to have non-block diagonal form. Using the Baker–Hausdorff formula, the transformed Hamiltonian can be rewritten as

$$\tilde{H} = \sum_{j=0} \frac{1}{j!} [H_0 + H_1, S]^{(j)} + \sum_{j=0} \frac{1}{j!} [H_2, S]^{(j)} \quad (1.49)$$

where $[a, b]^{(j)} = [\dots[a, b], b], \dots b]$ is nested commutator at j -th order. Up to now \tilde{H} still contains a off-diagonal block contribution \tilde{H}_n . Due to the property of S , they are expected to have the form $[H_0 + H_1, S]^{(2j+1)}$ and $[H_2, S]^{(2j)}$. In contrast, the block diagonal part \tilde{H}_d is expected to involve terms of the form $[H_0 + H_1, S]^{(2j)}$ and $[H_2, S]^{(2j+1)}$. In general it is hard to find in a closed form a unitary transformation S that eliminates the off-diagonal blocks term \tilde{H}_n . However, S could be approximated with a power expansion truncated at given order

$$S \simeq S^{(1)} + S^{(2)} + S^{(3)} + \dots \quad \text{with } S^{(j)} = \mathcal{O}((H')^j) \quad (1.50)$$

The constraint $\tilde{H}_n = 0$ can be satisfied by imposing the mutual cancellation of similar order of perturbation terms. This leads to a set of equations for each term of the power expansions $S^{(j)}$

$$[H_0, S^{(1)}] = -H_2 \quad (1.51)$$

$$[H_0, S^{(2)}] = -[H_1, S^{(1)}] \quad (1.52)$$

$$[H_0, S^{(3)}] = -[H_1, S^{(2)}] - \frac{1}{3} [[H_2, S^{(1)}], S^{(1)}] \quad (1.53)$$

⋮

From the above set of equations it can be seen that the l.h.s. is of the order $S^{(j)}$, while r.h.s is of the same order due to the product of expansion terms of $S^{(i)}$ with $i < j$ and perturbation Hamiltonian. Solution of this equations, i.e. the general form of $S^{(j)}$, can be found in Appendix B of reference [25]. Using the expansion (1.50) and substituting it into Eq.(1.49), the Hamiltonian \tilde{H} can be expressed as

$$\tilde{H} = H^{(0)} + H^{(1)} + H^{(2)} + H^{(3)} + \dots \quad (1.54)$$

We report here explicitly the entries of the first three expansion terms[25]

$$H_{m,m'}^{(0)} = (H_0)_{m,m'} \quad (1.55)$$

$$H_{m,m'}^{(1)} = H'_{m,m'} \quad (1.56)$$

$$H_{m,m'}^{(2)} = \frac{1}{2} \sum_l H'_{m,l} H'_{l,m'} \left[\frac{1}{E_m - E_l} + \frac{1}{E_{m'} - E_l} \right] \quad (1.57)$$

$$H_{m,m'}^{(3)} = -\frac{1}{2} \sum_{l,m''} \left[\frac{H'_{m,l} H'_{l,m''} H'_{m'',m'}}{(E_{m'} - E_l)(E_{m''} - E_l)} + \frac{H'_{m,m''} H'_{m'',l} H'_{l,m'}}{(E_m - E_l)(E_{m''} - E_l)} \right] + \quad (1.58)$$

$$+ \frac{1}{2} \sum_{l,l'} H'_{m,l} H'_{l,l'} H'_{l',m'} \left[\frac{1}{(E_m - E_l)(E_m - E_{l'})} + \frac{1}{(E_{m'} - E_l)(E_{m'} - E_{l'})} \right] \quad (1.59)$$

1.1.5 Non-relativistic expansion with Löwdin partitioning

Let us now apply the Löwdin partitioning to analyze the Dirac Hamiltonian Eq.(1.14) in the non relativistic limit. In this case the rest energy is a dominant energy scale with $|\hat{\boldsymbol{\pi}}| \ll m_0 c$ and $|eV| \ll m_0 c^2$. The Dirac Hamiltonian \hat{H}_D can thus be seen as describing a particle at rest that is weakly perturbed by the kinetic term, and can be decomposed according to Löwdin scheme as

$$H_0 = m_0 c^2 \beta \quad (1.60)$$

$$H' = c \boldsymbol{\alpha} \cdot \hat{\boldsymbol{\pi}} + qV = H_1 + H_2 \quad (1.61)$$

where

$$H_1 = \begin{pmatrix} qV & 0 \\ 0 & qV \end{pmatrix} \quad H_2 = \begin{pmatrix} 0 & c \boldsymbol{\sigma} \cdot \hat{\boldsymbol{\pi}} \\ c \boldsymbol{\sigma} \cdot \hat{\boldsymbol{\pi}} & 0 \end{pmatrix} \quad (1.62)$$

When the particle is at rest and free from the electromagnetic field, the eigenvalue problem $\hat{H}_D \psi = E \psi$ reduces to

$$m_0 c^2 \beta \psi = E \psi \quad (1.63)$$

and has four eigenstates grouped into two degenerate subsets

$$\psi_{A,1} = \begin{pmatrix} 1 \\ 0 \\ 0 \\ 0 \end{pmatrix} \quad \psi_{A,2} = \begin{pmatrix} 0 \\ 1 \\ 0 \\ 0 \end{pmatrix} \quad (1.64)$$

$$\psi_{B,1} = \begin{pmatrix} 0 \\ 0 \\ 1 \\ 0 \end{pmatrix} \quad \psi_{B,2} = \begin{pmatrix} 0 \\ 0 \\ 0 \\ 1 \end{pmatrix} \quad (1.65)$$

with corresponding energies

$$E_A = m_0c^2 \quad (1.66)$$

$$E_B = -m_0c^2 \quad (1.67)$$

The states (1.64) $\psi_{A,i} = \begin{pmatrix} \phi_U \\ 0 \end{pmatrix}$ with $i = 1,2$ identify the upper component ϕ_U of the 4-spinor and are expected to be dominant in non relativistic limit. In this way Löwdin partitioning becomes rather simple to implement

$$H'_{A,A} = qV \quad (1.68)$$

$$H'_{A,B} = H'_{B,A} = c\boldsymbol{\sigma} \cdot \hat{\boldsymbol{\pi}} \quad (1.69)$$

$$E_A - E_B = 2m_0c^2 \quad (1.70)$$

The expansion of transformed Hamiltonian up to third order terms can be written as [25]

$$H^{(0)} = m_0c^2\sigma_0 \quad (1.71)$$

$$H^{(1)} = qV \quad (1.72)$$

$$H^{(2)} = \frac{1}{2m_0}\boldsymbol{\sigma} \cdot \hat{\boldsymbol{\pi}}\boldsymbol{\sigma} \cdot \hat{\boldsymbol{\pi}} \quad (1.73)$$

$$\begin{aligned} H^{(3)} &= \frac{1}{4m_0^2c^2}\boldsymbol{\sigma} \cdot \hat{\boldsymbol{\pi}}qV\boldsymbol{\sigma} \cdot \hat{\boldsymbol{\pi}} - \frac{1}{8m_0^2c^2}[\boldsymbol{\sigma} \cdot \hat{\boldsymbol{\pi}}\boldsymbol{\sigma} \cdot \hat{\boldsymbol{\pi}}qV + qV\boldsymbol{\sigma} \cdot \hat{\boldsymbol{\pi}}\boldsymbol{\sigma} \cdot \hat{\boldsymbol{\pi}}] \\ &= \frac{1}{4m_0^2c^2}\boldsymbol{\sigma} \cdot \hat{\boldsymbol{\pi}}qV\boldsymbol{\sigma} \cdot \hat{\boldsymbol{\pi}} - \frac{1}{8m_0^2c^2}\{(\boldsymbol{\sigma} \cdot \hat{\boldsymbol{\pi}})^2, qV(\mathbf{r})\} \end{aligned} \quad (1.74)$$

With help of the identities (1.40-1.42) it is straightforward to simplify the above expansion terms, obtaining

$$H^{(0)} = m_0c^2\sigma_0 \quad (1.75)$$

$$H^{(1)} = qV \quad (1.76)$$

$$H^{(2)} = \frac{1}{2m_0}(\hat{\boldsymbol{\pi}}^2 - \hbar q\boldsymbol{\sigma} \cdot \mathbf{B}) \quad (1.77)$$

$$H^{(3)} = -\frac{q\hbar}{4m_0^2c^2}\boldsymbol{\sigma} \cdot (\mathbf{E} \times \hat{\boldsymbol{\pi}}) - \frac{q\hbar^2}{8m_0^2c^2}\nabla \cdot \mathbf{E} \quad (1.78)$$

The corrections up to second order correspond to already well known terms that can be observed already with the simplest non relativistic expansion Eq.(1.29), for instance $H^{(0)}$ is a rest energy, a constant offset and usually can be eliminated; $H^{(1)}$ is a potential energy and $H^{(2)}$ contain the kinetic energy and the coupling term of the total angular momentum with the magnetic field. On the other hand new correction terms are introduced only with $H^{(3)}$. As one can see, the Hamiltonian $H^{(1)} + H^{(2)} + H^{(3)}$ obtained from the Löwdin partitioning, coincides with the Hamiltonian (1.43) found with the perturbative method.

1.1.6 The case of an atomic central potential

Let us consider, in particular, the case of vanishing magnetic field ($\mathbf{A} = 0 \rightarrow \hat{\boldsymbol{\pi}} = \hat{\mathbf{p}}$) and of a central potential $V = V(r)$, where $r = |\mathbf{r}|$. The related electric field can be expressed as $\mathbf{E} = -\frac{\partial}{\partial r}V\mathbf{r}$, and Eq.(1.45) acquires the form[37]

$$H_{SO} = \frac{q\hbar}{4m_0^2c^2} \frac{\partial}{\partial r} V \boldsymbol{\sigma} \cdot \hat{\mathbf{L}} \quad (1.79)$$

where $\hat{\mathbf{L}} = \mathbf{r} \times \hat{\boldsymbol{\pi}}$ is the angular momentum operator. Introducing spin operator $\hat{\mathbf{S}} = \hbar\boldsymbol{\sigma}/2$ this term can be expressed in form that justify its name as a coupling between spin and orbit angular momentum operators

$$H_{so} = \zeta(r) \hat{\mathbf{L}} \cdot \hat{\mathbf{S}} \quad (1.80)$$

where we have introduced the radial function

$$\zeta(r) = \frac{q}{2m_0^2c^2} \frac{1}{r} \frac{\partial V}{\partial r} \quad (1.81)$$

It is straightforward to see that H_{so} does not commute with the angular momentum $\hat{\mathbf{L}}$. Neither does it commute with the spin $\hat{\mathbf{S}}$, which is no good quantum number, so that the spin degeneracy is lifted even for $\mathbf{B} = 0$. However, the scalar product $\hat{\mathbf{L}} \cdot \hat{\mathbf{S}}$ in the SO term (1.80) commutes with both $\hat{\mathbf{L}}^2$ and $\hat{\mathbf{S}}^2$, and recalling that the square of total angular momentum can be expressed as $\hat{\mathbf{J}}^2 = \hat{\mathbf{L}}^2 + \hat{\mathbf{S}}^2 + \hat{\mathbf{L}} \cdot \hat{\mathbf{S}}$, the SO term (1.80) can be rewritten as

$$H_{SO} = \frac{\zeta(r)}{2} (\hat{\mathbf{J}}^2 - \hat{\mathbf{L}}^2 - \hat{\mathbf{S}}^2) \quad (1.82)$$

Here the radial function $\zeta(r)$ commutes with the operators $\hat{\mathbf{J}}^2$, $\hat{\mathbf{L}}^2$, $\hat{\mathbf{S}}^2$. Moreover, $\hat{\mathbf{L}}^2$, $\hat{\mathbf{S}}^2$, $\hat{\mathbf{J}}^2$ and \hat{J}_z mutually commute and can be simultaneously diagonalized by states labelled by the 4 quantum integer numbers (l, j, s, m_j) corresponding to their eigenvalues, with $l = 0, 1, 2, \dots$, $j = |l - s|, |l - s| + 1, \dots, l + s$ and $m_j \in \{-j, j\}$. In particular, for an electron the spin quantum number is locked to $s = 1/2$, and one has $j = l \pm 1/2$. Furthermore, the atomic wavefunction is characterized by the additional shell number n related to the radial equation, so that the state can be labelled as $|n, j, l, m_j\rangle$ with $j = l \pm 1/2$. The expectation value $\langle H_{SO} \rangle \doteq \langle n, j, l, m_j | H_{SO} | n, j, l, m_j \rangle$ of the spin-orbit term (1.80) thus reads[30, 47]

$$\langle H_{SO} \rangle = \frac{\hbar^2 \lambda_{SO}}{2} \left[j(j+1) - l(l+1) - \frac{3}{4} \right] \quad (1.83)$$

Here the average value $\lambda_{SO} \doteq \langle \zeta(r) \rangle$ identifies the strength of the spin-orbit coupling correction to the non-relativistic atomic energy level. For a Coulomb potential $V(r) = -Z|e|/r$ and for the electron charge $q = -|e|$, Eq.(1.81) acquires the form

$$\zeta(r) = \frac{1}{2m_0^2 c^2} \frac{Ze^2}{r^3} \quad (1.84)$$

and one obtains[24, 47]

$$|\langle H_{SO} \rangle| \sim \hbar^2 \langle \zeta \rangle \sim \text{Ry}(Z\alpha)^2 \quad (1.85)$$

where $\alpha \simeq 1/137$ is the fine structure constant and Ry the binding energy of the hydrogen atom. This shows that the spin-orbit coupling is stronger for atoms with large atomic number Z .

1.2 Spin-orbit interaction in materials: Dresselhaus and Rashba couplings

In Sec.1.1.6 we have seen the effects of the spin-orbit coupling in a single atom. In present section we shall extend the analysis to the case of materials, where atoms are arranged together in a regular structure. The electronic orbitals of different atoms come together and hybridize forming the band structure of the solid determining the relevant properties of the material. Bulk conducting states around the band minima can be described by a parabolic effective model where the interaction with periodic crystal potential is taken into account by effective mass. Here below we shall first discuss the effects of the SOC term in the microscopic description of a solid. Then we shall focus on semiconductors, characterized by a Fermi energy in the middle of a sufficiently narrow energy gap separating the conduction and valence band, and we shall derive an effective model of a semiconductor heterojunction in the presence of external electric field.

Let us start by discussing in general terms the symmetry properties of SOC. Indeed as we have pointed out in previous section the spin-orbit coupling term is expected to lift the spin degeneracy. In the absence of SOC one can express spin degeneracy of dispersion relation as $\epsilon_{\downarrow}(k) = \epsilon_{\uparrow}(k)$, that can be obtained by combining time reversal symmetry (1.86) and spatial inversion symmetry (1.87)[19, 25]

$$\epsilon_{\uparrow}(k) = \epsilon_{\downarrow}(-k) \quad (1.86)$$

$$\epsilon_{\downarrow}(k) = \epsilon_{\downarrow}(-k) \quad (1.87)$$

There are in principle two ways to lift spin degeneracy, namely by breaking either the time reversal symmetry (1.86) or the spatial inversion symmetry (1.87). The former way can be pursued, for instance, by introducing magnetic field \mathbf{B} i.e. a Zeeman splitting. The latter way can be achieved by two main mechanisms in a material. The first one is the lack of bulk inversion asymmetry(BIA), i.e. the lack of inversion symmetry inside the unitary cell, like for instance in zinc-blended crystal structures, which do not have a center

of inversion. This asymmetry is known as Dresselhaus SOC[1] and its lowest order term involve third power of momentum operator[67, 87]. Properties of Dresselhaus term are completely determined by underlying material and cannot be controlled externally. The other mechanism to break Inversion symmetry is the structural inversion asymmetry(SIA) that has a macroscopic origin such as the surface irregularity or external electric fields[67, 87] and becomes dominant in semiconducting heterojunctions. In particular, this is the case of a two-dimensional electron gas(2DEG) and may be shown to be linked to Rashba SOC term that in the case of confinement in z direction[5, 67]

$$H_{so} \propto \boldsymbol{\sigma} \times \hat{\mathbf{p}} \cdot \hat{\mathbf{z}} \quad (1.88)$$

The Rashba SOC is the most relevant inversion symmetry breaking term in low dimensional materials and typically overwhelms the Dresselhaus term [87]. Furthermore, the Rashba coupling constant could be controlled with external electric field, thereby allowing many interesting application involving spin polarization manipulations and spin filtering.

1.2.1 $\mathbf{k} \cdot \mathbf{p}$ theory

The Schrödinger equation of an electron in a material in the absence of an externally applied magnetic field is obtained from Eq.(1.43) by taking the crystal potential $V_0(\mathbf{r})$ as a potential and by setting $\mathbf{A} = 0$. Furthermore, we shall neglect the Darwin term, which is relevant only for atoms with small atomic numbers. Using $q\mathbf{E} = -\nabla V_0$ and exploiting $\boldsymbol{\sigma} \cdot (\nabla V_0 \times \hat{\mathbf{p}}) = (\boldsymbol{\sigma} \times \nabla V_0) \cdot \hat{\mathbf{p}}$, one obtains

$$\left(\frac{\hat{\mathbf{p}}^2}{2m_0} + qV_0(\mathbf{r}) + \frac{\hbar}{4m_0^2c^2} \boldsymbol{\sigma} \cdot \nabla V_0 \times \hat{\mathbf{p}} \right) \Psi = E\Psi \quad (1.89)$$

Solving this equation in principle one could find the full set of eigenfunction Ψ and corresponding eigenvalue E . However, this is in practice quite hard even without atomic-spin orbit coupling, and some approximation must be invoked. The $\mathbf{k} \cdot \mathbf{p}$ method is a powerful technique that in principle allows to calculate with arbitrary precision all energy band spectrum $E_{n,\mathbf{k}}$ around an arbitrary point \mathbf{k}_0 [25]. It relies on the fact that, due to the discrete translational symmetry of crystal potential V_0 , the wavefunction can be expressed in Bloch form

$$\Psi_{\nu,\mathbf{k}}(\mathbf{r}) = e^{i\mathbf{k}\cdot\mathbf{r}} u_{\nu,\mathbf{k}}(\mathbf{r}) \quad (1.90)$$

where ν is the band index, the envelope plane wave is slowly varying on the lattice period while $u_{\nu,\mathbf{k}}(\mathbf{r})$ has the cell-periodicity of the lattice.

The action of the momentum operator on the envelope plane wave can be expanded using the product rule for differentiation, and the Schrödinger equation can be written as

$$\left[\frac{\hat{\mathbf{p}}^2}{2m_0} + V_0(\mathbf{r}) + \frac{\hbar^2\mathbf{k}^2}{2m_0} + \frac{\hbar}{m_0} \mathbf{k} \cdot \left(\hat{\mathbf{p}} + \frac{\hbar}{4m_0^2c^2} \boldsymbol{\sigma} \times \nabla V_0(\mathbf{r}) \right) + \frac{\hbar}{4m_0^2c^2} \hat{\mathbf{p}} \cdot \boldsymbol{\sigma} \times \nabla V_0(\mathbf{r}) \right] |\nu, \mathbf{k}\rangle = E_{\nu,\mathbf{k}} |\nu, \mathbf{k}\rangle \quad (1.91)$$

where $u_{\nu, \mathbf{k}}(\mathbf{r}) = \langle \mathbf{r} | \nu, \mathbf{k} \rangle$. Notably, spin is no longer a good quantum number for Eq.(1.91), because the Hamiltonian does not commute with any Pauli matrix. Thus the index ν identifies a band label that is not spin degenerate. There are typically two strategies to solve the eigenvalue problem Eq.(1.91). The first one will be discussed here below, while the second one will be illustrated in the next subsection.

Perturbative approach in \mathbf{k}

The first approach consists in performing a perturbative expansion in \mathbf{k} . To illustrate the idea, imagine one has solved the associated equation without the spin-orbit terms

$$\left[\frac{\hat{\mathbf{p}}^2}{2m_0} + V_0(\mathbf{r}) + \frac{\hbar^2 \mathbf{k}^2}{2m_0} + \frac{\hbar}{m_0} \mathbf{k} \cdot \hat{\mathbf{p}} \right] |n, s, \mathbf{k}\rangle = E_{n, \mathbf{k}} |n, s, \mathbf{k}\rangle \quad (1.92)$$

which exhibits spin-degenerate bands labelled by n , so that

$$|n, s, \mathbf{k}\rangle = |n, \mathbf{k}\rangle \otimes |s\rangle \quad (1.93)$$

with $s = \uparrow, \downarrow$ denoting the spin degeneracy. Because the Hamiltonian in Eq.(1.92) is periodic for each \mathbf{k} , for a fixed \mathbf{k}_0 the set of eigenstates $|n, s, \mathbf{k}_0\rangle$, with varying n and s , form a complete basis set. One can thus expand the actual eigenfunction $|\nu, \mathbf{k}\rangle$ of Eq.(1.91) as a linear combination of the basis $|n, s, \mathbf{k}_0\rangle$ of eigenfunctions of Eq.(1.92). It is important to mention that, although the exact form and energy of these states are unknown, they are not strictly necessary. What is more important, instead, is the symmetry property of states at the point \mathbf{k}_0 . Since the Hamiltonian must be invariant under transformation of the symmetry group of the problem one may deduce which term must appear in it[25]. It is thus worth performing a state expansion around the high symmetry points, since that would allow to reduce the number of parameters that can be treated as phenomenological. For this purpose one can consider the Γ -point at $\mathbf{k}_0 = 0$ that belong to Tetrahedral symmetry group T_d . [46] Along with the symmetry property it is also a suitable choice because for customary semiconductors the extreme of band can be found in Γ -point[48], and the states in this point are referred as *band edge states*. The full cell periodic wavefunction can be expressed as their linear combination

$$|\nu, \mathbf{k}\rangle = \sum_{m, s \in \{\uparrow, \downarrow\}} c_{\nu, (m, s)}(\mathbf{k}) |m, s\rangle \quad (1.94)$$

where $c_{\nu, (m, s)}(\mathbf{k}) \in \mathbb{C}$ are the expansion coefficient and the band edge states $|m, s\rangle = |m, 0\rangle \otimes |s\rangle$ are eigenfunctions of $\mathbf{k} = 0$ Hamiltonian (1.92) without spin-orbit coupling.

$$\langle m', s' | \frac{\mathbf{p}^2}{2m_0} + V_0 |m, s\rangle = E_{m, 0} \delta_{m', m} \delta_{s, s'} \quad (1.95)$$

Substituting the cell periodic wavefunction expansion into eq.(1.91) and projecting it on an arbitrary base $\langle m', s' |$ one can find¹

$$\sum_{m,s} \left[\left(E_{m,0} + \frac{\hbar^2 k^2}{2m_0} \right) \delta_{m',m} \delta_{s,s'} + \frac{\hbar}{m_0} \mathbf{k} \cdot \mathbf{P}_{(m',s'),(m,s)} + \Delta_{(m',s'),(m,s)} \right] c_{\nu,(m,s)}(\mathbf{k}) = E_{\nu,\mathbf{k}} c_{\nu,(m,s)}(\mathbf{k}) \quad (1.96)$$

$$\mathbf{P}_{(m',s'),(m,s)} = \langle m', s' | \mathbf{p} + \frac{\hbar}{4m_0^2 c^2} \boldsymbol{\sigma} \times \nabla V_0 | m, s \rangle \quad (1.97)$$

$$\Delta_{(m',s'),(m,s)} = \frac{\hbar}{4m_0^2 c^2} \langle m', s' | \mathbf{p} \cdot \boldsymbol{\sigma} \times \nabla V_0 | m, s \rangle \quad (1.98)$$

It is common practice in literature[25, 30] to neglect spin orbit term in (1.97) and in this way it can be rewritten as a momentum matrix

$$\mathbf{P}_{(m',s'),(m,s)} \simeq \langle m' | \hat{\mathbf{p}} | m \rangle \delta_{s',s} \quad (1.99)$$

In general, Eq. (1.96) is an infinite dimensional linear system whose solution are set of all expansion coefficient $\{c_{\nu,(m,s)}(\mathbf{k})\}$ and corresponding energies $\{E_{\nu,\mathbf{k}}\}$. However, due to the presence of the off-diagonal term as momentum $\mathbf{P}_{(m',s'),(m,s)}$ and atomic spin-orbit coupling $\Delta_{(m',s'),(m,s)}$ matrices, the expansion coefficients of different bands turn out to be coupled, thereby complicating the problem significantly.

Effective mass approximation.

We start by illustrating the diagonalization of (1.96) by means of the second order perturbation theory[25] considering $\mathbf{k} \cdot \mathbf{P}_{(m',s')}$ and $\Delta_{(m',s')}$ as a small perturbation. In this case the dispersion relation is quadratic in the wave vector \mathbf{k} and can be shown to acquire the form[4, 8]

$$E_{n,\mathbf{k}} = E_{n,0} + \frac{\hbar^2}{2m_0} \mathbf{k}^2 + \frac{\hbar^2}{m_0^2} \sum_{m \neq n} \frac{|\mathbf{k} \cdot \langle n | \hat{\mathbf{p}} | m \rangle|^2}{E_{n,0} - E_{m,0}} \quad (1.100)$$

which can also be rewritten as

$$E_{n,\mathbf{k}} = E_{n,0} + \frac{\hbar^2}{2} \sum_{\alpha,\beta \in (x,y,z)} k_\alpha \frac{1}{\mu_n^{\alpha,\beta}} k_\beta \quad (1.101)$$

through the effective mass tensor $\mu_n^{\alpha,\beta}$ [8]

$$\frac{1}{\mu_n^{\alpha,\beta}} = \frac{1}{m_0} \delta_{\alpha,\beta} + \frac{2}{m_0^2} \sum_{m \neq n} \frac{\langle m | \hat{p}_\alpha | n \rangle \langle n | \hat{p}_\beta | m \rangle}{E_{n,0} - E_{m,0}} \quad (1.102)$$

¹Where have been considered the mean value of an general operator to be defined as $A_{(m',s'),(m,s)} = \langle m', s' | \hat{A} | m, s \rangle = \int_{\text{unit cell}} \langle s' | u_{m',0}^\dagger(r) \hat{A} u_{m,0}(r) | s \rangle dr$

where $\alpha, \beta \in (x, y, z)$ and \hat{p}_α a component of momentum operator. As can be seen from dispersion relation (1.100) the second order corrections are proportional to the inverse band edge gap $E_{n,0} - E_{m,0}$. This expression holds as long as $|\mathbf{k}|$ is small. More quantitatively, it holds if the energy difference $|E_{n,\mathbf{k}} - E_{n,0}|$ remains much smaller than all band gaps $|E_{n,0} - E_{m,0}|$, i.e. if kinetic energy term $\hbar^2 \mathbf{k}^2 / 2m_0$ is smaller than the smallest band edge gap. For this reason in some semiconducting materials with narrow fundamental gap, namely direct gap between conducting and valence band, the parabolic effective model for conducting states can loose its validity[4]. One could in principle improve the calculations by going to higher orders in \mathbf{k} in the perturbation theory. However, this strategy is typically quite cumbersome. Kane adopted another approach to tackle the problem, instead.

1.2.2 The Kane model

The second approach to solve the problem Eq.(1.91) consists in diagonalizing it exactly, i.e. at arbitrary \mathbf{k} , within a *restricted* set of bands. Indeed one can observe that, as far as conduction properties are concerned, only the states close to the Fermi level are relevant. In this way one focuses on a limited subset of bands, while the rest can be treated as a perturbation. This is the procedure proposed by Kane and the resulting model is called the Kane model[4, 8]. Within this approximation, one can thus expand the actual state $|\nu, \mathbf{k}\rangle$ in Eq.(1.91) in terms of a restricted set of N band edge states $|m\rangle$

$$|\nu, \mathbf{k}\rangle \simeq \sum_{m=1}^N \tilde{c}_{\nu,m}(\mathbf{k}) |m\rangle \quad (1.103)$$

Importantly, in Kane's approach the band edge states $|m\rangle$ are not spin degenerate, since they are chosen in such a way to diagonalize the spin orbit term in Eq.(1.91) at $\mathbf{k} = 0$

$$\langle m' | \left[\frac{\hat{\mathbf{p}}^2}{2m_0} + V_0(\mathbf{r}) + \frac{\hbar}{4m_0^2 c^2} \hat{\mathbf{p}} \cdot \boldsymbol{\sigma} \times \nabla V_0(\mathbf{r}) \right] |m\rangle = E_{m,0} \delta_{m',m} \quad (1.104)$$

whereas for $\mathbf{k} \neq 0$ one obtains from Eq.(1.91) the following set of equations

$$\sum_m^N \left[\left(E_{m,0} + \frac{\hbar^2 k^2}{2m_0} \right) \delta_{m',m} + \frac{\hbar}{m_0} \mathbf{k} \cdot \mathbf{P}_{m',m} \right] \tilde{c}_{\nu,m}(\mathbf{k}) = E_{\nu,\mathbf{k}} \tilde{c}_{\nu,m}(\mathbf{k}) \quad (1.105)$$

where

$$\mathbf{P}_{m',m} \simeq \langle m' | \mathbf{p} | m \rangle \quad (1.106)$$

Despite looking similar to Eqs.(1.96)-(1.97), the set Eqs.(1.105) is a set of finite dimensional linear equations, since the number of considered states has been restricted to N . Note that, even if the new band edge set has been chosen in such a way to diagonalize the SOC term at $\mathbf{k} = 0$, there may still be off-diagonal terms in the momentum matrix (1.106) that would couple bands for $\mathbf{k} \neq 0$. Nevertheless, based on the symmetry considerations, it can be shown that the number of off-diagonal terms is significantly reduced and the remaining ones are parameterized by a single phenomenological parameter.

In order to implement the Kane approach, one has first to identify the basis $|m\rangle$ diagonalizing Eq.(1.104). As has been discussed in section 1.1.6, the spin orbit coupling term can be diagonalized with total angular momentum basis[30, 47] and therefore one may expect $|m\rangle \mapsto |J, m_J\rangle$. In this way the SO coupling term is expected to be diagonal and recalling Eq.(1.83)

$$\langle H_{SO} \rangle \propto \left[j(j+1) - l(l+1) - \frac{3}{4} \right] \quad (1.107)$$

whence one deduces that all states are degenerate with respect to the sign change of m_J . As will be seen below, the restricted set of band is composed by four elements, each with a twofold degeneracy corresponding to the opposite values of m_J [8]. We can proceed in three steps:

1. First of all let us discuss the eigenstates $|m\rangle$ in absence of the spin orbit coupling matrix, i.e. when the second term on the l.h.s of in Eq.(1.104) is vanishing. In this case the eigenstates are spin degenerate. Because spin is a merely dummy variable, it will be neglected for the moment and reintroduced properly later. Therefore the reduced Kane model is expected to take into account only 4 band edge states that can be constructed with hybridized atomic states. Indeed in IV-V semiconductors characterized by zinc-blended lattices there are 2 atoms per unit cell and the valence electron form tetrahedral bonds with nearest neighbors and give raise in this way binding and anti-bonding hybridized states. The wavefunction of the binding state is concentrated in the space between 2 atoms and thus promotes the covalent bonding, and vice versa for anti-bonding state wavefunction. Since solids consist of a large number of unit cells, bonding and anti-bonding levels are broader into Energy bands. The bonding states contribute to valence band, while the anti-bonding states to conducting band[8, 30]. At the high symmetry Γ -point these states are expected to transform according to the symmetry of the underlying lattice and may be identified with s-like conducting states $|S\rangle$ and triple degenerate p-like valence state $|X\rangle$, $|Y\rangle$ and $|Z\rangle$ [8]. This definition meant to highlight the equivalence with the atomic s- and p-state under symmetry transformation of the tetrahedral point group that is indeed the symmetry group of the blended lattices type[2–4, 8, 46]. Since the precise expression of the states has not been taken into account and only symmetry property have been invoked, the corresponding energy of the states are treated as phenomenological parameters that can be fit from experimental data

$$\left(\frac{\hat{\mathbf{p}}^2}{2m_0} + V_0(\mathbf{r}) \right) |S\rangle = E_{s,0}|S\rangle \quad (1.108)$$

$$\left(\frac{\hat{\mathbf{p}}^2}{2m_0} + V_0(\mathbf{r}) \right) |M\rangle = E_{p,0}|M\rangle \quad (1.109)$$

with $M \in \{X, Y, Z\}$ and can be defined the direct gap energy scale $E_0 = E_{s,0} - E_{p,0}$, indeed only the energy differences matter, rather than their absolute magnitudes. Exploiting the symmetry of the states can be show that the number of elements of

momentum matrix can be significantly reduced. Indeed by observing that

$$[H_0, \mathbf{r}] = -\frac{i\hbar}{m_0} \hat{\mathbf{p}} \quad (1.110)$$

one has[30]

$$-i\frac{\hbar}{m_0} \langle m' | \hat{\mathbf{p}} | m, \rangle = [E_{m',0} - E_{m,0}] \langle m' | \mathbf{r} | m \rangle \quad (1.111)$$

where $m', m \in \{S, X, Y, Z\}$ in this way degenerate p-like states are not mutually coupled. Therefore it is enough to introduce only one phenomenological parameter that would describe the coupling of the s-like and p-like states

$$i\frac{m_0}{\hbar} P_0 = \langle S | \hat{p}_x | X \rangle = \langle S | \hat{p}_y | Y \rangle = \langle S | \hat{p}_z | Z \rangle \quad (1.112)$$

2. Let us now construct eigenstates of the orbital angular momentum part $|l, l_z\rangle$. By analogy with atomic state the s-like states are characterized by state with angular momentum $l = 0$ in this way can be identified orbital angular momentum basis with

$$|0,0\rangle = |S\rangle \quad (1.113)$$

On the other hand p-like state are associated with $l = 1$ and orbital angular momentum basis can be expressed as combination of p-like states

$$|1,1\rangle = -\frac{1}{\sqrt{2}} (|X\rangle + i|Y\rangle) \quad (1.114)$$

$$|1,0\rangle = |Z\rangle \quad (1.115)$$

$$|1,-1\rangle = \frac{1}{\sqrt{2}} (|X\rangle - i|Y\rangle) \quad (1.116)$$

3. Finally, let us now re-introduce the spin degree of freedom by adding half integer spin states $|1/2, +1/2\rangle = |\uparrow\rangle$ and $|1/2, -1/2\rangle = |\downarrow\rangle$, the total angular momentum eigenfunctions are expressed as combination of states that satisfy the quantum number constraint $j = l \pm 1/2$ and $m_j \in \{-j, j\}$, and 8 band edge basis can be written

as [4, 8, 25, 30, 46]

$$|\frac{1}{2}, \frac{1}{2}\rangle = |0,0\rangle \otimes |\uparrow\rangle = |S, \uparrow\rangle \quad (1.117)$$

$$|\frac{1}{2}, -\frac{1}{2}\rangle = |0,0\rangle \otimes |\downarrow\rangle = |S, \downarrow\rangle \quad (1.118)$$

$$|\frac{3}{2}, \frac{1}{2}\rangle = \sqrt{\frac{2}{3}}|1,0\rangle \otimes |\uparrow\rangle + \sqrt{\frac{1}{3}}|1,1\rangle \otimes |\downarrow\rangle = \sqrt{\frac{2}{3}}|Z, \uparrow\rangle - \sqrt{\frac{1}{6}}(|X, \downarrow\rangle + i|Y, \downarrow\rangle) \quad (1.119)$$

$$|\frac{3}{2}, -\frac{1}{2}\rangle = \sqrt{\frac{1}{3}}|1, -1\rangle \otimes |\uparrow\rangle + \sqrt{\frac{2}{3}}|1,0\rangle \otimes |\downarrow\rangle = \sqrt{\frac{2}{3}}|Z, \downarrow\rangle + \sqrt{\frac{1}{6}}(|X, \uparrow\rangle - i|Y, \uparrow\rangle) \quad (1.120)$$

$$|\frac{3}{2}, \frac{3}{2}\rangle = |1,1\rangle \otimes |\uparrow\rangle = -\frac{1}{\sqrt{2}}(|X, \uparrow\rangle + i|Y, \uparrow\rangle) \quad (1.121)$$

$$|\frac{3}{2}, -\frac{3}{2}\rangle = |1, -1\rangle \otimes |\downarrow\rangle = \frac{1}{\sqrt{2}}(|X, \downarrow\rangle - i|Y, \downarrow\rangle) \quad (1.122)$$

$$|\frac{1}{2}, \frac{1}{2}\rangle = -\sqrt{\frac{1}{3}}|1,0\rangle \otimes |\uparrow\rangle + \sqrt{\frac{2}{3}}|1,1\rangle \otimes |\downarrow\rangle = -\sqrt{\frac{1}{3}}(|X, \downarrow\rangle + i|Y, \downarrow\rangle + |Z, \uparrow\rangle) \quad (1.123)$$

$$|\frac{1}{2}, -\frac{1}{2}\rangle = -\sqrt{\frac{2}{3}}|1, -1\rangle \otimes |\uparrow\rangle + \sqrt{\frac{1}{3}}|1,0\rangle \otimes |\downarrow\rangle = -\sqrt{\frac{1}{3}}(|X, \uparrow\rangle - i|Y, \uparrow\rangle - |Z, \downarrow\rangle) \quad (1.124)$$

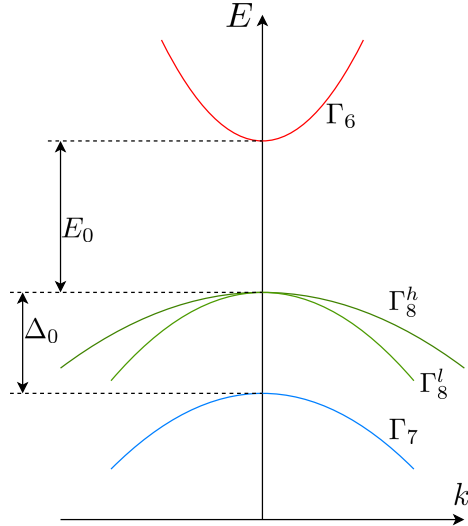


Figure 1.1: Band structure in the vicinity of the Γ -point. Conducting states correspond to the Γ_6 symmetry while valence to the Γ_7, Γ_8 symmetry. E_0 is the semiconductor energy gap and Δ_0 is splitting introduced by SOC term. Light holes Γ_8^l are associated with states $m_J = \pm 1/2$ and heavy holes Γ_8^h with $m_J = \pm 3/2$. [8]

The band structure is qualitatively depicted in Fig.(1.1), where E_0 is direct semiconductor gap and Δ_0 is valence band splitting due to the spin orbit coupling. States (1.117-1.118) are associated with Γ_6 conduction band and have zero angular momentum, therefore the spin-orbit terms is expected to vanish as well. On the other hand the valence band is formed by combination of p-like state (1.119-1.124), and are expected to be degenerate in absence of SOC. The effect of the SOC term is to split this 6 state into 2 group that contribute to different valence subband. First of all may be considered 4-th fold degenerate Γ_8 band to which belong states (1.119-1.122). The expectation value of SOC for Γ_8 band can be evaluated as $\langle H_{so} \rangle_{\Gamma_8} \propto \hbar^2/2$. On the other hand states (1.123-1.124) form 2-fold degenerate Γ_7 band and SOC energy contribution is $\langle H_{so} \rangle_{\Gamma_7} \propto -\hbar^2$. In this way valence subbands are splitted by spin orbit term, that can be treated as phenomenological parameter

$$\Delta_0 = \langle H_{so} \rangle_{\Gamma_8} - \langle H_{so} \rangle_{\Gamma_7} \propto \frac{3}{2} \hbar^2 \quad (1.125)$$

In conclusion one can notice that Γ_8 -band is fourfold degenerate only for $\mathbf{k} = 0$ instead for $\mathbf{k} \neq 0$ is expected to split into 2 sub band characterised by different effective mass namely light holes Γ_8^l and heavy holes Γ_8^h where former is characterized by $m_j = \pm 1/2$ and later is associated with $m_j = \pm 3/2$ More in details the difference between the light and heavy holes can be seen by enforcing the validity of the effective mass approximation Eq.(1.102) in the case of restricted state space and for the sake of simplicity considering $\alpha = \beta = z$. Using the definition of states (1.121-1.122), can be shown that heavy hole band Γ_8^h does not coupled with Γ_6 by momentum matrix

$$\left\langle \frac{1}{2}, \pm \frac{1}{2} \left| p_z \right| \frac{3}{2}, \pm \frac{3}{2} \right\rangle = 0 \quad (1.126)$$

therefore the effective mass of Γ_8^h states is the same as bare electron mass[8]. On the other hand states (1.119-1.120) are coupled with Γ_6 states by momentum matrix and their effective mass can be approximated as[8]

$$\frac{1}{m_{\Gamma_8^l}} = \frac{1}{m_0} - \frac{4P_0^2}{3\hbar E_0} \quad (1.127)$$

So far we have seen that band coupling term can be significantly simplified by applying symmetry considerations and by introducing an appropriate basis. A cell periodic wavefunction is approximated by a linear combination of finite number band edge basis $|m\rangle$ that can be labeled by the superindex $m = (j, j_z)$ as in Eqs.(1.117) to (1.124). Since the correspondence is established on the basis of the symmetry arguments, the specific form of the states is unimportant, and the corresponding energies and spin orbit splitting can be introduced as phenomenological parameter E_0 and Δ_0 , respectively

$$\langle m' | \left(\frac{\hat{\mathbf{p}}^2}{2m_0} + V_0(\mathbf{r}) + \frac{\hbar}{4m_0^2 c^2} \hat{\mathbf{p}} \cdot \boldsymbol{\sigma} \times \nabla V_0(\mathbf{r}) \right) | m \rangle = \begin{cases} 0 & \text{if } m, m' = 1, 2 \\ -E_0 \delta_{m', m} & \text{if } m, m' = 3 : 6 \\ -(E_0 + \Delta_0) \delta_{m', m} & \text{if } m, m' = 7, 8 \end{cases} \quad (1.128)$$

Since the basis states are expressed in term of s-like and p-like states [see Eqs.(1.117) to (1.124)], all non-vanishing entries of the momentum matrix (1.106) turn out to be proportional to phenomenological parameter P_0 defined through Eq.(1.112), and read

$$\mathbf{P}_{1,3} = i \frac{m_0 P_0}{\hbar} \sqrt{\frac{2}{3}} \begin{pmatrix} 0 \\ 0 \\ 1 \end{pmatrix} \quad \mathbf{P}_{1,4} = i \frac{m_0 P_0}{\hbar} \sqrt{\frac{1}{6}} \begin{pmatrix} 1 \\ -i \\ 0 \end{pmatrix} \quad \mathbf{P}_{1,5} = -i \frac{m_0 P_0}{\hbar} \sqrt{\frac{1}{2}} \begin{pmatrix} 1 \\ i \\ 0 \end{pmatrix} \quad (1.129)$$

$$\mathbf{P}_{1,7} = -i \frac{m_0 P_0}{\hbar} \sqrt{\frac{1}{3}} \begin{pmatrix} 0 \\ 0 \\ 1 \end{pmatrix} \quad \mathbf{P}_{1,8} = -i \frac{m_0 P_0}{\hbar} \sqrt{\frac{1}{3}} \begin{pmatrix} 1 \\ -i \\ 0 \end{pmatrix}$$

$$\mathbf{P}_{2,3} = -i \frac{m_0 P_0}{\hbar} \sqrt{\frac{1}{6}} \begin{pmatrix} 1 \\ i \\ 0 \end{pmatrix} \quad \mathbf{P}_{2,4} = i \frac{m_0 P_0}{\hbar} \sqrt{\frac{2}{3}} \begin{pmatrix} 0 \\ 0 \\ 1 \end{pmatrix} \quad \mathbf{P}_{2,6} = i \frac{m_0 P_0}{\hbar} \sqrt{\frac{1}{2}} \begin{pmatrix} 1 \\ -i \\ 0 \end{pmatrix} \quad (1.130)$$

$$\mathbf{P}_{2,7} = -i \frac{m_0 P_0}{\hbar} \sqrt{\frac{1}{3}} \begin{pmatrix} 1 \\ i \\ 0 \end{pmatrix} \quad \mathbf{P}_{2,8} = i \frac{m_0 P_0}{\hbar} \sqrt{\frac{1}{3}} \begin{pmatrix} 0 \\ 0 \\ 1 \end{pmatrix}$$

In this way Eq.(1.105) can be rewritten in matrix form

$$H \tilde{c}_\nu(\mathbf{k}) = E_{\nu, \mathbf{k}} \tilde{c}_\nu(\mathbf{k}) \quad (1.131)$$

where $\tilde{c}_\nu(\mathbf{k}) = (\tilde{c}_{m,i}(\mathbf{k}))_{i=1}^8$ is 8-component vector and H is 8×8 matrix[25]

$$H = \begin{pmatrix} \frac{\hbar^2 k^2}{2m_0} & 0 & i\sqrt{\frac{2}{3}}P_0 k_z & i\sqrt{\frac{1}{6}}P_0 k_- & -i\sqrt{\frac{1}{2}}P_0 k_+ & 0 & -i\sqrt{\frac{1}{3}}P_0 k_z & -i\sqrt{\frac{1}{3}}P_0 k_- \\ 0 & \frac{\hbar^2 k^2}{2m_0} & -i\sqrt{\frac{1}{6}}P_0 k_+ & i\sqrt{\frac{2}{3}}P_0 k_z & 0 & i\sqrt{\frac{1}{2}}P_0 k_- & -i\sqrt{\frac{1}{3}}P_0 k_+ & i\sqrt{\frac{1}{3}}P_0 k_z \\ -i\sqrt{\frac{2}{3}}P_0 k_z & i\sqrt{\frac{1}{6}}P_0 k_- & \frac{\hbar^2 k^2}{2m_0} - E_0 & 0 & 0 & 0 & 0 & 0 \\ -i\sqrt{\frac{1}{6}}P_0 k_+ & -i\sqrt{\frac{2}{3}}P_0 k_z & 0 & \frac{\hbar^2 k^2}{2m_0} - E_0 & 0 & 0 & 0 & 0 \\ i\sqrt{\frac{1}{2}}P_0 k_- & 0 & 0 & 0 & \frac{\hbar^2 k^2}{2m_0} - E_0 & 0 & 0 & 0 \\ 0 & -i\sqrt{\frac{1}{2}}P_0 k_+ & 0 & 0 & 0 & \frac{\hbar^2 k^2}{2m_0} - E_0 & 0 & 0 \\ i\sqrt{\frac{1}{3}}P_0 k_z & i\sqrt{\frac{1}{3}}P_0 k_- & 0 & 0 & 0 & 0 & \frac{\hbar^2 k^2}{2m_0} - E_0 - \Delta_0 & 0 \\ i\sqrt{\frac{1}{3}}P_0 k_+ & -i\sqrt{\frac{1}{3}}P_0 k_z & 0 & 0 & 0 & 0 & 0 & \frac{\hbar^2 k^2}{2m_0} - E_0 - \Delta_0 \end{pmatrix} \quad (1.132)$$

with $k_\pm = k_x \pm ik_y$.

1.3 The effects of confinement potentials

In this section I shall present the envelope function formalism that can be seen as a generalization of the $\mathbf{k} \cdot \mathbf{p}$ theory in the case of non-periodic potential[30] originated from either an external electric fields or internal irregularities[25]. The underlying hypothesis of this approximation is that the external potential $V(\mathbf{r})$ varies slowly over the crystal period. Indeed in each unit cell the external potential is perceived as constant energy

shift in this way different unperturbed band can be still considered independent since the coupling term is $\int_{\text{unit cell}} u_{\nu',k'}(\mathbf{r})^\dagger V(\mathbf{r}) u_{\nu,k}(\mathbf{r}) d\mathbf{r} \simeq \delta_{\nu',\nu} \delta_{k',k} V(\mathbf{r})$. In this way the effect of non-periodic potential can be taken into account on macroscopic level by a envelope function that may be seen as generalization of the envelope plane wave in the case of Bloch function.

We first present the envelope function formalism that allows to write a finite dimensional system of equation similar to Eq.(1.131) with the difference that the Hamiltonian in the case of the envelope function is expected to be a tensor instead of a matrix and the complex coefficients are substituted by functions. One can thus exploit the same band edge states and all the results discussed in the previous section. Next we use the envelope function approximation to derive the macroscopic model of the semiconductor hetero structure. The different material property in each level are taken into account by phenomenological parameters and the heterojunction is represented by a step-like profile of the phenomenological parameters. In this way at the interfaces between different materials one expects the discontinuity of the potential that seemingly violates the basic assumption on slowly varying potentials[25]. However, as long as the actual potential varies smoothly over the lattice spacing, this effective model is known to provide results in agreement with the experiments[8]. Finally we trace out the transversal degrees of freedom and present the effective model for 2DEG with the Rashba spin orbit term[30].

1.3.1 The envelope function approximation

So far we have considered only the crystal periodic potential $V_0(\mathbf{r})$, and thus the Bloch function $\Psi_{n,\mathbf{k}}$ indeed can be used. However, in the presence of an additional external potential $V(\mathbf{r})$ that is not necessarily periodic, the discrete translational symmetry is broken. The Schrödinger equation reads[25]

$$\left[\frac{\hat{\mathbf{p}}^2}{2m_0} + V_0(\mathbf{r}) + V(\mathbf{r}) + \frac{\hbar}{4m_0^2 c^2} \hat{\mathbf{p}} \cdot \boldsymbol{\sigma} \times \nabla V_0(\mathbf{r}) \right] \Psi = E\Psi \quad (1.133)$$

and the Bloch wavefunctions are no longer eigenfunctions. Nevertheless the total wavefunction can still be expanded in term of Bloch wavefunction

$$\Psi(\mathbf{r}) = \sum_{\nu,\mathbf{k}} a_{\nu,\mathbf{k}} \Psi_{\nu,\mathbf{k}}(\mathbf{r}) = \sum_{\nu,\mathbf{k}} a_{\nu,\mathbf{k}} e^{i\mathbf{k}\cdot\mathbf{r}} u_{\nu,\mathbf{k}}(\mathbf{r}) \quad (1.134)$$

or equivalently

$$|\Psi\rangle = \sum_{\nu,\mathbf{k}} a_{\nu,\mathbf{k}} e^{i\mathbf{k}\cdot\mathbf{r}} |\nu, \mathbf{k}\rangle \quad (1.135)$$

where $a_{n,\mathbf{k}}$ are coefficients. In analogy with $\mathbf{k} \cdot \mathbf{p}$ theory, the cell periodic part can be approximated as a combination of finite number of band edge basis at $\mathbf{k} = 0$ [25] therefore using the decomposition for cell periodic state (1.103) can be rewritten as

$$|\Psi\rangle \simeq \sum_{\nu,\mathbf{k}} \sum_m a_{\nu,\mathbf{k}} e^{i\mathbf{k}\cdot\mathbf{r}} \tilde{c}_{\nu,m}(\mathbf{k}) |m\rangle \quad (1.136)$$

where $|m\rangle$ are the band edge states (1.117-1.124) discussed in previous section. Finally, by introducing the function

$$f_m(\mathbf{r}) = \sum_{\nu, \mathbf{k}} a_{\nu, \mathbf{k}} \tilde{c}_{\nu, m}(\mathbf{k}) e^{i\mathbf{k} \cdot \mathbf{r}} \quad (1.137)$$

the total wavefunction can be expressed as[8, 25]

$$|\Psi\rangle \simeq \sum_m f_m(\mathbf{r}) |m\rangle \quad (1.138)$$

where the function $f_m(\mathbf{r})$ varies slowly in space and take into account the spatial dependence introduced by external field. It is commonly referred as envelope function, since it modulate the fast oscillating of the cell periodic part $|m\rangle$ [8, 30]. Finally the approximation of the wavefunction is plugged into Eq.(1.133) and projected on an arbitral basis $\langle m'|$, in this way can be found

$$\sum_m \left[\left(\frac{\hat{\mathbf{p}}^2}{2m_0} + V(\mathbf{r}) + E_m^{(0)} \right) \delta_{m', m} + \frac{1}{m_0} \hat{\mathbf{p}} \cdot \mathbf{P}_{m', m} \right] f_m(\mathbf{r}) = E f_{m'}(\mathbf{r}) \quad (1.139)$$

where band edge energy $E_m^{(0)}$ and momentum matrix $\mathbf{P}_{m', m}$ are the same that have been found in previous section and correspond respectively to Eq.(1.128) and Eq.(1.129-1.130). In this way the full problem of the bulk electron has been reformulated as the set of the second order differential equation that describes the system at a macroscopic level. The microscopic details corresponding to the fast oscillating cell periodic wavefunction are taken into account by 3 phenomenological parameter E_0, Δ_0, P_0 [8]. The system of coupled second order equation can be rewritten in matrix-form[30]

$$\mathbf{H} \mathbf{f} = E \mathbf{f} \quad (1.140)$$

where $\mathbf{f}(\mathbf{r}) = (f_m(\mathbf{r}))_{m=1}^8$ is a 8-component vector of envelope functions and \mathbf{H} is a 8×8 tensor that can be separated in 4 blocks[30]

$$\mathbf{H} = \begin{pmatrix} H_c & H_{cv} \\ H_{vc} & H_v \end{pmatrix} \quad (1.141)$$

where H_c is a tensor that describes the envelope function associated with conduction band Γ_6

$$H_c = \left(\frac{\hat{\mathbf{p}}^2}{2m_0} + V(\mathbf{r}) \right) 1_{2 \times 2} \quad (1.142)$$

On the other hand the H_v acts on the valence envelope functions. It is important to notice that the kinetic energy term can be neglected, indeed since the envelope function is assumed to vary slowly therefore one can expect that kinetic energy is negligible with respect to fundamental gap energy scale $\mathbf{p}^2/2m_0 \ll E_0$, that indeed is expected to be dominant[30].

$$H_v = (V(\mathbf{r}) - E_0) 1_{6 \times 6} - \begin{pmatrix} 0 & 0 & 0 & 0 & 0 & 0 \\ 0 & 0 & 0 & 0 & 0 & 0 \\ 0 & 0 & 0 & 0 & 0 & 0 \\ 0 & 0 & 0 & 0 & 0 & 0 \\ 0 & 0 & 0 & 0 & \Delta_0 & 0 \\ 0 & 0 & 0 & 0 & 0 & \Delta_0 \end{pmatrix} \quad (1.143)$$

And finally H_{cv} is the tensor that couples the envelope function of the conduction and valence bands

$$H_{cv} = i \begin{pmatrix} \sqrt{\frac{2}{3}} \frac{P_0}{\hbar} \hat{p}_z & \frac{1}{\sqrt{6}} \frac{P_0}{\hbar} \hat{p}_- & -\frac{1}{\sqrt{2}} \frac{P_0}{\hbar} \hat{p}_+ & 0 & -\frac{1}{\sqrt{3}} \frac{P_0}{\hbar} \hat{p}_z & -\frac{1}{\sqrt{3}} \frac{P_0}{\hbar} \hat{p}_- \\ -\frac{1}{\sqrt{6}} \frac{P_0}{\hbar} \hat{p}_+ & \sqrt{\frac{2}{3}} \frac{P_0}{\hbar} \hat{p}_z & 0 & \frac{1}{\sqrt{2}} \frac{P_0}{\hbar} \hat{p}_- & -\frac{1}{\sqrt{3}} \frac{P_0}{\hbar} \hat{p}_+ & \frac{1}{\sqrt{3}} \frac{P_0}{\hbar} \hat{p}_z \end{pmatrix} \quad (1.144)$$

where have been introduced $\hat{p}_\pm = \hat{p}_x \pm i\hat{p}_y$ and \hat{p}_i $i \in \{x, y, z\}$ are the i -th component of the momentum operator $\hat{\mathbf{p}}$. In order to guaranty the total Hamiltonian \mathbf{H} to be Hermitian one may expect $H_{vc} = H_{cv}^\dagger$.

1.3.2 SOC in a quantum well

At this point the microscopical details of the material have been taken into account with phenomenological parameters and the material is described with an effective model on the length scales much larger than the unit cell. In this way one may attempt to construct macroscopic model for inhomogeneous structure such as 2DEG that can be realized by growing in layers different types of materials or modulating doping density. Since microscopic details have been traced out, irregularities of the heterojunction can be neglected as well. The interface may be assumed to be perfectly flat and can be modulated with piecewise profile of band edge energy, even though the cell periodic wavefunctions are still assumed to be the same in all the materials[8].

I shall focus on the quantum well configuration of the conduction band, where the material A in the central region has the lowest conduction band edge energy and is interfaced from 2 sides with material B. We take the growth direction along (001) and heterojunction can be modulated with piecewise profile of the phenomenological parameters along z -axis

$$E_0(z) = E_0^B \Theta(|z| - d/2) + E_0^A \Theta(-|z| + d/2) \quad (1.145)$$

$$\Delta_0(z) = \Delta_0^B \Theta(|z| - d/2) + \Delta_0^A \Theta(-|z| + d/2) \quad (1.146)$$

where $\Theta(z)$ is heavy side function and d is the length of central region. It also can be introduce the external electric field $V_{ext}(z)$ slowly varying along the z -direction and the non-periodic potential can be decomposed as

$$V(z) = V_{ext}(z) + E_c(z) \quad (1.147)$$

where $E_c(z)$ is a profile of conduction band edge offset with $E_c^A = 0$ that form the quantum well potential for conduction electrons $E_c(z) = E_c^B \Theta(|z| - d/2)$. Finally can be introduced valence band edge energy

$$E_v(z) = V(z) - E_0(z) \quad (1.148)$$

the band structure of the heterojunction is pictured on the Fig.(1.2)

Since we are analyzing the case with vanishing magnetic field and external electric field only along z , the electron motion in $x - y$ plane can be considered free and the envelope function can be decomposed into in plane and transversal parts

$$\mathbf{f} = e^{ik_{\parallel}r_{\parallel}} \mathbf{g}(z) \quad (1.149)$$

included in the effective way. One way to do it would be by using the Löwdin partitioning. However the application turns out to be problematic, due to the space dependent diagonal term and as follow the right ordering of matrix term in perturbation expansion. Moreover, beyond the first few terms the perturbative approach becomes cumbersome. A more systematic approach is the "folding down" method[30], which consists in introducing a unitary matrix

$$U = \begin{pmatrix} 1_{2 \times 2} & -(H_c - E)^{-1} H_{cv} \\ -(H_c - E)^{-1} H_{vc} & 1_{6 \times 6} \end{pmatrix} \quad (1.153)$$

and the system of differential equations can be rewritten as

$$\tilde{H}\tilde{g} = E\tilde{g} \quad (1.154)$$

where

$$\tilde{g} = U^{-1}g \quad (1.155)$$

$$\tilde{H} = E + (H - E)U = \begin{pmatrix} \tilde{H}_c & 0 \\ 0 & \tilde{H}_v \end{pmatrix} \quad (1.156)$$

We first observe that, since the Hamiltonian (1.156) is dependent on the energy E , the system (1.154) must be treated in self consistent way. This may lead to non-parabolic dispersion relation even for in-plane motion and should be resolved approximately. On the other hand the valence and conduction bands are decoupled and in principle can be studied separately[30]. In this way if one is interested only in conduction band \mathbf{g}_c it is straightforward to see from definition of U that $\tilde{\mathbf{g}}_c = \mathbf{g}_c$ and the system of equation for conduction band envelope functions reduce to

$$\tilde{H}_c \begin{pmatrix} g_1 \\ g_2 \end{pmatrix} = E \begin{pmatrix} g_1 \\ g_2 \end{pmatrix} \quad (1.157)$$

with $\tilde{H}_c = H_c - H_{cv}(H_v - E)^{-1}H_{vc}$. In the case H_v is diagonal it is trivial to perform the inversion and the effective model for conduction band can be written

$$\tilde{H}_c = \left(-\frac{\hbar^2 k_{\parallel}^2}{2m_0} + \frac{p_z^2}{2m_0} + V_{ext}(z) + E_c(z) \right) 1_{2 \times 2} - \begin{pmatrix} M & N \\ N^* & M \end{pmatrix} \quad (1.158)$$

where the diagonal term

$$M = \frac{P_0^2}{3\hbar^2} \left(\frac{2}{E_v(z) - E} + \frac{1}{E_v(z) - \Delta_0(z) - E} \right) \hbar^2 k_{\parallel}^2 - \frac{P_0^2}{3} \frac{\partial}{\partial z} \left(\frac{2}{E_v(z) - E} + \frac{1}{E_v(z) - \Delta_0(z) - E} \right) \frac{\partial}{\partial z} \quad (1.159)$$

contributes to the effective mass. Indeed the first term is proportional to $\hbar^2 k_{\parallel}^2$ and thus can be associated with in-plane kinetic energy. On the other hand the second term is properly symmetrized momentum operator in the case of non uniform effective mass along z . In this way may be introduced the effective mass

$$\frac{1}{m^*(z, E)} = \frac{1}{m_0} - \frac{2P_0^2}{3\hbar^2} \left(\frac{2}{E_v(z) - E} + \frac{1}{E_v(z) - \Delta_0(z) - E} \right) \quad (1.160)$$

Instead the off-diagonal term is

$$N = \frac{P_0^2}{3} \frac{\partial}{\partial z} \left(\frac{2}{E_v(z) - E} + \frac{1}{E_v(z) - \Delta_0(z) - E} \right) ik_- = \alpha(z, E)(ik_x + k_y) \quad (1.161)$$

and thus can be identified with the Rashba Spin-orbit coupling term

$$H_{SO} = \alpha(z, E)(k_y \sigma_x - k_x \sigma_y) \quad (1.162)$$

with spin-orbit coupling

$$\alpha(z, E) = \frac{P_0^2}{3} \frac{\partial}{\partial z} \left(\frac{2}{E_v(z) - E} + \frac{1}{E_v(z) - \Delta_0(z) - E} \right) \quad (1.163)$$

It can be noticed that the effective mass $m^*(z, E)$ as well as the SOC constant $\alpha(z, E)$ are dependent on energy. Then, the Hamiltonian (1.158) leads to non parabolic dispersion relation and must be treated self-consistently. However conduction states of semiconductor materials typically have energy close to the band minima $E \sim E_c(z)$ and in the case of weak external electric field the dominant energies scales are expected to be $E_0(z)$ and $E_0(z) - \Delta_0(z)$. The effective mass and spin-orbit coupling can be approximated as power expansion in terms of

$$\frac{V_{ext}(z) + E_c(z) - E}{E_0(z)} \ll 1 \quad \frac{V_{ext}(z) + E_c(z) - E}{E_0(z) - \Delta_0(z)} \ll 1 \quad (1.164)$$

The effective mass is approximated to zero order

$$\frac{1}{m^*(z)} = \frac{1}{m_0} - \frac{2P_0^2}{3\hbar^2} \left(\frac{2}{E_0(z)} + \frac{1}{E_0(z) - \Delta_0(z)} \right) \quad (1.165)$$

On the other hand for SOC is kept up to first order term

$$\begin{aligned} \alpha(z, E) = \frac{P_0^2}{3} \frac{\partial}{\partial z} \left[\frac{1}{E_0(z) - \Delta_0(z)} - \frac{2}{E_0(z)} + \right. \\ \left. + \left(\frac{1}{(E_0(z) - \Delta_0(z))^2} - \frac{1}{E_0^2(z)} \right) (V_{ext}(z) + E_c(z) - E) \right] \end{aligned} \quad (1.166)$$

and recalling that the piecewise profiles (1.145-1.146) can be rewritten

$$\frac{1}{m^*(z)} = \frac{1}{m_0} - \frac{2P_0^2}{3\hbar^2} \left(\frac{1}{m_B} \Theta(|z| - d/2) - \frac{1}{m_A} \Theta(-|z| + d/2) \right) \quad (1.167)$$

$$\alpha(z, E) = \frac{P_0^2}{3} \frac{\partial}{\partial z} (R_B(z) \Theta(|z| - d/2) + R_A(z) \Theta(-|z| + d/2)) \quad (1.168)$$

with

$$\frac{1}{m_i} = \frac{2}{E_0^i} + \frac{1}{E_0^i - \Delta_0^i} \quad (1.169)$$

$$R_i(z) = \frac{1}{E_0^i - \Delta_0^i} - \frac{2}{E_0^i} + \left(\frac{1}{(E_0^i - \Delta_0^i)^2} - \frac{1}{(E_0^i)^2} \right) (V_{ext}(z) + E_c^i - E) \quad (1.170)$$

one can expand the derivative in Eq.(1.168) obtaining

$$\alpha(z) = \alpha_0(z) + \alpha_{int}(z) \quad (1.171)$$

Here $\alpha(z)$ is the bulk contribution of material and is raised by inversion asymmetry due to the external field

$$\alpha_0(z) = \frac{P_0^2}{3} \left(\frac{1}{(E_0(z) - \Delta_0(z))^2} - \frac{1}{E_0^2(z)} \right) \frac{\partial}{\partial z} V_{ext}(z) \quad (1.172)$$

whereas $\alpha_{int}(z)$ is the contribution caused by asymmetry introduced by interface and is proportional to delta functions at $-d/2$ and $d/2$.

$$\alpha_{int}(z) = (R_A(z) - R_B(z))(\delta(z + d/2) - \delta(z - d/2)) \quad (1.173)$$

Finally effective parabolic Hamiltonian can be written as

$$\tilde{H}_c = \left(\frac{\hbar^2 k_{\parallel}^2}{2m^*(z)} - \frac{\hbar^2 \partial}{2\partial z} \frac{1}{m^*(z)} \frac{\partial}{\partial z} + V_{ext}(z) + E_c(z) \right) \sigma_0 - \alpha(z)(k_y \sigma_x - k_x \sigma_y) \quad (1.174)$$

The discontinuity of the effective mass and spin orbit coupling at the interface in principle must be treated by appropriate boundary conditions, that should be derived imposing the continuity of envelope function $\mathbf{g}_c(z)$ and integrating the Heisenberg equation (1.157) across each interface. It can be found that boundary conditions couple the SOC to the motion along z [30]. However in the case of the quantum well for the conduction band, the low energy states are expected to be bound states[8] with small probability to be found near interface for deep enough well. In this way the influence of boundary conditions is significantly reduced and Hamiltonian Eq.(1.174) can be approximated to 2DEG Hamiltonian by tracing out z -degree of freedom[30]

$$H_{\parallel} = \langle \tilde{H}_c \rangle = \frac{\hbar^2 k_{\parallel}^2}{2m^*} \sigma_0 - \alpha_R(k_y \sigma_x - k_x \sigma_y) \quad (1.175)$$

where we define the spin-orbit coupling constant $\alpha_R = \langle \alpha_0(z) \rangle + \langle \alpha_{int}(z) \rangle$ and the emerging SOC term can be rewritten as Rashba spin orbit coupling[5, 67]

$$H_{SO} = \frac{\alpha_R}{\hbar} \boldsymbol{\sigma} \times \hat{\mathbf{p}} \cdot \hat{\mathbf{z}} \quad (1.176)$$

where $\hat{\mathbf{p}}$ is canonical momentum, $\hat{\mathbf{z}}$ is unitary vector along the growth direction (001) and α_R is Rashba spin orbit constant. In the following sections we shall drop the subscript and denote it simply as α .

1.4 SOC in 1D nanowires

In view of various technological applications a great deal of attention has been devoted to quasi 1D systems where, due to the spin orbit coupling, it is possible to implement precise electrical control of the spin precession. This is the case of nanowires. In order to describe

the theoretical model for nanowires, we start by observing that in the previous section we have derived the Hamiltonian of a quantum well where the confinement direction was z and the plane of the 2DEG was x - y . However, direction of the structure inversion asymmetry can equivalently be denoted by y and the 2DEG can be set in x - z plane. In this way the Rashba term can be obtained from Eq.(1.176) by simple rotation around x -axis that can be written in matrix form as

$$H = \begin{pmatrix} \frac{(\hat{p}_x^2 + \hat{p}_z^2)}{2m^*} - \frac{\alpha}{\hbar}\hat{p}_x & \frac{\alpha}{\hbar}\hat{p}_z \\ \frac{\alpha}{\hbar}\hat{p}_z & \frac{(\hat{p}_x^2 + \hat{p}_z^2)}{2m^*} + \frac{\alpha}{\hbar}\hat{p}_x \end{pmatrix} \quad (1.177)$$

where $\hat{p}_n = -i\hbar\partial_n$ with $n \in \{x, z\}$. One can now introduce a further confinement potential $V(z)$ along z and leave x direction free. The resulting structure is a nanowire. For the sake of simplicity we consider infinite potential well of the width W i.e.

$$V(z) = \begin{cases} 0 & 0 < z < W \\ \infty & \text{otherwise} \end{cases} \quad (1.178)$$

In this way one can decompose the original Hamiltonian as

$$H = H_z + H_{1D} + H_{mix} \quad (1.179)$$

$$H_z = \frac{\hat{p}_z^2}{2m^*}\sigma_0 + V(z)\sigma_0 \quad (1.180)$$

$$H_{1D} = \frac{\hat{p}_x^2}{2m^*}\sigma_0 - \frac{\alpha}{\hbar}\sigma_z\hat{p}_x \quad (1.181)$$

$$H_{mix} = \frac{\alpha}{\hbar}\sigma_x\hat{p}_z \quad (1.182)$$

where H_{mix} exhibits off diagonal term and to a first approximation can be considered as a perturbation. On the other hand it is straightforward to see that H_z and H_{1D} are diagonal

$$H_{1D}\phi_{s,k_x}(x) = \epsilon_s(k_x)\phi_{s,k_x}(x) \quad (1.183)$$

$$H_z\varphi_n(z) = E_n\varphi_n(z) \quad (1.184)$$

$\phi_{s,k_x}(x) = \chi_s e^{ik_x x}$ and χ_s is a spinor part of the wave function with $s \in \{\uparrow, \downarrow\}$, on the other hand $\varphi_n(z)$ with $n > 1$ is eigenstate of the well known solution of particle in the box problem[33] degenerate in spin degree of freedom with corresponding energy

$$E_n = \frac{n^2\pi^2\hbar^2}{2m^*W^2} \quad (1.185)$$

In this way the total wavefunction can be expressed as

$$\psi_{k_x,n,s}(x,z) = \phi_{s,k_x}(x)\varphi_n(z) = \chi_s e^{ik_x x}\varphi_n(z) \quad (1.186)$$

With the spectrum of 1D unperturbed problem is composed by band structure $E_{n,s}(k_x) = \epsilon_s(k_x) + E_n$. However H_{mix} present off diagonal term that can be shown to couple the

different bands m, m' , deforming in this way energy dispersion. Indeed in the absence of coupling term there would exist points k' such that $E_{m,\uparrow}(k') = E_{m',\downarrow}(k')$ restoring in this way spin degeneracy that isn't coherent with the symmetry of the problem and therefore each band is distorted in order to avoid crossings in the energy spectrum[67]. The coupling term can be seen more in details by tracing out trasversal degree of freedom

$$\left(E_n\delta_{m,n} + H_{1D}\delta_{m,n} + (H_{mix})_{m,n}\right)\chi_s e^{ik_x x} = \tilde{E}_{n,s}(k_x)\chi_s e^{ik_x x} \quad (1.187)$$

where $(H_{mix})_{m,n} = \int_W \varphi_m^\dagger(z) H_{mix} \varphi_n(z) dz$ and $\tilde{E}_{n,s}(k_x)$ band structure including the perturbation introduced by coupling. In the case of transversal confinement by an infinite potential well (1.178) the band mixing term can be expressed as[33]

$$(H_{mix})_{m,n} = i \frac{\alpha}{W} \frac{2mn}{m^2 - n^2} \left(1 - (-1)^{|m-n|}\right) \sigma_x \quad (1.188)$$

The problem can be solved by taking into account only a finite number of bands by means of the Löwdin partitioning discussed in Section 1.1.4. The distortion of energy spectrum significantly depends on the number of included bands and, in view of investigation of transport properties, the number of relevant bands must be carefully chosen in order to avoid systematic errors due to the truncation of the Hilbert space[33, 67]. For typical applications, the band coupling term can be neglected and the zero order perturbation expansion can be considered as valid. Indeed in the case where the band gap ΔE_n is very large, i.e. for separated energy bands, the energy scale of coupling term is insufficient to give relevant contribution. In this way one can consider the validity of this approximation by comparing energy scales of band gap and coupling term, that scales as[12, 39]

$$\Delta E_0 \sim \frac{\hbar^2}{m^* W^2} \quad (1.189)$$

$$(H_{mix})_{m,n} \sim \frac{\alpha}{W} \quad (1.190)$$

and imposing $|\langle m | H_{mix} | n \rangle / \Delta E_0| \ll 1$ one can find

$$W \ll \frac{\hbar^2}{\alpha m^*} \quad (1.191)$$

The typical materials used for quantum wires are InSb, InAs and GaAs[67]. These narrow-gap semiconductors have recently attracted a particular attention since they are characterized by a strong Rashba coupling and a large gyromagnetic factor that allow them exhibit large Zeeman splitting even for small external magnetic fields. In this way the maximal width of the confinement potential allowing to apply the independent band approximation can be estimated with typical values of effective mass and Rashba coupling constant. In the case of InSb one has $m^* = 0.015m_e$ and $\alpha \sim 10^{-11} eVm$, whence one deduces the constraint $W \ll 0.5\mu m$, which is well within reach of modern technology[12, 39]. Therefore it is realistic to implement full 1D nanowire describe by

$$\left(E_n + H_{1D}\right)\chi_s e^{ik_x x} = E_{n,s}(k)\chi_s e^{ik_x x} \quad (1.192)$$

where k_x has been redenoted as k to make the notation lighter. We first consider only the lowest band in the nanowire and neglect the energetically higher bands separated by energy gaps. This amounts to deal with a 1D system and one can drop the trasversal mode quantum number n . In this way the eigenvalue equation can be rewritten in k -space as

$$\left(\frac{\hbar^2 k^2}{2m^*} \sigma_0 - \alpha k \sigma_z \right) |s\rangle = E_s(k) |s\rangle \quad (1.193)$$

The above Equation is already diagonal and it is straightforward to identify the eigenvectors $|\uparrow\rangle = (1, 0)$, $|\downarrow\rangle = (0, 1)$ and the corresponding eigenvalues

$$E_{\uparrow}(k) = \frac{\hbar^2 k^2}{2m^*} - \alpha k \quad (1.194)$$

$$E_{\downarrow}(k) = \frac{\hbar^2 k^2}{2m^*} + \alpha k \quad (1.195)$$

The dispersion relation is depicted in Fig.1.3. Due to the Rashba spin orbit term, the spin degeneracy of the customary parabolic dispersion is lifted: The two parabolas related to each spin component are shifted laterally, in opposite directions, by the spin-orbit wave vector

$$k_{SO} = \frac{|\alpha|m^*}{\hbar^2} \quad (1.196)$$

and lowered by spin-orbit energy

$$E_{SO} = \frac{m^* \alpha^2}{2\hbar^2} = \frac{\hbar^2 k_{SO}^2}{2m^*} \quad (1.197)$$

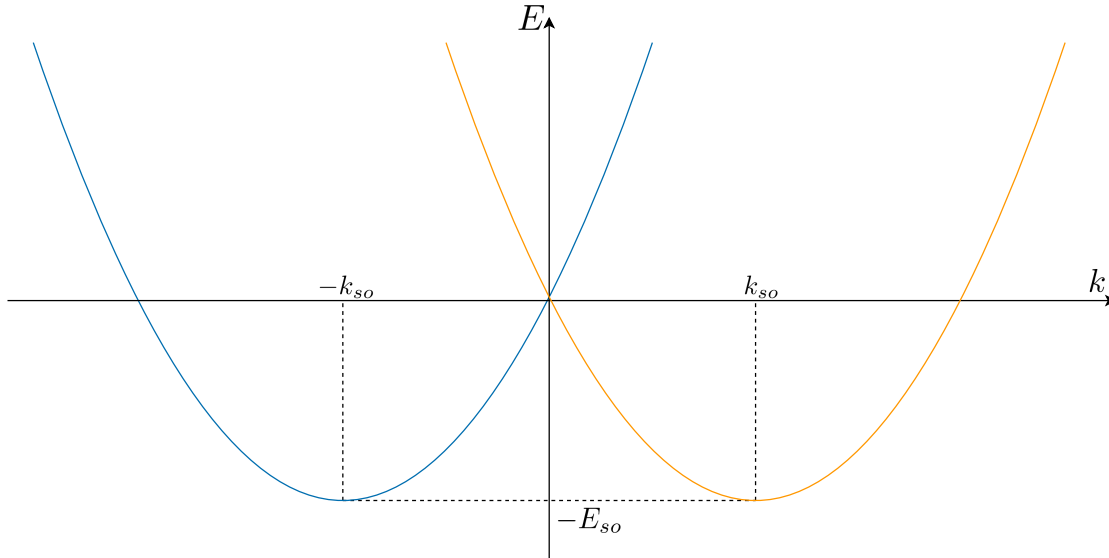


Figure 1.3: Orange line $E_{\uparrow}(k_x)$, Blue line $E_{\downarrow}(k_x)$

1.5 Applications of the spin-orbit coupling

In recent years the great interest was concern on the study and development of the techniques that allow to manipulate spin degree of freedom and to build the spin based devices and novel field has emerged: spinotronics[21, 22, 88]. The spinotronics devices allow to manipulate the information stored in spin degree of freedom rather than in charge and are expected to benefit of several advantages such as large switching rates, lower power consumption, increased integration densities with respect to conventional semiconductor devices[21].

The first generation of spinotronic devices are based on giant magneto-resistive (GMR) effect that introduces many common principles for other types of spinotronics devices. One of the simplest GMR based device is Spin-valve, that is composed by two ferromagnetic layers, iron or nickel alloy, sandwiching a thin nonmagnetic metal, usually copper. One of the two magnetic layers is “pinned” i.e., the magnetization in that layer is fairly insensitive to moderate magnetic fields, through which spin current is electrically injected[21]. Indeed in the ferromagnet material the population of states have preferred spin direction and in this way out going current is spin polarized and emerge net spin current. The other magnetic layer is “free” layer, and its magnetization can be changed by a relatively small magnetic field and detect spin current: in the case its polarization is align with injected spin, current doesn’t meet additional resistance and vice versa if free ferromagnet is antialigned. The resistance of the junction can thus be tuned within 5-10%[21]. The GMR spin valve has found extensive use in HDD read head[21, 88]. The improved version of GMR spin valve is the magnetic tunnel junction (MTJ) which exploits a similar principle, except that ferromagnet leads are separated by an insulating layer through which transmission occurs via tunneling. The MTJ exhibits larger resistance modulation(20% to 40%)[21]. It is applied in high information density HDD[88] and in integrated magnetic random access memory (MRAM) cells, which use magnetic hysteresis to store data and magnetoresistance to read data[21]. Compared to conventional solid state memory cell, MRAM exhibits a significant increase of read/write rate, lack of wear-out with write cycling and lower energy for writing[21].

The next generation of spintronic devices is based on spin dynamics, i.e. the modulation of the spin precession rate inside the material in contrast with spin torque based devices. To this purpose the SOC plays a key role: By modulating the SOC constant with a gate potential enables one to control the wave vector of the state at fixed energy. In turn, this leads to a differential phase shift between the two spin polarizations states, so that injected and detecting spin polarized current may lead to spin interference. This idea is at the core of the Datta-Das transistor or spin-FET[12]. The main advantages of a spin-FET are low energy consumption and fast switching speed since it does not involve creating or eliminating the electrical conducting channels during the switching, required by traditional FETs[67]. However the SOC introduces also some practical challenges. Indeed in the presence of momentum elastic scattering, SOC decreases the coherence length. This may lead to a vanishing spin polarized current, an effect known as weak antilocalization. Indeed random changes in the velocity of the electron due to scattering cause as well changes of the spin precession axis that leads to the spin relaxation. Even if the electrons are injected spin polarized into the system, they will go out of phase because

each individual electron has a different scattering history[87]. In this way in realization of SOC based device one is restricted to ballistic transport only and main length scale of device must be significantly smaller than the mean free path L_0 . Another technological problem originates from the resistance mismatch on the ferromagnetic/semiconductor interface, that cause the inefficient injection of the spin current, this problem however can be mitigated by use of exotic ferromagnetic alloys[26].

1.5.1 Datta-Das transistor

One of the first spin-FET devices have been proposed by Datta and Das in 1990[12], and is composed by a heterojunction in similar way of classical transistor presenting as well source, drain leads and gate that allow to control resistance of the transistor. The current modulation arises from spin precession due to the spin-orbit coupling in narrow-gap semiconductors, while magnetized contacts are used to inject and detect specific spin orientations, the schematic representation is pictured on the figure (1.4)[12]

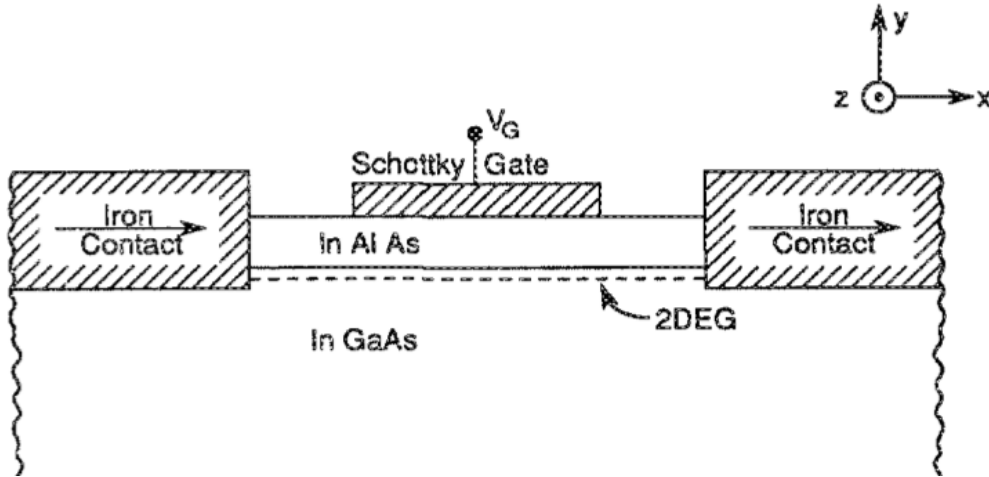


Figure 1.4: Datta-Das spin-FET structure. The iron contact are x -polarized ferromagnets that are responsible for injection and detection of spin current. The central region is composed by narrow gap semiconductor in which the Rashba spin orbit coupling is dominant and is controlled by gate potential V_G . Figure taken from Ref.[12]

The source and drain leads are ferromagnetic material magnetized along x direction, in this way injected spin current is polarized as well along x and can be expressed as combination of z up and down states

$$\begin{pmatrix} 1 \\ 1 \end{pmatrix} = \begin{pmatrix} 1 \\ 0 \end{pmatrix} + \begin{pmatrix} 0 \\ 1 \end{pmatrix} \quad (1.198)$$

States injected from ferromagnetic lead are propagated in the 2DEG in x/z plane, composed of narrow-gap semiconductor such as InGaAs, InAs or GaAs in which Rashba

SOC is dominant and are described by

$$H = \begin{pmatrix} \frac{\hbar^2(k_x^2+k_z^2)}{2m^*} - \alpha k_x & \alpha k_z \\ \alpha k_z & \frac{\hbar^2(k_x^2+k_z^2)}{2m^*} + \alpha k_x \end{pmatrix} \quad (1.199)$$

However from 2DEG Hamiltonian can be seen that the state are characterised by spin texture[89] and the spin orientation is perpendicular to the electron propagating direction, spanning from $(1, 1)^T$, $(1, -1)^T$ for transverse propagation i.e. $k_x = 0$ to $(1, 0)^T$, $(0, 1)^T$ for $k_z = 0$ [67]. In this way due to the angular spectrum the incoming states aren't forced to sharply spit in to different eigenvectors that as will be seen later give raise to interference, but rather goes preferentially into states with spin component along x that increase baseline transmission and reduce ability to modulate current. As consequence it is crucial to restrict the trasversal degree of freedom for instance with external potential, and consider in central region 1D electron transport[12]. Indeed as discussed in the previous section, in the case of a very narrow 1D wire, the different energy band aren't coupled and can be treated as identical bands separated by energy gap proportional to their band number. In this way in first approach one can consider case of the single mode and generalize to multiple band later. Propagating state in the 1D wire in the presence of Rashba coupling are described by Hamiltonian

$$H = \begin{pmatrix} \frac{\hbar^2 k^2}{2m^*} + \alpha k & 0 \\ 0 & \frac{\hbar^2 k^2}{2m^*} - \alpha k \end{pmatrix} \quad (1.200)$$

with eigenvector and corresponding eigenvalues

$$|+\rangle = \begin{pmatrix} 1 \\ 0 \end{pmatrix} \quad (1.201)$$

$$|-\rangle = \begin{pmatrix} 0 \\ 1 \end{pmatrix} \quad (1.202)$$

$$E_{\pm} = \frac{\hbar^2 k_x^2}{2m^*} \pm \alpha k_x \quad (1.203)$$

In this way injected x polarized state at fixed energy E is propagating towards the central region as combination of spin up $|+\rangle$ and spin down $|-\rangle$ with different wavevectors $k_{\pm} = \pm k_{SO} + \sqrt{k_{SO}^2 - \frac{2mE}{\hbar^2}}$, where $k_{SO} = |\alpha|m/\hbar^2$. The wave function in the central region can be written as

$$\phi(x) = \begin{pmatrix} 1 \\ 0 \end{pmatrix} e^{ik_+x} + \begin{pmatrix} 0 \\ 1 \end{pmatrix} e^{ik_-x} = \begin{pmatrix} e^{ik_+x} \\ e^{ik_-x} \end{pmatrix} \quad (1.204)$$

The injected electron is propagating in the central nanowire of the length L and at the end must be detected by ferromagnet polarized along x ; The transmission is maximum if the spin of incident electron is aligned with ferromagnet polarization. In this way transmission through nanowire is expected to be propotional to the probability of the state to be aligned with the polarizzation of drain ferromagnet at $x = L$ that reads

$$\left| \begin{pmatrix} 1, 1 \end{pmatrix} \begin{pmatrix} e^{ik_+L} \\ e^{ik_-L} \end{pmatrix} \right|^2 = 4 \cos^2((k_+ - k_-)\frac{L}{2}) \quad (1.205)$$

From which follows that current in principle can be modulated by a differential phase $\Delta\theta = (k_+ - k_-)L$ that allow to minimize current for $\Delta\theta = \pi$ and can be easily found to be [12, 20]

$$\Delta\theta = 2k_{SO}L = \frac{2m^*\alpha L}{\hbar^2} \quad (1.206)$$

As mentioned above, in the case of a narrow wire, the conducting states of all bands $E_{n,k}$ exhibit the same differential phase shift $\Delta\theta$, independent of the band index and the wave vector. Thus, differently from a typical quantum interference device that must be a single channel to properly operate, the Datta-Das transistor in principle can be realized as multi channel device that would operate properly for higher temperature and larger applied bias that is necessary for inducing Rashba spin orbit coupling [12]. The above results have been confirmed by more systematic investigation of the sub band coupling by [20] using the tight binding model. On the other hand in the case of wide confinement potential, the current modulation is expected to deviate from harmonic behaviour. Furthermore, the multi channel case must be considered since the phase shift has a more complicated dependence on energy and band index as result of band deformation [67].

The phase is proportional to the length of the central region and spin orbit constant that is its turn can be controlled by the gate potential. As mentioned above, in order to guaranty sufficiently large coherence length of spin current the spintronic device are limited to only ballistic transport, in this way one may argue if for practical realization of Datta-Das transistor the typical scale of coupling constant would be enough to introduce phase shift of π in the central region with length smaller then mean free path $L < L_0$. To this purpose one can compare the typical scales of Rashba coupling constant: $\alpha = 10^{-11} eV \cdot m$ and effective mass $m^* = 0.15m_e$ that give raise $L(\Delta\theta = \pi) = 0.8\mu m$ [26]. It is coherent with typical mean free path of high-mobility semiconductors at low temperatures $L_0 > 1\mu m$ [12].

The first implementation of Datta-Das transistor has been done by [39] with non-local measurement scheme, in which the current is injected in source ferromagnet after that a fraction of injected electrons have ballistic trajectories to the drain, which develops a voltage ΔV proportional to the projection of the electron spin on the magnetization orientation of drain ferromagnet as in Eq.(1.205). The quantum wire is realised in a InAs heterostructure with strong Rashba spin orbit coupling with the ferromagnetic contacts realised with $Ni_{81}Fe_{19}$ permalloy [39, 67]. In Fig.1.5.a) the experimental measurements of the drain voltage ΔV are reported. It can be indeed observed the typical oscillation depending on the gate voltage. Also it can be noticed that in the case of shorter length of the central region $L = 1.25\mu m$ the range of gate voltage is extended. This stems from the fact that the phase shift is proportional to L , so that electrons in a device with shorter electrode spacing require a larger range of λ and therefore a larger range of gate potential V_G as well [39]. In Fig.1.5.b) we have reported the measurements for a fixed length of the central region, at different temperatures. It can be observed that the oscillations caused by the spin precession are washed out for higher temperature due to inelastic scattering, which becomes more pronounced. Coherent effects are destroyed by localization effects.

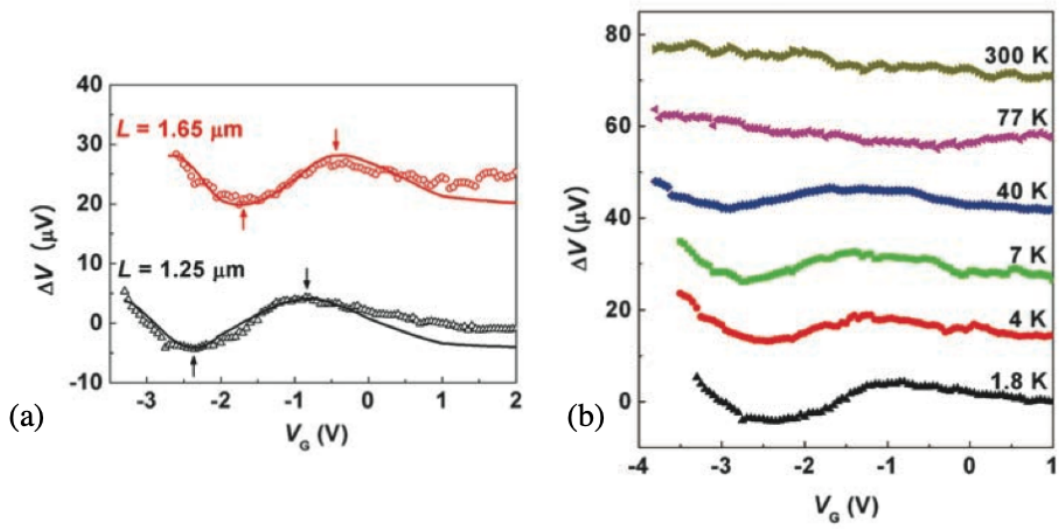


Figure 1.5: Experimental measurements of output voltage ΔV measured by [39]. The panel (a) the output voltage at fixed temperature as function of gate voltage V_G and different length of central nano wire $L = 1.65 \mu\text{m}$, $L = 1.25 \mu\text{m}$. The panel (b) measurements for different temperatures. Reference [39]

Chapter 2

The Scattering Matrix formalism

In this chapter I shall discuss the Scattering Matrix formalism, a general approach that allows one to investigate the conducting properties of a quantum mesoscopic system. In a nutshell, a mesoscopic system has a typical size that is much smaller than the phase breaking length, so that a propagating electron preserves its phase coherence and the wave nature of quantum particles emerges e.g. in interference phenomena. Furthermore, in the quantum mesoscopic regime, the transport properties also depend on the specific arrangement of elastic scattering centers in each sample. Semiclassical approaches, like Drude model or a Boltzmann kinetic theory, cannot be used to describe this regime, since they neglect the wavelike nature of particles. The Scattering Matrix formalism, developed by Landauer and Büttiker[14, 16, 17], is instead a fully quantum approach and establishes the correspondence between the quantum probability of a particle to be transmitted through a scattering region and its conduction properties.

This chapter is composed as follow. First of all I shall briefly discuss the relevant length scales characterizing a system and recall the definition of the quantum mesoscopic regime. Then, I shall illustrate a typical measurement setup involving a mesoscopic system and describe the model adopted by Landauer and Büttiker formalism to describe it. Finally, I will present the derivation of the conducting properties. In particular, I will focus on the linear response regime.

2.1 The quantum mesoscopic regime

One of the hallmarks of the wavelike nature of quantum particles is the fact that waves can interfere. However, in order to observe such phenomenon, a quantum particle must be able to preserve its phase coherence over the time and lengthscales characterizing the measurement. Let us consider a freely propagating electron wave $\Psi = e^{i(\mathbf{k}\cdot\mathbf{r}-Et/\hbar)}$, where \mathbf{k} and E denote its wavevector and energy, respectively. The electron can experience two sorts of scattering events, namely elastic and inelastic. The former scattering changes the wavevector $\mathbf{k} \rightarrow \mathbf{k}'$ but preserves the energy E , whereas the latter also affects the

energy. Elastic scattering events, typically due to static potentials, are reversible and do not affect the phase coherence of the quantum particle. In contrast, inelastic scattering events, caused by the interaction of the particle with the dynamical degrees of freedom of the environment, are typically irreversible and eventually destroy the phase coherence.

One thus typically introduces two relevant length scales. The length L_e denotes the typical lengthscale over which an electron experiences elastic scattering and is called *elastic mean free path*. In contrast, L_ϕ denotes the typical length an electron can travel before experiencing inelastic scattering and is called *phase breaking length*. Depending on the size L of the system, one can thus distinguish two regimes. A system with a size $L \gg L_\phi$ is referred to as a macroscopic system and does not exhibit phase coherence effects. In contrast, quantum coherence effects are expected to be observable in a system with a size $L \lesssim L_\phi$, which is thus called a quantum *mesoscopic system*.

When an electron Bloch wave propagates in a solid, elastic scattering is typically due to impurities or defects, whereas inelastic scattering occurs because of the interaction with the bath of the lattice vibrations (phonons) and/or the other electrons. On the one hand, it is precisely because of the energy exchange with the phonon bath that the electron gas can thermalize and reach the equilibrium state. On the other hand, from the quantum mechanical point of view, the equilibrium state is a mixed state where phase coherence is lost. Importantly, when temperature T is low, the lattice vibrations are suppressed and phonon scattering becomes more and more negligible. The phase breaking length L_ϕ thus increases when lowering the temperature, and an electron can travel a longer path without experiencing inelastic scattering processes. Typically one has $L_\phi \sim 1/T^p$, where p is a power that depends on the specific system. However, one can roughly claim that, as T is below the Kelvin range, L_ϕ is of the order of a μm , implying that nanosystems are mesoscopic. Indeed a number of genuine quantum interference phenomena have been experimentally observed in nanosystems. In this regime, transport properties (e.g. the resistivity) are determined only by the elastic scattering with impurities. One can further identify two mesoscopic subregimes[15]. In the diffusive regime, characterized by $L_e \ll L \lesssim L_\phi$, describes the situation where electrons experience various impurity scattering. This is typically the case of a metal. In contrast, the ballistic regime, characterized by $L_e \sim L \lesssim L_\phi$, identifies a mesoscopic system where impurity scattering is rare. Modern nanotechnology fabrication techniques based on semiconductors nowadays enable one to realize almost clean systems. This is thus the regime we shall focus on for the description of semiconductor nanowires with spin-orbit coupling.

Notably, the semiclassical approaches neglecting the wavelike nature of particles fail to describe mesoscopic systems, and a fully quantum approach is needed. The Scattering Matrix formalism developed by R. Landauer and M.Büttiker[6, 7, 14, 16, 17], is widely applied to the description of these systems. In this chapter we shall revise the main aspects that will be then applied to the investigation of the nanowire in next chapter.

2.2 Scheme of a typical measurement setup

A typical measurement setup for a quantum mesoscopic regime is sketched in Fig.2.1 and consists of three main components: the mesoscopic system itself, the left and right electrodes, and the leads connecting the electrodes to the mesoscopic system. Each component is characterized by a specific regime that we summarize here below.

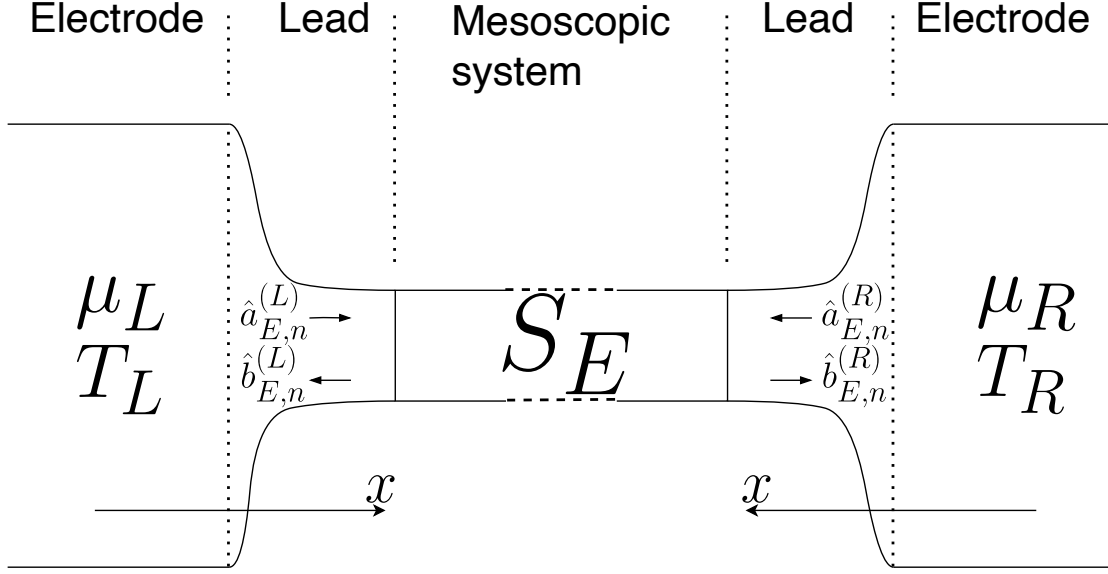


Figure 2.1: Measurements framework.

Electrodes (or reservoirs)

The electrodes are treated as macroscopic electron reservoirs with a typical size that is much longer than the phase coherence length, $L \gg L_\phi$. The energy level spectrum of these large electrodes is effectively a continuum. In each reservoir electrons experience inelastic scattering processes that lead to thermal equilibrium [15, 16], so their distribution is given by

$$\langle \hat{c}_E^{(\gamma)\dagger} \hat{c}_{E'}^{(\gamma)} \rangle = f_\gamma(E) \delta(E - E') \quad \gamma = R, L \quad (2.1)$$

where

$$f_\gamma(E) = \frac{1}{1 + e^{(E - \mu_\gamma)/k_B T_\gamma}} \quad (2.2)$$

is the equilibrium Fermi distribution of the left ($\gamma = L$) or the right ($\gamma = R$) electrode, with T_γ and μ_γ denoting its temperature and chemical potential, respectively.

Importantly, the electrodes are assumed to be statistically independent. Due to the temperature difference $\Delta T = T_L - T_R$ and chemical potential difference $\Delta\mu = \mu_L - \mu_R$, the overall system electrodes+mesoscopic system is in an out of equilibrium state and one

observes a flow of electric current. Nevertheless, each reservoir is only weakly perturbed by the small mesoscopic system, and its energy distribution can always be treated as the equilibrium one. The situation is different for the mesoscopic system, though.

Mesoscopic system

The mesoscopic system is characterized by a size $L \lesssim L_\phi$ smaller than phase breaking length L_ϕ . Here L can be taken as the longitudinal length, since the transversal size W of the mesoscopic system is typically shorter than the longitudinal size ($W < L \lesssim L_\phi$). By definition of quantum mesoscopic regime, electrons in the mesoscopic system can only experience elastic scattering processes, i.e. with impurities, while any inelastic scattering processes, e.g due to the coupling with the thermal bath, the electromagnetic environment and electron-electron interaction, can be neglected.

The chemical potential and/or temperature difference applied to the two electrodes induce a current flowing through the mesoscopic system, which is thus driven into an out-of-equilibrium state. The lack of inelastic processes implies that electrons in the mesoscopic system cannot thermalize and are intrinsically out of equilibrium and, differently from the macroscopic electrodes, one does not assume any distribution for the electrons in the mesoscopic system. The conducting properties are expected to be strongly dependent on the wavelike nature of electrons, and also on the specific arrangements of scattering centers.

The motion along the longitudinal direction is assumed to be free and is expected to be characterized by the continuum spectrum. In contrast, the motion in transverse direction is typically confined within a length scale W and is expected to yield a discrete transversal energy spectrum. In order to illustrate the effects of this confinement, let us imagine for simplicity that the transversal confinement is described by a hard wall potential, whose transverse states are characterized by discrete energy levels separated by

$$\Delta E_\perp \simeq \frac{\hbar^2 \pi^2}{2m^* W^2} \quad (2.3)$$

Comparing this energy scale with the thermal fluctuation energy $k_B T \simeq 25 \text{meV}$ for room temperature $T = 300^\circ \text{K}$, one can see that, if the transversal size of the system W is of the order of nanometers, one has $\Delta E_\perp \gg k_B T$. In this way the thermal fluctuation cannot induce the particle excitation between energy levels, and the quantum discreteness of the transversal spectrum emerges. In particular, this means that, for a fixed total energy E one can find only a finite number of transversal levels are compatible with a conducting longitudinal motion. Typically this regime is even more consistent, since the mesoscopic measurement set up is realized at the temperature significantly lower than the room temperature, in order to maximise the coherence length L_ϕ , therefore the thermal fluctuations are expected to be negligible[15].

Leads

The leads are assumed to be smoothly narrowing regions connecting the electrodes to the mesoscopic system. Moreover, they are treated as ideal ballistic conductors, where neither

elastic nor inelastic scattering occurs. Thus, electrons injected from the electrodes and propagating through the leads do not modify the occupation distribution with respect to the originating reservoir[15].

One may argue that such model of a scattering-free lead contacting the mesoscopic system and electrodes is unrealistic. Indeed physically the contact between two different materials typically exhibits a spurious contact resistance. However, such effect can actually be included as a potential barrier in the mesoscopic system itself. This means that the discussed idealized lead is in fact not unrealistic.

2.3 Landauer-Büttiker model for the setup

The Scattering matrix formalism developed by R.Landauer and M.Büttiker aims to derive the out of equilibrium properties of the typical setup outlined above. In this section I shall illustrate the main ingredients of this approach and the general procedure that allows to derive the the transport properties[14, 16, 17], focussing in particular on the linear response regime in the low temperature limit. In the next chapter I shall generalize and apply this approach to the case of the Rashba nanowire.

Let us denote by x the longitudinal direction of the mesoscopic system, and by y - z the transversal directions. We focus on a mesoscopic system with a short transversal size W of the nanometer scale. Since the electron motion is confined along the transversal direction, the current flow is only longitudinal ($\langle \hat{J}_x \rangle \neq 0$), while it vanishes in the transversal directions, $\langle \hat{J}_y \rangle = \langle \hat{J}_z \rangle = 0$. In turn, the continuity equation

$$\partial_t \hat{\rho}_{3D} = -\nabla \cdot \hat{\mathbf{J}}(\mathbf{r}) \quad , \quad (2.4)$$

where

$$\hat{\rho}_{3D}(\mathbf{r}) = \hat{\Psi}^\dagger(\mathbf{r})\hat{\Psi}(\mathbf{r}) \quad (2.5)$$

$$\hat{\mathbf{J}}(\mathbf{r}) = -\frac{i\hbar}{2m^*} \left(\hat{\Psi}^\dagger(\mathbf{r})\nabla\hat{\Psi}(\mathbf{r}) - \nabla\hat{\Psi}^\dagger(\mathbf{r})\hat{\Psi}(\mathbf{r}) \right) \quad (2.6)$$

are the electron density and the electron current density operators, implies that in the stationary out of equilibrium regime, where the expectation values are time-independent, one has

$$0 = \partial_t \langle \hat{\rho}_{3D}(\mathbf{r}) \rangle = -\nabla \cdot \langle \hat{\mathbf{J}}(\mathbf{r}) \rangle = -\partial_x \langle \hat{J}_x(\mathbf{r}) \rangle \quad (2.7)$$

Furthermore, due to the limited transversal size, it is worth introducing a longitudinal density $\hat{\rho}(x)$ and a longitudinal current density $\hat{I}(x)$ by integrating, at each longitudinal section x , over the transversal directions

$$\hat{\rho}(x) \doteq \iint dydz \hat{\rho}_{3D}(\mathbf{r}) \quad (2.8)$$

$$\hat{I}(x) \doteq \iint dydz \hat{J}_x(\mathbf{r}) \quad (2.9)$$

From Eq.(2.7) one has that

$$\partial_t \langle \hat{\rho}(x) \rangle = -\partial_x \langle \hat{I}(x) \rangle = 0 \quad (2.10)$$

This means that in stationary conditions the expectation value $\langle \hat{I}(x) \rangle$ of the longitudinal current is independent of the longitudinal position x . For this reason, we can evaluate it at any location. It is mathematically more suitable to evaluate it in the leads, where electrons are assumed to propagate freely.

2.3.1 Modelling the leads

Because in the leads no scattering events are assumed to occur, the electron Hamiltonian in the leads can be written as

$$H = -\frac{\hbar^2}{2m^*} \frac{\partial^2}{\partial x^2} + -\frac{\hbar^2}{2m^*} \left(\frac{\partial^2}{\partial y^2} + \frac{\partial^2}{\partial z^2} \right) + U(y, z) \quad (2.11)$$

where $U(y, z)$ is transversal confinement potential accounting for the small transversal size (e.g. infinite square well potential).

The Hamiltonian (2.11) is separable in the longitudinal (x) and the transversal (y, z) coordinates, and is diagonalized by eigenfunctions

$$\psi_{n,k}(\mathbf{r}) = \phi_n(y, z) e^{ikx} \quad (2.12)$$

where the plane wave e^{ikx} describes the free propagation along the longitudinal direction x , while the transversal wavefunction $\phi_n(y, z)$ are *localized* wavefunction, due to the confinement potential $U(y, z)$, which exhibit a *discrete* transversal energy spectrum U_n , with $n \in \mathbb{N}$. The total energy spectrum of the Hamiltonian (2.11) thus reads

$$E_n(k) = \frac{\hbar^2 k^2}{2m^*} + U_n \quad (2.13)$$

and consists of a sequence of one-dimensional parabolic subbands in k , labeled by the transversal quantum number n , and called the *channels*.

Because we deal with a many-electron problem, it is convenient to adopt the second quantization formalism. The Hamiltonian is

$$\hat{\mathcal{H}} = \int d\mathbf{r} \hat{\Psi}^\dagger(\mathbf{r}) H \hat{\Psi}(\mathbf{r}) \quad (2.14)$$

where H is the first-quantized Hamiltonian (2.11) and $\hat{\Psi}(\mathbf{r})$ is the electron field operator satisfying the fermionic anticommutator relation

$$\left\{ \hat{\Psi}(\mathbf{r}), \hat{\Psi}(\mathbf{r}') \right\} = 0 \quad \left\{ \hat{\Psi}(\mathbf{r}), \hat{\Psi}^\dagger(\mathbf{r}') \right\} = \delta(\mathbf{r} - \mathbf{r}') \quad (2.15)$$

In each lead $\gamma = L, R$ the electron field operator can be expanded in terms of the mode operators related to the propagating wavefunctions (2.12). The propagation direction is determined by the sign of the group velocity[10]

$$v_n(k) = \frac{1}{\hbar} \frac{\partial E_{k,n}}{\partial k} \quad (2.16)$$

In view of the spectrum (2.13), states with $k > 0$ propagate rightwards, while states with $k < 0$ propagate leftwards. However, in the Scattering matrix formalism, it is customary to reword that in terms of incoming and the outgoing modes. The incoming modes propagate from the reservoirs towards the mesoscopic system and are denoted by $\hat{a}_{n,k}^{(\gamma)}$, whereas the outgoing modes propagate from the mesoscopic system towards the reservoirs and are denoted by $\hat{b}_{n,k}^{(\gamma)}$ [14]. The expression thus acquires a different form depending on the lead $\gamma = L, R$ [16, 23].

$$\hat{\Psi}(\mathbf{r}, t) = \begin{cases} \frac{1}{\sqrt{\Omega}} \sum_n \sum_{k>0} e^{-iE_{k,n}t/\hbar} \left[\hat{a}_{n,k}^{(L)} e^{+ikx} + \hat{b}_{n,k}^{(L)} e^{-ikx} \right] \phi_n(y, z) & \mathbf{r} \in \text{Left Lead} \\ \frac{1}{\sqrt{\Omega}} \sum_n \sum_{k>0} e^{-iE_{k,n}t/\hbar} \left[\hat{a}_{n,k}^{(R)} e^{-ikx} + \hat{b}_{n,k}^{(R)} e^{+ikx} \right] \phi_n(y, z) & \mathbf{r} \in \text{Right Lead} \end{cases} \quad (2.17)$$

The anticommutation relations (2.15) of the field imply that that creation and annihilation operators satisfy

$$\{\hat{a}_{n,k}^{(\gamma)}, \hat{a}_{m,k'}^{(\gamma)}\} = 0 \quad \{\hat{b}_{n,k}^{(\gamma)}, \hat{b}_{m,k'}^{(\gamma)}\} = 0 \quad (2.18)$$

$$\{\hat{a}_{n,k}^{(\gamma)}, \hat{a}_{m,k'}^{(\beta)\dagger}\} = \delta_{\gamma,\beta} \delta_{n,m} \delta_{k,k'} \quad \{\hat{b}_{n,k}^{(\gamma)}, \hat{b}_{m,k'}^{(\beta)\dagger}\} = \delta_{\gamma,\beta} \delta_{n,m} \delta_{k,k'} \quad (2.19)$$

Importantly, since energy (and not wavevector) is conserved in the mesoscopic regime, it is more suitable to label operators and eigenstates with energy E rather than with wave vector. For a given value E of the total energy (2.13) only a limited number $N(E) = \sum_n \Theta(E - U_n)$ of parabolas lie below such value [15], and therefore exhibits conducting states, i.e. eigenstates (2.12) with a real $k \in \mathbb{R}$. These are called open channels or conducting channels.

For the open channels one can invert the dispersion relation (2.13) and express the positive wavevector as function of energy $k = k_n(E)$ with

$$k_n(E) = \frac{\sqrt{2m^*(E - U_n)}}{\hbar} \quad (2.20)$$

and the related (positive) velocity as

$$v_n(E) = v_n(k_n(E)) \quad (2.21)$$

Then, transforming the discrete sum over k in Eqs.(2.17) into the integration over the continuous variable E by means of

$$\sum_{k>0} \dots = \frac{\Omega}{2\pi} \int_0^\infty dk \dots = \Omega \int \frac{dE}{2\pi \hbar v_n(E)} \dots \quad (2.22)$$

where

$$\nu_n(E) = \frac{1}{\Omega} \sum_{k>0} \delta(E - E_n(k)) = \frac{1}{2\pi \hbar v_n(E)} \quad (2.23)$$

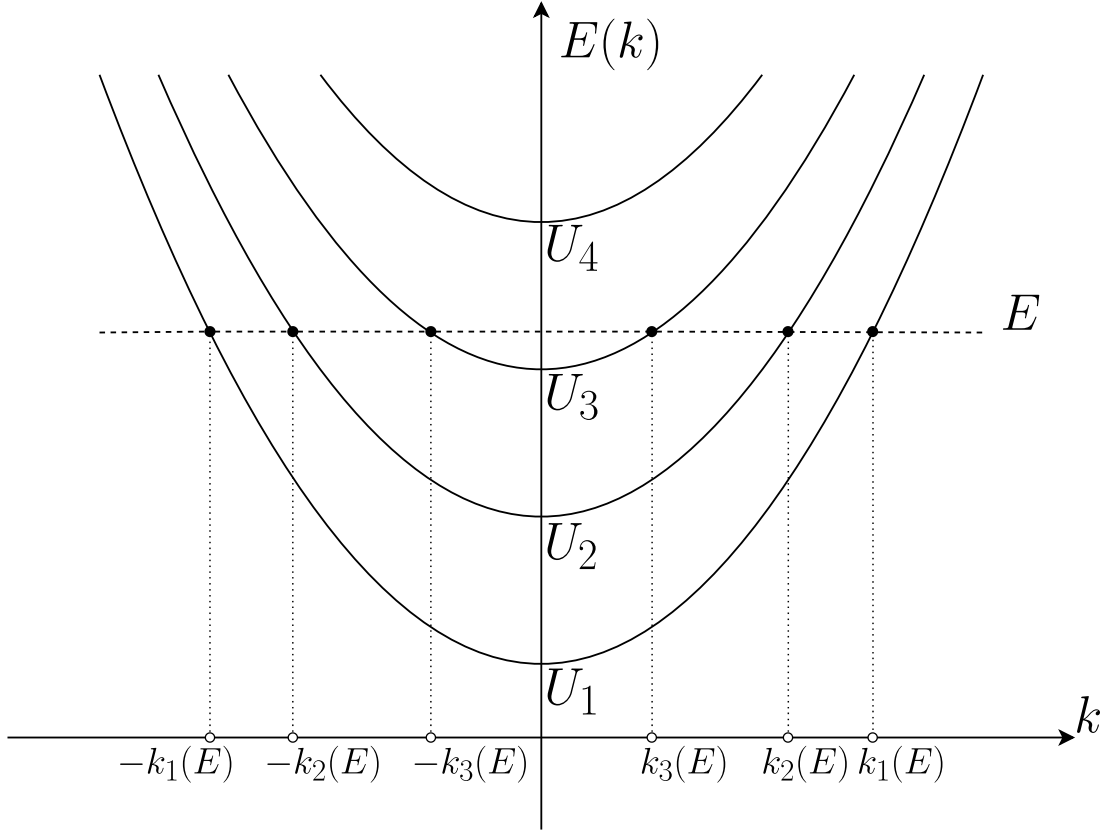


Figure 2.2: The dispersion relation of the leads (2.13) with 3 open channels $N(E) = 3$. For each fixed energy E can be found the correspondent modes $\pm k_n(E)$ with $n = 1, 2, 3$.

denotes the density of states per unit length and per propagation direction of the n -th channel, the electron field operator can be rewritten as

$$\hat{\Psi}(\mathbf{r}, t) = \begin{cases} \int dE \sum_n^{N(E)} \frac{e^{-iEt/\hbar}}{\sqrt{2\pi\hbar v_n(E)}} \left[\hat{a}_{n,E}^{(L)} e^{ik_n(E)x} + \hat{b}_{n,E}^{(L)} e^{-ik_n(E)x} \right] \phi_n(y, z) & \mathbf{r} \in \text{Left Lead} \\ \int dE \sum_n^{N(E)} \frac{e^{-iEt/\hbar}}{\sqrt{2\pi\hbar v_n(E)}} \left[\hat{a}_{n,E}^{(R)} e^{-ik_n(E)x} + \hat{b}_{n,E}^{(R)} e^{ik_n(E)x} \right] \phi_n(y, z) & \mathbf{r} \in \text{Right Lead} \end{cases} \quad (2.24)$$

where we have introduced the new energy mode operators[14, 15]

$$\hat{a}_{n,E}^{(\gamma)} = \sqrt{\frac{\Omega}{2\pi\hbar v_n(E)}} \hat{a}_{n,k}^{(\gamma)} \quad (2.25)$$

$$\gamma = L, R$$

$$\hat{b}_{n,E}^{(\gamma)} = \sqrt{\frac{\Omega}{2\pi\hbar v_n(E)}} \hat{b}_{n,k}^{(\gamma)} \quad (2.26)$$

satisfy the anticommutation relations

$$\{\hat{a}_{n,E}^{(\gamma)}, \hat{a}_{m,E'}^{(\beta)\dagger}\} = \delta_{\gamma,\beta} \delta_{n,m} \delta(E - E') \quad \{\hat{b}_{n,E}^{(\gamma)}, \hat{b}_{m,E'}^{(\beta)\dagger}\} = \delta_{\gamma,\beta} \delta_{n,m} \delta(E - E') \quad (2.27)$$

Notably, because the incoming states originate from the related reservoir, their expectation values are simply given by Eq.(2.1)

$$\langle \hat{a}_{n,E}^{(\gamma)\dagger} \hat{a}_{n,E'}^{(\gamma)} \rangle = f_\gamma(E) \delta(E - E') \quad (2.28)$$

where $f_\gamma(E)$ its Fermi equilibrium function of the related reservoir. Because in the lead no thermalization occurs (inelastic scattering is absent), the outgoing mode have a *different* (and a priori unknown) distribution $\langle \hat{b}_E^{(\gamma)\dagger} \hat{b}_E^{(\gamma)} \rangle$. Thus, although the electrodes are assumed to be at equilibrium, the leads and the mesoscopic system are intrinsically out of equilibrium[15]. In the above customary derivation, the spin degree of freedom does not play any other role than a dummy degeneracy variable. In the next chapter we shall generalize the Scattering Matrix approach to the case of Rashba nanowire where spin acts not trivially.

2.3.2 The Scattering Matrix of the mesoscopic system

While in the leads the transverse channels are separate and independent by construction, in the mesoscopic system, characterized by various elastic scattering centers, electrons can scatter from one channel to the other elastically, i.e. along a horizontal line at energy E line, as sketched in Fig.2.3. The energy distributions $\langle \hat{a}_{n,E}^{(\gamma)\dagger} \hat{a}_{n,E}^{(\gamma)} \rangle$ of the incoming channels can be controlled through the electrodes (see Eqs.(2.1)), whereas the energy distribution $\langle \hat{b}_{n,E}^{(\gamma)\dagger} \hat{b}_{n,E}^{(\gamma)} \rangle$ of the outgoing channels depends on the specific scattering centers of the mesoscopic system and is a priori unknown. One can thus think of the incoming channels as "the input" and the outgoing channels as "the output", and the mesoscopic system as a "black-box" connecting the latter to the former at each given energy E (see Fig.2.3). The mathematical object encoding such black box is the Scattering matrix, denoted by S , which that linearly relates the incoming and the outgoing modes

$$\begin{pmatrix} \hat{\mathbf{b}}_E^{(L)} \\ \hat{\mathbf{b}}_E^{(R)} \end{pmatrix} = \begin{pmatrix} S_E \end{pmatrix} \begin{pmatrix} \hat{\mathbf{a}}_E^{(L)} \\ \hat{\mathbf{a}}_E^{(R)} \end{pmatrix} \quad (2.29)$$

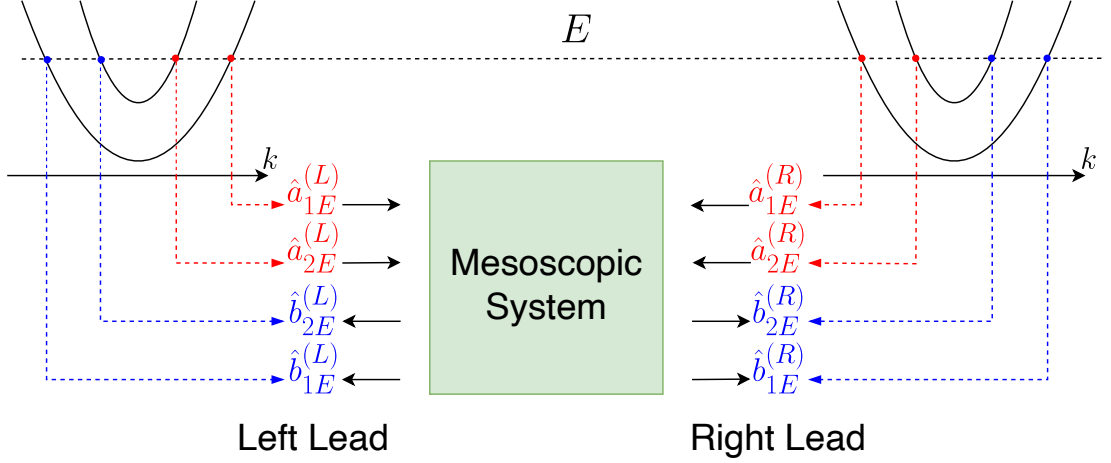


Figure 2.3: Black box model in the case of two conducting channels; Reg lines represent incoming modes, blue lines are outgoing modes

where $\hat{\mathbf{a}}_E^{(\gamma)} = [\hat{a}_{n,E}^{(\gamma)}]_{n=1}^{N(E)}$, $\hat{\mathbf{b}}_E^{(\gamma)} = [\hat{b}_{n,E}^{(\gamma)}]_{n=1}^{N(E)}$ are vectors of mode operators in lead γ . In components, one has

$$\hat{b}_{n,E}^{(\gamma)} = \sum_{\alpha,l} S_{\gamma,n;\alpha,l}(E) \hat{a}_{l,E}^{(\alpha)} \quad \hat{b}_{n,E}^{(\gamma)\dagger} = \sum_{\alpha,l} \hat{a}_{l,E}^{(\alpha)\dagger} S_{\gamma,n;\alpha,l}^*(E) \quad (2.30)$$

The idea underlying the Landauer-Büttiker formalism is that, by re-expressing the outgoing mode operators in terms of the incoming ones through the Scattering Matrix, the distribution $\langle \hat{b}_{n,E}^{(\gamma)\dagger} \hat{b}_{n,E}^{(\gamma)} \rangle$ of the outgoing channels, as well as the incoming-outgoing correlations $\langle \hat{a}_{n,E}^{(\gamma)\dagger} \hat{b}_{n,E}^{(\gamma)} \rangle$ and $\langle \hat{b}_{n,E}^{(\gamma)\dagger} \hat{a}_{n,E}^{(\gamma)} \rangle$, can be re-expressed in terms of the distributions of the incoming channels, which are known from Eq.(2.1). Explicitly

$$\langle \hat{a}_{n,E}^{(\gamma)\dagger} \hat{a}_{n,E}^{(\gamma)} \rangle = f_{\gamma}(E) \delta(E - E') \quad (2.31)$$

$$\langle \hat{b}_{n,E}^{(\gamma)\dagger} \hat{b}_{m,E'}^{(\beta)} \rangle = \left(\sum_{\alpha,l} S_{\gamma,n;\alpha,l}^* S_{\beta,m;\alpha,l} f_{\alpha}(E) \right) \delta(E - E') \quad (2.32)$$

$$\langle \hat{b}_{n,E}^{(\gamma)\dagger} \hat{a}_{m,E'}^{(\beta)} \rangle = S_{\gamma,n;\beta,m}^* f_{\beta}(E) \delta(E - E') \quad (2.33)$$

$$\langle \hat{a}_{n,E}^{(\gamma)\dagger} \hat{b}_{m,E'}^{(\beta)} \rangle = S_{\beta,m;\gamma,n} f_{\gamma}(E) \delta(E - E') \quad (2.34)$$

Note that all the mode distributions and the correlations are proportional to $\delta(E - E')$, i.e. diagonal in energy, consistently with the fact that energy is conserved in the mesoscopic regime.

Unitarity of the Scattering Matrix

Notably, the scattering matrix is unitary

$$S^{-1} = S^{\dagger} \quad (2.35)$$

to guarantee the current conservation [10, 15, 17]. This can be illustrated phenomenologically by focussing on the case of one single band. In the left lead the incoming average current in the interval dE around energy E is given by[16, 17]

$$dI_{in}(E) = v(E)n_{in}(E)\nu(E)dE \quad (2.36)$$

where $v(E)$ and $n_{inc}(E)$ are the group velocity and the occupation number of the band, whereas $\nu(E) = 1/(2\pi\hbar v(E))$ is the density of states per unit length and propagation direction (see Eq.(2.23)), so that $d\rho(E) = n_{inc}(E)\nu(E)dE$ is the incoming electron density per unit length. Note that this expression is universal in the sense that it is independent of the particular property of the lead and its quantum channel[17]. The total current in the left lead is the difference between the incoming and the outgoing term

$$dI^{(\gamma)}(E) = dI_{in}^{(\gamma)}(E) - dI_{out}^{(\gamma)}(E) = \frac{1}{2\pi\hbar}[n_{in}^{(\gamma)}(E) - n_{out}^{(\gamma)}(E)]dE \quad (2.37)$$

Imposing the current conservation $dI^{(L)}(E) = -dI^{(R)}(E)$ one finds

$$n_{in}^{(L)}(E) + n_{in}^{(R)}(E) = n_{out}^{(L)}(E) + n_{out}^{(R)}(E) \quad (2.38)$$

Considering that $n_{in}^{(\gamma)}(E) = \hat{\mathbf{a}}_E^{(\gamma)\dagger}\hat{\mathbf{a}}_E^{(\gamma)}$ and $n_{out}^{(\gamma)}(E) = \hat{\mathbf{b}}_E^{(\gamma)\dagger}\hat{\mathbf{b}}_E^{(\gamma)}$ [36]

$$\left(\hat{\mathbf{a}}_E^{(L)\dagger}, \hat{\mathbf{a}}_E^{(R)\dagger} \right) \begin{pmatrix} \hat{\mathbf{a}}_E^{(L)} \\ \hat{\mathbf{a}}_E^{(R)} \end{pmatrix} = \left(\hat{\mathbf{b}}_E^{(L)\dagger}, \hat{\mathbf{b}}_E^{(R)\dagger} \right) \begin{pmatrix} \hat{\mathbf{b}}_E^{(L)} \\ \hat{\mathbf{b}}_E^{(R)} \end{pmatrix} \quad (2.39)$$

finally using Eq.(2.29)

$$\left(\hat{\mathbf{a}}_E^{(L)\dagger}, \hat{\mathbf{a}}_E^{(R)\dagger} \right) \begin{pmatrix} \hat{\mathbf{a}}_E^{(L)} \\ \hat{\mathbf{a}}_E^{(R)} \end{pmatrix} = \left(\hat{\mathbf{a}}_E^{(L)\dagger}, \hat{\mathbf{a}}_E^{(R)\dagger} \right) S_E^\dagger S_E \begin{pmatrix} \hat{\mathbf{a}}_E^{(L)} \\ \hat{\mathbf{a}}_E^{(R)} \end{pmatrix} \quad (2.40)$$

therefore current is conserved only if the scattering matrix is unitary.

The scattering matrix (2.29) is customarily written in block form

$$\begin{pmatrix} \hat{\mathbf{b}}_E^{(L)} \\ \hat{\mathbf{b}}_E^{(R)} \end{pmatrix} = \begin{pmatrix} r & t' \\ t & r' \end{pmatrix} \begin{pmatrix} \hat{\mathbf{a}}_E^{(L)} \\ \hat{\mathbf{a}}_E^{(R)} \end{pmatrix} \quad (2.41)$$

where r and r' denote the matrices of reflection amplitudes, while t and t' are the matrices of transmission amplitudes. For instance, the reflection probability from the channel n to the channel m in the left lead is

$$R_{m,n}(E) = |r_{m,n}|^2 \quad (2.42)$$

whereas the transmission probability from the channel n in the left lead to the channel m in right lead is[17]

$$T_{m,n}(E) = |t_{m,n}|^2 \quad (2.43)$$

Similarly

$$R'_{m,n}(E) = |r'_{m,n}|^2 \quad (2.44)$$

$$T'_{m,n}(E) = |t'_{m,n}|^2 \quad (2.45)$$

denote the reflection probability from the n -th channel to the m -th channel in the right lead and the transmission probability from the n -th channel in the right lead to the m -th channel in the left lead, respectively. Exploiting the unitarity of the scattering matrix one has

$$\sum_m [R_{m,n}(E) + T_{m,n}(E)] = 1 \quad (2.46)$$

which reflects the fact that a particle inside a channel n is either reflected or transmitted into some other channel m [15]. Finally, one can introduce the transmission function

$$\tilde{T}(E) = \sum_m \sum_n T_{m,n}(E) = \sum_m \sum_n T'_{m,n}(E) \quad (2.47)$$

which can also be re-expressed using Eq.(2.46)

$$\tilde{T}(E) = N(E) - \sum_m \sum_n R_{m,n}(E) = N(E) - \sum_m \sum_n R'_{m,n}(E) \quad (2.48)$$

where we recall that $N(E)$ is the number of open channels at the energy E .

Example of Scattering matrix: the case of δ -potential

So far, the general properties of the Scattering matrix have been discussed. Here I wish to present an illustrative example of computation of the scattering matrix by means of Transfer Matrix approach. This general method, originally developed in context of optical systems[18], allows to find the solutions for the wave-like propagation and can be applied to arbitrary forms of the scattering potential. Differently the scattering matrix, which connects the outgoing to the incoming operators, the transfer matrix connects operators at opposite sides of the scattering center or region. In quantum mechanics the perhaps most representative applications of this approach are the quantum well problem[8] and delta-potential scattering[36].

Let us illustrate the latter case by considering a one-dimensional free electron gas in the presence of the two impurities, located at positions x_0 and x_1 , that can be modeled with a δ -potential. The second-quantization Hamiltonian reads

$$\hat{\mathcal{H}} = \int dx \hat{\Psi}^\dagger(x) \left(-\frac{\hbar^2}{2m^*} \frac{\partial^2}{\partial x^2} + \Lambda_0 \delta(x - x_0) + \Lambda_1 \delta(x - x_1) \right) \hat{\Psi}(x) \quad (2.49)$$

and implies the following Heisenberg equation for the electron field operator $\hat{\Psi}$

$$i\hbar \frac{\partial}{\partial t} \hat{\Psi}(x, t) = -\frac{\hbar^2}{2m^*} \frac{\partial^2}{\partial x^2} \hat{\Psi}(x, t) + \Lambda_0 \delta(x - x_0) \hat{\Psi}(x, t) + \Lambda_1 \delta(x - x_1) \hat{\Psi}(x, t) \quad (2.50)$$

While in the regions out of the impurities ($x \neq x_0, x_1$) the Heisenberg equation above is equivalent to a customary free electron model, for $x = x_0, x_1$ the δ potential induces boundary conditions. The field is continuous at each impurity location $\hat{\Psi}(x_j^-, t) = \hat{\Psi}(x_j^+, t)$ with $x_j^\pm = x_j \pm \epsilon$ ($j = 0, 1$ and $\epsilon \rightarrow 0$). However, its first derivative should be discontinuous, since the second derivative of the field $\partial_x^2 \hat{\Psi}(x, t)$ in Eq.(2.50) exhibits δ -like singularities, in order to compensate the δ -functions at $x = x_0, x_1$. Such discontinuity can be determined by integrating the Heisenberg equation (2.50) over an infinitesimal interval around x_j , that lead to the boundary conditions

$$\begin{cases} \hat{\Psi}(x_j^-, t) = \hat{\Psi}(x_j^+, t) \\ \partial_x \hat{\Psi}(x_j^+, t) - \partial_x \hat{\Psi}(x_j^-, t) = \tilde{\Lambda}_j \hat{\Psi}(x_j, t) \end{cases} \quad j = 0, 1 \quad (2.51)$$

where $\tilde{\Lambda}_j = \frac{2m^*}{\hbar^2} \Lambda_j$. Due to the energy conservation in the mesoscopic system, the general solution of the Hesinberg equation can be written as a superposition of the stationary solutions $\hat{\Psi}_E(x, t) = e^{-iEt/\hbar} \hat{\Psi}_E(x)$, where field $\hat{\Psi}_E(x)$ is a linear combination of the plane wave modes

$$\hat{\Psi}_E(x) = \begin{cases} \frac{1}{\sqrt{2\pi\hbar v(E)}} \left[\hat{a}_E^{(L)} e^{ik(E)x} + \hat{b}_E^{(L)} e^{-ik(E)x} \right] & x < x_0 \\ \frac{1}{\sqrt{2\pi\hbar v(E)}} \left[\hat{\gamma}_E^+ e^{ik(E)x} + \hat{\gamma}_E^- e^{-ik(E)x} \right] & x_0 < x < x_1 \\ \frac{1}{\sqrt{2\pi\hbar v(E)}} \left[\hat{a}_E^{(R)} e^{-ik(E)x} + \hat{b}_E^{(R)} e^{ik(E)x} \right] & x > x_1 \end{cases} \quad (2.52)$$

where $k(E) = \sqrt{2m^*E}/\hbar$ and the set of fermionic operators $\hat{\gamma}_E^+, \hat{\gamma}_E^-$ describe the propagating waves between the two impurities. Notably for the external region $x < x_0$ and $x > x_1$ we use the incoming $\hat{a}_E^{(\beta)}$ and out going $\hat{b}_E^{(\beta)}$ operators analogous to the ones used in the lead field operator (2.24). Substituting the Ansatz (2.52) into the boundary condition (2.51), one finds

$$\begin{pmatrix} \hat{\gamma}_E^+ \\ \hat{\gamma}_E^- \end{pmatrix} = W_E(x_0) \begin{pmatrix} \hat{a}_E^{(L)} \\ \hat{b}_E^{(L)} \end{pmatrix} \quad (2.53)$$

which expresses the operators on the right of the x_0 -impurity as a function of the operators on the left of such impurity. Similarly, one also finds

$$\begin{pmatrix} \hat{b}_E^{(R)} \\ \hat{a}_E^{(R)} \end{pmatrix} = W_E(x_1) \begin{pmatrix} \hat{\gamma}_E^+ \\ \hat{\gamma}_E^- \end{pmatrix} \quad (2.54)$$

which expresses the operators on the right of the x_1 -impurity as a function of the operators on its left. Here $W_E(x_j)$ is a 2×2 boundary matrix

$$W_E(x_j) = \begin{pmatrix} 1 - i \frac{\tilde{\Lambda}_j}{2k(E)} & -i \frac{\tilde{\Lambda}_j}{2k(E)} e^{-i2k(E)x_j} \\ i \frac{\tilde{\Lambda}_j}{2k(E)} e^{i2k(E)x_j} & 1 + i \frac{\tilde{\Lambda}_j}{2k(E)} \end{pmatrix} \quad (2.55)$$

It can be observed that $\det(W_E(x_j)) = 1$ and $(W_E(x_j))_{1,2} = (W_E^*(x_j))_{2,1}$. By combining Eqs.(2.53) and (2.54), one can write

$$\begin{pmatrix} \hat{b}_E^{(R)} \\ \hat{a}_E^{(R)} \end{pmatrix} = W_E \begin{pmatrix} \hat{a}_E^{(L)} \\ \hat{b}_E^{(L)} \end{pmatrix} \quad (2.56)$$

where the total Transfer matrix $W_E = W_E(x_0) \cdot W_E(x_1)$ expresses the operators on the right of the two-impurity scattering region as a function of the operators on its left. Assuming for simplicity $\tilde{\Lambda}_0 = \tilde{\Lambda}_1 = \tilde{\Lambda}$ and introducing the energy scale $E_\Lambda = \frac{m^*}{2\hbar^2} \Lambda^2$, the entries of the total transfer matrix read

$$(W_E)_{1,1} = \left(1 - i\sqrt{\frac{E_\Lambda}{E}}\right)^2 - \left(i\sqrt{\frac{E_\Lambda}{E}}\right)^2 e^{2ik(E)(x_1-x_0)} \quad (2.57)$$

$$(W_E)_{1,2} = i\sqrt{\frac{E_\Lambda}{E}} \left[\left(1 - i\sqrt{\frac{E_\Lambda}{E}}\right) e^{-2ik(E)x_0} + \left(1 + i\sqrt{\frac{E_\Lambda}{E}}\right) e^{-2ik(E)x_1} \right] \quad (2.58)$$

$$(W_E)_{2,1} = (W_E^*)_{1,2} \quad (2.59)$$

$$(W_E)_{2,2} = \left(1 - i\sqrt{\frac{E_\Lambda}{E}}\right)^2 - \left(i\sqrt{\frac{E_\Lambda}{E}}\right)^2 e^{2ik(E)(x_1-x_0)} \quad (2.60)$$

recalling the properties of the determinant of the matrix product one can find $\det(W_E) = \det(W_E(x_0))\det(W_E(x_1)) = 1$.

By re-expressing the relation Eq.(2.56) in favour of the incoming operators, it is straightforward to find the scattering matrix

$$S_E = \frac{1}{(W_E)_{2,2}} \begin{pmatrix} -(W_E)_{1,2} & 1 \\ 1 & (W_E)_{2,1} \end{pmatrix} \quad (2.61)$$

and the transmission function can be computed in closed form as

$$T(E) = \left| \frac{1}{(W_E)_{2,2}} \right|^2 = \frac{1}{1 + 4\frac{E_\Lambda}{E} \left[\cos(2k(E)L) + \sqrt{\frac{E_\Lambda}{E}} \sin(2k(E)L) \right]^2} \quad (2.62)$$

where $L = x_1 - x_0$. Notably the transmission function exhibits an oscillatory behavior that is a hallmark of the interference phenomena in the region between two impurities.

2.3.3 Electrical current

The electrical current operator is obtained by multiplying the longitudinal current operator defined in Eq.(2.9) by the electrical charge q

$$\hat{I}_c(x) = q \iint dydz \hat{J}_x = -i \frac{q\hbar}{2m^*} \iint dydz \left(\hat{\Psi}^\dagger(\mathbf{r}) \frac{\partial \hat{\Psi}(\mathbf{r})}{\partial x} - \frac{\partial \hat{\Psi}^\dagger(\mathbf{r})}{\partial x} \hat{\Psi}(\mathbf{r}) \right) \quad (2.63)$$

and can be expressed in terms of the energy mode operators using the expression (2.24) of the electron field operator. For instance, in the left lead one obtains

$$\begin{aligned} \hat{I}_c^{(L)}(x) = & - \int dE \int dE' e^{i(E-E')t/\hbar} \iint dydz \sum_{n=1}^{N(E)} \sum_{m=1}^{N(E')} \frac{iq\hbar}{2m^*} \frac{\phi_m^*(y,z)\phi_n(y,z)}{2\pi\hbar\sqrt{v_n(E)v_m(E')}} \times \\ & \times \left[i(k_n(E) + k_m(E')) \left(\hat{a}_{n,E}^{(L)\dagger} \hat{a}_{m,E'}^{(L)} e^{-i(k_n(E)-k_m(E'))x} - \hat{b}_{n,E}^{(L)\dagger} \hat{b}_{m,E'}^{(L)} e^{+i(k_n(E)-k_m(E'))x} \right) - \right. \\ & \left. - i(k_n(E) - k_n(E')) \left(\hat{a}_{n,E}^{(L)\dagger} \hat{b}_{m,E'}^{(L)} e^{i(k_n(E)+k_m(E'))x} - \hat{b}_{n,E}^{(L)\dagger} \hat{a}_{m,E'}^{(L)} e^{-i(k_n(E)+k_m(E'))x} \right) \right] \end{aligned}$$

Exploiting the orthonormality of the transversal wavefunctions $\int dx dy \phi_m^*(y,z)\phi_n(y,z) = \delta_{n,m}$, and recalling that $v_n(E) = \hbar k_n/m^*$, one finds

$$\begin{aligned} \hat{I}_c^{(L)}(x) = & \frac{q}{2\pi\hbar} \int dE \int dE' e^{i(E-E')t/\hbar} \times \tag{2.64} \\ & \times \sum_{n=1}^{\min(N(E), N(E'))} \left[\frac{v_n(E) + v_n(E')}{2\sqrt{v_n(E)v_n(E')}} \left(\hat{a}_{n,E}^{(L)\dagger} \hat{a}_{n,E'}^{(L)} e^{-i(k_n(E)-k_n(E'))x} - \hat{b}_{n,E}^{(L)\dagger} \hat{b}_{n,E'}^{(L)} e^{i(k_n(E)-k_n(E'))x} \right) + \right. \\ & \left. + \frac{v_n(E) - v_n(E')}{2\sqrt{v_n(E)v_n(E')}} \left(\hat{a}_{n,E}^{(L)\dagger} \hat{b}_{n,E'}^{(L)} e^{i(k_n(E)+k_n(E'))x} - \hat{b}_{n,E}^{(L)\dagger} \hat{a}_{n,E'}^{(L)} e^{-i(k_n(E)+k_n(E'))x} \right) \right] \end{aligned}$$

Average current

In order to compute the expectation value of the current operator (2.64) we observe from Eq.(2.31) that, due to the energy conservation, all expectation values of the mode operator products are diagonal in energy, i.e. proportional to $\delta(E - E')$. Thus the contribution from the last line of Eq.(2.64) vanishes, and one obtains a quite simple expression

$$I_c^{(L)} \doteq \langle \hat{I}_c^{(L)}(x) \rangle = \frac{q}{2\pi\hbar} \int dE \sum_{n=1}^{N(E)} \left(\langle \hat{a}_{n,E}^{(L)\dagger} \hat{a}_{n,E} \rangle - \langle \hat{b}_{n,E}^{(L)\dagger} \hat{b}_{n,E} \rangle \right) \tag{2.65}$$

As expected from the continuity equation, at stationarity the average current (2.65) is time and space independent. We now recall that that outgoing mode operators $\hat{b}_{n,E}^{(j)}$ are related to the incoming mode operators $\hat{a}_{n,E}^{(j)}$ through the scattering matrix Eq.(2.29) through Eqs.(2.30).

Exploiting Eqs.(2.31) one finds

$$\begin{aligned}
 I_c^{(L)} &\doteq \langle \hat{I}_c^{(L)}(x) \rangle = \frac{q}{2\pi\hbar} \int dE \sum_{n=1}^{N(E)} \left(f_L(E) - \sum_{\gamma,i} |S_{L,n;\gamma,i}|^2 f_\gamma(E) \right) = \\
 &= \frac{q}{2\pi\hbar} \int dE \sum_{n=1}^{N(E)} \left(\left(1 - \sum_i |S_{L,n;L,i}|^2 \right) f_L(E) - \sum_i |S_{L,n;R,i}|^2 f_R(E) \right) = \\
 &= \frac{q}{2\pi\hbar} \int dE \left(\left(N(E) - \sum_{i,n=1}^{N(E)} |r'_{n,i}|^2 \right) f_L(E) + \left(\sum_{i,n=1}^{N(E)} |t_{n,i}|^2 \right) f_L(E) \right) = \\
 &= \frac{q}{2\pi\hbar} \int dE \left(\left(N(E) - \sum_{i,n=1}^{N(E)} R'_{n,i} \right) f_L(E) + \left(\sum_{i,n=1}^{N(E)} T_{n,i} \right) f_L(E) \right)
 \end{aligned} \tag{2.66}$$

Recalling the expressions (2.47) and (2.48) of the transmission function the current acquires a simple form[16, 17]

$$I_c^{(L)} = \frac{q}{h} \int dE \tilde{T}(E) [f_L(E) - f_R(E)] \tag{2.67}$$

where we have used the Planck constant $h = 2\pi\hbar$.

2.3.4 Thermal current

Next let us discuss the thermal current inside the leads. Since the electrode is connected only to the mesoscopic system, all the heat generated inside the reservoir will leak into the leads. In this way can be written the continuity equation for heat density[71]

$$\dot{Q}^{(L)} = -J_Q^{(L)} \tag{2.68}$$

where $\dot{Q}^{(L)}$ s time derivative of the heat density and $J_Q^{(L)}$ is heat current floating out of the electrode. Recalling the first law of thermodynamics $dQ = dU + dW$ one obtain

$$\dot{Q}^{(L)} = \dot{U}^{(L)} - \dot{W}^{(L)} \tag{2.69}$$

where $\dot{U}^{(L)}$ is energy flux into left reservoir and $\dot{W}^{(L)}$ is the work done on left reservoir per unit time. Since the volume of reservoir is assumed to be constant the only source of work done on the reservoir is caused by the change of particle number inside of it and therefore[71]

$$\dot{W}^{(L)} = \mu_L \dot{N}^{(L)} \tag{2.70}$$

where μ_L is chemical potential of the left reservoir and $\dot{N}^{(L)}$ is the particle flux through the left lead that can be expressed with the Landauer-Büttiker formalism

$$\dot{N}^{(L)} = \frac{1}{2\pi\hbar} \int dE \tilde{T}(E) [f_L(E) - f_R(E)] \tag{2.71}$$

On the other hand the energy flux can be written as

$$\dot{U}^{(L)} = \frac{1}{2\pi\hbar} \int dE E \tilde{T}(E) [f_L(E) - f_R(E)] \quad (2.72)$$

and therefore the heat current can be expressed as[10, 71]

$$J_Q^{(L)} = \frac{1}{h} \int dE (E - \mu_L) \tilde{T}(E) [f_L(E) - f_R(E)] \quad (2.73)$$

2.3.5 Linear response regime

The results (2.67)-(2.73) are general and allow one to calculate charge and heat current inside the leads. However, through the Fermi distribution functions they exhibit a non linear dependence on the chemical potential μ_γ and the temperature T_γ of the electrodes $\gamma = L, R$. In the linear response regime, the difference in chemical potentials and temperatures of the electrode Fermi functions f_L and f_R are assumed to be small as compared to the values $\mu = E_F$, T characterizing the equilibrium of the entire system reservoir+mesoscopic sample[10]

$$\begin{aligned} \mu_\gamma &= E_F + qV_\gamma \\ T_\gamma &= T + \Theta_\gamma \end{aligned} \quad (2.74)$$

One can then obtain simplified linearized expressions by approximating the Fermi function as[10, 78]

$$f_\gamma(E) \simeq f_0 - \frac{\partial f_0}{\partial E} \left(qV_\gamma + \frac{E - E_F}{T} \Theta_\gamma \right) \quad \gamma = L, R \quad (2.75)$$

where f_0 denotes the full equilibrium Fermi function. Substituting Eq.(2.75) into Eq.(2.67) one obtains the linearized charge current

$$I_c = -\frac{q}{h} \int dE \tilde{T}(E) \frac{\partial f_0}{\partial E} \left[q(V_L - V_R) + \frac{E - E_F}{T} (\Theta_L - \Theta_R) \right] \quad (2.76)$$

Similarly, the heat current (2.73) neglecting the second order perturbation term can be written as

$$J_Q = -\frac{1}{h} \int dE (E - E_F) \tilde{T}(E) \frac{\partial f_0}{\partial E} \left[q(V_L - V_R) + \frac{E - E_F}{T} (\Theta_L - \Theta_R) \right] \quad (2.77)$$

Finally, defining the applied voltage difference and the temperature difference

$$\Delta V \doteq V_L - V_R = (\mu_L - \mu_R)/q \quad (2.78)$$

$$\Delta T \doteq T_L - T_R = \Theta_L - \Theta_R \quad (2.79)$$

the above equations (2.76) and (2.77) can be written as linear response regime[10, 16]

$$I = G\Delta V + L\Delta T \quad (2.80)$$

$$J_Q = M\Delta V + N\Delta T \quad (2.81)$$

with coefficients[10, 62]

$$G = -\frac{q^2}{h} \int dE \tilde{T}(E) \frac{\partial f_0}{\partial E} \quad (2.82)$$

$$L = -\frac{q}{hT} \int dE \tilde{T}(E) (E - E_F) \frac{\partial f_0}{\partial E} \quad (2.83)$$

$$M = TL \quad (2.84)$$

$$N = -\frac{1}{hT} \int dE \tilde{T}(E) (E - E_F)^2 \frac{\partial f_0}{\partial E} \quad (2.85)$$

In the low temperature limit the linear coefficients can be further simplified using the Sommerfield expansion[48]. In particular, while for G the zero order is non vanishing, for the other coefficients the second order of the expansion is the leading term, and one obtains[10, 62]

$$G = \frac{q^2}{h} \tilde{T}(E_F) \quad (2.86)$$

$$L = \frac{q\pi k_B^2 T}{6\hbar} \left. \frac{\partial \tilde{T}(E)}{\partial E} \right|_{E_F} \quad (2.87)$$

$$M = \frac{q\pi k_B^2 T^2}{6\hbar} \left. \frac{\partial \tilde{T}(E)}{\partial E} \right|_{E_F} \quad (2.88)$$

$$N = \frac{\pi k_B^2 T}{6\hbar} \tilde{T}(E_F) \quad (2.89)$$

The quantum of conductance

Notably in the case of perfect transmission, $\tilde{T}(E) \equiv 1$, one can find $G \propto N(E_F)$ and therefore each channel contribute a quantum of conductance

$$G_0 = \frac{q^2}{h} \quad (2.90)$$

that is an upper bound for a quantum wire[17, 78]. It is a universal quantity, since it only depends on constants of nature and is independent of the specific measurement set up. Moreover, this implies that its inverse identifies, and commonly referred a resistance $R_Q = G_0^{-1} = h/q^2$, whihc is referred to as the quantum of resistance. or also as the contact resistance. This conclusion may seem to be counterintuitive, since it is at first unexpected to find a resistance in a perfectly transmitting system. However, it arises from the interface between regions with intrinsically different properties, namely the mesoscopic system and the electrode. Indeed, differently from the mesoscopic system, in the electrodes inelastic scattering occur and lead to thermalization: An electron outgoing from the mesoscopic system and entering the electrode is redistributed among several modes and thermalized according to the equilibrium distribution function of that electrode, of the electrode[15], losing the initial information on the conducting modes and on the phase of the mesoscopic system. This irreversible process is linked with dissipation and is the source of the quantum

of resistance, which is therefore also called the contact resistance. The quantization of conductance, theoretically predicted by Büttiker[11] was observed for the first time in experiments carried out in quantum point contacts in a two-dimensional electron gas[9, 13]

Chapter 3

Rashba Nanowire exposed to an external magnetic field

In this chapter I shall focus on the transport properties of a nanowire (NW) with Rashba spin-orbit coupling (RSOC). In particular, I shall discuss the case of a nanowire exposed to an external magnetic field, uniformly applied along the entire length of the nanowire. Due to the interplay between the actual magnetic field and the effective Rashba "magnetic field", this setup has received a great deal of attention in last years, since it allows to realise some interesting physical effects, such as the presence of helical states, namely states characterized by a locking between the direction of propagation and the spin orientation. While helical states are known to exist at the boundaries of a two-dimensional topological insulator, NWs enable one to realize actual one-dimensional helical channels.

I shall first describe the general properties and the main energy scales characterizing a NW with a spatially homogeneous RSOC. Indeed the RSOC constant can be modulated by applying the gate voltage applied either between the NW and the substrate or by suitable metallic gates. In this way, various physically interesting regimes can be realized. Then, I shall focus on the case of an inhomogeneous RSOC, which can also be realized by applying different gate potentials on different portions of the NW. This inhomogeneous configurations lead to interesting transport phenomena that I shall analyze by applying the Scattering Matrix formalism described in the previous Chapter.

3.1 Nanowire with a homogeneous RSOC

Let us consider a Rashba NW where one single transversal channel is active in the physically relevant energy range. The electron dynamics is thus effectively described by a purely 1D model along the longitudinal direction, which we denote by x . The NW is supposed to be deposited on a substrate and/or to be coupled to a metallic gate, and such SIA gives rise to an electric field perpendicular to the substrate plane, which results in a Rashba "effective magnetic field" lying in the substrate plane but orthogonal to the NW axis. As sketched in Fig.3.1, we shall denote by y the direction perpendicular to the substrate and by z the direction of the Rashba magnetic field. Notably, the Rashba RSOC can be tuned

by the gate voltage applied between the NW and the substrate and/or additional gates. In InSb or InAs NWs such RSOC can be particularly high [40, 45, 56, 57, 61, 81]. In turn, the RSOC lifts the spin degeneracy of the bands, and one must take into account such additional, intrinsic, degree of freedom, that effectively acts as a separate channel[23]. As has been discussed in chapter 1.4, an electron in a 1D Rashba NW is described by the first-quantized Hamiltonian

$$H = -\frac{\hbar^2}{2m^*}\partial_x^2\sigma_0 + i\alpha\sigma_z\partial_x \quad (3.1)$$

where α is the RSOC strength and x is the longitudinal direction of the NW. In the following, it will particularly important to include also the effects of an additional Zeeman coupling, due to an external magnetic field \mathbf{B} applied perpendicularly to Rashba spin orbit coupling term z . For the sake of simplicity we shall take the magnetic field along the longitudinal NW direction x , i.e. $\mathbf{B} = B_x\hat{e}_x$. The related Zeeman energy contribution is $h_{\perp} = g\mu_B B_x$ where g is gyromagnetic factor, and

$$\mu_B = \frac{e\hbar}{2m^*} \quad (3.2)$$

is the Bohr magneton, with e denoting the electron charge. The Hamiltonian of 1D single channel NW can thus be rewritten as

$$H = \frac{p_x^2}{2m^*}\sigma_0 - \frac{\alpha}{\hbar}p_x\sigma_z - h_{\perp}\sigma_x \quad (3.3)$$

where σ_x, σ_z are Pauli matrices, and σ_0 is identity matrix. Notably, while RSOC preserves the time-reversal symmetry $\mathcal{T} = i\sigma_y K$, where K denotes complex conjugation, the external magnetic field breaks it.

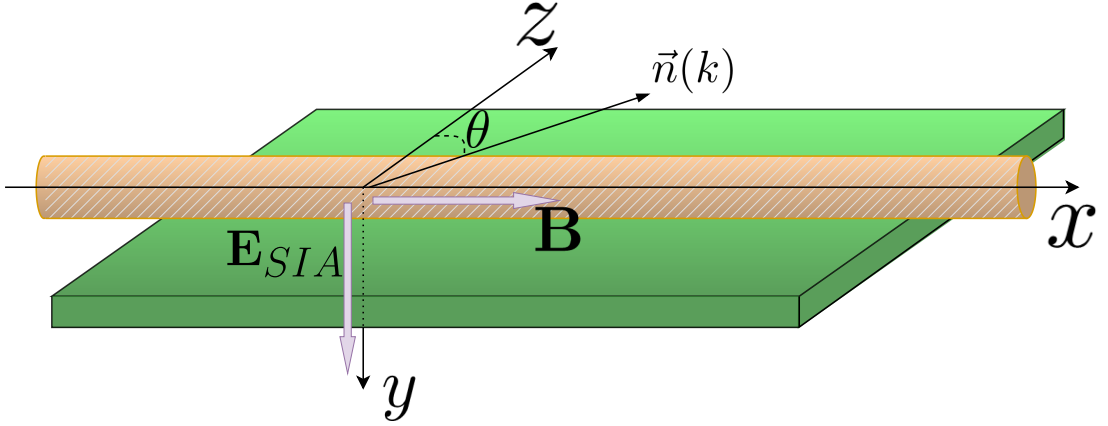


Figure 3.1: Schematic of the Rashba NW on the substrate. The external electric field \mathbf{E}_{SIA} , caused by SIA at the interface between the NW and substrate, gives rise to the RSOC. The spin quantization axis \vec{n} lies in x - z substrate plane, and is determined by both the Rashba effective "magnetic field" and the actual Zeeman magnetic field \mathbf{B} .

Since we shall deal with many electrons, we shall adopt the second-quantization formalism, and the NW Hamiltonian will be described by

$$\hat{\mathcal{H}} = \int dx \hat{\Psi}^\dagger(x) \left[-\frac{\hbar^2}{2m^*} \partial_x^2 \sigma_0 + i\alpha \sigma_z \partial_x - \sigma_x h_\perp \right] \hat{\Psi}(x) \quad (3.4)$$

where we have introduced the electron field operator $\hat{\Psi}(x)$ satisfying the fermionic anti-commutation relations (2.15).

Importantly, the presence of the spin-orbit term in the Hamiltonian (3.4) yields an unconventional expression for the current operator. Indeed the Heisenberg Equation $i\hbar \dot{\hat{\Psi}}(x, t) = [\hat{\Psi}(x, t), \hat{\mathcal{H}}]$ dictated by the Hamiltonian (3.4) for the field operator $\hat{\Psi}$ is

$$i\hbar \frac{\partial \hat{\Psi}(x, t)}{\partial t} = -\frac{\hbar^2}{2m^*} \partial_x^2 \hat{\Psi}(x, t) + i\sigma_z \alpha \partial_x \hat{\Psi}(x, t) - \sigma_x h_\perp \hat{\Psi}(x, t) \quad (3.5)$$

and its adjoint equation reads

$$-i\hbar \frac{\partial \hat{\Psi}^\dagger(x, t)}{\partial t} = -\frac{\hbar^2}{2m^*} \partial_x^2 \hat{\Psi}^\dagger(x, t) - i\sigma_z \alpha \partial_x \hat{\Psi}^\dagger(x, t) - \sigma_x h_\perp \hat{\Psi}^\dagger(x, t) \quad (3.6)$$

Multiplying Eq.(3.5) by $\hat{\Psi}^\dagger$ on the left and Eq.(3.6) on the right by $\hat{\Psi}$ and subtracting the two resulting equations, one obtains the continuity equation

$$\partial_t \hat{\rho} + \partial_x \hat{J} = 0 \quad (3.7)$$

where

$$\hat{\rho}(x, t) = \hat{\Psi}^\dagger(x, t) \hat{\Psi}(x, t) \quad (3.8)$$

is the particle density, while

$$\hat{J}(x, t) = -i \frac{\hbar}{2m^*} \left(\hat{\Psi}^\dagger(x, t) \partial_x \hat{\Psi}(x, t) - \partial_x \hat{\Psi}^\dagger(x, t) \hat{\Psi}(x, t) \right) - \frac{\alpha}{\hbar} \hat{\Psi}^\dagger \sigma_z \hat{\Psi} \quad (3.9)$$

is the particle current density and consists of two contributions[84]. The first term is the customary expression for the current operator and stems from the kinetic energy

$$\hat{J}_{kin} = -\frac{i\hbar}{2m^*} \left(\hat{\Psi}^\dagger(x) \frac{\partial \hat{\Psi}(x)}{\partial x} - \frac{\partial \hat{\Psi}^\dagger(x)}{\partial x} \hat{\Psi}(x) \right) \quad (3.10)$$

whereas the second term in Eq.(3.9) stems from the RSOC

$$\hat{J}_{so} = -\frac{\alpha}{\hbar} \hat{\Psi}^\dagger(x) \sigma_z \hat{\Psi}(x) \quad (3.11)$$

3.1.1 Spectrum

Since the single-particle Hamiltonian (3.3) commutes with the momentum operator $p_x = -i\hbar \partial_x$, it is suitable to rewrite the many-particle Hamiltonian (3.4) in k -space as

$$\hat{\mathcal{H}} = \sum_k \hat{C}_k^\dagger H(k) \hat{C}_k \quad (3.12)$$

where $\hat{C}_k = \begin{pmatrix} \hat{c}_{k\uparrow} \\ \hat{c}_{k\downarrow} \end{pmatrix}$ are the Fourier mode operators related to the field $\hat{\Psi}$ through

$$\hat{\Psi}(x) = \frac{1}{\sqrt{\Omega}} \sum_k e^{ikx} \begin{pmatrix} \hat{c}_{k\uparrow} \\ \hat{c}_{k\downarrow} \end{pmatrix} \quad (3.13)$$

with Ω denoting the NW length, whereas

$$H(k) = \epsilon_k^0 \sigma_0 - \alpha k \sigma_z - h_{\perp} \sigma_x = \begin{pmatrix} \epsilon_k^0 - \alpha k & -h_{\perp} \\ -h_{\perp} & \epsilon_k^0 + \alpha k \end{pmatrix} \quad (3.14)$$

is a k -dependent 2×2 -matrix, with

$$\epsilon_k^0 = \frac{\hbar^2 k^2}{2m^*} \quad (3.15)$$

denoting the customary parabolic band in the absence of RSOC and Zeeman terms. From Eq.(3.14), we expect the spin quantization axis to lie in x - z plane, as depicted on Fig.3.1, and to be intermediate between the directions x and z dictated by the Zeeman and Rashba terms, respectively. Explicitly, such direction forms with the z -axis an angle $\theta(k)$ that depends on the wavevector k and is identified by the unit vector

$$\vec{n}(k) = (\sin(\theta(k)), 0, \cos(\theta(k))) \quad (3.16)$$

where the angle $\theta(k) \in [-\pi, \pi]$ is defined through

$$\begin{cases} \sin(\theta(k)) = \frac{h_{\perp}}{\sqrt{\alpha^2 k^2 + h_{\perp}^2}} \\ \cos(\theta(k)) = \frac{\alpha k}{\sqrt{\alpha^2 k^2 + h_{\perp}^2}} \end{cases} \quad (3.17)$$

In turn, Eq.(3.14) can be rewritten as

$$H(k) = \epsilon_k^0 \sigma_0 - \sqrt{\alpha^2 k^2 + h_{\perp}^2} \vec{n}(k) \cdot \vec{\sigma} \quad (3.18)$$

whence one can straightforwardly deduce the spectrum, consisting of two bands

$$E_1(k) = \epsilon_k^0 - \sqrt{h_{\perp}^2 + (\alpha k)^2} \quad (3.19)$$

$$E_2(k) = \epsilon_k^0 + \sqrt{h_{\perp}^2 + (\alpha k)^2} \quad (3.20)$$

As compared to the NW spectrum without magnetic field (see Fig.1.3), the two bands (3.19) and (3.20) are separated by a gap $\Delta = 2E_Z$ at $k = 0$ opened up by the Zeeman term, as shown in Fig.3.2.

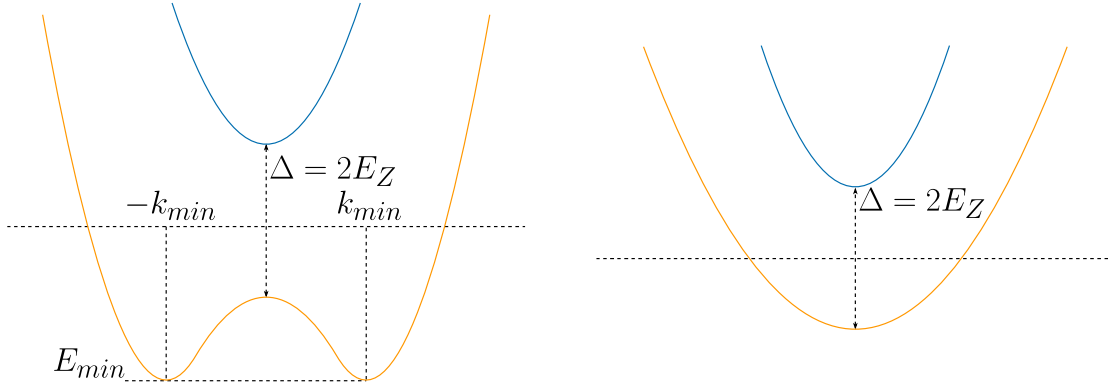
Notably, the problem is characterized by two energy scales, namely

$$E_{SO} = \frac{m^* \alpha^2}{2\hbar^2} \quad (\text{spin-orbit energy}) \quad (3.21)$$

$$E_Z = |h_{\perp}| \quad (\text{Zeeman energy}) \quad (3.22)$$

Depending on the values of E_{SO} and E_Z , from Eqs.(3.19)-(3.20) one can identify two relevant regimes:

- $E_Z < 2E_{SO}$ (Rashba dominated regime), illustrated in Fig.3.2a, in which the lowest band exhibits a local maximum at $k = 0$ and two local minima at $k = \pm k_{min}$ with $k_{min} = k_{SO}(1 + (h_{\perp}/2E_{SO})^2)$ with energy $E_{min} = E_-(k_{min}) = -E_{SO}(1 + (h_{\perp}/2E_{SO})^2)$;
- $2E_{SO} < E_Z$ (Zeeman dominated regime), illustrated in Fig.3.2b, in which both energy bands exhibit minima at $k = 0$ and resemble Zeeman dispersion relations.



(a) Rashba dominated regime $E_Z < 2E_{SO}$ where $E_{min} = -E_{SO}(1 + (h_{\perp}/2E_{SO})^2)$ and $k_{min} = k_{SO}(1 + (h_{\perp}/2E_{SO})^2)$

(b) Zeeman dominated regime $E_Z > 2E_{SO}$

Figure 3.2: Dispersion relation in Rashba and Zeeman dominated regimes.

The spectrum (3.19, 3.20) and the spin direction angle θ in Eq.(3.17) can also be re-expressed in terms of these energy scales as

$$E_1(k) = \epsilon_k^0 - \sqrt{E_Z^2 + 4\epsilon_k^0 E_{SO}} \quad (3.23)$$

$$E_2(k) = \epsilon_k^0 + \sqrt{E_Z^2 + 4\epsilon_k^0 E_{SO}} \quad (3.24)$$

and

$$\begin{cases} \sin(\theta(k)) = \text{sgn}(h_{\perp}) \frac{E_Z}{\sqrt{E_Z^2 + 4\epsilon_k^0 E_{SO}}} \\ \cos(\theta(k)) = 2\text{sgn}(\alpha k) \sqrt{\frac{\epsilon_k^0 E_{SO}}{E_Z^2 + 4\epsilon_k^0 E_{SO}}} \end{cases} \quad (3.25)$$

respectively.

3.1.2 Eigenstates

Propagating modes

Propagating modes are eigenfunctions of the Hamiltonian (3.3) of the form

$$\psi_k(x) = \frac{1}{\sqrt{\Omega}} e^{ikx} \chi(k) \quad (3.26)$$

where $k \in \mathbb{R}$ and $\chi(k)$ is a 2×1 spinor, eigenvector of the Hamiltonian matrix (3.14). For each wavevector k , there are two of such eigenvectors, χ_1 and χ_2

$$H(k)\chi_{1,2} = E_{1,2}(k)\chi_{1,2} \quad (3.27)$$

with corresponding eigenvalues given in Eqs.(3.23)-(3.24). The explicit expression of $\chi_{1,2}$ reads ¹

$$\chi_1(k) = \begin{pmatrix} \cos\left(\frac{\theta(k)}{2}\right) \\ \sin\left(\frac{\theta(k)}{2}\right) \end{pmatrix} \quad \chi_2(k) = \begin{pmatrix} -\sin\left(\frac{\theta(k)}{2}\right) \\ \cos\left(\frac{\theta(k)}{2}\right) \end{pmatrix} \quad (3.28)$$

as can straightforwardly be deduced from the expression (3.18) of the Hamiltonian in terms of the unit vector $\vec{n}(k)$. Introducing the unitary matrix $\Xi = (\chi_1, \chi_2)$, whose columns are such eigenvectors, and exploiting the property

$$\Xi^\dagger(k)H(k)\Xi(k) = \begin{pmatrix} E_1(k) & 0 \\ 0 & E_2(k) \end{pmatrix} \quad (3.29)$$

the Hamiltonian (3.12) is rewritten in a diagonalized form

$$\hat{\mathcal{H}} = \sum_k \left(E_1(k) \hat{\gamma}_{1k}^\dagger \hat{\gamma}_{1k} + E_2(k) \hat{\gamma}_{2k}^\dagger \hat{\gamma}_{2k} \right) \quad (3.30)$$

where the diagonalizing operators $\hat{\gamma}_{1k}$ and $\hat{\gamma}_{2,k}$ are related to the Fourier modes through

$$\hat{C}_k = \begin{pmatrix} \hat{c}_{k\uparrow} \\ \hat{c}_{k\downarrow} \end{pmatrix} = \Xi(k) \begin{pmatrix} \hat{\gamma}_{1k} \\ \hat{\gamma}_{2,k} \end{pmatrix} = \chi_1(k) \hat{\gamma}_{1k} + \chi_2(k) \hat{\gamma}_{2k} \quad (3.31)$$

Substituting Eq.(3.31) into Eq.(3.13), one can see that the eigenstates χ_1 and χ_2 correspond to plane waves, i.e. to propagating modes

$$\hat{\Psi}(x) = \frac{1}{\sqrt{\Omega}} \sum_k e^{ikx} (\chi_1(k) \hat{\gamma}_{1k} + \chi_2(k) \hat{\gamma}_{2k}) \quad (3.32)$$

¹From trigonometric formulas one has $\cos(\theta(k)/2) = \sqrt{[1 + \cos(\theta(k))]/2}$ and $\sin(\theta(k)/2) = \text{sgn}(h_\perp) \sqrt{[1 - \cos(\theta(k))]/2}$, where $\cos(\theta(k))$ is given by Eq.(3.17).

Evanescent modes

Together with the propagating modes, one can also identify evanescent modes, namely eigenfunctions of the Hamiltonian (3.3) of the form

$$\psi_\kappa(x) = e^{\kappa x} \xi(\kappa) \quad (3.33)$$

where $\kappa \in \mathbb{R}$, and $\xi(\kappa)$ is 2×1 vector. These solutions exponentially decay for either $x \rightarrow \infty$ or $x \rightarrow -\infty$, depending on whether $\kappa < 0$ or $\kappa > 0$. Although in the case of a homogeneous NW these eigenfunctions are *not* part of the Hilbert space since they are not normalizable, they will play a crucial role later when considering the inhomogeneous problem, where the solution is built up using both the propagating and the evanescent modes of each locally homogeneous region. For this reason it is worth describing them here.

When the NW Hamiltonian (3.3) is applied to evanescent waves (3.33), the Schrödinger equation $H\psi_\kappa(x) = E\psi_\kappa(x)$ in κ -space reduces to an eigenvalue problem for a non-Hermitian matrix

$$\begin{pmatrix} -\epsilon_\kappa^0 + i\alpha\kappa & -h_\perp \\ -h_\perp & -\epsilon_\kappa^0 - i\alpha\kappa \end{pmatrix} \xi(\kappa) = E \xi(\kappa) \quad (3.34)$$

with

$$\epsilon_\kappa^0 = \frac{\hbar^2 \kappa^2}{2m^*} \quad . \quad (3.35)$$

One can easily find the eigenvalues

$$E_1(\kappa) = -\epsilon_\kappa^0 - \sqrt{E_Z^2 - 4\epsilon_\kappa^0 E_{SO}} \quad (3.36)$$

$$E_2(\kappa) = -\epsilon_\kappa^0 + \sqrt{E_Z^2 - 4\epsilon_\kappa^0 E_{SO}} \quad (3.37)$$

and the eigenvectors

$$\xi_1(\kappa) = \frac{1}{\sqrt{2}} \begin{pmatrix} e^{-i \arctan(\sinh(\theta(\kappa)))} \\ 1 \end{pmatrix} \quad \xi_2(\kappa) = \frac{1}{\sqrt{2}} \begin{pmatrix} -e^{i \arctan(\sinh(\theta(\kappa)))} \\ 1 \end{pmatrix} \quad (3.38)$$

where the angle $\theta(\kappa)$ is defined with

$$\sinh(\theta(\kappa)) = 2\text{sgn}(\alpha\kappa) \sqrt{\frac{\epsilon_\kappa^0 E_{SO}}{E_Z^2 - 4\epsilon_\kappa^0 E_{SO}}} \quad (3.39)$$

Note that, differently from the propagating states, the spinor (3.38) of evanescent modes lies in x - y plane rather than x - z -plane.

3.1.3 The Rashba dominated regime: helical states

Let us examine in more details the NW in the Rashba dominated regime $E_Z < 2E_{SO}$. In particular, it is possible to show that, in the deep Rashba dominated regime $E_Z \ll 2E_{SO}$, the states inside the magnetic gap energy range $|E| < E_Z \ll 2E_{SO}$ are *helical*, i.e. they

exhibit a locking between the propagation direction and the spin orientation[44, 54, 55, 58, 65, 66, 72, 75, 82, 85]. For instance right-moving electrons are characterized by (say) spin- \uparrow , whereas left-moving electrons are characterized by the opposite orientation, i.e. spin- \downarrow . Helical conducting channels have been observed at the boundaries of a 2D Topological Insulator[32, 34, 42, 43, 51, 53, 76]. However, the helical states realized with NWs have some peculiarities: First they are genuine 1D channels, instead of edge states of a 2D material. Second, their helicity, i.e. the sign determining which spin orientation is locked to which propagation direction, is controlled by the sign of the RSOC. The helicity of the Rashba states inside the energy gap is represented qualitatively on the Figure 3.3.

In order to illustrate how this effect arises, we first observe that the direction of the quantization axis (3.16) is determined by the sign of the product αk . In particular, the change $\alpha k \mapsto -\alpha k$ leads the unit vector \vec{n} in Eq.(3.16) to be reflected with respect to x -axis, for a given sign of α it is equivalent to

$$\theta(-k) = \pi - \theta(k) \quad (3.40)$$

Therefore one can write explicitly the spinor part of the conducting states inside the gap for the left propagating modes $\chi_1(k)$ and right propagating modes $\chi_1(-k)$

$$\begin{cases} \chi_1(k) = \begin{pmatrix} \cos(\frac{\theta(k)}{2}) \\ \sin(\frac{\theta(k)}{2}) \end{pmatrix} \\ \chi_1(-k) = \begin{pmatrix} \cos(\frac{\pi}{2} - \frac{\theta(k)}{2}) \\ \sin(\frac{\pi}{2} - \frac{\theta(k)}{2}) \end{pmatrix} = \begin{pmatrix} \sin(\frac{\theta(k)}{2}) \\ \cos(\frac{\theta(k)}{2}) \end{pmatrix} \end{cases} \quad (3.41)$$

In particular, in the regime $|E| \ll E_Z \ll 2E_{SO}$ one finds that $k \approx \pm 2k_{SO}$, up to $O((E_Z/2E_{SO})^2)$, and from Eq(3.25) that angle $\theta(k)$ becomes independent on k and assume only two values $\theta \simeq 0, \pi$ according to the sign of α

$$\begin{cases} \sin(\frac{\theta(k)}{2}) \simeq \sqrt{\frac{1}{2}(1 - \text{sgn}(\alpha))} \\ \cos(\frac{\theta(k)}{2}) \simeq \sqrt{\frac{1}{2}(1 + \text{sgn}(\alpha))} \end{cases} \quad (3.42)$$

Substituting Eqs.(3.42) in Eq.(3.41), one realizes that spinors become eigenvectors of σ_z , namely $|\uparrow\rangle = (1, 0)^T$ and $|\downarrow\rangle = (0, 1)^T$ and the states with opposite wave vectors and velocities turn out to have opposite spin orientation. For instance in the case $\alpha > 0$ the states with $k \simeq +2k_{SO}$ are right-moving and have spin- \uparrow , whereas the states with $k \simeq -2k_{SO}$ are left-moving and have spin- \downarrow

$$\chi_1(2k_{SO}) \simeq \begin{pmatrix} 1 \\ 0 \end{pmatrix} \quad \chi_1(-2k_{SO}) \simeq \begin{pmatrix} 0 \\ 1 \end{pmatrix} \quad (3.43)$$

These states are thus characterized by a positive helicity. For $\alpha < 0$ one obtains helical states with negative helicity, namely right-moving states have spin- \downarrow , while left-moving states have spin- \uparrow . As we shall discuss here below, this behaviour is typically well captured

by the massless Dirac-like model. However, near $k = 0$, one may identify as well a gapped modes described by the massive Dirac-like model, shown in Figure 3.3. For energy inside the gap these modes should give rise to the evanescent solution, that as pointed out in the previous sections may be crucial in the case of inhomogeneous RSOC constant. Therefore one should consider more systematic approach that would allow to capture all relevant aspects of the problem.

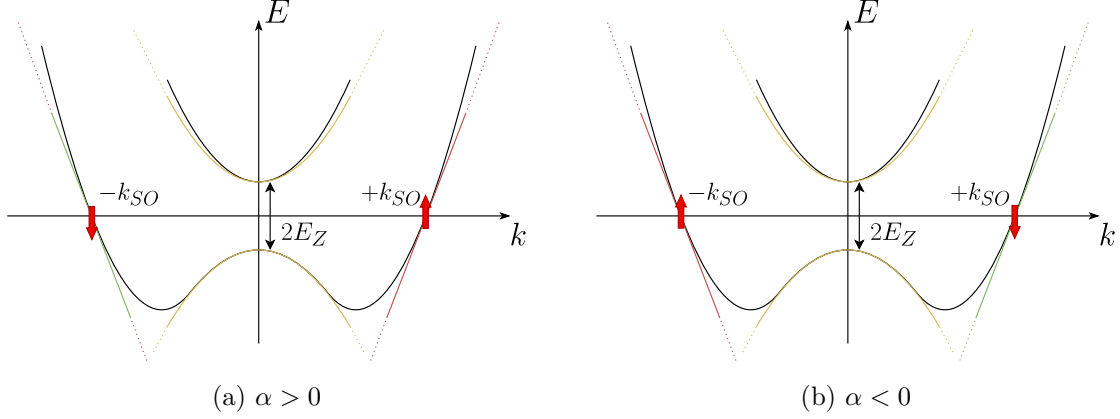


Figure 3.3: Spin-momentum locking in the case of deep Rashba dominated regime $E_Z \ll 2E_{SO}$. The green and red lines represent massless Dirac-like modes and correspond respectively to the spin-down and spin-up branches. The yellow lines are massive Dirac-like modes.

In order to investigate more in details the properties of the helical Rashba states within the regime $|E| \ll E_Z \ll 2E_{SO}$ let us derive the effective model, namely the linear expansion in low energy excitations with respect to the fully occupied ground state that is assumed to be a Fermi sea $|FS\rangle$ with all NW modes occupied for $E < 0$. For this purpose first of all the Hamiltonian (3.12) should be rewritten in term of main energy scales E_{SO} and E_Z

$$\hat{\mathcal{H}} = \sum_k \hat{C}_k^\dagger \left(\frac{\hbar^2}{2m^*} (k\sigma_0 - s_\alpha k_{SO}\sigma_z)^2 - E_{SO}\sigma_0 - E_Z\sigma_x \right) \hat{C}_k \quad (3.44)$$

where $s_\alpha = \text{sgn}(\alpha)$ and we assume $h_\perp > 0$ for definiteness. After that we proceed by expanding it around $k \sim \pm 2k_{SO}$ and $k = 0$.

Expansion near $k = \pm 2k_{SO}$.

In order to extract the low energy Hamiltonian governing the dynamics of helical states near the two Fermi points $k = \pm 2k_{SO}$. Specifically, let us for instance focus on the vicinity of $2s_\alpha k_{SO}$, which thus corresponds to $+2k_{SO}$ if $\alpha > 0$ ($s_\alpha = +1$) and $-2k_{SO}$ if $\alpha < 0$ ($s_\alpha = -1$) and consider a small deviation q from it, by setting $k = 2s_\alpha k_{SO} + q$, with

$|q| \ll k_{SO}$. Then, the Rashba NW Hamiltonian (3.44) can be rewritten as

$$\hat{\mathcal{H}}_{NW} \Big|_{k \simeq +2s_\alpha k_{SO}} \simeq \sum_{|q| \ll k_{SO}} \hat{C}_{2s_\alpha k_{SO}+q}^\dagger \begin{pmatrix} \frac{\hbar^2}{2m^*}(q + s_\alpha k_{SO})^2 - E_{SO} & -E_Z \\ -E_Z & \frac{\hbar^2}{2m^*}(q + 3s_\alpha k_{SO})^2 - E_{SO} \end{pmatrix} \hat{C}_{2s_\alpha k_{SO}+q} \quad (3.45)$$

and, neglecting the quadratic terms in q , the expression can be simplified to

$$\hat{\mathcal{H}}_{NW} \Big|_{k \simeq +2k_{SO}} \simeq \sum_{|q| \ll k_{SO}} \hat{C}_{2s_\alpha k_{SO}+q}^\dagger \begin{pmatrix} s_\alpha \hbar v_{SO} q & -E_Z \\ -E_Z & 3s_\alpha \hbar v_{SO} q + 8E_{SO} \end{pmatrix} \hat{C}_{2s_\alpha k_{SO}+q} \quad (3.46)$$

where $v_{SO} = \hbar k_{SO}/m^*$. By diagonalizing the block matrix

$$H(q) = \begin{pmatrix} s_\alpha \hbar v_{SO} q & -E_Z \\ -E_Z & 3s_\alpha \hbar v_{SO} q + 8E_{SO} \end{pmatrix} \quad (3.47)$$

one finds eigenvalues

$$E_1(q) = s_\alpha \hbar v_{SO} q + 4E_{SO} - \sqrt{16E_{SO}^2 + E_Z^2 + 8E_{SO}s_\alpha \hbar v_{SO} q + (\hbar v_{SO} q)^2} \quad (3.48)$$

$$E_2(q) = 3s_\alpha \hbar v_{SO} q + 4E_{SO} + \sqrt{16E_{SO}^2 + E_Z^2 + 8E_{SO}s_\alpha \hbar v_{SO} q + (\hbar v_{SO} q)^2} \quad (3.49)$$

Recalling that in deep Rashba dominated regime the spin orbit energy E_{SO} is the dominant energy scale ($E_Z, \hbar v_{SO}|q| \ll E_{SO}$) one can expand the above eigenvalues up to first order in $\hbar v_{SO}|q|/E_{SO}$ and E_Z/E_{SO} , obtaining

$$E_1(q) \simeq s_\alpha \hbar v_{SO} q \quad (3.50)$$

$$E_2(q) = 8E_{SO} \left(1 + \mathcal{O} \left(\frac{\hbar v_{SO} q}{E_{SO}} \right) \right) \quad (3.51)$$

One can thus see that in this regime the eigenvalues are equal to the diagonal terms of the matrix (3.47), which are energetically quite separated. For this reason the off diagonal Zeeman terms that couples the spin- \uparrow and spin- \downarrow components of $\hat{C}_{2s_\alpha k_{SO}+q}^\dagger$ acts as a weak perturbation and eventually can be neglected. Furthermore, since we are interested in the low energy sector $|E| \ll E_Z$, the large energy $E_2 \sim 8E_{SO}$ characterized by the spin- \downarrow electrons can be neglected, and only the low energy $E_1 \sim s_\alpha \hbar v_{SO} q$ describing spin- \uparrow electrons must be retained. The Hamiltonian (3.46) thus reduced to

$$\hat{\mathcal{H}}_{NW} \Big|_{k \simeq +2s_\alpha k_{SO}} \simeq \sum_{|q| \ll k_{SO}} s_\alpha \hbar v_{SO} q \hat{c}_{2s_\alpha k_{SO}+q, \uparrow}^\dagger \hat{c}_{2s_\alpha k_{SO}+q, \uparrow} \quad , \quad (3.52)$$

One can follow a similar approach near the $-2s_\alpha k_{SO}$ Fermi point, this time finding that only the spin- \downarrow states matter, from which follows

$$\hat{\mathcal{H}}_{NW} \Big|_{k \simeq -2s_\alpha k_{SO}} \simeq - \sum_{|q| \ll k_{SO}} s_\alpha \hbar v_{SO} q \hat{c}_{-2s_\alpha k_{SO}+q, \downarrow}^\dagger \hat{c}_{-2s_\alpha k_{SO}+q, \downarrow} \quad , \quad (3.53)$$

By combining Eqs.(3.52)-(3.53) one thus obtains the low energy Hamiltonian near the $k = \pm 2k_{SO}$ points

$$\hat{\mathcal{H}}_{NW}\Big|_{k \simeq \pm 2k_{SO}} \simeq \sum_{|q| \ll k_{SO}} \hbar s_{\alpha} v_{SO} q \begin{pmatrix} \hat{\zeta}_{q\uparrow}^{\dagger} & \hat{\zeta}_{q\downarrow}^{\dagger} \end{pmatrix} \sigma_z \begin{pmatrix} \hat{\zeta}_{q\uparrow} \\ \hat{\zeta}_{q\downarrow} \end{pmatrix} \quad (3.54)$$

where we have redenoted

$$\begin{cases} \hat{\zeta}_{q\uparrow} \doteq \hat{c}_{2s_{\alpha}k_{SO}+q,\uparrow} \\ \hat{\zeta}_{q\downarrow} \doteq \hat{c}_{-2s_{\alpha}k_{SO}+q,\downarrow} \end{cases} \quad (3.55)$$

From the expression of the Hamiltonian (3.54) it is clear that and that $\hat{\zeta}_{q\uparrow,\downarrow}$ describe *massless* propagating modes.

Expansion near $k = 0$.

Beside the propagating modes, however, one can identify as well gapped (i.e. massive) modes, related to the upper and lower bands for $k \sim 0$ and sketched by yellow lines in Fig.3.3. In order to extract the low energy contribution from these modes, one can expand Eqs.(3.44) near $k \sim 0$

$$\hat{\mathcal{H}}_{NW}\Big|_{k \simeq 0} \simeq \sum_{|q| \ll k_{SO}} \hat{C}_q^{\dagger} \begin{pmatrix} -s_{\alpha} \hbar v_{SO} q & -E_Z \\ -E_Z & -s_{\alpha} \hbar v_{SO} q \end{pmatrix} \hat{C}_q \quad (3.56)$$

This time the diagonal entries of the matrix in Eq.(3.56) have relatively low energies comparable to the off-diagonal Zeeman term E_Z , and thus spin- \uparrow and spin- \downarrow components get coupled. The low energy effective model reads

$$\begin{aligned} \hat{\mathcal{H}}_{NW}\Big|_{k \simeq 0} \simeq & - \sum_{|q| \ll k_{SO}} \hbar s_{\alpha} v_{SO} q \begin{pmatrix} \hat{\eta}_{q\uparrow}^{\dagger} & \hat{\eta}_{q\downarrow}^{\dagger} \end{pmatrix} \sigma_z \begin{pmatrix} \hat{\eta}_{q\uparrow} \\ \hat{\eta}_{q\downarrow} \end{pmatrix} \\ & - E_Z \sum_{|q| \ll k_{SO}} \begin{pmatrix} \hat{\eta}_{q\uparrow}^{\dagger} & \hat{\eta}_{q\downarrow}^{\dagger} \end{pmatrix} \sigma_x \begin{pmatrix} \hat{\eta}_{q\uparrow} \\ \hat{\eta}_{q\downarrow} \end{pmatrix} \end{aligned} \quad (3.57)$$

where the newly redenoted operators

$$\begin{cases} \hat{\eta}_{q\uparrow} \doteq \hat{c}_{q\uparrow} \\ \hat{\eta}_{q\downarrow} \doteq \hat{c}_{q\downarrow} \end{cases} \quad (3.58)$$

describe *massive* modes, due to the Zeeman term.

Low energy Hamiltonian

Summing up Eqs.(3.54) and (3.57) one obtains a low-energy NW Hamiltonian. Moreover, we observe that the obtained effective model shares the low energy sector with a model

where the constraints on wave vector q is removed. Thus, we can argue that the low energy behaviour of the Rashba NW is described by the model

$$\begin{aligned} \hat{\mathcal{H}}_{LEM} = & \sum_{q=-\infty}^{+\infty} \begin{pmatrix} \hat{\zeta}_{q\uparrow}^\dagger & \hat{\zeta}_{q\downarrow}^\dagger \end{pmatrix} \begin{pmatrix} \hbar v_{SO} q & 0 \\ 0 & -\hbar v_{SO} q \end{pmatrix} \begin{pmatrix} \hat{\zeta}_{q\uparrow} \\ \hat{\zeta}_{q\downarrow} \end{pmatrix} \\ & + \sum_{q=-\infty}^{+\infty} \begin{pmatrix} \hat{\eta}_{q\uparrow}^\dagger & \hat{\eta}_{q\downarrow}^\dagger \end{pmatrix} \begin{pmatrix} -\hbar v_{SO} q & -E_Z \\ -E_Z & \hbar v_{SO} q \end{pmatrix} \begin{pmatrix} \hat{\eta}_{q\uparrow} \\ \hat{\eta}_{q\downarrow} \end{pmatrix} \end{aligned} \quad (3.59)$$

that involves both massless Dirac modes ζ and massive Dirac modes η . Introducing the corresponding fields

$$\zeta_\sigma(x) = \frac{1}{\sqrt{\Omega}} \sum_q \zeta_{q,\sigma} e^{iqx} \quad \eta_\sigma(x) = \frac{1}{\sqrt{\Omega}} \sum_q \eta_{q,\sigma} e^{iqx} \quad (3.60)$$

where $\sigma = \{\uparrow, \downarrow\}$ the second-quantization Hamiltonian can be expressed as

$$\hat{\mathcal{H}}_{LEM} = \int dx \hat{\Phi}^\dagger(x) \left(s_\alpha v_{SO} \tau_z \sigma_z \hat{p}_x - \frac{E_Z}{2} (\tau_0 - \tau_z) \sigma_x \right) \hat{\Phi}(x) \quad (3.61)$$

where we have introduced Pauli-like matrices τ_z and τ_0 that act on the massive-massless space of the pseudospin $\hat{\Phi}(x) = (\zeta_\uparrow(x), \zeta_\downarrow(x), \eta_\uparrow(x), \eta_\downarrow(x))^T$.

Following a similar approach, one can perform the expansion of the field components (3.13)

$$\hat{\Psi}_\uparrow(x) = \frac{1}{\sqrt{\Omega}} \sum_k c_{k,\uparrow} e^{ikx} \simeq \frac{1}{\sqrt{\Omega}} \sum_{|q| \ll k_{SO}} e^{i(2k_{so}+q)x} \zeta_{q,\uparrow} + \frac{1}{\sqrt{\Omega}} \sum_{|q| \ll k_{SO}} e^{iqx} \eta_{q,\uparrow} \quad (3.62)$$

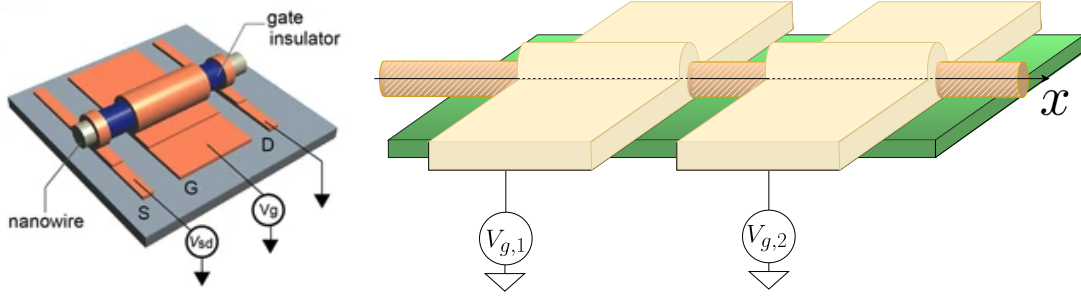
$$\hat{\Psi}_\downarrow(x) = \frac{1}{\sqrt{\Omega}} \sum_k c_{k,\downarrow} e^{ikx} \simeq \frac{1}{\sqrt{\Omega}} \sum_{|q| \ll k_{SO}} e^{i(-2k_{so}+q)x} \zeta_{q,\downarrow} + \frac{1}{\sqrt{\Omega}} \sum_{|q| \ll k_{SO}} e^{iqx} \eta_{q,\downarrow} \quad (3.63)$$

extending again validity of the model, field operator can be written more compactly as

$$\hat{\Psi}(x) = \begin{pmatrix} e^{2is_\alpha k_{SO} x} \zeta_\uparrow(x) + \eta_\uparrow(x) \\ e^{-2is_\alpha k_{SO} x} \zeta_\downarrow(x) + \eta_\downarrow(x) \end{pmatrix} \quad (3.64)$$

3.2 The case of inhomogeneous RSOC

As we have discussed in chapter 1, the strength of the RSOC can be controlled by the external electric field, typically by applying the a gate potential V_g to a gate separated from the NW with a insulating layer e.g. aluminium oxide, as sketched in Fig.3.4a. Notably, to recent advances in gating techniques[63, 68, 83, 92] enable one to experimentally control both the magnitude[64, 70, 73, 79, 86, 87, 91] and the sign[27, 64] of the RSOC. Thus, by applying different gate potentials to different portions of the NW, an inhomogeneous profile on the RSOC can be realized, as illustrated in Fig.3.4b for the case of two gates $V_{g,1}$ and $V_{g,2}$.



(a) Schematic representation of the experimental set up [83]. (b) Configuration with two gate for different pieces of the Nanowire.

Figure 3.4: Set up of the gate controlled Rashba SOC.

Motivated by these experimental trigger, we now wish to extend our analysis to a NW with inhomogeneous RSOC profile $\alpha(x)$. Since the space-dependent $\alpha(x)$ does not commute with the momentum operator p_x , in order to ensure that the SOC Hamiltonian term is Hermitian, the product between α and p_x must be replaced by their anticommutator

$$H_R = \frac{\alpha}{\hbar} p_x \mapsto H_R = \frac{1}{2\hbar} \{\alpha(x), p_x\} \quad (3.65)$$

and the second-quantized Hamiltonian of the inhomogeneous NW becomes

$$\hat{\mathcal{H}} = \int \hat{\Psi}^\dagger(x) \left(\frac{p_x^2}{2m^*} \sigma_0 - \frac{\sigma_z}{2\hbar} \{\alpha(x), p_x\} - \sigma_x h_\perp \right) \hat{\Psi}(x) = \quad (3.66)$$

$$= \int \hat{\Psi}^\dagger(x) \left(\frac{p_x^2}{2m^*} \sigma_0 - \sigma_z \left(\frac{\alpha(x)}{\hbar} p_x - \frac{i}{2} \partial_x \alpha \right) - \sigma_x h_\perp \right) \hat{\Psi}(x) \quad (3.67)$$

The expression for the density and current operators in the inhomogeneous case are again dictated by the Hamiltonian (3.67) and the continuity equation. Repeating the same procedure outlined at the end of Sec.3.1 for the homogeneous case, one obtains

$$\hat{\rho}(x, t) = \hat{\Psi}^\dagger(x, t) \hat{\Psi}(x, t) \quad (3.68)$$

$$\hat{J}(x, t) = -i \frac{\hbar}{2m^*} \left(\hat{\Psi}^\dagger(x, t) \partial_x \hat{\Psi}(x, t) - \partial_x \hat{\Psi}^\dagger(x, t) \hat{\Psi}(x, t) \right) - \frac{\alpha(x)}{\hbar} \hat{\Psi}^\dagger \sigma_z \hat{\Psi} \quad (3.69)$$

which generalizes to the inhomogeneous case the expression (3.9) given in Sec.3.1.

In general, since $[p_x, H] \neq 0$, the inhomogeneous problem is complex and cannot be diagonalized exactly by planewaves. However, since any profile $\alpha(x)$ can ultimately be approximated with a piecewise constant profile (as sketched in Fig.3.5), we shall consider such type of profile and we shall build up the solution of the inhomogeneous problem by suitably matching the electron field operator in each locally homogeneous portion of the NW. Then, by applying the Scattering Matrix Formalism[36, 90], where the external regions act like the leads and the inhomogeneous profile determines the Scattering

region, we shall compute the transport properties through the inhomogeneous NW in the mesoscopic regime, focussing in particular on the linear coefficients derived in Chapter 2

$$G = \frac{q^2}{h} \tilde{T}(E_F) \quad (3.70)$$

$$L = \frac{q\pi k_b^2 T}{6\hbar} \left. \frac{\partial \tilde{T}(E)}{\partial E} \right|_{E_F} \quad (3.71)$$

$$M = \frac{q\pi k_b^2 T^2}{6\hbar} \left. \frac{\partial \tilde{T}(E)}{\partial E} \right|_{E_F} = TL \quad (3.72)$$

$$N = \frac{q\pi k_b^2 T}{6\hbar} \tilde{T}(E_F) = \frac{\pi^2 k_b^2 T}{3q} G \quad (3.73)$$

where $\tilde{T}(E) = \sum_{n,m} S_{L,nR,m}^\dagger S_{L,nR,m}$ and S is scattering matrix that will be derived in following sections.

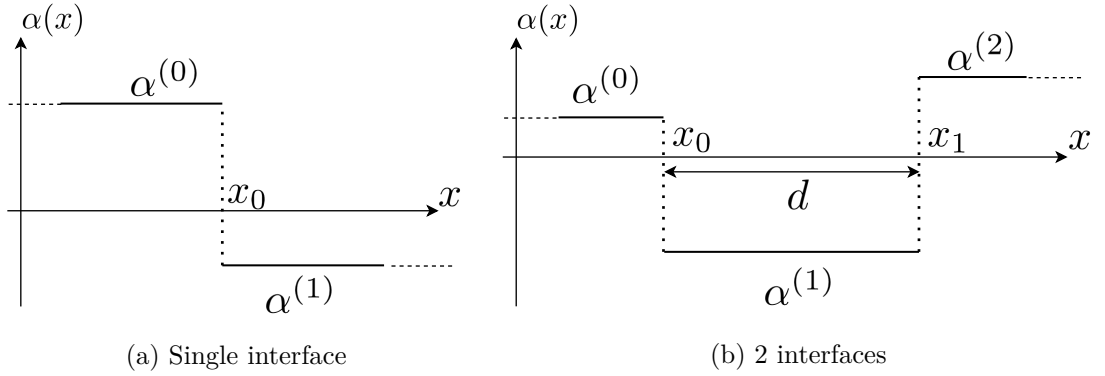


Figure 3.5: A piecewise constant profile of SOC $\alpha(x)$

3.2.1 Relabelling the states in terms of energy

The solution of the inhomogeneous problem will be built by suitably matching the wavefunctions of each piecewise homogeneous NW region. The propagating eigenstates Eqs.(3.26) and the evanescent eigenstates Eqs.(3.33) found in Sec.3.1 for the homogeneous problem are labelled by their wavevectors k and κ , respectively. However, as pointed out in chapter 2, in order to investigate the NW properties in the mesoscopic regime, the first step is to relabel such states in terms of energy rather than wavevector, since energy is the conserved quantity in such regime. The electron field operator will be thus expressed as an energy superposition of energy modes, as in Eq.(2.24).

Propagating states. As far as the propagating modes are concerned, inverting the relations (3.19)-(3.20) in favour of the energy, one finds for each energy E two possible values of (positive) wavevector

$$k_{\pm}(E) = \frac{\sqrt{2m^*}}{\hbar} \sqrt{E + 2E_{SO} \pm \sqrt{4EE_{SO} + 4E_{SO}^2 + E_Z^2}} \quad (3.74)$$

At each energy E there are a priori four wavevectors, namely two positive ones, $k_{\pm}(E)$, and two negative ones $-k_{\pm}(E)$. However, only real wavevectors ($k \in \mathbb{R}$) actually describe propagating modes, and must be retained. For them, the magnitude $v = \hbar^{-1}|\partial_k E|$ of the group velocity is expressed as a function of energy as

$$v_{\eta}(E) = \frac{\hbar k_{\eta}(E)}{m^*} \frac{\sqrt{4EE_{so} + 4E_{so}^2 + E_Z^2}}{\left|2E_{so} + \eta\sqrt{4EE_{so} + 4E_{so}^2 + E_Z^2}\right|} \quad \eta = \pm \quad (3.75)$$

The eigenvectors (3.28) can also be re-expressed in terms of energy

$$\chi_1(\pm k_{\eta}(E)) = \begin{pmatrix} \cos\left(\frac{1}{2}\theta(\pm k_{\eta}(E))\right) \\ \sin\left(\frac{1}{2}\theta(\pm k_{\eta}(E))\right) \end{pmatrix} \quad \chi_2(\pm k_{\eta}(E)) = \begin{pmatrix} -\sin\left(\frac{1}{2}\theta(\pm k_{\eta}(E))\right) \\ \cos\left(\frac{1}{2}\theta(\pm k_{\eta}(E))\right) \end{pmatrix} \quad (3.76)$$

where

$$\cos\left(\frac{\theta(\pm k_{\eta}(E))}{2}\right) = \sqrt{\frac{1}{2} \left(1 \pm \operatorname{sgn}(\alpha) \frac{\sqrt{4E_{so}(E + 2E_{so}) + \eta 4E_{so}\sqrt{4EE_{so} + 4E_{so}^2 + E_Z^2}}}{\left|\sqrt{4EE_{so} + 4E_{so}^2 + E_Z^2} + \eta 2E_{so}\right|} \right)} \quad (3.77)$$

$$\sin\left(\frac{\theta(\pm k_{\eta}(E))}{2}\right) = \operatorname{sgn}(h_{\perp}) \sqrt{\frac{1}{2} \left(1 \mp \operatorname{sgn}(\alpha) \frac{\sqrt{4E_{so}(E + 2E_{so}) + \eta 4E_{so}\sqrt{4EE_{so} + 4E_{so}^2 + E_Z^2}}}{\left|\sqrt{4EE_{so} + 4E_{so}^2 + E_Z^2} + \eta 2E_{so}\right|} \right)} \quad (3.78)$$

Evanescent states. One can proceed in a similar way for the evanescent modes. Their spectrum (3.36, 3.37) can be inverted in favour of energy, obtaining

$$\kappa_{\pm}(E) = \frac{\sqrt{2m^*}}{\hbar} \sqrt{-(E + 2E_{so}) \pm \sqrt{4EE_{so} + 4E_{so}^2 + E_Z^2}} \quad (3.79)$$

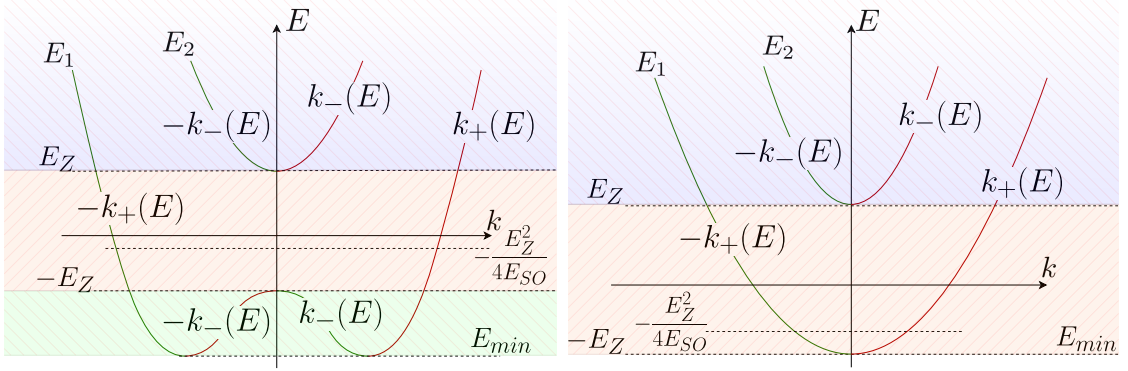
One can express the evanescent spinors (3.38) in term of energy

$$\xi_1(\pm \kappa_{\eta}(E)) = \frac{1}{\sqrt{2}} \begin{pmatrix} e^{\mp i \arctan(\sinh(\theta(\kappa_{\eta}(E))))} \\ 1 \end{pmatrix} \quad (3.80)$$

$$\xi_2(\pm \kappa_{\eta}(E)) = \frac{1}{\sqrt{2}} \begin{pmatrix} -e^{\pm i \arctan(\sinh(\theta(\kappa_{\eta}(E))))} \\ 1 \end{pmatrix} \quad (3.81)$$

where

$$\sinh(\theta(\kappa_{\eta}(E))) = \operatorname{sgn}(\alpha) \frac{\sqrt{-4E_{so}(E + 2E_{so}) + \eta 4E_{so}\sqrt{4EE_{so} + 4E_{so}^2 + E_Z^2}}}{\left|\sqrt{4EE_{so} + 4E_{so}^2 + E_Z^2} - \eta 2E_{so}\right|} \quad (3.82)$$



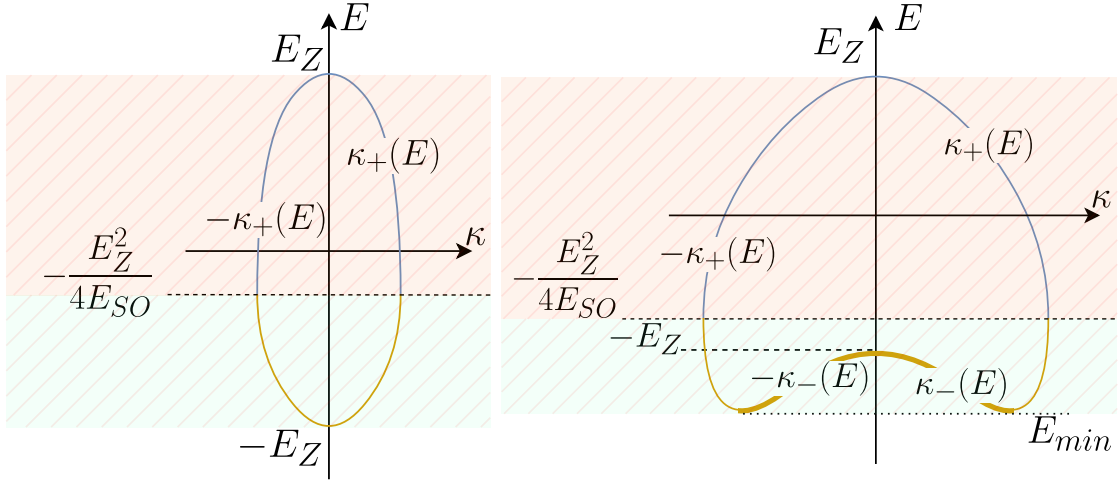
(a) Rashba dominated regime $E_Z < 2E_{SO}$, (b) Zeeman dominated regime $E_Z > 2E_{SO}$. where $E_{min} = -E_{SO} (1 + E_Z^2/4E_{SO}^2)$. With $E_{min} = -E_Z$.

Figure 3.6: The NW propagating modes. Panel (a) for Rashba dominated regime, panel (b) for the Zeeman dominated regimes. Red and green curves describe modes propagating rightwards and leftwards, respectively. Alongside is represented the wave vector that is associated to the corresponding band in each energy range.

Rashba dominated regime ($E_Z < 2E_{SO}$) ($E_{min} = -E_{SO} (1 + E_Z^2/4E_{SO}^2)$)

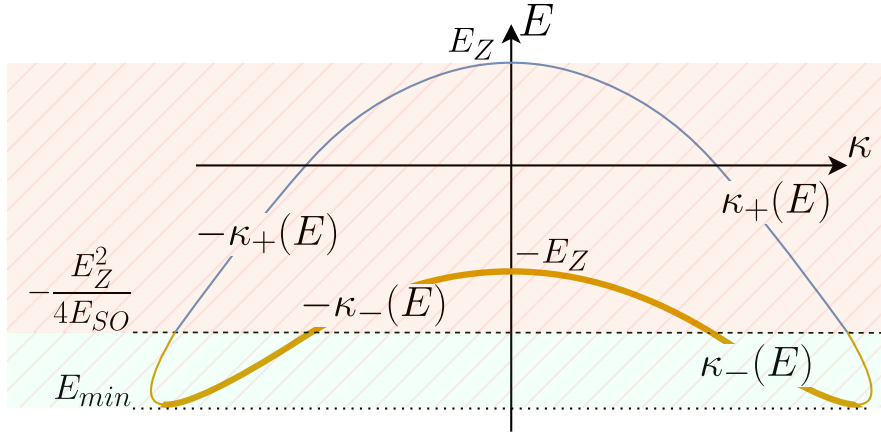
energy range	propagating states	velocity	evanescent states
$E_{min} < E < -E_Z$	4 propagating states $\chi_1(\pm k_-(E))e^{\pm ik_-(E)x}$ $\chi_1(\pm k_+(E))e^{\pm ik_+(E)x}$ $[k_{\pm}(E) \in E_1 \text{ band}]$	$\mp v_-(E)$ $\pm v_+(E)$	No evanescent modes
$-E_Z < E < -\frac{E_Z^2}{4E_{SO}}$	2 propagating states $\chi_1(\pm k_+(E))e^{\pm ik_+(E)x}$ $[k_+(E) \in E_1 \text{ band}]$	$\pm v_+(E)$	$\xi_1(\pm \kappa_+(E))e^{\pm \kappa_+(E)}$ $[\kappa_+(E) \in E_1 \text{ band}]$
$-\frac{E_Z^2}{4E_{SO}} < E < E_Z$	2 propagating states $\chi_1(\pm k_+(E))e^{\pm ik_+(E)x}$ $[k_+(E) \in E_1 \text{ band}]$	$\pm v_+(E)$	$\xi_2(\pm \kappa_+(E))e^{\pm \kappa_+(E)}$ $[\kappa_+(E) \in E_2 \text{ band}]$
$E_Z < E$	4 propagating states $\chi_2(\pm k_-(E))e^{\pm ik_-(E)x}$ $\chi_1(\pm k_+(E))e^{\pm ik_+(E)x}$ $[k_+(E) \in E_1 \text{ band}]$ $[k_-(E) \in E_2 \text{ band}]$	$\pm v_-(E)$ $\pm v_+(E)$	No evanescent modes

Table 3.1: Eigenstates of the NW in the Rashba dominated regime. The wavevectors k_{\pm} and κ_{\pm} are given by Eqs.(3.74) and (3.79). The spinors $\chi_{1,2}$ and the velocities of the propagating modes are given in Eq.(3.76) and Eq.(3.75), respectively, while the spinors ξ for the evanescent modes are given in Eqs.(3.80, 3.81).



(a) Rashba dominated regime
 $E_Z < 2E_{SO}$

(b) Weakly Zeeman dominated regime $2E_{SO} < E_Z < 4E_{SO}$, with $E_{min} = -E_{SO} \left(1 + \frac{E_Z^2}{4E_{SO}^2}\right)$.



(c) Strongly Zeeman dominated regime $4E_{SO} < E_Z$,
 with $E_{min} = -E_{SO} \left(1 + \frac{E_Z^2}{4E_{SO}^2}\right)$.

Figure 3.7: Evanescent mode inversion. Panel (a) is Rashba dominated regime $E_Z < E_{SO}$, panel (b) is a weak Zeeman dominated regime with $2E_{so} < E_Z < 4E_{so}$ and panel (c) is a strong Zeeman dominated regime $4E_{SO} < E_Z$. The thin lines correspond to $\pm\kappa_+(E)$ while the bold lines to $\pm\kappa_-(E)$. A orange line represent the energy band $E_1(\kappa)$ and blue line is $E_2(\kappa)$ energy band.

The three possible regimes

Depending on the value of E_{SO} and E_Z on the energy E , the nature (propagating/evanescent) and the type (upper/lower band) of NW states changes. In Table 3.1 we have summarized the expression of the eigenfunctions (propagating and evanescent) in the Rashba-dominated regime, for each energy value E . In particular, propagating states exist for

Weak Zeeman regime ($2E_{SO} < E_Z < 4E_{SO}$)

energy range	propagating states	velocity	evanescent states
$-E_{SO} \left(1 + \frac{E_Z^2}{4E_{SO}^2}\right) < E < -E_Z$	no propagating states		$\xi_1(\pm\kappa_+(E))e^{\pm\kappa_+(E)x}$ $\xi_1(\pm\kappa_-(E))e^{\pm\kappa_-(E)x}$ [$\kappa_{\pm}(E) \in E_1$ band]
$-E_Z < E < -\frac{E_Z^2}{4E_{SO}}$	2 propagating states $\chi_1(\pm k_+(E))e^{\pm i k_+(E)x}$ [$k_+(E) \in E_1$ band]	$\pm v_+(E)$	$\xi_1(\pm\kappa_+(E))e^{\pm\kappa_+(E)}$ [$\kappa_+(E) \in E_1$ band]
$-\frac{E_Z^2}{4E_{SO}} < E < E_Z$	2 propagating states $\chi_1(\pm k_+(E))e^{\pm i k_+(E)x}$ [$k_+(E) \in E_1$ band]	$\pm v_+(E)$	$\xi_2(\pm\kappa_+(E))e^{\pm\kappa_+(E)}$ [$\kappa_+(E) \in E_2$ band]
$E > E_Z$	4 propagating states $\chi_2(\pm k_-(E))e^{\pm i k_-(E)x}$ $\chi_1(\pm k_+(E))e^{\pm i k_+(E)x}$ [$k_-(E) \in E_2$ band] [$k_+(E) \in E_1$ band]	$\pm v_-(E)$ $\pm v_+(E)$	no evanescent states

Table 3.2: Eigenstates of the NW in the weak Zeeman dominated regime. The wavevectors k_{\pm} and κ_{\pm} are given by Eqs.(3.74) and (3.79). The spinors $\chi_{1,2}$ and the velocities of the propagating modes are given in Eq.(3.76) and Eq.(3.75), respectively, while the spinors ξ for the evanescent modes are given in Eqs.(3.80, 3.81).

$E > E_{min}$, that is also highlighted in Fig.3.6(a), where red and green curves denote right- and left-moving propagating states, respectively. Their wavevectors are given by Eq.(3.74), the spinors χ_1 and χ_2 , related to the lower and upper band, respectively, are given in Eq.(3.76), while the velocities are given in Eq.(3.75). In contrast, evanescent modes exist for $|E| < E_Z$, as shown in Fig.3.7(a), their wavevectors are given in Eqs.(3.79), and the related spinors, related to the upper and lower band, are given in Eqs.(3.80)-(3.81).

As far as the Zeeman-dominated regime is concerned ($2E_{SO} < E_Z$), propagating modes exist for $E > -E_Z$ (see Fig.3.6(b)), while evanescent modes exist for $E_{min} < E < E_Z$. However, the explicit expression and type (upper/lower band) of the NW states also depends whether the NW is in the weak Zeeman subregime ($2E_{SO} < E_Z < 4E_{SO}$) or in the strong Zeeman subregime ($4E_{SO} < E_Z$), as shown in Figs.3.7(b) and (c). The expressions of eigenstates in the weak and strong Zeeman regimes are summarized in Tables 3.2 and 3.3, respectively. Details about the derivation can be found in Appendix A.1 and A.2.

Strong Zeeman regime ($4E_{SO} < E_Z$)

energy range	propagating states	velocity	evanescent states
$-E_{SO} \left(1 + \frac{E_Z^2}{4E_{SO}^2}\right) < E < -\frac{E_Z^2}{4E_{SO}}$	no propagating states		$\xi_1(\pm\kappa_-(E))e^{\pm\kappa_-(E)x}$ $\xi_1(\pm\kappa_+(E))e^{\pm\kappa_+(E)x}$ [$\kappa_{\pm}(E) \in E_1$ band]
$-\frac{E_Z^2}{4E_{SO}} < E < -E_Z$	no propagating states		$\xi_1(\pm\kappa_-(E))e^{\pm\kappa_-(E)x}$ $\xi_2(\pm\kappa_+(E))e^{\pm\kappa_+(E)x}$ [$\kappa_-(E) \in E_1$ band] [$\kappa_+(E) \in E_2$ band]
$-E_Z < E < E_Z$	2 propagating states $\chi_1(\pm k_+(E))e^{\pm i k_+(E)x}$ [$k_+(E) \in E_1$ band]	$\pm v_+(E)$	$\xi_2(\pm\kappa_+(E))e^{\pm\kappa_+(E)x}$ [$\kappa_+(E) \in E_2$ band]
$E > E_Z$	4 propagating states $\chi_2(\pm k_-(E))e^{\pm i k_-(E)x}$ $\chi_1(\pm k_+(E))e^{\pm i k_+(E)x}$ [$k_-(E) \in E_2$ band] [$k_+(E) \in E_1$ band]	$\pm v_-(E)$ $\pm v_+(E)$	no evanescent states

Table 3.3: Eigenstates of the NW in the strong Zeeman dominated regime. The wavevectors k_{\pm} and κ_{\pm} are given by Eqs.(3.74) and (3.79). The spinors $\chi_{1,2}$ and the velocities of the propagating modes are given in Eq.(3.76) and Eq.(3.75), respectively, while the spinors ξ for the evanescent modes are given in Eqs.(3.80, 3.81).

3.2.2 Results for the conductance of the single interface problem

We start by discussing the case of one single interface located at $x = x_0$, as depicted on the Figure 3.5a. The spin orbit coupling profile is thus

$$\alpha(x) = \begin{cases} \alpha^{(0)} & x < x_0 \\ \alpha^{(1)} & x > x_0 \end{cases} \quad (3.83)$$

The Hamiltonian (3.67) can be rewritten in this case as

$$\hat{\mathcal{H}} = \int dx \hat{\Psi}^\dagger(x, t) \left(-\frac{\hbar^2}{2m^*} \sigma_0 \partial_x^2 + i\sigma_z \left(\alpha(x) \partial_x + \frac{\alpha^{(1)} - \alpha^{(0)}}{2} \delta(x - x_0) \right) - h_{\perp} \sigma_x \right) \hat{\Psi}(x, t) \quad (3.84)$$

As one can see, a δ -term appears at the interface, due to the derivative of the SOC profile in Eq.(3.67). Although this seems at first similar to the problem of scattering off a δ -potential, the discontinuity of the SOC cannot be recast as an effective scalar potential, as one can see by deriving the field boundary conditions at the interface.

Boundary conditions

First of all observe that the Heisenberg equation for the field operator in the case of piecewise constant SOC profile (3.83) reads

$$i\hbar \frac{\partial}{\partial t} \hat{\Psi}(x, t) = \left(-\frac{\hbar^2}{2m^*} \sigma_0 \partial_x^2 + i\sigma_z \left(\alpha(x) \partial_x + \frac{\alpha^{(1)} - \alpha^{(0)}}{2} \delta(x - x_0) \right) - h_{\perp} \sigma_x \right) \hat{\Psi}(x, t) \quad (3.85)$$

From Eq.(3.85) we deduce that the field operator must be continuous at the interface

$$\hat{\Psi}(x_0^-, t) = \hat{\Psi}(x_0^+, t) \quad (3.86)$$

where $x_0^{\pm} \doteq x_0 \pm \epsilon$, with $\epsilon \rightarrow 0$ [90]. However the derivative $\partial_x \hat{\Psi}$ of the field must exhibit a discontinuity in order to compensate for the $\delta(x - x_0)$ appearing in Eq.(3.85). In order to determine such discontinuity, one can integrate Eq.(3.85) on the infinitesimal interval $[x_0^-; x_0^+]$ around interface,

$$\begin{aligned} i\hbar \frac{\partial}{\partial t} \int_{x_0-\epsilon}^{x_0+\epsilon} dx \hat{\Psi}(x, t) &= \quad (3.87) \\ &= \int_{x_0-\epsilon}^{x_0+\epsilon} \left(-\frac{\hbar^2}{2m^*} \sigma_0 \partial_x^2 + i\sigma_z \left(\alpha(x) \partial_x + \frac{\alpha^{(1)} - \alpha^{(0)}}{2} \delta(x - x_0) \right) - h_{\perp} \sigma_1 \right) \hat{\Psi}(x, t) dx \end{aligned}$$

obtaining

$$0 = -\frac{\hbar^2}{2m^*} \sigma_0 \left(\partial_x \hat{\Psi}(x_0^+) - \partial_x \hat{\Psi}(x_0^-) \right) + i\sigma_3 \frac{\alpha^{(1)} - \alpha^{(0)}}{2} \hat{\Psi}(x_0) \quad (3.88)$$

which can be rewritten, with the help of Eq.(3.86), as

$$\left(\frac{\hbar^2}{2m} \sigma_0 \partial_x - i \frac{\alpha^{(0)}}{2} \sigma_3 \right) \hat{\Psi}(x_0^-, t) = \left(\frac{\hbar^2}{2m} \sigma_0 \partial_x - i \frac{\alpha^{(1)}}{2} \sigma_3 \right) \hat{\Psi}(x_0^+, t) \quad (3.89)$$

Finally the full set of boundary conditions (3.86) and (3.89) can also be rewritten in terms of the spin-orbit energy

$$\begin{cases} \hat{\Psi}(x_0^-, t) = \hat{\Psi}(x_0^+, t) \\ \left(\sigma_0 \partial_x - i \operatorname{sgn}(\alpha^{(0)}) k_{SO}^{(1)} \sigma_3 \right) \hat{\Psi}(x_0^-, t) = \left(\sigma_0 \partial_x - i \operatorname{sgn}(\alpha^{(1)}) k_{SO}^{(1)} \sigma_3 \right) \hat{\Psi}(x_0^+, t) \end{cases} \quad (3.90)$$

where

$$k_{SO}^{(j)} \doteq \frac{m^* |\alpha^{(j)}|}{\hbar^2} \quad j = 0, 1 \quad (3.91)$$

denotes the spin-orbit wavevector in each region. In particular, one can notice the difference between the boundary conditions Eqs.(3.90) originating from the piecewise RSOC and the boundary conditions (2.51) obtained from the conventional δ -potential scattering reported in the section 2.3.2. In particular, in the former case the first derivative is discontinuous by an imaginary unit. Nevertheless it can be shown that the derivative of the particle density $\hat{\rho} = \hat{\Psi}^\dagger \hat{\Psi}$ as well as the z component of spin density $\hat{s}_z = \hat{\Psi}^\dagger \sigma_z \hat{\Psi}$ are continuous[90].

Transfer Matrix

Exploiting the boundary conditions (3.90) it is now possible to derive the Transfer Matrix. To this purpose, we first exploit the fact that, since the system is mesoscopic, energy is conserved, and we can write the general solution as a superposition over the energy E of stationary solutions $\hat{\Psi}_E(x, t) = \hat{\Psi}_E(x) e^{-iEt/\hbar}$. In turn, the field $\hat{\Psi}_E(x)$ in the j -th region ($j = 0, 1$) is the superposition of all possible modes (propagating and evanescent) characterizing the region at fixed energy E . These modes can be selected from Tables 3.1, 3.2 and 3.3, depending on the parameter regime (Rashba-dominated, weakly or strongly Zeeman dominated) and the energy sub-range. Let us suppose, for instance, that the region j with a RSOC $\alpha^{(j)}$ is in the Rashba dominated regime ($2E_{SO}^{(j)} > E_Z$). Then, the field operator $\hat{\Psi}_E(x)$ acquires a different expression $\hat{\Psi}_E(x)$ depending on the energy sub-range. Explicitly:

(1) for $E > E_Z$ (above the gap) one has

$$\hat{\Psi}_E^{(j)}(x) = \frac{1}{\sqrt{2\pi\hbar}} \left[\frac{1}{\sqrt{v_+^{(j)}(E)}} \left(\hat{c}_E^{(j)} \chi_1^{(j)}(k_+^{(j)}(E)) e^{ik_+^{(j)}(E)x} - i\hat{d}_E^{(j)} \chi_1^{(j)}(-k_+^{(j)}(E)) e^{-ik_+^{(j)}(E)x} \right) + \frac{1}{\sqrt{v_-^{(j)}(E)}} \left(\hat{f}_E^{(j)} \chi_2^{(j)}(k_-^{(j)}(E)) e^{ik_-^{(j)}(E)x} - i\hat{g}_E^{(j)} \chi_2^{(j)}(-k_-^{(j)}(E)) e^{-ik_-^{(j)}(E)x} \right) \right] \quad (3.92)$$

(2) for $|E| < E_Z$ (inside the magnetic gap) one has

$$\hat{\Psi}_{2,E}^{(j)}(x) = \frac{1}{\sqrt{2\pi\hbar}} \left[\frac{1}{\sqrt{v_+^{(j)}(E)}} \left(\hat{c}_E^{(j)} \chi_1^{(j)}(k_+^{(j)}(E)) e^{ik_+^{(j)}(E)x} - i\hat{d}_E^{(j)} \chi_1^{(j)}(-k_+^{(j)}(E)) e^{-ik_+^{(j)}(E)x} \right) + \frac{1}{\sqrt{v_-^{(j)}(E)}} \left(\hat{f}_E^{(j)} \chi_2^{(j)}(k_-^{(j)}(E)) e^{ik_-^{(j)}(E)x} - i\hat{g}_E^{(j)} \chi_2^{(j)}(-k_-^{(j)}(E)) e^{-ik_-^{(j)}(E)x} \right) \right] \quad (3.93)$$

$$+ \hat{f}_E^{(j)} \xi_{n_E}^{(j)}(\kappa_+^{(j)}(E)) e^{\kappa_+^{(j)}(E)x} + \hat{g}_E^{(j)} \xi_{n_E}^{(j)}(-\kappa_+^{(j)}(E)) e^{-\kappa_+^{(j)}(E)x}$$

with $n_E = 2$ for $E > -\frac{E_Z^2}{4E_{SO}}$ and $n_E = 1$ for $E < -\frac{E_Z^2}{4E_{SO}}$.

(3) for energy $E < -E_Z$ (below the gap) one has

$$\hat{\Psi}_{3,E}^{(j)}(x) = \frac{1}{\sqrt{2\pi\hbar}} \left[\frac{1}{\sqrt{v_+^{(j)}(E)}} \left(\hat{c}_E^{(j)} \chi_1^{(j)}(k_+^{(j)}(E)) e^{ik_+^{(j)}(E)x} - i\hat{d}_E^{(j)} \chi_1^{(j)}(-k_+^{(j)}(E)) e^{-ik_+^{(j)}(E)x} \right) + \frac{1}{\sqrt{v_-^{(j)}(E)}} \left(\hat{f}_E^{(j)} \chi_1^{(j)}(k_-^{(j)}(E)) e^{ik_-^{(j)}(E)x} - i\hat{g}_E^{(j)} \chi_1^{(j)}(-k_-^{(j)}(E)) e^{-ik_-^{(j)}(E)x} \right) \right] \quad (3.94)$$

Here we have used the fact that the velocity of incoming and outgoing modes has opposite sign and we have introduced the notation

$$k_\eta^{(j)}(E) = k_\eta(E; \alpha^{(j)}) \quad \kappa_\eta^{(j)}(E) = \kappa_\eta(E; \alpha^{(j)}) \quad v_\eta^{(j)}(E) = v_\eta(E; \alpha^{(j)}) \quad (3.95)$$

$$\chi_n^{(j)}(k) = \chi_n(k; \alpha^{(j)}) \quad \xi_n^{(j)}(\kappa) = \xi_n(\kappa; \alpha^{(j)}) \quad (3.96)$$

whereas $\hat{c}_E^{(j)}$, $\hat{d}_E^{(j)}$, $\hat{f}_E^{(j)}$ and $\hat{g}_E^{(j)}$ denote the fermionic operator with energy E in the j -th region. Using the field expansion (3.92-3.94), in general one can rewrite the boundary conditions (3.90) in a matrix form

$$M_E^{(0)}(x_0) \begin{pmatrix} \hat{c}_E^{(0)} \\ \hat{d}_E^{(0)} \\ \hat{f}_E^{(0)} \\ \hat{g}_E^{(0)} \end{pmatrix} = M_E^{(1)}(x_0) \begin{pmatrix} \hat{c}_E^{(1)} \\ \hat{d}_E^{(1)} \\ \hat{f}_E^{(1)} \\ \hat{g}_E^{(1)} \end{pmatrix} \quad (3.97)$$

where $M^{(j)}(x_0) \in \mathbb{C}^{4 \times 4}$ is 4×4 complex boundary matrix, which columns $\left(M^{(j)}(x)\right)_m$ are reported in the Appendix(C) for each energy range. In turn, from the boundary matrix can be found the transfer matrix $W_E(x_0) = \left(M_E^{(1)}(x_0)\right)^{-1} M_E^{(0)}(x_0)$ that describe how operators on the right of interface at x_0 depend from the operators on the left

$$\begin{pmatrix} \hat{c}_E^{(1)} \\ \hat{d}_E^{(1)} \\ \hat{f}_E^{(1)} \\ \hat{g}_E^{(1)} \end{pmatrix} = W_E(x_0) \begin{pmatrix} \hat{c}_E^{(0)} \\ \hat{d}_E^{(0)} \\ \hat{f}_E^{(0)} \\ \hat{g}_E^{(0)} \end{pmatrix} \quad (3.98)$$

Scattering Matrix

From Eq.(3.98) it is now possible to compute the scattering Matrix. For this purpose first of all one should introduce the incoming $\hat{a}_{n,E}$ and outgoing $\hat{b}_{n,E}$ particle operators. The incoming modes are states moving toward the interface, namely right-moving modes on the left of the interface and left-moving modes on the right of the interface, whereas the outgoing modes are the ones emerging from the interface towards the leads and are thus left-(right-)moving on the left(right) hand side of the interface. As discussed in Section 3.2.1, the correspondence of the modes and the sign of the velocity is summarized In Tables 3.1, 3.2 and 3.3, therefore one finds that operators $\hat{c}_{1,E}$ and $\hat{c}_{2,E}$ are always expected to be propagating and furthermore $\hat{c}_{1,E}$ is characterized by positive group velocity and $\hat{c}_{2,E}$ with negative one. Therefore it is straightforward to find the mapping to incoming/outgoing operators(see fig.3.8,3.8b)

$$\hat{c}_E^{(0)} \mapsto \hat{a}_{1,E}^{(0)} \quad \hat{d}_E^{(0)} \mapsto \hat{b}_{1,E}^{(0)} \quad (3.99)$$

$$\hat{c}_E^{(1)} \mapsto \hat{b}_{1,E}^{(1)} \quad \hat{d}_E^{(1)} \mapsto \hat{a}_{1,E}^{(1)} \quad (3.100)$$

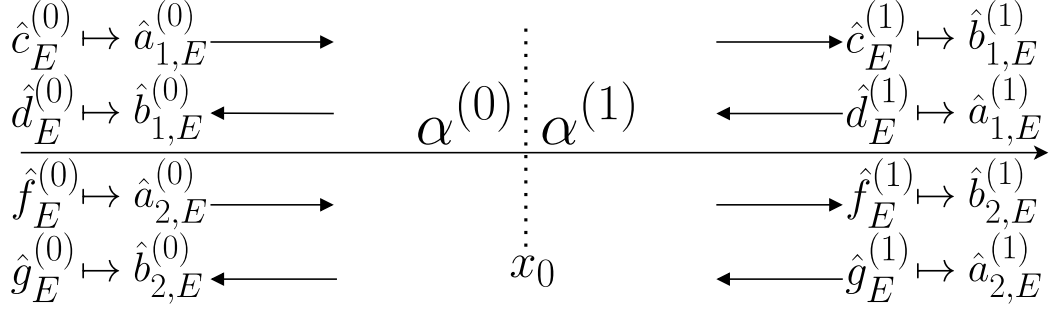
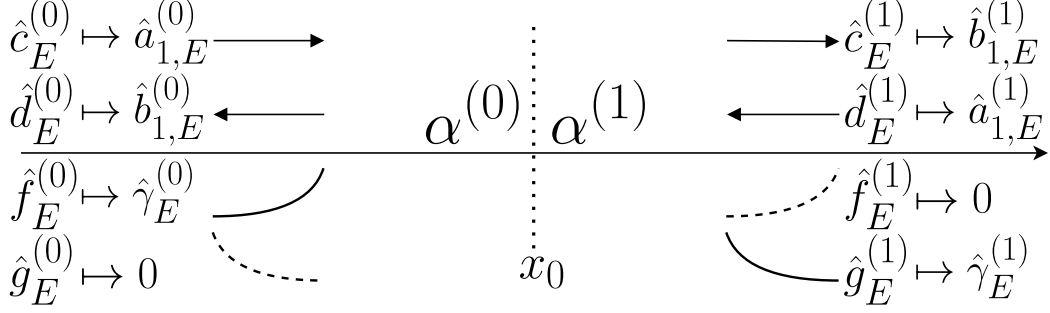
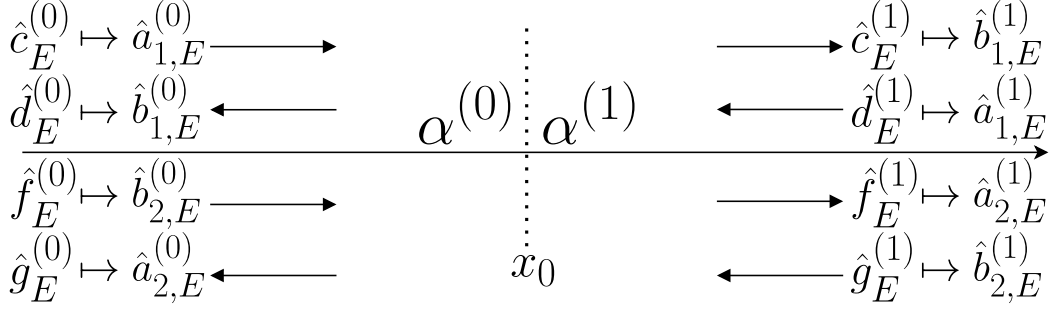

 (a) Over the gap energy range $E > E_Z$

 (b) In the gap energy range $|E| < E_Z$.

 (c) Under the gap energy range $E < -E_Z$

 Figure 3.8: Incoming/outgoing modes mapping in the $|E| > E_Z$ energy range

On the other hand for operators $\hat{c}_{3,E}$ and $\hat{c}_{4,E}$ one has to distinguish between the energy out of the gap, where modes are propagating, and the energy inside the gap, where they are evanescent. First of all let us consider out of the gap energy range, in particular for $E > E_Z$ one can find that $\hat{c}_{3,E}$ is associate with positive group velocity and $\hat{c}_{4,E}$ with negative one (see Fig.3.8a), and therefore

$$\hat{f}_E^{(0)} \mapsto \hat{a}_{2,E}^{(0)} \quad \hat{g}_E^{(0)} \mapsto \hat{b}_{2,E}^{(0)} \quad (3.101)$$

$$\hat{f}_E^{(1)} \mapsto \hat{b}_{2,E}^{(1)} \quad \hat{g}_E^{(1)} \mapsto \hat{a}_{2,E}^{(1)} \quad (3.102)$$

Instead in the case of $E < -E_Z$ and Rashba dominated regime one finds the opposite(see Fig.3.8c)

$$\hat{f}_E^{(0)} \mapsto \hat{b}_{2,E}^{(0)} \quad \hat{g}_E^{(0)} \mapsto \hat{a}_{2,E}^{(0)} \quad (3.103)$$

$$\hat{f}_E^{(1)} \mapsto \hat{a}_{2,E}^{(1)} \quad \hat{g}_E^{(1)} \mapsto \hat{b}_{2,E}^{(1)} \quad (3.104)$$

Finally, for energies $|E| < E_Z$ inside the magnetic gap, the operators $\hat{c}_{3,E}, \hat{c}_{4,E}$ are associated with evanescent modes. In order to ensure the wavefunction normalization, we have to rule out the operators of the divergent modes

$$\hat{f}_E^{(0)} \mapsto \hat{\gamma}_E^{(0)} \quad \hat{g}_E^{(0)} \mapsto 0 \quad (3.105)$$

$$\hat{f}_E^{(1)} \mapsto 0 \quad \hat{g}_E^{(1)} \mapsto \hat{\gamma}_E^{(1)} \quad (3.106)$$

as represented in Fig.3.8b.

Equation (3.98) can thus be rewritten by elucidating the incoming/outgoing mode nature. For $|E| > E_Z$ one can write

$$\begin{pmatrix} \hat{a}_{1,E}^{(1)} \\ \hat{b}_{1,E}^{(1)} \\ \hat{a}_{2,E}^{(1)} \\ \hat{b}_{2,E}^{(1)} \end{pmatrix} = W_E(x_0) \begin{pmatrix} \hat{a}_{1,E}^{(0)} \\ \hat{b}_{1,E}^{(0)} \\ \hat{a}_{2,E}^{(0)} \\ \hat{b}_{2,E}^{(0)} \end{pmatrix} \quad (3.107)$$

while for $|E| < E_Z$ one can write

$$\begin{pmatrix} \hat{a}_{1,E}^{(1)} \\ \hat{b}_{1,E}^{(1)} \\ 0 \\ \hat{\gamma}_E^{(1)} \end{pmatrix} = W_E(x_0) \begin{pmatrix} \hat{a}_{1,E}^{(0)} \\ \hat{b}_{1,E}^{(0)} \\ \hat{\gamma}_E^{(0)} \\ 0 \end{pmatrix} \quad (3.108)$$

Now that we have derived the Transfer Matrix $W_E(x_0)$ of the interface, we can determine the Scattering Matrix, which expresses the *outgoing* mode operators $\hat{b}_{n,E}$ in terms of the *incoming* mode operators $\hat{a}_{n,E}$. Explicitly, for energies $|E| > E_Z$ one has four propagating modes and Eq.(3.107) can be expressed as

$$\begin{pmatrix} \hat{b}_{1,E}^{(L)} \\ \hat{b}_{2,E}^{(L)} \\ \hat{b}_{1,E}^{(R)} \\ \hat{b}_{2,E}^{(R)} \end{pmatrix} = S_E \begin{pmatrix} \hat{a}_{1,E}^{(L)} \\ \hat{a}_{2,E}^{(L)} \\ \hat{a}_{1,E}^{(R)} \\ \hat{a}_{2,E}^{(R)} \end{pmatrix} \quad (3.109)$$

In general it is not trivial to determine an analytical expression for the scattering matrix, since it requires the inversion and multiplication of 4×4 boundary matrix M . Nevertheless,

the transmission function can be easily computed numerically with the help of scripting languages as Python or Wolfram Mathematica.

For the energy range $|E| < E_Z$ inside the gap, Eq.(3.108), restricted to the propagating modes, implies

$$\begin{pmatrix} \hat{b}_{1,E}^{(L)} \\ \hat{b}_{1,E}^{(R)} \end{pmatrix} = S_E \begin{pmatrix} \hat{a}_{1,E}^{(L)} \\ \hat{a}_{1,E}^{(R)} \end{pmatrix} \quad (3.110)$$

and the Scattering Matrix is 2×2 .

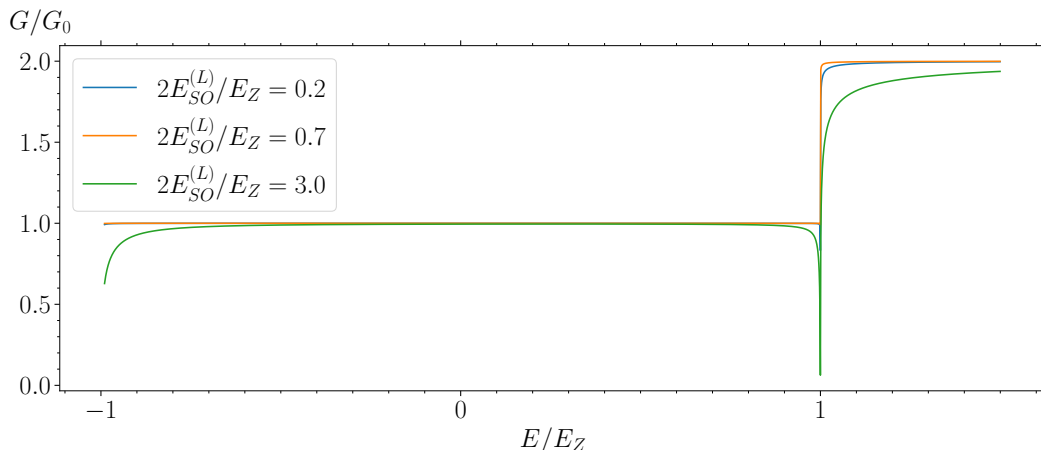
Conductance of the single interface problem

From the above results on the Scattering Matrix we can now compute the transport properties in the problem of a single interface separating two regions with different RSOC. For definiteness, we set the RSOC on the right side to a positive value, for a spin-orbit energy $2E_{SO}^{(R)}/E_Z = 0.5$ corresponding to the Zeeman dominated regime. The RSOC on the left side, however, is set to different values (and sign) in order to sample all relevant regimes. In a compact notation, we will write such sign in front of the spin-orbit energy $E_{SO}^{(L)}$.

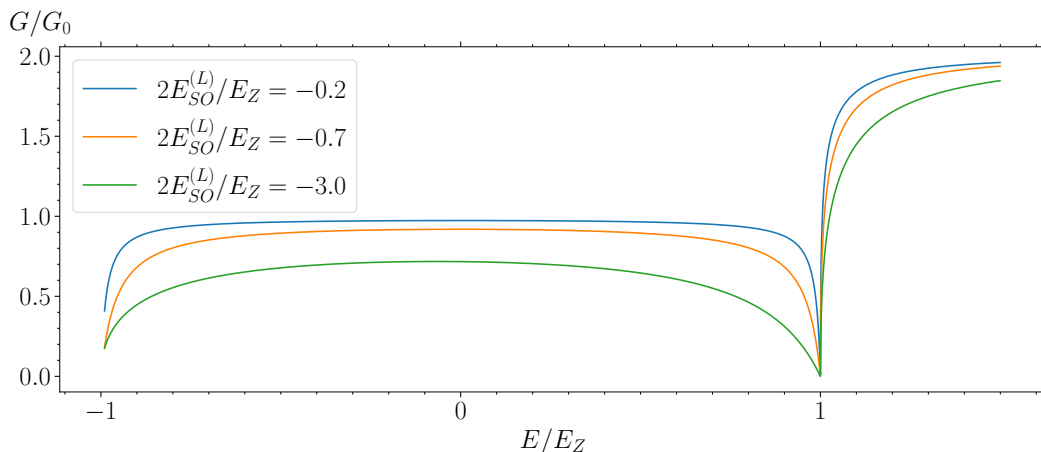
Specifically, Fig.3.9(a) shows the conductance G (in units of the conductance quantum $G_0 = e^2/h$) as a function of energy E/E_Z in the case where the spin-orbit energy on the left side has the same sign as the spin-orbit energy on the right side. One observes a practically perfect transmission, namely $G = G_0$ inside the gap and $G = 2G_0$ outside the gap, regardless of the value of spin-orbit energy $E_{SO}^{(L)}$. In particular, when the left side is in the Zeeman dominated regime like the right side, i.e for $2E_{SO}^{(L)}/E_Z = 0.2, 0.7$ (blue and orange curves, respectively), the behavior resembles a step-function, and the difference between the weak and strong Zeeman regimes is negligible. In contrast, if the left region is in the Rashba dominated regime, $2E_{SO}^{(L)}/E_Z = 3$ (green curve), a deviation from perfect transmission is observed only at the magnetic gap edges $E/E_Z \simeq \pm 1$, where suppression cusps occur.

A different scenario emerges when the RSOC takes opposite sign across the interface (Fig.3.9(b)). While transmission is practically perfect when the left hand side is in the strong Zeeman regime (blue curve), it reduces when one enters the weak Zeeman regime (orange curve) and even more when the Rashba dominated regime (green curve) is reached. We can, however, observe some features that are common to these cases. The conductance is roughly symmetric with respect to the midgap energy value $E = 0$, and gets strongly suppressed at the edges $E/E_Z \simeq \pm 1$ of the magnetic gap, where it exhibits a cusp singularity.

The important role of the RSOC sign can also be highlighted by considering an interface where both sides are in the same regime and by looking at the conductance G as function of energy $E/E_{SO}^{(R)}$, for various values of the Zeeman energy E_Z . Specifically, in Fig.3.10(a), which describes the case where the RSOC takes the *same* sign across the interface ($E_{SO}^{(L)}/E_{SO}^{(R)} = 0.8$), all curves exhibit a perfect transmission for $E > -E_Z$, with a step-like behavior characterizing the number of propagating channels (1 or 2). Here the Zeeman energy only controls a number of such channels, i.e. the value at which the jump



(a) The RSOC has the same sign in both sides of the interface.



(b) The RSOC takes opposite sign on the two interface sides.

Figure 3.9: The conductance of the single interface $E_{SO}^{(L)}|E_{SO}^{(R)}$ in units of conductance quantum $G_0 = e^2/h$ as a function of the energy E/E_Z for fixed spin-orbit energy on the right $2E_{SO}^{(R)}/E_Z = 0.5$ (Zeeman dominated regime) and for various values of spin-orbit energy on the left side: strong Zeeman regime (blue curve), weak Zeeman regime (orange curve), Rashba dominated regime (green curve)

occurs. Note in particular the conductance maximum $G = 2G_0$ of the blue curve at negative energies: This is due to the fact that, when both sides are in the Rashba dominated regime, two conducting channels are present also for energies below the magnetic gap, i.e. for $E_{min} \leq E \leq -E_Z$ (see Fig.3.6(a)).

Figure 3.10(b) then describes the case of *opposite* RSOC sign across the interface (compactly denoted as $E_{SO}^{(L)}/E_{SO}^{(R)} = -0.8$). The conductance behavior is now non-monotonic and strongly dependent on the value of the Zeeman energy. Indeed E_Z determines not

only the location of the suppression cusps at the magnetic gap edges, but also the magnitude of G in the entire energy range. In particular, when the NW is in the Rashba dominated regime (blue curve), the transmission is significantly suppressed inside and below the magnetic gap.

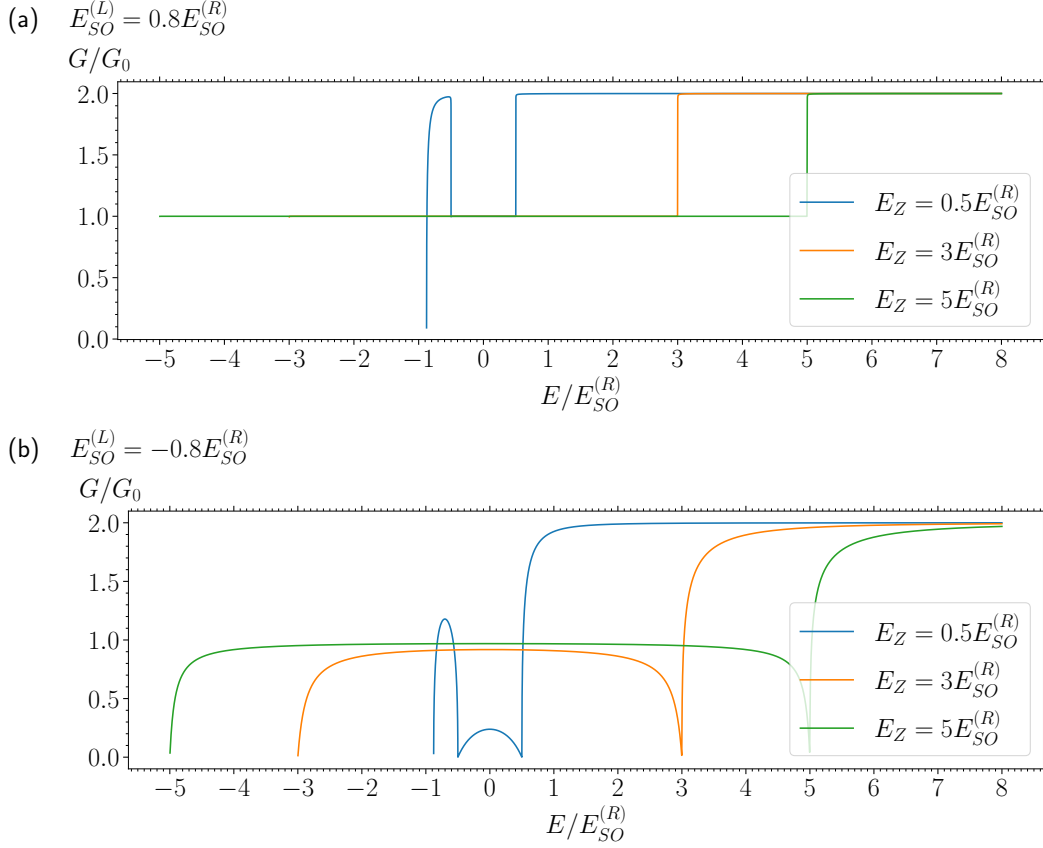


Figure 3.10: The conductance of the single interface $E_{SO}^{(L)} \left| E_{SO}^{(R)} \right.$ in units of the conductance quantum $G_0 = e^2/h$ is plotted as function of the energy $E/E_{SO}^{(R)}$ for fixed $E_{SO}^{(L)}/E_{SO}^{(R)}$ and for different values of the ratio $E_Z/E_{SO,R}$. (a) the case where the RSOC takes the same sign on both interface sides. The transmission is perfect and the Zeeman energy E_Z only controls the number of propagating channels (0, 1 or 2). (b) the RSOC has opposite signs across the interface. In this case the Zeeman energy also determines the magnitude of conductance over the entire energy range. Note that, when both sides are in the Rashba-dominated regime (blue curves) a peak of $2G_0$ conductance is present for $E_{min} < E < -E_Z$, i.e. for $-0.878 < E/E_{SO}^{(R)} < -0.5$, due to the presence of two propagating channels below the magnetic gap energy (see Fig.3.6(a)).

The role of evanescent modes

As we have seen above in Fig.3.9(a), when the sign of the RSOC is the same on both sides of the interface, the conductance is practically perfect over a wide range of energies, regardless of the energy regime of the two regions (Zeeman-Zeeman or Rashba-Zeeman), while one could naively expect a lower conductance value when the two interface sides are in the opposite energy regime, due to a misalignment of the electron spin of the propagating modes. The reason for this seemingly surprising result is that, although the current is carried by the propagating modes only, the evanescent modes also contribute to it indirectly, as they are crucial in realizing the spinor matching of the wavefunction at the interface.

To illustrate the role of the evanescent modes, we consider again the configuration of Fig.3.9(a): While the interface right side is fixed to the Zeeman-dominated regime ($2E_{SO}^{(R)}/E_Z = 0.5$), we shall compare the case where the left region is in the Zeeman-dominated regime ($2E_{SO}^{(L)}/E_Z = 0.7$) and the case where it is in the Rashba dominated regime ($2E_{SO}^{(L)}/E_Z = 3.0$). We focus for definiteness on the scattering problem at $E = 0$, i.e. in the middle of the magnetic gap. From the NW eigenstates Eqs.(3.76), one can find that, when the left side is also in the Zeeman regime, the spin of the propagating mode incoming from the left lies in the x - z plane and forms an angle $\theta \simeq 0.17\pi$ with the z -axis, which is very similar to the angle $\theta \simeq 0.21\pi$ of the propagating mode outgoing to the right side. The almost perfect transmission is thus due to the pretty good spin matching of the propagating modes at the interface. In this case the evanescent modes have a negligible weight, as illustrated in Fig.3.11a, where the spatial profile of the wavefunction at $E = 0$ (spin- \uparrow and spin- \downarrow components) is plotted, together with its evanescent part.

In contrast, when the left side is in the Rashba dominated regime, the spin of the incoming mode forms an angle $\theta \simeq 0.05\pi$ that is very different from the one of the transmitted wave on the right side ($\theta \simeq 0.21\pi$). At first, one could thus expect a low transmission. However, this time the presence of the evanescent modes is significant, as shown by the wavefunction spatial profile in Fig.3.11b. Their spin, lying in the x - y plane and almost directed along the x -axis, is able to compensate for the spin misalignment of the propagating modes. This ensures a correct spin wavefunction matching (3.90) without any significant reflection, and one obtains again an almost perfect transmission. Thus, differently from the customary homogeneous case, in inhomogeneous RSOC problems the evanescent modes can play a crucial role in general in determining transport properties, as we shall see again in Chapter 4.

Finally, when the two sides have opposite RSOC signs, the spin angle difference between the incoming mode and the transmitted mode is too large to be compensated by the presence of evanescent modes. The spin wavefunction matching (3.90) can only be ensured by the presence of a reflected wave, causing a conductance suppression shown above in Fig.3.9(b).

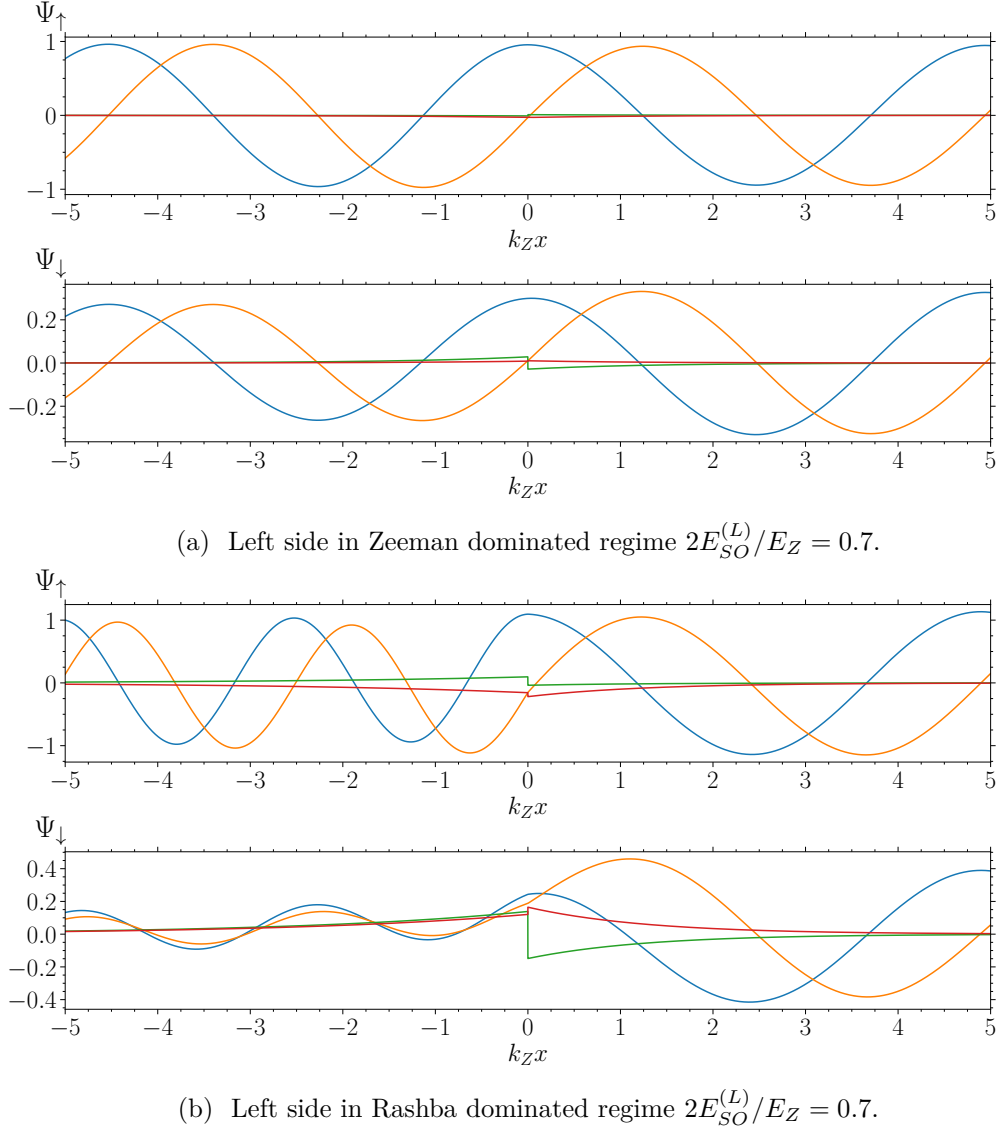


Figure 3.11: The spatial profile of the wavefunction $\Psi(x)$ for $E = 0$, $2E_{SO}^{(R)}/E_Z = 0.5$ and interface at $x = 0$, the upper panel of each plot represent a spin up component Ψ_{\uparrow} while the lower panel a spin down component Ψ_{\downarrow} . Notably in the case of Zeeman dominated regime, (plot (a) and right hand side of the interface of plot (b)) the propagating states (oscillating lines) are characterized by both spin-up and -down components. On the other hand in Rashba dominated regime the spin-up component is dominant (left hand side of the interface on plot (b)). Blue and orange lines are respectively real and imaginary part of the wavefunction; Green and red lines are respectively real and imaginary part of evanescent mode.

3.2.3 Generalization to multiple interfaces

It is straightforward to generalise the same approach to the case of multiple interfaces. The transfer matrix $W_E(x_j) = \left(M_E^{(j+1)}(x_j)\right)^{-1} M_E^{(j)}(x_j)$ across each interface, located at x_j , can be computed as in the previous case. After that one can observe that the operators on right of x_i are the same as the operators on the left of x_{j+1} , as sketched in Fig.3.12, therefore the transfer matrix across two consecutive interfaces can be written as the product $W_E(x_{j+1})W_E(x_j)$ of the two single-interface transfer matrices. Similarly, one can chain all of N interfaces and write the total transfer matrix $W_E = \prod_{j=0}^N W_E(x_{N-j})$ for the whole scattering regions, in analogy with Eq.(3.98)

$$\begin{pmatrix} \hat{c}_E^{(R)} \\ \hat{d}_E^{(R)} \\ \hat{f}_E^{(R)} \\ \hat{g}_E^{(R)} \end{pmatrix} = W_E \begin{pmatrix} \hat{c}_E^{(L)} \\ \hat{d}_E^{(L)} \\ \hat{f}_E^{(L)} \\ \hat{g}_E^{(L)} \end{pmatrix} \quad (3.111)$$

where apex L and R mark the rightmost and leftmost operators w.r.t. the scattering

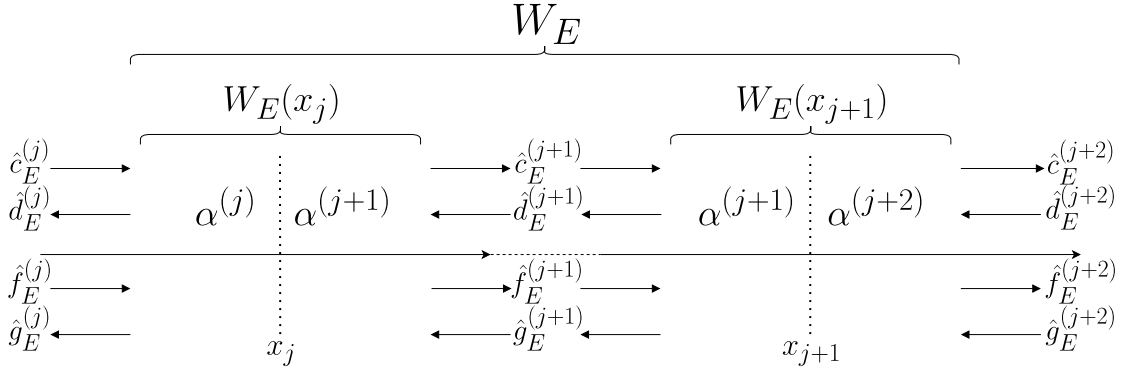


Figure 3.12: Generalization of the transfer matrix to multiple interfaces.

region. The correspondence with the incoming/outgoing operators can be established in the similar way as in the case of single interface case with the help of Eq.(3.99-3.106). In turn, the scattering matrix can be derived from Eq.(3.111) for $|E| > E_Z$

$$\begin{pmatrix} \hat{b}_{1,E}^{(L)} \\ \hat{b}_{2,E}^{(L)} \\ \hat{b}_{1,E}^{(R)} \\ \hat{b}_{2,E}^{(R)} \end{pmatrix} = S_E \begin{pmatrix} \hat{a}_{1,E}^{(L)} \\ \hat{a}_{2,E}^{(L)} \\ \hat{a}_{1,E}^{(R)} \\ \hat{a}_{2,E}^{(R)} \end{pmatrix} \quad (3.112)$$

On the other hand for $|E| < E_Z$ Eq.(3.111) can be rewritten as

$$\begin{pmatrix} \hat{b}_{1,E}^{(L)} \\ \hat{b}_{1,E}^{(R)} \end{pmatrix} = S_E \begin{pmatrix} \hat{a}_{1,E}^{(L)} \\ \hat{a}_{1,E}^{(R)} \end{pmatrix} \quad (3.113)$$

3.2.4 Results for the conductance of the double interface problem

Let us now apply the general approach described in the previous section to the case where we have two interfaces. This configuration enables us to describe two physically interesting setups. The first one is when a NW with finite length d and RSOC is contacted to two normal metallic leads without RSOC. The second situation is where the two outer regions represents two portions of a NW, coupled to different gate voltages and thereby characterized by different RSOC, which are separated by an inner region without RSOC that can be considered as a magnetic barrier.

Setup 1: Finite nanowire contacted to metallic leads

Let us start by considering a NW with RSOC and a finite length d contacted to two leads without RSOC ($E_{SO}^{(1)}, E_{SO}^{(2)} = 0$). The magnetic field is applied everywhere. This setup is sketched in Fig.3.13. Since the pure Zeeman regime was considered in the outer regions, it is sufficient to limit the energy interval to $E > -E_Z$ since there are no propagating modes in the leads for $E < -E_Z$.

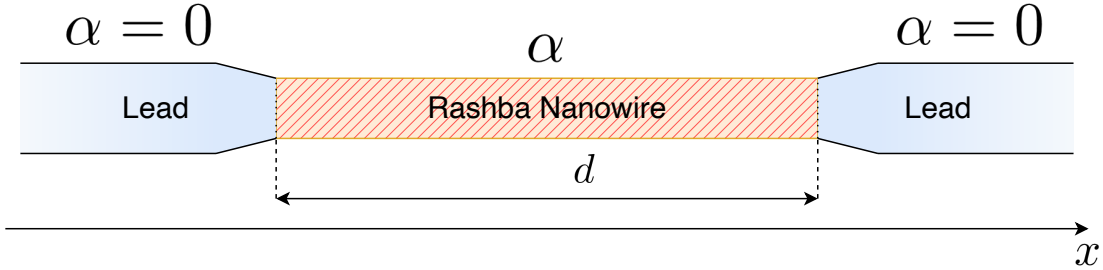


Figure 3.13: Metallic lead model $0|\alpha|0$

In Fig.3.14 we have reported the conductance G/G_0 as a function of energy E/E_Z . The three panels refer to different values of the NW length d , in terms of the spin-orbit length k_{SO}^{-1} . In particular, Fig.3.14(a) describes the case of a short NW ($k_{SO} d = 0.3$). The outer regions, where the RSOC is absent, are by definition in the strongly Zeeman-dominated regime, whereas for the central region we have taken three different values of RSOC, i.e. three different values for the ratio E_{SO}/E_Z of spin-orbit energy to Zeeman energy. For $E_{SO}/E_Z = 0.1, 0.4$, the central region is in the strongly and weakly Zeeman dominated regime (blue and orange curves) respectively, and a practically perfect transmission can be observed. For $E_{SO}/E_Z = 10$ (green curve), the central region is in the Rashba-dominated regime. In this case the conductance G/G_0 is strongly suppressed near the lower gap edge $E/E_Z = -1$, and it monotonically increases with energy reaching a perfect transmission in the middle of the gap $E = 0$.

The scenario starts to change when the length of the NW becomes comparable with the spin-orbit length, as can be seen from Fig.3.14(b) where $k_{SO} d = 1$. While the transmission G/G_0 remains perfect for the entire energy range when the central region is in the strongly Zeeman dominated regime (blue curve), it exhibits suppression cusps near

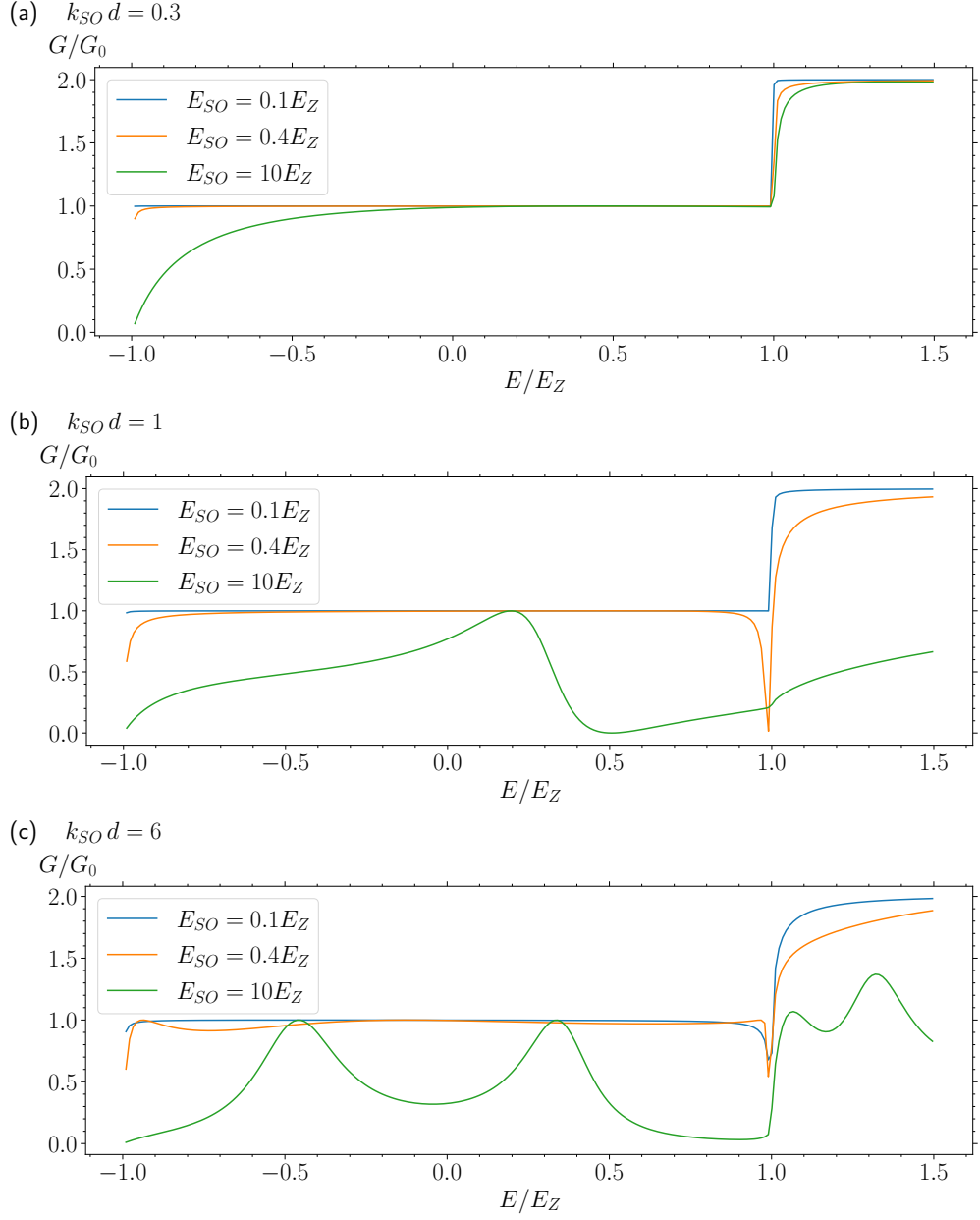


Figure 3.14: The conductance of the lead Model $0|E_{SO}|0$ in units of $G_0 = e^2/h$ is plotted as function of the energy E/E_Z , for different values of the spin-orbit energy of the central region, which is in the strongly Zeeman dominated regime for $E_{SO} = 0.1E_Z$ (blue curve), in the weakly dominated Zeeman regime for $E_{SO} = 0.4E_Z$ (orange curve), and in the Rashba dominated regime for $E_{SO} = 10E_Z$ (green curve). The three panels refer to three different values of the NW length d , in units of the spin-orbit length k_{SO}^{-1} .

the boundaries of the magnetic gap ($E/E_Z \sim \pm 1$) in the case of weakly Zeeman dominated regime (orange curve). Moreover, if the central region is in the Rashba-dominated regime, the transmission significantly deviates from 1 over the entire energy range and, in particular, it acquires a non monotonic behavior.

This behavior becomes even more clear in the case of a long NW ($k_{SO} d = 6$), illustrated in Fig.3.14(c), where the green curve features an oscillatory behavior, with perfect transmission reached for $E/E_Z \simeq -0.55$ and $E/E_Z \simeq 0.4$, and a suppression near the gap edges $E = \pm E_Z$. A long NW thus behaves like a sort of spin-dependent Fabry-Pérot interferometer: The spin-dependent backscattering of the electronic waves at the NW/lead interfaces causes a constructive/destructive interference pattern that depends on the ratio of the electron wavelength, determined by its energy E , to the NW length d , causing an enhancement or suppression of the conductance.

Setup 2: The magnetic barrier configuration $E_{so,L}|0|E_{so,R}$

Let us now discuss a setup where two portions of the NW are coupled to different gates and thereby acquire different values of RSOC in different regions. The two regions are separated by a region of length d where the RSOC is assumed to be negligible ($E_{SO}^{(1)} = 0$). This setup is sketched in Fig.3.15.

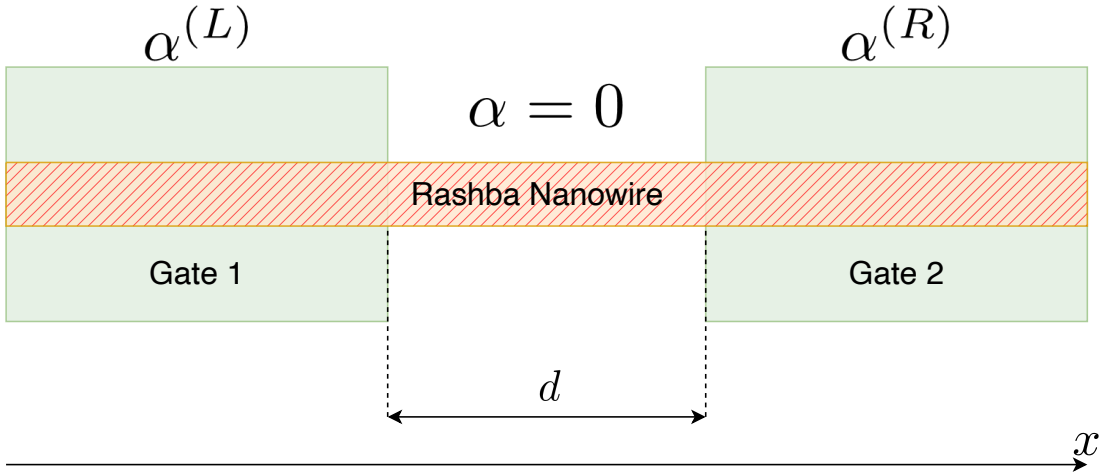


Figure 3.15: Configuration with different gates.

The central region, where the RSOC is absent, is in the strongly Zeeman-dominated regime. For definiteness, we set the outer gated regions to the Rashba dominated regime ($E_{SO}^{(R)} = 3E_Z$) where, as discussed in Sec.3.1.3, the states inside the gap energy range are helical, with an helicity depending on the sign of RSOC. We shall set the RSOC to be positive in the right region, while for the left region we will consider both positive and negative sign. This will be compactly denoted through a 'sign' attributed to the spin-orbit energy $E_{SO}^{(L)}$ of the left region. The behavior of the conductance G significantly depends on whether the two outer regions have the same or opposite sign of the RSOC, and on

the value d of the separation between the gates compared to the Zeeman length k_Z^{-1} , as illustrated in Fig.3.16. In particular, Fig.3.16(a) shows the case of a short separation ($k_Z d = 0.3$). If the left region has the same RSOC sign as the right region, the conductance inside the gap is perfect (orange curve), while if the sign of the RSOC on the left is opposite to the right one the conductance is suppressed inside the gap energy range (blue curve). In this case the behaviour of the conductance is thus similar to the case of a single interface (see Fig.3.9).

However, for an intermediate distance between the gates, $k_Z d = 1$, we observe from Fig.3.16(b) that the behavior of the conductance qualitatively changes. In the case of equal RSOC signs the conductance is almost ideal except for a suppression in the range $E_Z/2 < E < E_Z$, whereas in the case of opposite RSOC signs the conductance is almost perfect in the entire energy range. As a whole, the difference between the two cases of equal or opposite RSOC in Fig.3.16(b) is reduced, as compared to the short separation case of Fig.3.16(a). This is due to the fact that, for larger separation d , the electron spin has a spatial room to re-adapt to the different orientation imposed by the opposite RSOC sign. Finally, in the case of large separation $k_Z d = 6$, illustrated in Fig.3.16(c), the behaviour of the conductance is almost identical in both cases of equal or opposite RSOC signs, except for a small difference near the gap edge $E/E_Z = +1$.

We conclude by observing that, since both regions are in the Rashba-dominated regime and the RSOC sign determines the helicity of the helical states, the setup with opposite RSOC signs induced by the gates implements a peculiar setup, namely a junction of helical states with opposite helicity. This non trivial problem represents the so called Dirac paradox, and will be discussed more in details in following chapter. Note that such a configuration, which is rather easily realized in NWs through appropriate gating, would be quite hard to implement in the helical edge states of a 2D Topological Insulator.

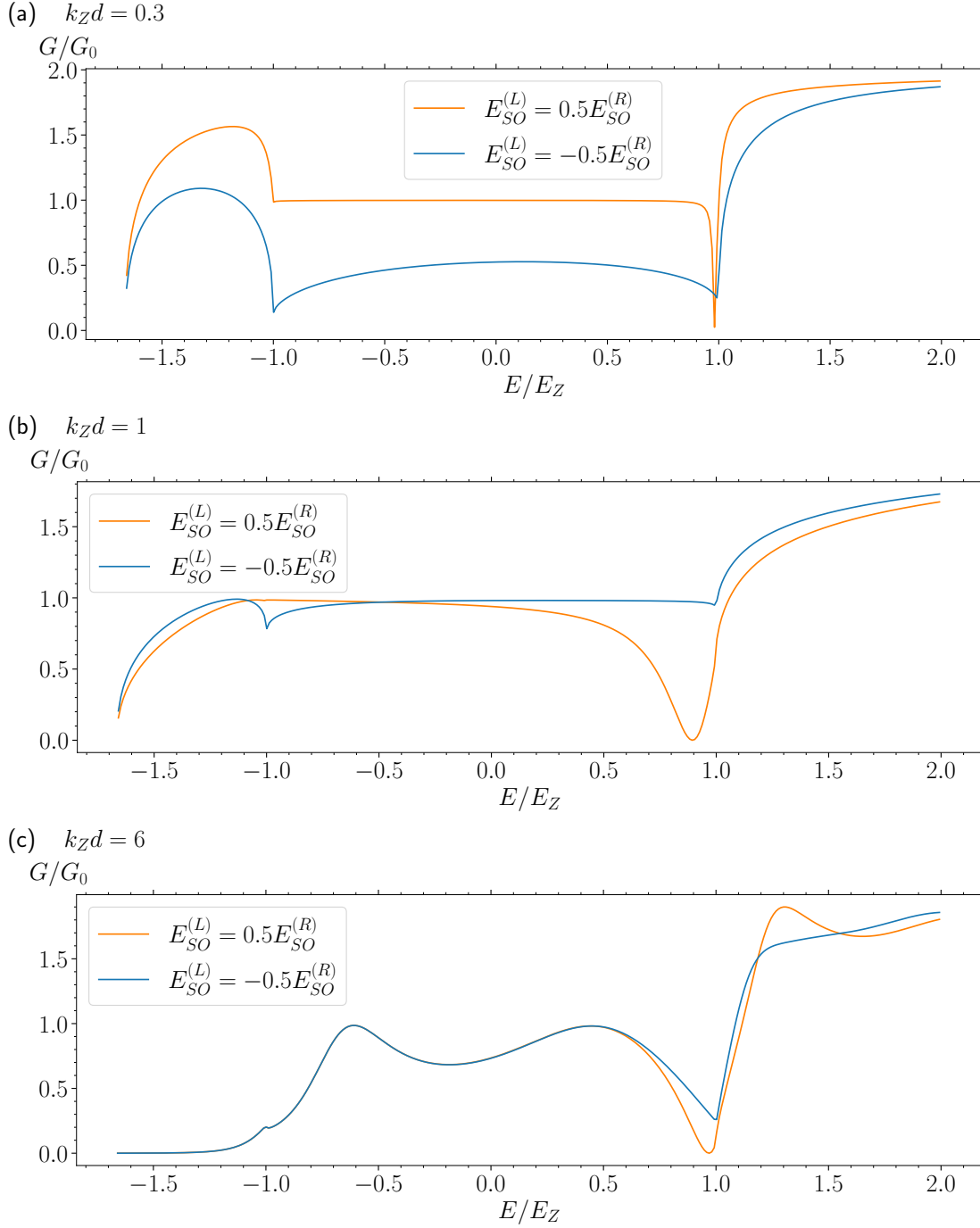


Figure 3.16: The conductance of the magnetic barrier $E_{SO}^{(L)}|0\rangle\langle E_{SO}^{(R)}$ in units of conductance quantum $G_0 = e^2/h$ as function of the energy E/E_Z , for a fixed NW length d . The right region is assumed to be in the Rashba-dominated regime ($E_{SO}^{(R)} = 3E_Z$). The various curves refer to different values of RSOC of the left region. Orange line $E_{SO}^{(L)} = 0.5E_{SO}^{(R)}$, blue line $E_{SO}^{(L)} = -0.5E_{SO}^{(R)}$.

Chapter 4

The Dirac paradox and its realization with nanowires

In this chapter I shall discuss a paradoxical situation that emerges in Dirac materials, called the Dirac paradox, and then I shall analyze its implementation with spin-orbit nanowires.

In various materials on the spotlight of Condensed Matter research, such as graphene, topological insulators and Weyl semimetals, the electronic properties turn out to be well described by an effective massless Dirac Hamiltonian[31, 38, 43, 49, 51, 77, 80], rather than the customary Schrödinger Hamiltonian. Notably, massless Dirac states are characterized by an helicity, i.e. a locking of their spin orientation to their momentum. The Dirac paradox arises when a junction between two materials with opposite helicity is formed: An electron impinging from one side of the interface can seemingly neither be transmitted nor reflected, precisely because of the locking between spin and momentum. This configuration has been investigated in a junction between two 3D topological insulators, whose conducting states flow on the surface and are described by a 2D massless Dirac Hamiltonian. In that case the Dirac paradox has been solved by finding that electrons leak along the interface surface. However, in 1D Dirac heterojunctions, this escape possibility does not exist and the solution to the paradox is less trivial. This is what I shall discuss in the first part of this chapter. In particular, I will show that, when the customary case of purely massless Dirac modes is considered, the solution of the paradox either is trivial or does not exist, depending on the way the helicity crossover occurs across the interface. Then, I will demonstrate that, when additional massive Dirac modes are taken into account, a non trivial solution exists and a tunable transmission can be found.

In the second part of the chapter, I will discuss the implementation of the 1D Dirac paradox. In particular, while the Dirac paradox configuration would be quite hardly feasible with the helical edge states of Topological Insulators, I will argue that it can be realized with spin-orbit nanowires. Indeed, as shown in chapter 3.1.3, in the deep Rashba-dominated regime $E_Z \ll 2E_{SO}$ the nanowire exhibits 1D massless Dirac helical states inside the magnetic gap, whose helicity is determined by the sign of the RSOC. One can thus find that the setup with an inhomogeneous RSOC profile, analogous to

“Magnetic barrier configuration” (see Fig.3.15), where in outer regions the RSOC takes opposite signs, precisely realizes the 1D Dirac paradox configuration. Notably, we shall show that such inhomogeneous setup is precisely described by the massless+massive Dirac model mentioned above. Thus, while massive modes are usually neglected when the RSOC can be considered homogeneous, they become important in inhomogeneous RSOC setups also at low energy. Indeed, although massive modes carry no current directly, they can indirectly determine the conductance by guaranteeing the spin wavefunction matching at inhomogeneities.

4.1 Dirac paradox

Let us first briefly recall that the electronic properties of various materials, in physically realistic regimes, are well described by an effective Dirac model. In analogy with Eq.(1.14) one has

$$H = v_F \boldsymbol{\alpha} \cdot \hat{\mathbf{p}} + \Delta \beta \quad (4.1)$$

where the light velocity and the mass terms appearing in the actual relativistic version are replaced by parameters of the material, namely the Fermi velocity ($c \mapsto v_F$) and the gap between two valence and conduction bands ($m_0 c^2 \mapsto \Delta$). In the 1D case one needs only two anticommuting matrices that can be chosen to be $\alpha_1 \doteq \sigma_z$ and $\beta \doteq \sigma_x$

$$H_{1D} = v_F \sigma_z \hat{p}_x + \Delta \sigma_x \quad (4.2)$$

where $\hat{p}_x = -i\hbar\partial_x$. It can be easily seen that the Hamiltonian H_{1D} commutes with the momentum operator and therefore it can be diagonalized with the planewaves

$$\psi_k(x) = \omega e^{ikx} \quad (4.3)$$

where ω is a 2×1 spinor eigenvector. The Hamiltonian (4.2) can be rewritten in k -space

$$H = v_F \hbar k \sigma_z + \Delta \sigma_x \quad (4.4)$$

and its eigenvalues

$$E_{\pm}(k) = \pm \sqrt{\Delta^2 + v_F^2 \hbar^2 k^2} \quad (4.5)$$

describe two electronic bands separated by a gap $E_+(0) - E_-(0) = 2\Delta$ at $k = 0$. Since the Hamiltonian (4.4) is expressed as a combination of two Pauli matrices, the spin of its eigenvectors lie in x - z spin-plane depending and the specific direction depends on the ratio of the kinetic and mass terms. Notably, for energy inside the gap ($|E| < \Delta$), the Hamiltonian (4.2) formally admits evanescent solutions too. These evanescent massive states in principle can be obtained with the mapping $k \mapsto -i\kappa$. The spin of the related eigenvectors in this case lies in the x - y plane. In particular, for $E = 0$, it can be shown to align with y axis and to take the form

$$\omega_0 = \frac{1}{\sqrt{2}} \begin{pmatrix} -i \\ 1 \end{pmatrix} \quad (4.6)$$

One can obtain the massless case by setting $\Delta \rightarrow 0$. In this limit the Dirac Hamiltonian (4.2) reduces to

$$H_{1D} = v_F \sigma_z \hat{p}_x \quad (4.7)$$

and the spinor eigenvectors can be easily identified with

$$\omega_{\uparrow} = \begin{pmatrix} 1 \\ 0 \end{pmatrix} \quad \omega_{\downarrow} = \begin{pmatrix} 0 \\ 1 \end{pmatrix} \quad (4.8)$$

with corresponding eigenvalues

$$E_{\uparrow}(k) = v_F \hbar k \quad (4.9)$$

$$E_{\downarrow}(k) = -v_F \hbar k \quad (4.10)$$

One can observe that the massless Dirac states are characterized by spin momentum locking and therefore one can define a helicity operator as

$$\hat{\lambda} = \frac{\sigma_z \hat{p}_x}{|\hat{p}_x|} \quad (4.11)$$

that indeed commutes with the Dirac Hamiltonian. In particular, from Eqs.(4.9)-(4.10) we note that electron states with positive energy $E > 0$ are characterized by a positive helicity ($\langle \hat{\lambda} \rangle > 0$), since the positive wavevectors correspond to the spin- \uparrow , while negative wavevectors to spin- \downarrow . States with negative energy have negative helicity ($\langle \hat{\lambda} \rangle < 0$). Notably, the opposite situation occurs in the case negative Fermi velocity $v_F \mapsto -v_F$.

4.1.1 Massless Dirac heterojunctions

Let us now consider the interface between two massless Dirac materials characterized by opposite Fermi velocity i.e. $v_F^{(L)}$ on the left and $v_F^{(R)}$ on the right such that $v_F^{(R)} = -v_F^{(L)}$. The second-quantization Hamiltonian describing the helical states present on the two bulk sides of the interface reads

$$\hat{\mathcal{H}}^{(L/R)} = v_F^{(L/R)} \int \hat{\Psi}^\dagger(x) \sigma_z p_x \hat{\Psi}(x) dx \quad (4.12)$$

where $\hat{\Psi} = (\hat{\Psi}_{\uparrow}, \hat{\Psi}_{\downarrow})^T$ is the 2×1 electron field operator. One thus has states with opposite helicity i.e. $\langle \hat{\lambda}^{(L)} \rangle = -\langle \hat{\lambda}^{(R)} \rangle$. If one analyzes the scattering problem across the interface, one finds a paradoxical situation, depicted on the Fig.4.1: The states incident on the interface can seemingly neither be transmitted nor be reflected, due to spin conservation. Indeed let us for instance consider an electron wave incoming from left. It cannot be transmitted because in this case it should flip the spin to match the helicity of outgoing state on the right. At the same time, it cannot be reflected either, due to the spin-momentum locking. This dilemma is called Dirac paradox. This problem has been widely discussed in the literature[52, 59, 60] in the context of 3D Topological Insulators (TIs), where the interface between two TIs with surface states with opposite helicity is considered. It has been shown that in the case of 3D TI this paradox is solved by surface

gapless state emerging from hybridization of states from each TI, that absorb the incident modes. This means that electrons can leak along the interface surface separating the two TIs. In the one dimensional case, however, there is not enough degree of freedom to give raise for localized state and alternative mechanism should emerge that would allow the conservation of momentum and spin.

The solution of the 1D version of the paradox may change significantly depending on the model used to describe how the interface interpolates from the $\hat{\mathcal{H}}_L$ to the $\hat{\mathcal{H}}_R$ bulk Hamiltonians. Here we first discuss examples that realise the Dirac paradox using the massless modes only.

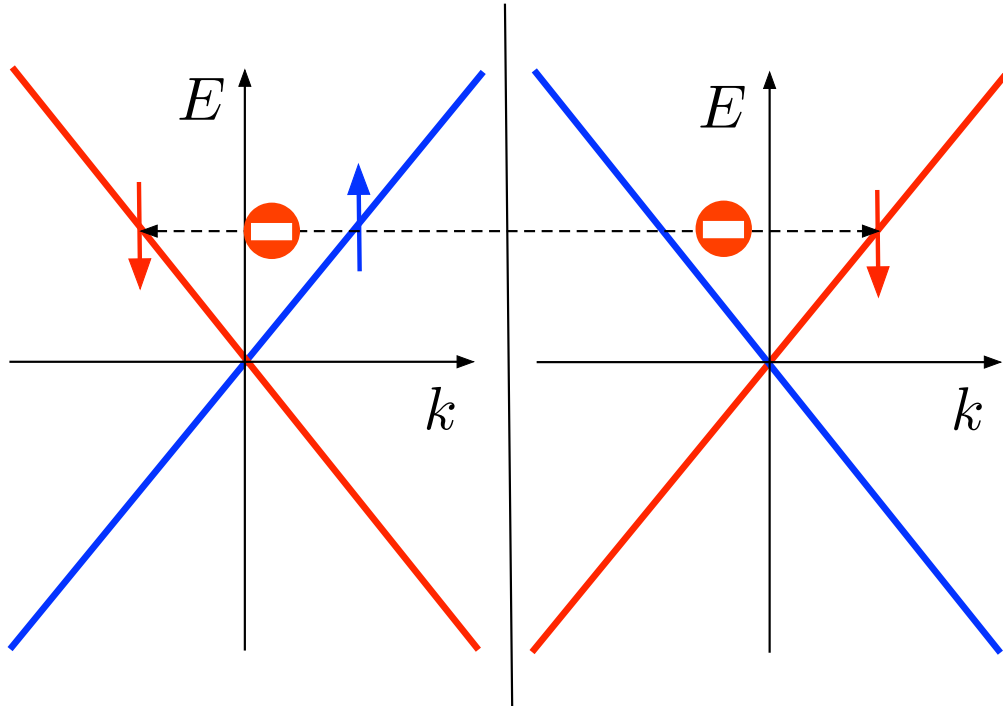


Figure 4.1: Illustration of the Dirac paradox. On each interface side the blue line represents the spin- \uparrow branch of the massless dispersion relation, while red line the spin- \downarrow branch. On the left side of the interface the right-moving states are associated with spin- \uparrow and left-moving states with spin- \downarrow , while the opposite occurs on the right side of the interface: the two interface sides are characterized by an opposite helicity. A spin- \uparrow incoming from the left can seemingly be neither transmitted nor reflected, due to spin conservation.

Model 1: velocity sign change

The simplest way to model the interface between helical states is to consider the spatially dependent profile of the Fermi velocity $v(x)$ such that $v(x \rightarrow -\infty) = v_F^{(L)}$ and $v(x \rightarrow \infty) = v_F^{(R)}$. In this case the momentum operator does not commute with the velocity profile and therefore one should replace their product by a half of their anti-commutator

$v_F p_x \mapsto \frac{1}{2}\{v(x), p_x\}$ and the second-quantization Hamiltonian become

$$\hat{\mathcal{H}} = \int \hat{\Psi}^\dagger(x) \sigma_z \frac{\{v(x), p_x\}}{2} \hat{\Psi}(x) dx \quad (4.13)$$

The Heisenberg equation associated to the Hamiltonian above can be written as

$$\partial_t \hat{\Psi} = -\sigma_z \left(v(x) \partial_x \hat{\Psi} + \frac{\partial_x v}{2} \hat{\Psi} \right) \quad (4.14)$$

Following the approach described in the chapter 3.1 one can find the associated current operator

$$\hat{J}(x) = e v(x) \hat{\Psi}^\dagger(x) \sigma_z \hat{\Psi}(x) \quad (4.15)$$

where e is the electron charge.

We consider the stationary solutions of Heisenberg equation that can be expressed in the form $\hat{\Psi}(x, t) = \hat{\Psi}_E(x) e^{-iEt/\hbar}$. Substituting it into Eq.(4.14) and multiplying the left side by σ_z one can find

$$\partial_x \hat{\Psi}_E = v^{-1}(x) \left(-\frac{\partial_x v}{2} \sigma_0 + i \frac{E}{\hbar} \sigma_z \right) \hat{\Psi}_E \quad (4.16)$$

which solution can be found by integrating both sides in dx' over the interval $[x, x_R]$ where x_R is a reference point

$$\hat{\Psi}_E(x) = \exp \left[-\frac{1}{2} \int_{x_R}^x \frac{\partial_x v}{v(x')} dx' \right] \times \exp \left[i E \sigma_z \int_{x_R}^x \frac{dx'}{\hbar v(x')} \right] \hat{\Psi}_E(x_R) \quad (4.17)$$

Taking advantage of $\partial_x \ln |v(x)| = \partial_x v / v(x)$ one can express the above solution as

$$\hat{\Psi}_E(x) = \sqrt{\frac{v(x_R)}{v(x)}} \exp \left[i \sigma_z \int_{x_R}^x k_E(x') dx' \right] \hat{\Psi}_E(x_R) \quad (4.18)$$

where we defined $k_E(x) = E/\hbar v(x)$. Finally one can introduce the the field operator at the reference point x_R

$$\hat{\Psi}_E(x_R) = \frac{u}{\sqrt{2\pi\hbar|v(x_R)|}} \hat{a}_E \quad (4.19)$$

where u is a space-independent 2×1 spinor and \hat{a}_E the corresponding energy- E mode operator fulfilling $\{a_E, a_{E'}^\dagger\} = \delta(E - E')$. For each energy value E there are two independent solutions, related to two orthogonal choices for the spinor u . In this way Eq.(4.18) takes the form

$$\hat{\Psi}_E(x) = \frac{1}{\sqrt{2\pi\hbar|v(x)|}} e^{i\sigma_z \int_{x_R}^x k_E(x') dx'} u \hat{a}_E \quad (4.20)$$

from which follows that at any space point- x , including possible discontinuity points of $v(x)$, the following boundary condition holds

$$\sqrt{|v(x^+)|} \hat{\Psi}_E(x^+) = \sqrt{|v(x^-)|} \hat{\Psi}_E(x^-) \quad (4.21)$$

where $x^\pm = x \pm \varepsilon$ with $\varepsilon \rightarrow 0$.

Notably, in the case where the velocities v_L on the left and v_R on the right have the same sign, the velocity profile changes only in magnitude without vanishing in any point. In this case one can express the Hamiltonian (4.13) in equivalent form

$$\hat{\mathcal{H}} = \int \hat{\Psi}^\dagger(x) \sigma_z \sqrt{v(x)} \left[p_x \sqrt{v(x)} \right] \hat{\Psi}(x) dx \quad (4.22)$$

The solution of this model has been discussed in Ref.[41], where those authors have found a perfect transmission independently on the values of the velocity on the left/right.

However, in the case of the Dirac paradox, the velocity profile $v(x)$ *vanishes* at some point x_0 in order to allow the sign change of the Fermi velocity. This significantly complicates the problem. In particular one can observe that $k_E(x) \rightarrow \infty$ for $x \rightarrow x_0$, in this way the phase of the Eq.(4.20) is well defined only if the integral $\int_{x_R}^x k_E(x') dx'$ is finite, that corresponds to $|v(x)| = \mathcal{O}(|x - x_0|^\alpha)$ with $0 < \alpha < 1$. Moreover the field operator (4.20) is expected to diverge as $\hat{\Psi}_E \sim 1/\sqrt{|v(x)|}$ for $x \rightarrow x_0$. Nevertheless the current Eq.(4.15) is still finite due to the boundary conditions (4.21). Indeed using the stationary solution for the field operator (4.20) one can write

$$\hat{J}_E(x) = \text{sgn}(v(x)) \frac{e}{2\pi} u^\dagger \sigma_z u \hat{a}_E^\dagger \hat{a}_E \quad (4.23)$$

Notably, at the point x_0 where the velocity profile changes the sign, the current fulfills $J_E(x_0^-) = -J_E(x_0^+)$. Since a discontinuity is incompatible with the continuity equation, which implies that for a stationary state the average current is spatially homogeneous (see chapter 3.1). One concludes that the only way to achieve it with Eq.(4.23) is $\hat{J}_E(x) \equiv 0 \forall x$ and therefore $u^\dagger \sigma_z u = 0$. In this way one can immediately identify two candidate for the spinor part of the eigenstate with $u_+ = (1, e^{i\phi})^T/\sqrt{2}$ and $u_- = (e^{-i\phi}, -1)^T/\sqrt{2}$, where ϕ is an arbitrary phase. Since each spinor eigenvector consists of both spin- \uparrow and spin- \downarrow components, one may conclude that on each interface side both an incoming and an outgoing bulk states must be present. In this way one cannot assign a separate weights to this modes, and it is impossible to construct a scattering state solution.

In conclusion, this model characterized by a spatially dependent velocity profile, implies that there is no solution to the Dirac paradox, since it is impossible to build a scattering state that would satisfy the continuity equation. The only physically available solution must involve the modes injected from both sides. Furthermore one may notice that the model (4.13) involves only of the σ_z -component of spin and the velocity profile only affects its magnitude and sign. In this sense this model is purely scalar.

Model 2: spin-active interface

The alternative model of the Dirac paradox is given by the Hamiltonian

$$\hat{\mathcal{H}} = v_F \int \hat{\Psi}^\dagger(x) \left(e^{-i\theta(x)\sigma_x/2} p_x \sigma_z e^{+i\theta(x)\sigma_x/2} \right) \hat{\Psi}(x) dx \quad (4.24)$$

where the crossover between the regions is achieved by rotation of the σ_z spin around the x -axis, rather than the direct inversion of the Fermi velocity as in the case of previous model. In particular the space-dependent phase $\theta(x)$ is expected to span from $\theta_L = 0$ for $x \rightarrow -\infty$ to $\theta_R = \pi$ for $x \rightarrow +\infty$.

Note that, in contrast to the scalar model (4.13), the model (4.24) involves the full SU(2) spin structure. Thus the Hamiltonian terms at two different space points do not commute in general. As previously shown, using Hamiltonian (4.24), one can derive the Heisenberg equation

$$\partial_t \hat{\Psi}(x) = -v_F \sigma_z e^{-i\theta(x)\sigma_x/2} \partial_x \left(e^{i\theta(x)\sigma_x/2} \hat{\Psi}(x) \right) \quad (4.25)$$

and the current operator

$$\begin{aligned} \hat{J}(x) &= ev_F \hat{\Psi}^\dagger(x) \left(e^{-i\theta(x)\sigma_x/2} \sigma_z e^{+i\theta(x)\sigma_x/2} \right) \hat{\Psi}(x) = \\ &= ev_F \hat{\Psi}^\dagger(x) [\sigma_z \cos \theta(x) - \sigma_y \sin \theta(x)] \hat{\Psi}(x) \end{aligned} \quad (4.26)$$

Integrating the Heisenberg equation around any point x , one can obtain the boundary condition

$$e^{i\theta(x^+)\sigma_x/2} \hat{\Psi}(x^+) = e^{i\theta(x^-)\sigma_x/2} \hat{\Psi}(x^-) \quad (4.27)$$

that, indeed, implies the continuity of the current operator (4.26). Furthermore in the case of a step-like profile of the phase $\theta(x)$, i.e. $\theta(x < 0) = 0$ and $\theta(x > 0) = \pi$ with an interface at $x_0 = 0$, the boundary conditions become

$$\begin{cases} \hat{\Psi}_\uparrow(0^+) &= i \hat{\Psi}_\downarrow(0^-) \\ \hat{\Psi}_\downarrow(0^+) &= i \hat{\Psi}_\uparrow(0^-) \end{cases} \quad (4.28)$$

One can notice that the spin-flip has been introduced at the interface. This effect can be seen explicitly by considering the scattering states solution of Heisenberg equation (4.25)

$$\psi_E(x) = \begin{cases} \begin{pmatrix} 1 \\ 0 \end{pmatrix} e^{iEx/\hbar v_F} \hat{a}_E^{(L)} + \begin{pmatrix} 0 \\ 1 \end{pmatrix} e^{-iEx/\hbar v_F} \hat{b}_E^{(L)} & x < 0 \\ \begin{pmatrix} 0 \\ 1 \end{pmatrix} e^{iEx/\hbar v_F} \hat{b}_E^{(R)} + \begin{pmatrix} 1 \\ 0 \end{pmatrix} e^{-iEx/\hbar v_F} \hat{a}_E^{(R)} & x > 0 \end{cases} \quad (4.29)$$

where $\hat{a}_E^{(j)}$, $\hat{b}_E^{(j)}$ are respectively the incident/reflected energy- E mode operators on the left (L) or right (R) side of the interface at $x_0 = 0$. Substituting the scattering state (4.29) into boundary conditions (4.28) one finds

$$\begin{cases} \hat{a}_E^{(R)} &= i \hat{b}_E^{(L)} \\ \hat{b}_E^{(R)} &= i \hat{a}_E^{(L)} \end{cases} \quad (4.30)$$

from which scattering matrix (2.29) can be derived

$$S = \begin{pmatrix} 0 & -i \\ i & 0 \end{pmatrix} \quad (4.31)$$

and it is straightforward to see that the transmission is perfect for any energy and Fermi velocity.

We thus deduce that the spin-flip processes at the interface, introduced by the model 2, give a trivial solution of the Dirac paradox.

4.2 Dirac Heterojunctions with massless and massive modes

So far we have discussed two models that realize the Dirac paradox with purely massless Dirac modes. Depending on the specific way the crossover between regions with different helicity is modelled, we have obtained somewhat opposite results. While Model 1 predicts that the only physical solution is not a scattering state (it describes particle injection from both sides) and carries no current, Model 2 does allow a perfect transmission across the interface through the introduction of spin-flip processes on the interface. Here we introduce an essentially different model to answer the Dirac paradox, which involves both massless and *massive* Dirac modes. As we shall see, such model does allow to obtain a tunable transmission coefficient without involving any spin-flip processes at the interface.

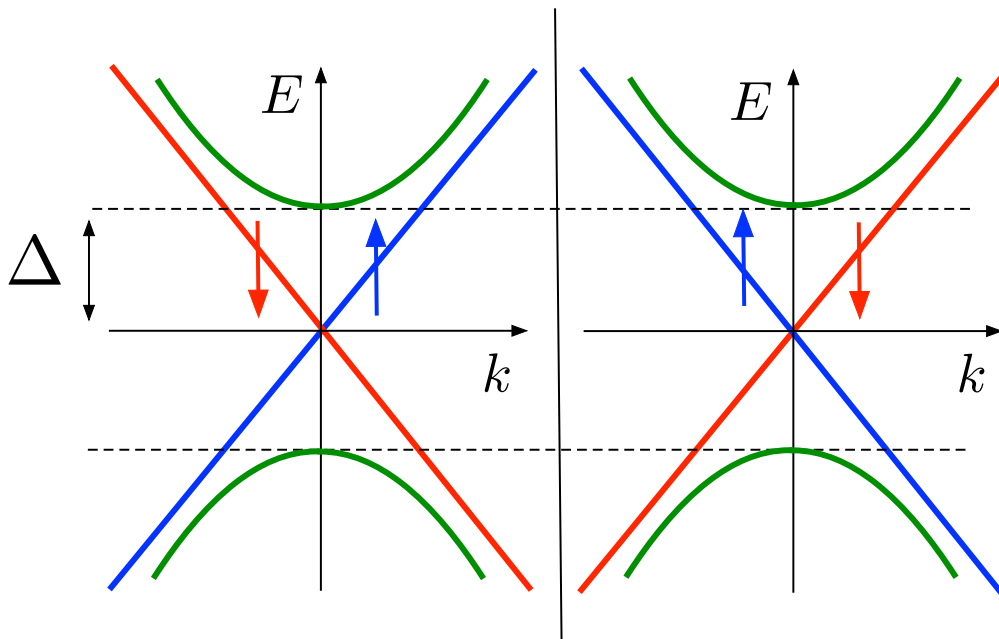


Figure 4.2: The band structure of the massless+massive Dirac model implementing the Dirac paradox. In analogy with the Fig.4.1 red and blue lines represent the massless modes, while green curves represent massive bands with gap 2Δ at $k = 0$.

Let us thus assume that that, each side of the interface is characterized by massive and massless Dirac fermions, as sketched in Fig.4.2. The two bulks of each interface side

is thus modelled with the following Hamiltonians

$$\hat{\mathcal{H}}^{(L)} = +v_F \int \hat{\Psi}^\dagger(x) \tau_z \sigma_z p_x \hat{\Psi}(x) dx - \frac{\Delta}{2} \int \hat{\Psi}^\dagger(x) (\tau_0 - \tau_z) \sigma_x \hat{\Psi}(x) dx \quad (4.32)$$

$$\hat{\mathcal{H}}^{(R)} = -v_F \int \hat{\Psi}^\dagger(x) \tau_z \sigma_z p_x \hat{\Psi}(x) dx - \frac{\Delta}{2} \int \hat{\Psi}^\dagger(x) (\tau_0 - \tau_z) \sigma_x \hat{\Psi}(x) dx \quad (4.33)$$

where $\hat{\Psi} = (\hat{\zeta}_\uparrow, \hat{\zeta}_\downarrow, \hat{\eta}_\uparrow, \hat{\eta}_\downarrow)^T$. Here σ_0 is the 2×2 identity matrix, whereas $\boldsymbol{\sigma} = (\sigma_x, \sigma_y, \sigma_z)$ are the Pauli matrices acting on the spin space, whereas τ_0 and $\boldsymbol{\tau} = (\tau_x, \tau_y, \tau_z)$ are the corresponding matrices acting on the massless-massive degree of freedom, which we can dub pseudospin. The second term in Eqs.(4.32)-(4.33) introduces a gap term *only* for modes $\hat{\eta}_\uparrow$ and $\hat{\eta}_\downarrow$. Thus, $\hat{\zeta}_\uparrow, \hat{\zeta}_\downarrow$ and $\hat{\eta}_\uparrow, \hat{\eta}_\downarrow$ correspond to the massless and massive fields, respectively. In particular, later we shall be interested in the energy range inside the mass gap $|E| < \Delta$ where the massive modes are gapped and do not carry any current, so that only massless modes are propagating. The different sign in the first terms of Eqs.(4.32)-(4.33) corresponds to the opposite helicity for both component of the pseudospin $\hat{\Psi}$, and thus in particular on the massless modes.

In order to model the crossover between the two bulks (4.32) and (4.33) across the interface, we introduce a 4×4 spatially varying matrix $U(x)$, which acts on the $\hat{\Psi}$ -spinor and takes two constant values in the bulk of the two regions

$$U(x) \rightarrow \begin{cases} U^{(L)} & \text{for } x \in \text{bulk of the left side} \\ U^{(R)} & \text{for } x \in \text{bulk of the right side} \end{cases} \quad (4.34)$$

The model adopted for the entire Dirac-heterojunction is thus

$$\hat{\mathcal{H}} = v_F \int \hat{\Psi}^\dagger(x) U^\dagger(x) \tau_z \sigma_z p_x (U(x) \hat{\Psi}(x)) dx - \frac{\Delta}{2} \int \hat{\Psi}^\dagger(x) (\tau_0 - \tau_z) \sigma_x \hat{\Psi}(x) dx \quad (4.35)$$

where requirements

$$U^{(L)\dagger} \tau_z \sigma_z U^{(L)} = +\tau_z \sigma_z \quad (4.36)$$

$$U^{(R)\dagger} \tau_z \sigma_z U^{(R)} = -\tau_z \sigma_z \quad (4.37)$$

on the $U^{(L/R)}$ matrices implement the different helicity sign on the first term of Eq.(4.35), in order to recover Eqs.(4.32)-(4.33) in the bulks. For example, it can be observed that a possible choice for a $U(x)$ -matrix fulfilling Eqs.(4.36)-(4.37) is $U(x) = \exp[i\theta(x)\tau_x\sigma_0/2]$ with the space dependent phase $\theta(x)$ that varies from $\theta_L = 0$ to $\theta_R = \pi$. With this choice, the model (4.35) describes the interface in an analogous way as a spin-active model (4.24), but this is now done by rotating the *pseudo spin* (instead of the actual spin), around x -axis. Below we shall discuss more general expressions for the $U^{(L)}$ and $U^{(R)}$ matrices, and we shall discuss how they can be linked to realistic systems, such as nanowire with RSOC in low energy deep Rashba-dominated regime.

For simplicity, we shall assume a piecewise constant profile for the transformation $U(x)$

$$U(x) = \begin{cases} U^{(L)} & x < x_0 \\ U^{(R)} & x > x_0 \end{cases} \quad (4.38)$$

We can consider the Heisenberg equation associated with the model (4.35)

$$i\hbar\partial_t\hat{\Psi}(x,t) = -i\hbar v_F U^\dagger(x)\tau_z\sigma_z\partial_x\left(U(x)\hat{\Psi}(x,t)\right) \quad (4.39)$$

and its conjugate

$$i\hbar\partial_t\hat{\Psi}^\dagger(x,t) = -i\hbar v_F\partial_x\left(\hat{\Psi}^\dagger(x,t)U^\dagger(x)\right)\tau_z\sigma_zU(x) \quad (4.40)$$

By adding Eq.(4.39) multiplied by $\hat{\Psi}^\dagger$ on the left to Eq.(4.40) multiplied by $\hat{\Psi}$ on the right, we obtain the continuity equation for the density $\hat{\rho} = \hat{\Psi}^\dagger\hat{\Psi}$ and the current operator

$$\hat{J}(x) = ev_F\hat{\Psi}^\dagger(x)U^\dagger(x)\tau_z\sigma_zU(x)\hat{\Psi}(x) \quad (4.41)$$

Furthermore, by integrating the Heisenberg Eq(4.39) over an infinitesimal interval around interface located at x_0 , we obtain

$$U^{(R)}\hat{\Psi}(x_0^+) = U^{(L)}\hat{\Psi}(x_0^-) \quad (4.42)$$

or equivalently

$$\hat{\Psi}(x_0^+) = \mathbf{M}\hat{\Psi}(x_0^-) \quad , \quad (4.43)$$

where $\mathbf{M} = (U^{(R)})^{-1}U^{(L)}$ is the transfer matrix. As consequence of Eqs.(4.36)-(4.37) the transfer matrix \mathbf{M} must fulfill

$$\mathbf{M}^\dagger\tau_z\sigma_z\mathbf{M} = -\tau_z\sigma_z \quad (\text{Requirement \#1}) \quad (4.44)$$

Importantly, here we want to avoid trivial solutions of the Dirac paradox like in the case of the model (4.24). Thus, in order to rule out the possibility of a spin active interface, we introduce a second constraint that ensures the transfer matrix \mathbf{M} to be diagonal in spin space, i.e.

$$\mathbf{M} \text{ must involve only } \sigma_0 \text{ and } \sigma_z \quad (\text{Requirement \#2}) \quad . \quad (4.45)$$

We conclude this section with a remark. Taking the limit $x \rightarrow x_0^\pm$ of the current (4.41) and recalling the conditions (4.36)-(4.37) one finds an opposite sign for the expressions $\hat{J}(x_0^\pm) = \mp ev_F\hat{\Psi}^\dagger(x_0^\pm)\tau_z\sigma_z\hat{\Psi}(x_0^\pm)$ obtained from the two interface sides. At first, this might look like a discontinuity of the current, which is physically not allowed by the continuity equation in the stationary regime. However, such discontinuity is only seeming. Indeed from Eq.(4.43) we observe that the field $\hat{\Psi}$ is itself discontinuous. Such discontinuity is due to a $\delta(x)$ -term arising from $p_xU(x)$ in the Heisenberg Equation (4.39), applied to $U(x)$ in Eq.(4.38). The discontinuity of the field compensates for such sign change and returns a continuous current, as can also be seen by inserting Eq.(4.42) into Eq.(4.41).

4.2.1 Derivation of the transfer matrix

In the previous section we have determined the requirements (4.44)-(4.45) that the transfer matrix \mathbf{M} must fulfill in order to model the Dirac paradox in a setup without spin-flip

process at the interface. Let us now discuss the general form of the transfer matrix that would fulfill such constraints. It is straightforward to see that \mathbf{M} should be expressed as a combination of $\sigma_{\uparrow} = (\sigma_0 + \sigma_z)/2$, $\sigma_{\downarrow} = (\sigma_0 - \sigma_z)/2$ only and therefore can be expressed as

$$\mathbf{M} = \mathbf{M}_{\uparrow}\sigma_{\uparrow} + \mathbf{M}_{\downarrow}\sigma_{\downarrow} \quad , \quad (4.46)$$

where $\mathbf{M}_{\uparrow,\downarrow}$ are 2×2 matrices that operate on the massless-massive pseudospin space. In particular one can observe that with help of the properties $\sigma_{\uparrow,\downarrow}^2 = \sigma_{\uparrow,\downarrow}$ and $\sigma_{\uparrow}\sigma_{\downarrow} = [\sigma_{\uparrow}, \sigma_z] = [\sigma_{\downarrow}, \sigma_z] = 0$, the condition Eq.(4.44) can be rewritten for each pseudo spin transfer matrix $\mathbf{M}_{\uparrow,\downarrow}$ as

$$\mathbf{M}_{\sigma}^{\dagger}\tau_z\mathbf{M}_{\sigma} = -\tau_z \quad \sigma = \uparrow, \downarrow \quad (4.47)$$

that, in turn, for each spin sector $\sigma = \uparrow, \downarrow$ can be fulfilled by a generic 2×2 complex matrix

$$\mathbf{M}_{\sigma} = \begin{pmatrix} a_{\sigma} & b_{\sigma} \\ c_{\sigma} & d_{\sigma} \end{pmatrix} \quad (4.48)$$

the entries of which satisfy $|c_{\sigma}|^2 - |a_{\sigma}|^2 = 1$, $|b_{\sigma}|^2 - |d_{\sigma}|^2 = 1$ and $a_{\sigma}^*b_{\sigma} = c_{\sigma}^*d_{\sigma}$ and therefore one obtains

$$\mathbf{M}_{\sigma} = e^{i\nu_{\sigma}} \begin{pmatrix} i\beta_{\sigma}e^{-i\gamma_{\sigma}} & (1 - i\beta_{\sigma})e^{i\chi_{\sigma}} \\ (1 + i\beta_{\sigma})e^{-i\chi_{\sigma}} & -i\beta_{\sigma}e^{i\gamma_{\sigma}} \end{pmatrix} \quad , \quad (4.49)$$

Notably, for each spin sector $\sigma = \uparrow, \downarrow$, the matrix \mathbf{M}_{σ} depends of 4 real parameters $\chi_{\sigma}, \gamma_{\sigma}, \beta_{\sigma}, \nu_{\sigma}$. We thus have 8 parameters as a whole. Furthermore one has the properties $\mathbf{M}_{\sigma}^{-1}(\beta_{\sigma}, \chi_{\sigma}, \nu_{\sigma}, \gamma_{\sigma}) = \mathbf{M}_{\sigma}(\beta_{\sigma}, \chi_{\sigma}, -\nu_{\sigma}, -\gamma_{\sigma})$ and $\det(\mathbf{M}_{\sigma}) = -\exp[2i\nu_{\sigma}]$. The full transfer matrix \mathbf{M} is obtained by substituting Eq.(4.49) into Eq.(4.46) and in general can be written as

$$\mathbf{M} = \begin{pmatrix} i\beta_{\uparrow}e^{i(\nu_{\uparrow}-\gamma_{\uparrow})} & 0 & (1 - i\beta_{\uparrow})e^{i(\nu_{\uparrow}+\chi_{\uparrow})} & 0 \\ 0 & i\beta_{\downarrow}e^{i(\nu_{\downarrow}-\gamma_{\downarrow})} & 0 & (1 - i\beta_{\downarrow})e^{i(\nu_{\downarrow}+\chi_{\downarrow})} \\ (1 + i\beta_{\uparrow})e^{i(\nu_{\uparrow}-\chi_{\uparrow})} & 0 & -i\beta_{\uparrow}e^{i(\nu_{\uparrow}+\gamma_{\uparrow})} & 0 \\ 0 & (1 + i\beta_{\downarrow})e^{i(\nu_{\downarrow}-\chi_{\downarrow})} & 0 & -i\beta_{\downarrow}e^{i(\nu_{\downarrow}+\gamma_{\downarrow})} \end{pmatrix} \quad (4.50)$$

Consistently with the constrain (4.45), the entries of the transfer matrix (4.50) that are responsible for direct spin-flip, i.e. coupling of different spin components, are vanishing. Finally it is also possible to derive the explicit expression for $U^{(L)}$ and $U^{(R)}$. First of all we observe that the requirement (4.36) is satisfied with $U^{(L)} = \tau_0\sigma_0$ and $U^{(R)} = \mathbf{M}^{-1}$, that in turn can be easily find by recalling the property $\mathbf{M}^{-1}(\boldsymbol{\beta}, \boldsymbol{\chi}, \boldsymbol{\nu}, \boldsymbol{\gamma}) = \mathbf{M}(\boldsymbol{\beta}, \boldsymbol{\chi}, -\boldsymbol{\nu}, -\boldsymbol{\gamma})$ of the transfer matrix, where each bold symbols labels the pair of related parameters, e.g. $\boldsymbol{\beta} = (\beta_{\uparrow}, \beta_{\downarrow})$.

4.2.2 Scattering states

Since we have found the general expression (4.50) of the transfer matrix, we can now focus on the scattering state solution. We recall that the 4×1 spinor $\hat{\Psi}$ of the model (4.35) consists of both massless $\hat{\zeta}_{\uparrow}, \hat{\zeta}_{\downarrow}$ and massive $\hat{\eta}_{\uparrow}, \hat{\eta}_{\downarrow}$ modes. Inside the gap ($|E| < \Delta$), massless modes are propagating, while massive modes are evanescent. In particular, at

$E = 0$, i.e. in the middle of the massive energy gap, one can construct the scattering state

$$\hat{\Psi}_E(x) = \begin{cases} \hat{a}^{(L)} \begin{pmatrix} 1 \\ 0 \\ 0 \\ 0 \end{pmatrix} e^{ik_0x} + \hat{b}^{(L)} \begin{pmatrix} 0 \\ 1 \\ 0 \\ 0 \end{pmatrix} e^{-ik_0x} + \frac{\hat{c}^{(L)}}{\sqrt{2}} \begin{pmatrix} 0 \\ 0 \\ -i \\ 1 \end{pmatrix} e^{\kappa_0x} & x < x_0 \\ \hat{a}^{(R)} \begin{pmatrix} 1 \\ 0 \\ 0 \\ 0 \end{pmatrix} e^{-ik_0x} + \hat{b}^{(R)} \begin{pmatrix} 0 \\ 1 \\ 0 \\ 0 \end{pmatrix} e^{ik_0x} + \frac{\hat{c}^{(R)}}{\sqrt{2}} \begin{pmatrix} 0 \\ 0 \\ -i \\ 1 \end{pmatrix} e^{-\kappa_0x} & x > x_0 \end{cases} \quad (4.51)$$

where $k_0 = 0$, $\kappa_0 = \Delta/\hbar v_F$. Following the notation used in chapter 2, we have introduced the incoming and outgoing operators $\hat{a}^{(\gamma)}$ and $\hat{b}^{(\gamma)}$ on the left side ($\gamma = L$) and right side ($\gamma = R$) of the interface. Notably, the massless propagating states $\hat{\zeta}_\uparrow, \hat{\zeta}_\downarrow$ (the upper two components of $\hat{\Psi}_E$), have opposite helicity on the two sides of the interface: On the left side right-moving and left-moving states have spin- \uparrow and spin- \downarrow , respectively, whereas the opposite occurs on the right side. This indeed corresponds to the premises of the Dirac paradox. The $\hat{c}^{(L)}$ and $\hat{c}^{(R)}$ operators are associated with evanescent massive modes $\hat{\eta}_\uparrow, \hat{\eta}_\downarrow$ (the lower two components of $\hat{\Psi}_E$).

By plugging Eq.(4.51) into Eq.(4.43) and by exploiting Eq.(4.50), one can find the following relations

$$\begin{pmatrix} \hat{b}^{(L)} \\ \hat{b}^{(R)} \end{pmatrix} = S \begin{pmatrix} \hat{a}^{(L)} \\ \hat{a}^{(R)} \end{pmatrix} \quad (4.52)$$

and

$$\begin{pmatrix} \hat{c}^{(L)} \\ \hat{c}^{(R)} \end{pmatrix} = \tilde{S} \begin{pmatrix} \hat{a}^{(L)} \\ \hat{a}^{(R)} \end{pmatrix} \quad (4.53)$$

Here

$$S = \frac{ie^{-i\Delta\chi}}{(1-i\beta_\uparrow)(1+i\beta_\downarrow)} \begin{pmatrix} e^{i\Delta\nu} + e^{-i\Delta\gamma}\beta_\uparrow\beta_\downarrow & i(e^{i(\gamma_\downarrow-\nu_\uparrow)}\beta_\downarrow - e^{i(\gamma_\uparrow-\nu_\downarrow)}\beta_\uparrow) \\ i(e^{i(\nu_\uparrow-\gamma_\downarrow)}\beta_\downarrow - e^{i(\nu_\downarrow-\gamma_\uparrow)}\beta_\uparrow) & e^{-i\Delta\nu} + e^{i\Delta\gamma}\beta_\uparrow\beta_\downarrow \end{pmatrix} \quad (4.54)$$

is the Scattering Matrix returning the outgoing propagating modes in terms of the incoming propagating modes, with $\Delta\chi \doteq \chi_\uparrow - \chi_\downarrow$, $\Delta\nu \doteq \nu_\uparrow - \nu_\downarrow$ and $\Delta\gamma \doteq \gamma_\uparrow - \gamma_\downarrow$, whereas

$$\tilde{S} = \frac{\sqrt{2}e^{-i\chi_\uparrow}}{1-i\beta_\uparrow} \begin{pmatrix} \beta_\uparrow e^{-i\gamma_\uparrow} & ie^{-i\nu_\uparrow} \\ ie^{+i\nu_\uparrow} & \beta_\uparrow e^{i\gamma_\uparrow} \end{pmatrix} \quad (4.55)$$

is the matrix yielding the evanescent modes in terms of the incoming propagating modes.

Let us now emphasize the differences with respect to the models 1 and 2 that are purely based on massless modes and that we have discussed in Sec.4.1.1. Just like Model 1 [see Eq.(4.13)], the massless+massive model (4.35) does not involve any spin-active interface. However, while Model 1 has no scattering state solution to the paradox and exhibits a vanishing transmission, the massless+massive model (4.35) admits a solution in terms of scattering states. In particular, from the scattering matrix (4.54) it is straightforward to obtain the transmission coefficient as

$$T = |S_{1,2}|^2 = |S_{2,1}|^2 = \frac{\beta_{\uparrow}^2 + \beta_{\downarrow}^2 - 2\beta_{\uparrow}\beta_{\downarrow} \cos \varphi}{(1 + \beta_{\uparrow}^2)(1 + \beta_{\downarrow}^2)} \quad (4.56)$$

which depends on the 3 parameters β_{\uparrow} , β_{\downarrow} and $\varphi = \Delta\gamma + \Delta\nu$. Furthermore, differently from Model 2 [see Eq.(4.24)], which directly introduces a spin-flip process at the interface, in model (4.35) transmission of an incoming state with spin- \uparrow to an outgoing state with spin- \downarrow is possible because of the mediation of the massive evanescent states, as will be highlighted here below.

The role of the evanescent modes

In order to highlight the role of the massive modes in the transmission process, one can focus on the state with a mode incident only from the left side, by setting $\hat{a}^{(R)} \rightarrow 0$. Assuming $\gamma_{\sigma} = \chi_{\sigma} = \nu_{\sigma} = 0$ and an interface position at $x_0 = 0$, we insert the scattering state (4.51) into the transfer matrix equation (4.43), obtaining

$$\begin{pmatrix} 0 \\ \hat{b}^{(R)} \\ \frac{-i}{\sqrt{2}}\hat{c}^{(R)} \\ \frac{1}{\sqrt{2}}\hat{c}^{(R)} \end{pmatrix} = \begin{pmatrix} i\beta_{\uparrow} & 0 & (1 - i\beta_{\uparrow}) & 0 \\ 0 & i\beta_{\downarrow} & 0 & (1 - i\beta_{\downarrow}) \\ (1 + i\beta_{\uparrow}) & 0 & -i\beta_{\uparrow} & 0 \\ 0 & (1 + i\beta_{\downarrow}) & 0 & -i\beta_{\downarrow} \end{pmatrix} \begin{pmatrix} \hat{a}^{(L)} \\ \hat{b}^{(L)} \\ \frac{-i}{\sqrt{2}}\hat{c}^{(L)} \\ \frac{1}{\sqrt{2}}\hat{c}^{(L)} \end{pmatrix} \quad (4.57)$$

Let us start by analyzing the case $\beta_{\uparrow} = 0$. In this case the above system becomes

$$\begin{pmatrix} 0 \\ \hat{b}^{(R)} \\ \frac{-i}{\sqrt{2}}\hat{c}^{(R)} \\ \frac{1}{\sqrt{2}}\hat{c}^{(R)} \end{pmatrix} = \underbrace{\begin{pmatrix} 0 & 0 & 1 & 0 \\ 0 & i\beta_{\downarrow} & 0 & 1 - i\beta_{\downarrow} \\ 1 & 0 & 0 & 0 \\ 0 & 1 + i\beta_{\downarrow} & 0 & -i\beta_{\downarrow} \end{pmatrix}}_{\mathbf{M}} \begin{pmatrix} \hat{a}^{(L)} \\ \hat{b}^{(L)} \\ \frac{-i}{\sqrt{2}}\hat{c}^{(L)} \\ \frac{1}{\sqrt{2}}\hat{c}^{(L)} \end{pmatrix} \quad (4.58)$$

This configuration is schematically represented in Fig.4.3(a). In particular, the left panel pictures the scattering wavefunction, where wavy lines correspond to the propagating modes and the green solid line represents an evanescent mode, with the blue and red color indicating spin- \uparrow and spin- \downarrow components, respectively. The right panel illustrates how the transfer matrix connects the modes across the interface (black lines). One can observe that a spin- \uparrow particle incoming from the left ($\hat{a}^{(L)}$, blue wiggly line) is connected by transfer matrix \mathbf{M} only with a massive state $\hat{c}^{(R)}$ on the right through the entry $M_{31} = 1$. However, since this evanescent mode (green box) is characterized by a spinor with *both* spin components, it is linked back to the outgoing spin- \downarrow massless mode $\hat{b}^{(L)}$ on the left

by the matrix entry $M_{42} = 1 + i\beta_{\downarrow}$. In turn, the latter is also coupled, through the entry $M_{22} = i\beta_{\downarrow}$, to the spin- \downarrow transmitted mode $\hat{b}^{(R)}$ on the right. In this way the presence of the evanescent massive mode with the spin orthogonal to spin of propagating modes mediates and indirectly allows an effective spin-flip transmission between propagating massless states with opposite helicity.

Next, let us consider the the opposite configuration, namely the case $\beta_{\downarrow} = 0$. In this case Eq.(4.57) reduces to

$$\begin{pmatrix} 0 \\ \hat{b}^{(R)} \\ \frac{-i}{\sqrt{2}}\hat{c}^{(R)} \\ \frac{1}{\sqrt{2}}\hat{c}^{(R)} \end{pmatrix} = \underbrace{\begin{pmatrix} i\beta_{\uparrow} & 0 & 1 - i\beta_{\uparrow} & 0 \\ 0 & 0 & 0 & 1 \\ 1 + i\beta_{\uparrow} & 0 & -i\beta_{\uparrow} & 0 \\ 0 & 1 & 0 & 0 \end{pmatrix}}_{\mathbf{M}} \begin{pmatrix} \hat{a}^{(L)} \\ \hat{b}^{(L)} \\ \frac{-i}{\sqrt{2}}\hat{c}^{(L)} \\ \frac{1}{\sqrt{2}}\hat{c}^{(L)} \end{pmatrix} \quad (4.59)$$

This configuration is pictured in Fig.4.3(b). Similarly to the previous case, the mode $\hat{a}^{(L)}$ incoming from the left side is connected with the evanescent mode $\hat{c}^{(R)}$ on the right side through the $M_{31} = 1 + i\beta_{\uparrow}$, which in turn gives rise to the outgoing mode $\hat{b}^{(L)}$ on the left through the connection $M_{24} = 1$. However, in contrast with the case of $\beta_{\uparrow} = 0$, the path for the outgoing mode on the right is completely different. Indeed, due to the $M_{33} = -i\beta_{\uparrow}$ entry, a connection between massive modes on opposite sides of the interface opens up. Moreover, the outgoing mode $\hat{b}^{(R)}$ on the right is connected to the massive mode on the left with $M_{42} = 1$. Despite these differences, the transmission between massless propagating states with opposite helicity again occurs due to the presence of the evanescent modes on both sides of the interface.

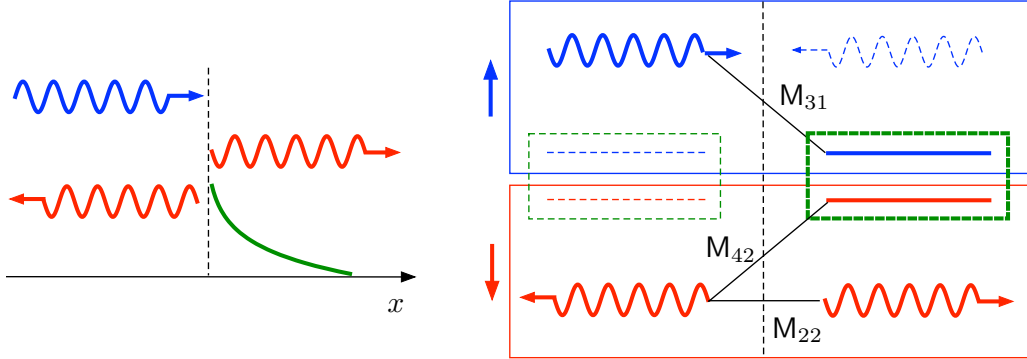
In the most general case, one has that both β_{\uparrow} and β_{\downarrow} are finite and the transmission coefficient (4.56) results from a combination of the two previous cases. Finally we observe that, if both β_{\uparrow} and β_{\downarrow} vanish, one finds a zero transmission. In this case the mechanism that suppresses the transmission can be explained by observing that the transfer matrix (4.50) becomes $\mathbf{M} = \tau_x \sigma_0$ and therefore the boundary conditions can be written as

$$\begin{cases} \hat{\zeta}_{\sigma}(0^+) = \hat{\eta}_{\sigma}(0^-) \\ \hat{\eta}_{\sigma}(0^+) = \hat{\zeta}_{\sigma}(0^-) \end{cases} \quad \sigma = \uparrow, \downarrow \quad (4.60)$$

Each incoming massless mode of a given spin is coupled uniquely to the massive evanescent mode with the same spin component on the other side of the interface.

In conclusion, we have obtained that, although in energy range inside the gap the massive evanescent modes carry no current directly, they are crucial in the inhomogeneous setup such as the Dirac paradox. Indeed massive modes are localized at the interface and indirectly couple the two spin channels. This is what enables an *effective spin-flip transmission* between propagating states with opposite helicity. Moreover, the resulting transmission coefficient is tunable from 0 to 1 through the 3 parameters β_{\uparrow} , β_{\downarrow} and φ [see Eq.(4.56)].

(a) $\beta_{\uparrow} = 0$



(b) $\beta_{\downarrow} = 0$

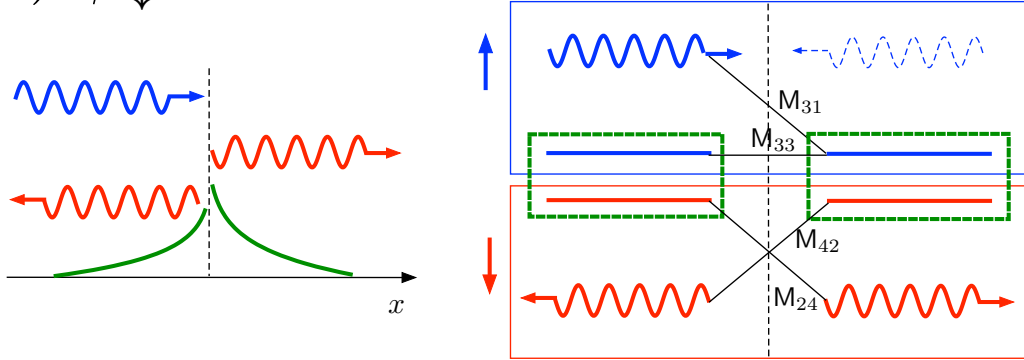


Figure 4.3: The left-hand side of each panel depicts the scattering state wavefunction of a particle injected from the left. The blue and red colors correspond to the spin- \uparrow and spin- \downarrow components of the spinor eigenstate, respectively. Wavy lines are associated with propagating states, in particular the incoming modes are always characterized by spin- \uparrow while outgoing modes by spin- \downarrow . The solid green lines corresponds the evanescent wave of the massive mode. The right side of each panel illustrates the transmission process described correspondingly with Eq.(4.58)-(4.59). The black lines are associated with entries of the transfer matrix that connect non vanishing contribution to the scattering state. Panel (a) refers to the case $\beta_{\uparrow} = 0$: The evanescent mode appears only on the right side of the interface. Here $M_{31} = 1$, $M_{42} = 1 + i\beta_{\downarrow}$ and $M_{22} = i\beta_{\downarrow}$. Panel (b) describes the case $\beta_{\downarrow} = 0$: The evanescent modes arise on both sides of the junction. Here $M_{31} = 1 + i\beta_{\uparrow}$, $M_{33} = -i\beta_{\uparrow}$ and $M_{24} = M_{42} = 1$. In this way, although the transfer matrix presents the direct connection only between the states with the same spin, the evanescent modes of the massive field indirectly allow a spin-flip transmission between the propagating modes.

4.3 Realization with spin-orbit nanowires

In the previous section we have discussed the massless+massive model that admits non trivial solutions to the Dirac paradox in 1D. Here we present its possible implementation. First of all it worth recalling that the 1D helical Dirac states can be found at the edges of a quantum spin Hall system[28, 34, 35, 50, 69]. However, in that case the interface between two regions would be a line that in principle could provide the electrons with a way to escape the paradox, like in the case of 3D Topological insulators. In this section I show that a genuinely 1D Dirac paradox can be realized with a Rashba NW in the presence of the Zeeman splitting. As has been shown in chapter 3.1.3, a NW in the deep Rashba-dominated regime ($E_Z \ll 2E_{SO}$) exhibits massless helical states, whose helicity can be controlled by the sign of the RSOC. However, as shown in Section 3.1.3, the low-energy Physics of NWs actually involves both the massless helical modes near $k \sim \pm 2k_{SO}$ and the massive modes near $k \sim 0$, which both enter in the low-energy electron field operator Eq.(3.64). Remarkably, the NW low energy Hamiltonian (3.61) has precisely the same structure as the Hamiltonians (4.32) and (4.33) of the massless+massive model describing the bulk of the two sides of the Dirac paradox problem, upon identifying $v_{SO} \rightarrow v_F$, $E_Z \rightarrow \Delta$ and $\hat{\Phi} \rightarrow \hat{\Psi}$. Note that the sign s_α of the RSOC in Eq. (3.61) determines the sign of the velocity on each interface side. In the literature about low energy transport properties in NWs, a uniform RSOC is typically assumed and the massive modes are neglected, since they simply carry no current. However, as we have discussed above, massive modes become important in inhomogeneous RSOC problems.

Let us revisit the “magnetic barrier” setup discussed in the previous chapter (see Fig.3.15) and focus in particular on the case where the RSOC in the two outer regions is equal in magnitude but opposite in sign. In a physically realistic setup, this two regions are separated by a region with negligible RSOC, so that

$$\alpha(x) = \begin{cases} +\alpha > 0 & \text{for } x < -d/2 \quad (\text{region 1}) \\ 0 & \text{for } |x| < d/2 \quad (\text{region 2}) \\ -\alpha < 0 & \text{for } x > +d/2 \quad (\text{region 3}) \end{cases} \quad (4.61)$$

with $\alpha > 0$. Furthermore we assume that the outer regions 1 and 3 are in deep Rashba-dominated regime ($2E_{SO} \gg E_Z$), while the internal regions 2 is obviously in the strongly Zeeman dominated regime.

Following the discussion of the inhomogeneous NW in Sec.3.2, the matching condition Eq.(3.90) can be written explicitly for the left interface at $x_0 = -d/2$ as

$$\begin{cases} \hat{\Psi}(x_0^-, t) = \hat{\Psi}(x_0^+, t) \\ \left(\sigma_0 \partial_x - i k_{SO} \sigma_3 \right) \hat{\Psi}(x_0^-, t) = \sigma_0 \partial_x \hat{\Psi}(x_0^+, t) \end{cases} \quad (4.62)$$

and for right interface at $x_1 = d/2$ as

$$\begin{cases} \hat{\Psi}(x_1^-, t) = \hat{\Psi}(x_1^+, t) \\ \sigma_0 \partial_x \hat{\Psi}(x_1^-, t) = \left(\sigma_0 \partial_x + i k_{SO} \sigma_3 \right) \hat{\Psi}(x_1^+, t) \end{cases} \quad (4.63)$$

As we have seen in the Section 3.2.4 in general the transmission coefficient can be computed numerically. However for the energy window $|E| \ll E_Z \ll 2E_{SO}$ one can use the low energy model in order to find analytical results. Indeed using the low energy expression for the field (3.64), the stationary field operator Ansatz can be written in each region as

$$\hat{\Psi}_E(x) = \begin{cases} \begin{pmatrix} e^{2ik_{SO}x} \zeta_{\uparrow}(x) + \eta_{\uparrow}(x) \\ e^{-2ik_{SO}x} \zeta_{\downarrow}(x) + \eta_{\downarrow}(x) \end{pmatrix} & x < -d/2 \\ \frac{\hat{h}_E}{\sqrt{2}} \begin{pmatrix} 1 \\ 1 \end{pmatrix} e^{ik_{2,E}x} + \frac{\hat{g}_E}{\sqrt{2}} \begin{pmatrix} 1 \\ 1 \end{pmatrix} e^{-ik_{2,E}x} + \frac{\hat{d}_E}{\sqrt{2}} \begin{pmatrix} 1 \\ -1 \end{pmatrix} e^{\kappa_{2,E}x} + \frac{\hat{f}_E}{\sqrt{2}} \begin{pmatrix} 1 \\ -1 \end{pmatrix} e^{-\kappa_{2,E}x} & |x| < d/2 \\ \begin{pmatrix} e^{-2ik_{SO}x} \zeta_{\uparrow}(x) + \eta_{\uparrow}(x) \\ e^{2ik_{SO}x} \zeta_{\downarrow}(x) + \eta_{\downarrow}(x) \end{pmatrix} & x > d/2 \end{cases} \quad (4.64)$$

where $\hat{h}_E, \hat{g}_E, \hat{d}_E$ and \hat{f}_E are mode operators and $k_{2,E} = k_Z \sqrt{1 + E/E_Z}$, $\kappa_{2,E} = k_Z \sqrt{1 - E/E_Z}$. This field operator can be used in matching conditions (4.62)-(4.63), which in turn can be rewritten for the interface at $x_0 = -d/2$ as

$$\begin{cases} e^{-ik_{SO}d} \hat{\zeta}_{\uparrow}(-d/2) + \hat{\eta}_{\uparrow}(-d/2) = \hat{\Psi}_{E\uparrow}(-d/2) \\ e^{+ik_{SO}d} \hat{\zeta}_{\downarrow}(-d/2) + \hat{\eta}_{\downarrow}(-d/2) = \hat{\Psi}_{E\downarrow}(-d/2) \\ +ik_{SO} \left[e^{-ik_{SO}d} \hat{\zeta}_{\uparrow}(-d/2) - \hat{\eta}_{\uparrow}(-d/2) \right] = \partial_x \hat{\Psi}_{E\uparrow}(-d/2) \\ -ik_{SO} \left[e^{+ik_{SO}d} \hat{\zeta}_{\downarrow}(-d/2) - \hat{\eta}_{\downarrow}(-d/2) \right] = \partial_x \hat{\Psi}_{E\downarrow}(-d/2) \end{cases} \quad (4.65)$$

and for the interface $x_1 = +d/2$ as

$$\begin{cases} \hat{\Psi}_{E\uparrow}(d/2) = e^{-ik_{SO}d} \hat{\zeta}_{\uparrow}(d/2) + \hat{\eta}_{\uparrow}(d/2) \\ \hat{\Psi}_{E\downarrow}(d/2) = e^{+ik_{SO}d} \hat{\zeta}_{\downarrow}(d/2) + \hat{\eta}_{\downarrow}(d/2) \\ \partial_x \hat{\Psi}_{E\uparrow}(d/2) = -ik_{SO} \left[e^{-ik_{SO}d} \hat{\zeta}_{\uparrow}(d/2) - \hat{\eta}_{\uparrow}(d/2) \right] \\ \partial_x \hat{\Psi}_{E\downarrow}(d/2) = +ik_{SO} \left[e^{+ik_{SO}d} \hat{\zeta}_{\downarrow}(d/2) - \hat{\eta}_{\downarrow}(d/2) \right] \end{cases} \quad (4.66)$$

To be consistent with the limit of low energy physics, we have neglected the derivatives $\partial_x \hat{\zeta}$ and $\partial_x \hat{\eta}$ of the slowly varying fields with respect to the term proportional to k_{SO} , since they involve wavevectors $|q| \ll k_{SO}$. The boundary conditions can be reformulated in a matrix form as

$$\mathbf{P} \begin{pmatrix} \hat{\zeta}_{\uparrow}(-d/2) \\ \hat{\zeta}_{\downarrow}(-d/2) \\ \hat{\eta}_{\uparrow}(-d/2) \\ \hat{\eta}_{\downarrow}(-d/2) \end{pmatrix} = \mathbf{V}(-d/2) \begin{pmatrix} \hat{h} \\ \hat{g} \\ \hat{d} \\ \hat{f} \end{pmatrix} \quad (4.67)$$

$$\mathbf{V}(d/2) \begin{pmatrix} \hat{h} \\ \hat{g} \\ \hat{d} \\ \hat{f} \end{pmatrix} = \mathbf{Q} \begin{pmatrix} \hat{\zeta}_{\uparrow}(d/2) \\ \hat{\zeta}_{\downarrow}(d/2) \\ \hat{\eta}_{\uparrow}(d/2) \\ \hat{\eta}_{\downarrow}(d/2) \end{pmatrix}, \quad (4.68)$$

with

$$\mathbf{P} = \begin{pmatrix} e^{-ik_{SO}d} & 0 & 1 & 0 \\ 0 & e^{ik_{SO}d} & 0 & 1 \\ k_{SO}e^{-ik_{SO}d} & 0 & -k_{SO} & 0 \\ 0 & -k_{SO}e^{ik_{SO}d} & 0 & k_{SO} \end{pmatrix}, \quad (4.69)$$

$$\mathbf{Q} = \begin{pmatrix} e^{-ik_{SO}d} & 0 & 1 & 0 \\ 0 & e^{ik_{SO}d} & 0 & 1 \\ -k_{SO}e^{-ik_{SO}d} & 0 & k_{SO} & 0 \\ 0 & k_{SO}e^{ik_{SO}d} & 0 & -k_{SO} \end{pmatrix} \quad (4.70)$$

and

$$\mathbf{V}(x) = \frac{1}{\sqrt{2}} \times \begin{pmatrix} e^{ik_{2,E}x} & e^{-ik_{2,E}x} & e^{\kappa_{2,E}x} & e^{-\kappa_{2,E}x} \\ e^{ik_{2,E}x} & e^{-ik_{2,E}x} & -e^{\kappa_{2,E}x} & -e^{-\kappa_{2,E}x} \\ ik_{2,E}e^{ik_{2,E}x} & -ik_{2,E}e^{-ik_{2,E}x} & \kappa_{2,E}e^{\kappa_{2,E}x} & -\kappa_{2,E}e^{-\kappa_{2,E}x} \\ ik_{2,E}e^{ik_{2,E}x} & -ik_{2,E}e^{-ik_{2,E}x} & -\kappa_{2,E}e^{\kappa_{2,E}x} & \kappa_{2,E}e^{-\kappa_{2,E}x} \end{pmatrix} \quad (4.71)$$

The correspondence of the low energy fields in the outer regions can be found by rewriting the boundary conditions Eq.(4.65)-(4.65) in a transfer matrix form (4.43)

$$\begin{pmatrix} \hat{\zeta}_{\uparrow}(d/2) \\ \hat{\zeta}_{\downarrow}(d/2) \\ \hat{\eta}_{\uparrow}(d/2) \\ \hat{\eta}_{\downarrow}(d/2) \end{pmatrix} = \mathbf{M}_E \begin{pmatrix} \hat{\zeta}_{\uparrow}(-d/2) \\ \hat{\zeta}_{\downarrow}(-d/2) \\ \hat{\eta}_{\uparrow}(-d/2) \\ \hat{\eta}_{\downarrow}(-d/2) \end{pmatrix} \quad (4.72)$$

where $\mathbf{M}_E = \mathbf{Q}^{-1}\mathbf{V}(d/2)\mathbf{V}^{-1}(-d/2)\mathbf{P}$ is a transfer matrix that depend on energy E and the length of the central region d through two dimensionless parameters k_Zd and $k_{SO}d$.

We consider for simplicity the middle of the gap, $E = 0$, which turns out to be a representative value for the entire low energy range $|E| \ll E_Z$. Notably in the case of deep Rashba dominated regime $k_Zd \ll k_{SO}d$, we can treat k_Zd as a small parameter, while retaining a finite value for $k_{SO}d$. One can thus expand the transfer matrix $\mathbf{M}_{E=0}$ in powers of k_Zd , up to $\mathcal{O}((k_Zd)^4)$ and find

$$\mathbf{M}_0 \simeq \begin{pmatrix} ik_{SO}d/2 & A & (1 - ik_{SO}d/2)e^{ik_{SO}d} & B \\ A^* & -ik_{SO}d/2 & B^* & (1 + ik_{SO}d/2)e^{-ik_{SO}d} \\ (1 + ik_{SO}d/2)e^{-ik_{SO}d} & -B & -ik_{SO}d/2 & A^*e^{2ik_{SO}d} \\ -B^* & (1 - ik_{SO}d/2)e^{ik_{SO}d} & Ae^{-2ik_{SO}d} & ik_{SO}d/2 \end{pmatrix} \quad (4.73)$$

where

$$A = i \frac{-6 + k_{SO}d(k_{SO}d + 6i)}{12k_{SO}d} e^{2ik_{SO}d} (k_Zd)^2 \quad (4.74)$$

$$B = -i \frac{(k_{SO}d)^2 + 6}{12k_{SO}d} e^{ik_{SO}d} (k_Zd)^2 \quad (4.75)$$

Notably the entries that couple spin- \uparrow to spin- \downarrow components are proportional to A , B and therefore are of the order $\mathcal{O}((k_Z d)^2)$. Thus, these terms can be neglected in the limit $k_Z d \ll 1$ with respect to other entries, which order is $\mathcal{O}(1)$. Therefore the transfer matrix can be approximated as

$$\mathbf{M}_0 \simeq \begin{pmatrix} i\frac{k_{SO}d}{2} & 0 & (1 - i\frac{k_{SO}d}{2})e^{ik_{SO}d} & 0 \\ 0 & -i\frac{k_{SO}d}{2} & 0 & (1 + i\frac{k_{SO}d}{2})e^{-ik_{SO}d} \\ (1 + i\frac{k_{SO}d}{2})e^{-ik_{SO}d} & 0 & -i\frac{k_{SO}d}{2} & 0 \\ 0 & (1 - i\frac{k_{SO}d}{2})e^{ik_{SO}d} & 0 & i\frac{k_{SO}d}{2} \end{pmatrix}. \quad (4.76)$$

One can immediately recognize the similarity between Eq.(4.76) and the transfer matrix of the massless+massive Dirac model Eq.(4.50), discussed above. The correspondence can be explicitly highlight by identifying $\beta_\uparrow = -\beta_\downarrow = k_{SO}d/2$, $\chi_\uparrow = -\chi_\downarrow = k_{SO}d$ and $\gamma_\uparrow = \gamma_\downarrow = \nu_\uparrow = \nu_\downarrow = 0$. In this way, whenever the central region can be considered much shorter compared to the Zeeman wavelength $l_Z = k_Z^{-1}$ characterising locally the wavefunction therein, the transfer matrix \mathbf{M}_0 does not couple the spin components of outer regions and becomes *independent* of the Zeeman energy E_Z . However it still couples massless and massive modes and still depends on $k_{SO}d$. This parameter represents the ratio between the crossover region length d and the spin-orbit length $l_{SO} = k_{SO}^{-1}$, and may be finite because of the deep Rashba-dominated regime $k_Z \ll k_{SO}$.

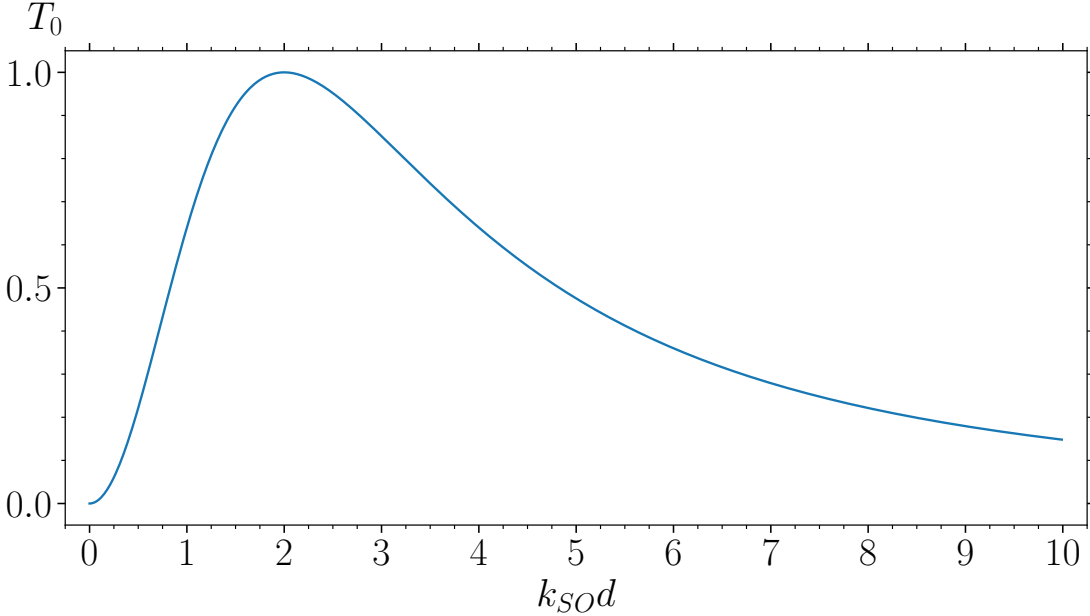


Figure 4.4: The transmission coefficient (4.77), plotted as a function of $k_{SO}d$, covers the entire range $T_0 \in [0,1]$.

In analogy with the Eq.(4.56) one obtains the transmission coefficient related to the

transfer matrix (4.76) as

$$T_0 = \frac{(k_{SO}d)^2}{(1 + (k_{SO}d/2)^2)^2} \quad , \quad (4.77)$$

As a function of $k_{SO}d$, T_0 varies over the full range $T_0 \in [0,1]$, as shown in Fig.4.4. For small values $k_{SO}d \ll 1$ the transmission is low, $T_0 \sim (k_{SO}d)^2$, whereas for finite values of $k_{SO}d$ we note from Fig.4.4 that T_0 increases, and a perfect transmission $T_0 = 1$ is obtained for $k_{SO}d = 2$. Then, for large values of $k_{SO}d$ the transmission decreases again as $T_0 \sim 16/(k_{SO}d)^2$.

4.3.1 Transmission coefficient in the case of InSb

Let us now consider the particular implementation of the Rashba NW with InSb, where the effective electron mass is $m^* = 0.015m_e$. Two NW regions are coupled with two different metallic gates, which induce opposite RSOC signs, and are separated by a crossover region with length $d = 100\text{nm}$ and with a negligible RSOC. The numerical results of the conductance G/G_0 at midgap ($E = 0$) is shown, in units of the conductance quantum $G_0 = e^2/h$, as a function of the spin-orbit energy E_{SO} in Fig.4.4(a). Each solid line corresponds to a different value of the Zeeman energy E_Z . The dashed curve corresponds to the analytical solution (4.77) found in the low-energy limit, where external regions are effectively described by the massless+massive Dirac model. In particular for $E_{SO} \rightarrow 0$ the exact transmission coefficient tends to 1. This is because in this limit all three NW regions are characterized by exactly same regime, i.e. Zeeman dominated regime. However, as soon as spin orbit energy becomes sufficiently large to make the outer regions enter the deep Rashba dominated regime ($2E_{SO} \gg E_Z$) all the curves converge to the low-energy limit Eq.(4.77), independently on the particular value of Zeeman energy. This is indeed a hallmark of the Dirac paradox regime. As we have discussed, in this case the transmission takes place even without the spin-flip processes at the interface by the mediation of the massive modes localized at the interface. In Fig.4.4(b) we display the same plot, zoomed to a realistic range of spin orbit energy values, i.e. up to $E_{SO} = 0.5\text{meV}$. We fix the maximum Zeeman energy to be $E_Z = 0.1\text{meV}$, so that the Rashba dominated regime in outer region can be reached. Again, as E_{SO} increases, all curves merge to the analytical result obtained with the massless+massive model (dashed curve).

In conclusion, the 1D Dirac paradox configuration can be realized with a spin-orbit NW that is suitably coupled to two gates, and its linear conductance G can be tuned over a large range of values by modulating the spin orbit energy. This can be realistically done via the gate voltage.

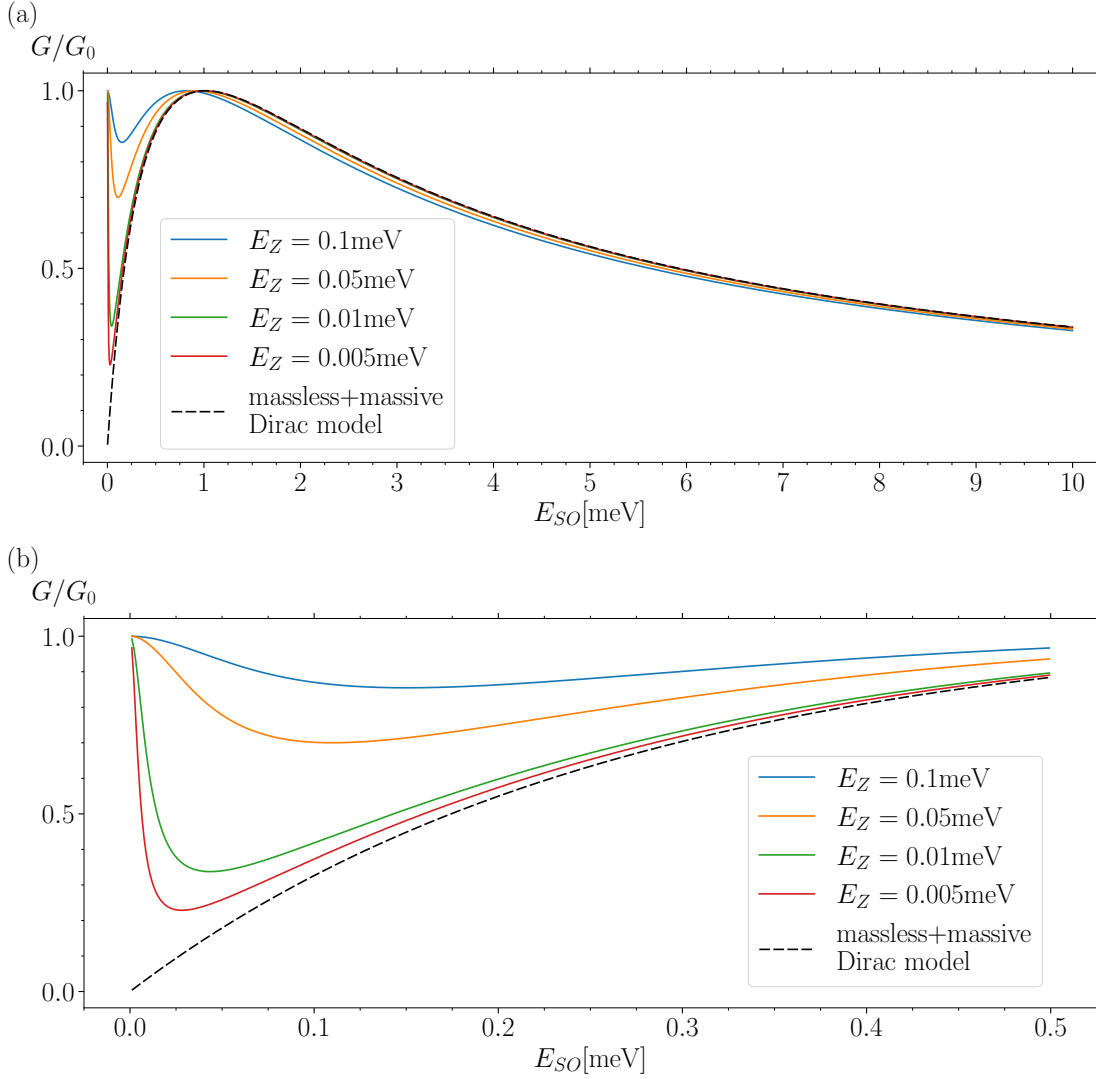


Figure 4.5: The Dirac paradox configuration realized with a InSb NW setup where two outer gated regions are characterized by opposite RSOC and the central region has a width $d = 100$ nm. The midgap conductance G , obtained from the numerically exact solution with the profile (4.61), is plotted in units of the conductance quantum G_0 as a function of the spin orbit energy, for different values of the external magnetic field E_Z (solid curves). At each value of E_Z , when the Rashba-dominated regime ($2E_{SO} \gg E_Z$) is reached, the various solid curves all tend to the dashed curve describing the result Eq.(4.77), obtained in the low energy limit from the effective massless+massive Dirac model. Panel (b) is a zoom of panel (a) in the regime of spin-orbit values that are realistic with present gating techniques.

Chapter 5

Conclusions

In this thesis I have investigated the coherent electron transport in a nanowire with spin-orbit coupling. These systems are currently on the spotlight of Condensed matter physics, in view of their technological versatility and their potential application in various research areas, ranging from topological systems to quantum information and quantum engines.

In the first chapter I have reviewed the origin of the spin-orbit coupling from the Dirac Equation, recalling its implications— on atomic physics and on solid state systems. I have specifically discussed the Rashba spin-orbit coupling (RSOC), which arises from the structural inversion asymmetry present in various semiconductor heterojunctions, including nanowires (NWs) on a substrate.

In the second chapter I have revisited the main aspects of quantum mesoscopic physics, i.e. the regime where quantum coherence of electron waves is preserved. I have briefly reviewed the Scattering Matrix formalism developed by Landauer & Büttiker, which allows to derive a general expression of the current through a mesoscopic system, relating the conducting properties to its Scattering matrix.

I have then combined the ingredients presented in Chapters 1 and 2 to analyze the coherent transport in a NW with RSOC exposed to an additional magnetic field applied along the NW axis. The interplay between the Rashba and Zeeman terms is known to imply non-trivial spin properties for the energy spectrum and the eigenstates of the NW. Depending on the value of the spin-orbit energy E_{SO} and the Zeeman splitting energy E_Z , two relevant regimes can be identified: The Zeeman dominated regime ($E_{SO} < 2E_Z$) and the Rashba dominated regime ($2E_Z < E_{SO}$), as shown in Fig.3.2. In particular, in the latter regime the propagating states inside the magnetic gap ($|E| < E_Z$) are helical, i.e. they are characterized by spin-momentum locking, and are described by a massless Dirac model.

While most theoretical approaches in the literature consider the NW as infinitely long and with a homogeneous RSOC, in a realistic setup the NW has a finite length, it is contacted to electrodes (reservoirs) and coupled to metallic gates, which enable one to locally control the RSOC in different NW portions. In order to take these aspects into account, I have adopted an inhomogeneous RSOC model that was recently used in the group of my supervisor to predict equilibrium properties of a NW coupled to two metallic electrodes. I

have extended the application of this model to investigate the out of equilibrium transport properties of the NW.

This original research work is illustrated in the second part of Chapter 3 and in Chapter 4. In particular, in Chap.3.2, I have applied the Landauer-Büttiker formalism to compute the conducting properties of a NW with a piecewise constant RSOC profile. Specifically, I have combined my analytical calculations of the boundary matrix stemming from the Heisenberg equation with a numerical code I have written in Python to determine the Scattering matrix of the inhomogeneous NW. Thereby I could extract the NW conductance and its dependence on the energy, the RSOC and magnetic field. This approach is quite general and can be applied to analyze various configurations. For definiteness, I have focussed on a few physically relevant cases. The results can be summarized as follows:

1) *Single Interface between two NW portions with different RSOC.* In this case I have pointed out that the transmission strongly depends on the relative sign of the RSOC in the two regions. Specifically, for equal RSOC signs the transmission across the interface is practically perfect, even when the two regions are in opposite regimes (e.g. Zeeman and Rashba dominated) (see Fig.3.9(a)). This is due to the support of evanescent modes that allow the wavefunction spin matching at the interface that the propagating modes alone cannot guarantee. In contrast, when the RSOC takes opposite signs across the interface, the conductance gets suppressed with increasing the spin-orbit energy (see Fig.3.9(b));

2) *Finite length NW contacted to metallic leads.* In this case the finite length of the NW determines an inhomogeneity of the RSOC at the NW/lead contacts, and makes the NW behave like a sort of spin-dependent Fabry-Pérot interferometer for electron waves (see Fig.3.13). The conductance thus depends on the constructive/destructive interference effects of the electron waves, determined by the ratio of the NW length to the electron wavelength. In particular, when the NW length is comparable or longer than the spin-orbit length, i.e. for strong RSOC, the transmission coefficients acquires a non monotonic behavior (see Fig.3.14(b) and (c));

3) *“Magnetic barrier configuration”*, where two gated NW portions with different RSOC are separated by a distance d of purely Zeeman coupling (see Fig.3.15). The behavior of the conductance G significantly depends on the relative sign of the RSOC in the two regions and on the distance between them. In particular, while for short separation one recovers the results of the single interface problem, i.e. an almost perfect conductance for equal RSOC and a conductance suppression for opposite RSOC signs (see Fig.3.16(a)), for larger separation the electron spin has sufficient spatial room to re-adapt to the different orientation imposed by the opposite RSOC sign, and the behaviour of the conductance is energy dependent but almost identical in both cases of equal and opposite RSOC signs, Fig.3.16(c).

Finally, in Chapter 4 I have investigated the Dirac paradox problem and its implementation with NWs. The paradox consists in the fact that, at the interface between two massless Dirac models with opposite helicity, a transversally impinging electron can seemingly neither be transmitted nor reflected, due to the locking between spin and momentum (see Fig.4.1). As compared to the higher dimensional cases previously analyzed

in the literature, the paradox in one spatial dimension is more interesting, since electrons cannot leak along the interface. Thus, in the first part of Chapter 4 I have discussed this case on general grounds, analyzing various models for interfaces between Dirac states with opposite helicity. I have first shown that models involving purely massless Dirac modes lead to either no solution of the paradox (i.e. it is impossible to construct eigenstates in the form of a scattering state), or to a trivial solution of the paradox (the interface directly introduces spin-flip processes). Then, by introducing a model involving both massless and massive Dirac modes (see Fig.4.2), I have shown that, despite direct spin-flip processes at the interface are forbidden, one obtains a non-trivial solution of the Dirac paradox, where properly defined scattering state solutions are possible. Indeed the transmission of an incoming massless electron impinging with spin- \uparrow into an outgoing electron with spin- \downarrow is accomplished indirectly, assisted by massive modes that, despite carrying no current for energies inside their gap, guarantee the spin component matching (see Fig.4.3). In this way the transmission coefficient depends in general on three parameters and is thus tunable from 0 to 1.

In the second part of Chapter 4, I have then shown that this model for the one-dimensional Dirac paradox can be realized in NWs. Notably, while the Dirac paradox configuration would be extremely hard to realize with the helical states of a two-dimensional topological insulator, in NWs this is possible because the helicity of the helical states emerging in a NW in the strong Rashba-dominated regime is determined by the sign of the RSOC, which in turn can be controlled by suitable gates in two NW portions. For definiteness, I have considered the physically realistic parameters for a InSb NW. I computed numerically the exact transmission coefficient, which in general depends on the spin-orbit energy E_{SO} , the Zeeman energy E_Z and the distance between the two regions with opposite RSOC sign. However, as the spin-orbit energy increases and the NW reaches the Rashba-dominated regime, the Dirac paradox configuration can be realized. In this case the dependence on the Zeeman energy is lost and the transmission coefficient only depends on the spin-orbit energy (solid curves of Fig.4.5) and perfectly agrees with the result obtained from the massless+massive Dirac model introduced in the first part of Chapter 4 (dashed curve of Fig.4.5). This result shows that, in contrast to the usual low-energy model adopted in the literature for NW, which only involves massless helical modes, in an inhomogenous configuration like the Dirac paradox the actual low-energy properties are described by both massless and massive Dirac modes, near the NW Fermi points $k \sim \pm 2k_{SO}$ and $k \sim 0$, respectively. These results are described in a research article that is currently under review: L. Gogin *et. al* “*The Dirac paradox in 1+1 dimensions and its realization with spin-orbit coupled nanowires*”, cond-mat arXiv:2109.07355

Appendix A

Energy relabelling of eigenfunctions

The eigenfunctions of the NW with homogeneous RSOC found in section 3.1 are labeled by a wave vector. To treat the inhomogeneous RSOC case, the eigenfunctions are constructed by matching the eigenfunctions of the various regions. However, in order to apply the Scattering Matrix Formalism, we first need to re-express the eigenfunctions in terms of energy, since this is the quantity that is preserved in the mesoscopic regime. In this Appendix we provide some details about such relabelling.

Propagating modes

$$\psi_{k,n}(x) = \chi_n(k)e^{ikx} \quad (\text{A.1})$$

where $n = \{1, 2\}$ and energy dispersion relation is

$$E_1(k) = \epsilon_k^0 - \sqrt{E_Z^2 + 4\epsilon_k^0 E_{SO}} \quad (\text{A.2})$$

$$E_2(k) = \epsilon_k^0 + \sqrt{E_Z^2 + 4\epsilon_k^0 E_{SO}} \quad (\text{A.3})$$

with $\epsilon_k^0 = \frac{\hbar^2 k^2}{2m^*}$ and $k \in \mathbb{R}$. The spinor eigenvectors can be written as

$$\chi_1(k) = \begin{pmatrix} \cos\left(\frac{\theta(k)}{2}\right) \\ \sin\left(\frac{\theta(k)}{2}\right) \end{pmatrix} \quad \chi_2(k) = \begin{pmatrix} -\sin\left(\frac{\theta(k)}{2}\right) \\ \cos\left(\frac{\theta(k)}{2}\right) \end{pmatrix} \quad (\text{A.4})$$

where

$$\cos\left(\frac{\theta(k)}{2}\right) = \sqrt{\frac{1 + \cos(\theta(k))}{2}} \quad (\text{A.5})$$

$$\sin\left(\frac{\theta(k)}{2}\right) = \text{sgn}(h_\perp) \sqrt{\frac{1 - \cos(\theta(k))}{2}} \quad (\text{A.6})$$

and

$$\cos(\theta(k)) = 2\text{sgn}(\alpha k) \sqrt{\frac{\epsilon_k^0 E_{SO}}{\epsilon_k^0 E_{SO} + E_Z^2}} \quad (\text{A.7})$$

Evanescent modes

These states can be obtained with mapping $k \mapsto -i\kappa$ and eigenfunction reads

$$\psi_{\kappa,n}(x) = \xi_n(\kappa)e^{\kappa x} \quad (\text{A.8})$$

where $n = \{1, 2\}$ and energy dispersion

$$E_1(\kappa) = -\epsilon_\kappa^0 - \sqrt{E_Z^2 - 4\epsilon_\kappa^0 E_{SO}} \quad (\text{A.9})$$

$$E_2(\kappa) = -\epsilon_\kappa^0 + \sqrt{E_Z^2 - 4\epsilon_\kappa^0 E_{SO}} \quad (\text{A.10})$$

with $\epsilon_\kappa^0 = \frac{\hbar^2 \kappa^2}{2m^*}$ and $\kappa \in \mathbb{R}$. The spinor part of evanescent state may be written as

$$\xi_1(\kappa) = \frac{1}{\sqrt{2}} \begin{pmatrix} e^{-i \arctan(\sinh(\theta(\kappa)))} \\ 1 \end{pmatrix} \quad \xi_2(\kappa) = \frac{1}{\sqrt{2}} \begin{pmatrix} -e^{i \arctan(\sinh(\theta(\kappa)))} \\ 1 \end{pmatrix} \quad (\text{A.11})$$

where

$$\sinh(\theta(\kappa)) = \text{sgn}(\alpha\kappa) 2\sqrt{\frac{\epsilon_\kappa^0 E_{SO}}{E_Z^2 - 4\epsilon_\kappa^0 E_{SO}}} \quad (\text{A.12})$$

As pointed out in the chapter 2, in order to investigate the conducting properties the eigenfunctions should be labeled by energy. In this appendix we present the complete discussion of the inversion of the dispersion relation for propagating as well as evanescent modes

A.1 Propagating modes

First of all let us consider the propagating modes. The dispersion relation (A.2- A.3) can be rewritten as

$$E_1(k) - \epsilon_k^0 = -\sqrt{E_Z^2 + 4\epsilon_k^0 E_{SO}} \quad (\text{A.13})$$

$$E_2(k) - \epsilon_k^0 = \sqrt{E_Z^2 + 4\epsilon_k^0 E_{SO}} \quad (\text{A.14})$$

Raising both side of equation above to the second power, one loose the track of the correspondent band and for a given energy obtain

$$\epsilon_k^{0^2} - 2(E + 2E_{SO})\epsilon_k^0 + E^2 - E_Z^2 = 0 \quad (\text{A.15})$$

that, in turn, can be easily solved and wave vector can be expressed as function of energy

$$k_\pm(E) = \frac{\sqrt{2m}}{\hbar} \sqrt{E + 2E_{SO} \pm \sqrt{4EE_{SO} + 4E_{SO}^2 + E_Z^2}} \quad (\text{A.16})$$

with $k_\pm(E) \in \mathbb{R}^+$, however this condition is not true for all energy ranges and in order to find the correct domain of validity one have to introduce the constrain for $k_+(E)$

$$E + 2E_{SO} + \sqrt{4EE_{SO} + 4E_{SO}^2 + E_Z^2} > 0 \quad (\text{A.17})$$

	Rashba regime $E_Z < 2E_{SO}$	Zeeman regime $2E_{SO} < E_Z$
$E < -E_{SO} \left(1 + \frac{E_Z^2}{4E_{SO}^2}\right)$	No real solutions	No real solutions
$-E_{SO} \left(1 + \frac{E_Z^2}{4E_{SO}^2}\right) < E < -E_Z$	$k_{\pm}(E) \in \mathbb{R}$	No real solutions
$-E_Z < E < E_Z$	$k_+(E) \in \mathbb{R}$	$k_+(E) \in \mathbb{R}$
$E > E_Z$	$k_{\pm}(E) \in \mathbb{R}$	$k_{\pm}(E) \in \mathbb{R}$

Table A.1: Real solutions of $k_{\pm}(E)$ for each energy range in Rashba dominated and Zeeman dominated regimes.

and for $k_-(E)$

$$E + 2E_{SO} - \sqrt{4EE_{SO} + 4E_{SO}^2 + E_Z^2} > 0 \quad (\text{A.18})$$

the solutions of which can be found on the Table A.1

In this way the wave vector for each fixed energy have been found, however it is still does not clear which spinor eigenvector should be used. The correspondence of the energy band and wave vector can be found by substitution of a given wave vector $k_n(E)$ in the the dispersion relation (A.2-A.3) and finding the combination of indices (n, m) such that satisfy

$$E_m(k_n(E)) = E \quad (\text{A.19})$$

the summary of the solution can be found in Table A.2

	Rashba regime $E_Z < 2E_{SO}$	Zeeman regime $2E_{SO} < E_Z$
$-E_{SO} \left(1 + \frac{E_Z^2}{4E_{SO}^2}\right) < E < -E_Z$	$k_+(E)$ belong to E_1 $k_-(E)$ belong to E_1	No real solutions
$ E < E_Z$	$k_+(E)$ belong to E_1	$k_+(E)$ belong to E_1
$E > E_Z$	$k_+(E)$ belong to E_1 $k_-(E)$ belong to E_2	$k_+(E)$ belong to E_1 $k_-(E)$ belong to E_2

Table A.2: The real solutions of $k_{\pm}(E)$ and their corresponding energy bands

Once the expression of the wave vector in function of energy have been found, one can use this results to express the spinor in term of energy ass well. Indeed taking the absolute value of Eq.(A.13, A.14) one can find

$$\sqrt{E_Z^2 + 4E_{so}\epsilon_{k_{\eta}(E)}^0} = \left| 2E_{so} + \eta\sqrt{4EE_{so} + 4E_{so}^2 + E_Z^2} \right| \quad (\text{A.20})$$

in this way Eq.(A.7) can be rewritten as

$$\cos(\theta(\pm k_{\eta}(E))) = \pm 2\text{sgn}(\alpha) \frac{\sqrt{E_{SO} \left(E + 2E_{SO} \pm \sqrt{4EE_{SO} + 4E_{SO}^2 + E_Z^2} \right)}}{\left| 2E_{so} + \eta\sqrt{4EE_{so} + 4E_{so}^2 + E_Z^2} \right|} \quad (\text{A.21})$$

finally combining Eq.(A.21) with Eq.(A.5) one can obtain the expressions for $\cos\left(\frac{\theta(\pm k_{\eta}(E))}{2}\right)$ and $\sin\left(\frac{\theta(\pm k_{\eta}(E))}{2}\right)$ reported in Eqs.(3.77, 3.78), that in turn can be used for the spinors

(3.76)

$$\chi_1(\pm k_\eta(E)) = \begin{pmatrix} \cos\left(\frac{\theta(\pm k_\eta(E))}{2}\right) \\ \sin\left(\frac{\theta(\pm k_\eta(E))}{2}\right) \end{pmatrix} \quad \chi_2(\pm k_\eta(E)) = \begin{pmatrix} -\sin\left(\frac{\theta(\pm k_\eta(E))}{2}\right) \\ \cos\left(\frac{\theta(\pm k_\eta(E))}{2}\right) \end{pmatrix} \quad (\text{A.22})$$

In conclusion let us introduced the group velocity that in general is defined as

$$v_1(k) = \frac{\partial}{\hbar \partial k} E_1(k) = \frac{\hbar}{m^*} k \left(1 - \frac{2E_{SO}}{\sqrt{E_Z^2 + 4\epsilon_k^0 E_{SO}}} \right) \quad (\text{A.23})$$

$$v_2(k) = \frac{\partial}{\hbar \partial k} E_2(k) = \frac{\hbar}{m^*} k \left(1 + \frac{2E_{SO}}{\sqrt{E_Z^2 + 4\epsilon_k^0 E_{SO}}} \right) \quad (\text{A.24})$$

that with help of the Eq.(A.16, A.20) can be rewritten in term of energy

$$v_1(\pm k_\eta(E)) = \pm k_\eta(E) \frac{\hbar}{m^*} \frac{|2E_{so} + \eta \sqrt{4EE_{so} + 4E_{so}^2 + E_Z^2}| - 2E_{SO}}{|2E_{so} + \eta \sqrt{4EE_{so} + 4E_{so}^2 + E_Z^2}|} \quad (\text{A.25})$$

$$v_2(\pm k_\eta(E)) = \pm k_\eta(E) \frac{\hbar}{m^*} \frac{|2E_{so} + \eta \sqrt{4EE_{so} + 4E_{so}^2 + E_Z^2}| + 2E_{SO}}{|2E_{so} + \eta \sqrt{4EE_{so} + 4E_{so}^2 + E_Z^2}|} \quad (\text{A.26})$$

One can observe that if $k_+(E) \in E_1$ the numerator of Eq.(A.25) can always be simplified as

$$\left| 2E_{so} + \sqrt{4EE_{so} + 4E_{so}^2 + E_Z^2} \right| - 2E_{SO} = \sqrt{4EE_{so} + 4E_{so}^2 + E_Z^2} \quad (\text{A.27})$$

on the other hand, for $E < -E_Z$ (i.e. $k_-(E) \in E_1$), it can be shown that $2E_{so} - \sqrt{4EE_{so} + 4E_{so}^2 + E_Z^2} > 0$ and the numerator of Eq.(A.25) can be expressed as

$$\left| 2E_{so} - \sqrt{4EE_{so} + 4E_{so}^2 + E_Z^2} \right| - 2E_{SO} = -\sqrt{4EE_{so} + 4E_{so}^2 + E_Z^2} \quad (\text{A.28})$$

Instead in the case $E > E_Z$ (i.e. $k_-(E) \in E_2$) one finds $2E_{so} - \sqrt{4EE_{so} + 4E_{so}^2 + E_Z^2} < 0$ and the numerator of Eq.(A.26) can be simplified as

$$\left| 2E_{so} - \sqrt{4EE_{so} + 4E_{so}^2 + E_Z^2} \right| + 2E_{SO} = \sqrt{4EE_{so} + 4E_{so}^2 + E_Z^2} \quad (\text{A.29})$$

In conclusion we can summarise the above results by introducing the group velocity as a function of energy

$$v_{\eta,\pm}(E) = \pm \text{sgn}((E+E_Z)(1-\eta)+(1+\eta)) \frac{\hbar k_\eta(E)}{m^*} \frac{\sqrt{4EE_{so} + 4E_{so}^2 + E_Z^2}}{|2E_{so} + \eta \sqrt{4EE_{so} + 4E_{so}^2 + E_Z^2}|} \quad (\text{A.30})$$

the absolute value of which $|v_{\eta,\pm}(E)| = v_\eta(E)$ is given in Eq.(3.75).

A.2 Evanescent modes

In analogy with the propagating modes the dispersion relation of evanescent modes (A.9, A.10) can be inverted as well and wave vector can be expressed as function of energy

$$\kappa_{\pm}(E) = \frac{\sqrt{2m}}{\hbar} \sqrt{-(E + 2E_{SO}) \pm \sqrt{4EE_{SO} + 4E_{SO}^2 + E_Z^2}} \quad (\text{A.31})$$

with $\kappa_1(E), \kappa_2(E) \in \mathbb{R}^+$ and the correct domain is fixed with constrain for $\kappa_+(E)$

$$-(E + 2E_{SO}) + \sqrt{4EE_{SO} + 4E_{SO}^2 + E_Z^2} > 0 \quad (\text{A.32})$$

and for $\kappa_-(E)$

$$-(E + 2E_{SO}) - \sqrt{4EE_{SO} + 4E_{SO}^2 + E_Z^2} > 0 \quad (\text{A.33})$$

which solution are summarized in Table A.3

	$E_Z < 2E_{SO}$	$2E_{SO} < E_Z$
$E < -E_{SO} \left(1 + \frac{E_Z^2}{4E_{SO}^2}\right)$	No real solutions	No real solutions
$-E_{SO} \left(1 + \frac{E_Z^2}{4E_{SO}^2}\right) < E < -E_Z$	No real solutions	$\kappa_{\pm}(E) \in \mathbb{R}$
$-E_Z < E < E_Z$	$\kappa_+(E) \in \mathbb{R}$	$\kappa_+(E) \in \mathbb{R}$
$E > E_Z$	No real solutions	No real solutions

Table A.3: Real solutions of $\kappa_{\pm}(E)$ for each energy range and Regime.

In this way have been found the wave vector for each energy range however it is not straightforward to which energy band belong each wave vector. This correspondence can be found analogously with the case of propagation modes, namely for a given κ_n must be found a set of indices (n, m) such that satisfy

$$E_n(\kappa_m(E)) = E \quad (\text{A.34})$$

Notably one find a subdivision of Zeeman dominated regime into 2 subranges namely weak Zeeman dominated regime for $2E_{so} < E_Z < 4E_{so}$ and strong Zeeman dominated regime for $4E_{so} < E_Z$, that can be found in Table A.4.

	$E_Z < 2E_{SO}$	$2E_{SO} < E_Z < 4E_{SO}$
$-E_{SO} \left(1 + \frac{E_Z^2}{4E_{SO}^2}\right) < E < -E_Z$	No real solutions	$\kappa_{\pm}(E)$ both belong to E_1
$-E_Z < E - \frac{E_Z^2}{4E_{SO}}$	$\kappa_+(E)$ belong to E_2	$\kappa_+(E)$ belong to E_2
$-\frac{E_Z^2}{4E_{SO}} < E < E_Z$	$\kappa_+(E)$ belong to E_1	$\kappa_+(E)$ belong to E_1
		$4E_{SO} < E_Z$
$-E_{SO} \left(1 + \frac{E_Z^2}{4E_{SO}^2}\right) < E < -\frac{E_Z^2}{4E_{SO}}$		$\kappa_{\pm}(E)$ both belong to E_1
$-\frac{E_Z^2}{4E_{SO}} < E < -E_Z$		$\kappa_+(E)$ belong to E_2 $\kappa_-(E)$ belong to E_1
$-E_Z < E < E_Z$		$\kappa_+(E)$ belong to E_2

Table A.4: The real solutions of $\kappa_{\pm}(E)$ and their corresponding spinor part of the wavefunction

Appendix B

Current operator in the presence of Rashba coupling.

As we have seen in Sec.3.1, in the case of Rashba nanowire the current operator turns out to consist of 2 terms: the first one is the customary expression and can be called the kinetic current (3.10), whereas the second term raises from spin orbit coupling

$$\hat{\mathbf{J}}_{SO} = -\frac{\alpha}{\hbar} \hat{\Psi}^\dagger(x) \sigma_z \hat{\Psi}(x) \quad (\text{B.1})$$

In this way the total current operator can be expressed in term of spectrum as

$$\hat{\mathbf{J}} = \int dE \left(\hat{J}_{kin}(E) + \hat{J}_{SO}(E) \right) \quad (\text{B.2})$$

where in analogy with the field operator each term is expressed as piecewise function for each energy range and involve the square product of corresponding field operator (3.92, 3.93, 3.94) and their complex conjugate[23]

$$\hat{J}_{kin}(E) = J_{kin}^{(1)}(E) \Theta(E - E_Z) + J_{kin}^{(2)}(E) \Theta(E_Z - |E|) + J_{kin}^{(3)}(E) \Theta(E_Z - E) \quad (\text{B.3})$$

$$\hat{J}_{SO}(E) = J_{SO}^{(1)}(E) \Theta(E - E_Z) + J_{SO}^{(2)}(E) \Theta(E_Z - |E|) + J_{SO}^{(3)}(E) \Theta(E_Z - E) \quad (\text{B.4})$$

For the sake of simplicity we consider the current only in the left lead and in the gap energy range $J_{kin}^{(2)}(E)$, $J_{SO}^{(2)}(E)$.

Kinetic term. First of all let us to discuss the kinetic current contribution. Inside the gap energy range current operator has relatively simple expression since there present only one conducting channel

$$J_{kin}^{(2)}(E) = -\frac{i\hbar}{2m^*} \frac{ik_1(E)}{\pi\hbar|v_+(E)|} \left[\chi_1^T(k_+(E)) \chi_1(k_+(E)) \hat{a}_{1,E}^\dagger \hat{a}_{1,E} - \right. \quad (\text{B.5})$$

$$\left. - \chi_1^T(-k_+(E)) \chi_1(-k_+(E)) \hat{b}_{1,E}^\dagger \hat{b}_{1,E} \right] \quad (\text{B.6})$$

observe that

$$\chi_1^T(\pm k_n(E))\chi_1(\pm k_n(E)) = 1 \quad (\text{B.7})$$

in this way the kinetic term can be simplified as

$$J_{kin}^{(2)}(E) = \frac{\hbar}{2m^*} \frac{k_+(E)}{\pi\hbar|v_+(E)|} \left[\hat{a}_{1,E}^\dagger \hat{a}_{1,E} - \hat{b}_{E,1}^\dagger \hat{b}_{1,E} \right] \quad (\text{B.8})$$

SOC term. On the other hand the SOC term can be written

$$\begin{aligned} J_{SO}^{(2)}(E) = -\frac{\alpha}{\hbar} \frac{1}{2\pi\hbar|v_+(E)|} & \left[\chi_1^T(k_+(E))\sigma_z\chi_1(k_+(E))\hat{a}_{1,E}^\dagger\hat{a}_{1,E} + \right. \\ & + \chi_1^T(-k_+(E))\sigma_z\chi_1(k_+(E))\hat{b}_{1,E}^\dagger\hat{b}_{1,E} \\ & + \chi_1^T(-k_+(E))\sigma_z\chi_1(k_+(E))\hat{b}_{1,E}^\dagger\hat{a}_{1,E}e^{i2k_+(E)x} \\ & \left. + \chi_1^T(k_+(E))\sigma_z\chi_1(k_+(E))\hat{a}_{1,E}^\dagger\hat{b}_{1,E}e^{-i2k_+(E)x} \right] \end{aligned} \quad (\text{B.9})$$

observe that

$$\chi_1^T(\pm k_+(E))\sigma_z\chi_1(\pm k_+(E)) = \pm \cos(\theta(k_+(E))) \quad (\text{B.10})$$

$$\chi_1^T(\pm k_+(E))\sigma_z\chi_1(\pm k_+(E)) = 0 \quad (\text{B.11})$$

In this way the spin orbit term simplifies as

$$J_{SO}^{(2)}(E) = -\frac{\alpha \cos(\theta(k_+(E)))}{\hbar} \frac{1}{2\pi\hbar|v_+(E)|} [\hat{a}_{1,E}^\dagger\hat{a}_{1,E} - \hat{b}_{1,E}^\dagger\hat{b}_{1,E}] \quad (\text{B.12})$$

In conclusion the total current can be expressed

$$J_{kin}^{(2)}(E) + J_{SO}^{(2)}(E) = \frac{k_+(E) - k_{so} \cos(\theta(k_+(E)))}{2\pi m^* |v_+(E)|} \left[\hat{a}_{1,E}^\dagger \hat{a}_{1,E} - \hat{b}_{1,E}^\dagger \hat{b}_{1,E} \right] \quad (\text{B.13})$$

with $k_{so} = |\alpha|m^*/\hbar^2$. Recalling that

$$v_+(E) = k_+(E) \frac{\hbar}{m^*} \left(1 - \frac{\lambda k_{SO}}{\sqrt{E_Z^2 + \lambda^2 k_+^2(E)}} \right) \quad (\text{B.14})$$

$$\cos(\theta(k_+(E))) = \frac{\lambda k_+(E)}{\sqrt{E_Z^2 + \lambda^2 k_+^2(E)}} \quad (\text{B.15})$$

the total current in side the gap can be expressed

$$J_{kin}^{(2)}(E) + J_{SO}^{(2)}(E) = \frac{1}{2\pi\hbar} \left[\hat{a}_{1,E}^\dagger \hat{a}_{1,E} - \hat{b}_{1,E}^\dagger \hat{b}_{1,E} \right] \quad (\text{B.16})$$

It can be noticed that the current operator has exactly the form reported by Büttiker in Eq.(2.65) in the presence of single channel[14, 16, 17]. Following a similar approach,

one can also find the current contribution in the other energy ranges. In contrast to the present case, however, due to the non orthogonality of the spinor components, the kinetic and spin-orbit current terms alone result to be space dependent due to the mixed terms $\hat{b}_{n,E}^\dagger \hat{a}_{m,E}$ that couple the injected and reflected modes of different channels[23]. Nevertheless summing both terms, off diagonal contributions drop out, and one obtains the customary Landauer-Büttiker formula. The main difference with the energy range within the gap is the presence of the an additional channel due to the spin degree of freedom and therefore one can summarise the result as

$$J(E) = \frac{1}{2\pi\hbar} \sum_n^{N(E)} [\hat{a}_{n,E}^\dagger \hat{a}_{n,E} - \hat{b}_{n,E}^\dagger \hat{b}_{n,E}] \quad (\text{B.17})$$

with $N(|E| < E_Z) = 1$ and $N(|E| > E_Z) = 2$. In this way one can indeed take advantages of results computed in previous chapter and compute the conducting properties with help of the scattering matrix only.

Appendix C

Details about the transfer matrix.

In this appendix we provide details about boundary matrix $M^{(j)}(x_i)$ from the Eq.(3.97) of the single interface problem in the NW. The column of the transfer matrix are expected to be 4-component vectors and are derived from the corresponding eigenfunction. I use the simplified notation in order to represent each column: as multiplication of a vector of 2×2 matrix which entries are identity matrix σ_0 and $A^{(i)}(x) = x\sigma_0 - i\text{sgn}(\alpha^{(i)})k_{SO}^{(i)}\sigma_z$ in this way a generic column reads

$$\begin{pmatrix} \sigma_0 \\ A^{(i)}(ik) \end{pmatrix} \chi e^{ikx} = \begin{pmatrix} \chi_{\uparrow} e^{ikx} \\ \chi_{\downarrow} e^{ikx} \\ (ik - i\text{sgn}(\alpha^{(i)})k_{SO}^{(i)})\chi_{\uparrow} e^{ikx} \\ (ik + i\text{sgn}(\alpha^{(i)})k_{SO}^{(i)})\chi_{\downarrow} e^{ikx} \end{pmatrix} \quad (\text{C.1})$$

From the discussion in previous chapter one can conclude that for each regimes must be used different energies range according to which must be chosen eigenfunctions. However in general can be identified in total 4 energies ranges nominated *I*), *II*), *III*), *IV*). In the case of Rashba dominated regime and Weak Zeeman regime this energy ranges are

$$I) \quad -E_{SO} \left(1 + \frac{E_Z^2}{4E_{SO}^2} \right) < E < -E_Z \quad (\text{C.2})$$

$$II) \quad -E_Z < E - \frac{E_Z^2}{4E_{SO}} \quad (\text{C.3})$$

$$III) \quad -\frac{E_Z^2}{4E_{SO}} < E < E_Z \quad (\text{C.4})$$

$$IV) \quad E_Z < E \quad (\text{C.5})$$

On the other hand for Strong Zeeman regime must be used

$$I) \quad -E_{SO} \left(1 + \frac{E_Z^2}{4E_{SO}^2} \right) < E < -\frac{E_Z^2}{4E_{SO}} \quad (C.6)$$

$$II) \quad -\frac{E_Z^2}{4E_{SO}} < E < -E_Z \quad (C.7)$$

$$III) \quad -E_Z < E < E_Z \quad (C.8)$$

$$IV) \quad E_Z < E \quad (C.9)$$

	$E_Z < 2E_{SO}$	$2E_{SO} < E_Z < 4E_{SO}$	$4E_{SO} < E_Z$
I)	1) $\begin{pmatrix} \sigma_0 \\ A(ik_+) \end{pmatrix} \chi_1(k_+)e^{ik_+x}$ 2) $\begin{pmatrix} \sigma_0 \\ A(-ik_+) \end{pmatrix} \chi_1(-k_+)e^{-ik_+x}$ 3) $\begin{pmatrix} \sigma_0 \\ A(ik_-) \end{pmatrix} \chi_1(k_-)e^{ik_-x}$ 4) $\begin{pmatrix} \sigma_0 \\ A(-ik_-) \end{pmatrix} \chi_1(-k_-)e^{-ik_-x}$	1) $\begin{pmatrix} \sigma_0 \\ A(\kappa_+) \end{pmatrix} \xi_1(\kappa_+)e^{\kappa_+x}$ 2) $\begin{pmatrix} \sigma_0 \\ A(-\kappa_+) \end{pmatrix} \xi_1(-\kappa_+)e^{-\kappa_+x}$ 3) $\begin{pmatrix} \sigma_0 \\ A(\kappa_-) \end{pmatrix} \xi_1(\kappa_-)e^{\kappa_-x}$ 4) $\begin{pmatrix} \sigma_0 \\ A(-\kappa_-) \end{pmatrix} \xi_1(-\kappa_-)e^{-\kappa_-x}$	1) $\begin{pmatrix} \sigma_0 \\ A(\kappa_+) \end{pmatrix} \xi_1(\kappa_+)e^{\kappa_+x}$ 2) $\begin{pmatrix} \sigma_0 \\ A(-\kappa_+) \end{pmatrix} \xi_1(-\kappa_+)e^{-\kappa_+x}$ 3) $\begin{pmatrix} \sigma_0 \\ A(\kappa_-) \end{pmatrix} \xi_1(\kappa_-)e^{\kappa_-x}$ 4) $\begin{pmatrix} \sigma_0 \\ A(-\kappa_-) \end{pmatrix} \xi_1(-\kappa_-)e^{-\kappa_-x}$
II)	1) $\begin{pmatrix} \sigma_0 \\ A(ik_+) \end{pmatrix} \chi_1(k_+)e^{ik_+x}$ 2) $\begin{pmatrix} \sigma_0 \\ A(-ik_+) \end{pmatrix} \chi_1(-k_+)e^{-ik_+x}$ 3) $\begin{pmatrix} \sigma_0 \\ A(\kappa_+) \end{pmatrix} \xi_1(\kappa_+)e^{\kappa_+x}$ 4) $\begin{pmatrix} \sigma_0 \\ A(-\kappa_+) \end{pmatrix} \xi_1(-\kappa_+)e^{-\kappa_+x}$	1) $\begin{pmatrix} \sigma_0 \\ A(ik_+) \end{pmatrix} \chi_1(k_+)e^{ik_+x}$ 2) $\begin{pmatrix} \sigma_0 \\ A(-ik_+) \end{pmatrix} \chi_1(-k_+)e^{-ik_+x}$ 3) $\begin{pmatrix} \sigma_0 \\ A(\kappa_+) \end{pmatrix} \xi_1(\kappa_+)e^{\kappa_+x}$ 4) $\begin{pmatrix} \sigma_0 \\ A(-\kappa_+) \end{pmatrix} \xi_1(-\kappa_+)e^{-\kappa_+x}$	1) $\begin{pmatrix} \sigma_0 \\ A(\kappa_+) \end{pmatrix} \xi_2(\kappa_+)e^{\kappa_+x}$ 2) $\begin{pmatrix} \sigma_0 \\ A(-\kappa_+) \end{pmatrix} \xi_2(-\kappa_+)e^{-\kappa_+x}$ 3) $\begin{pmatrix} \sigma_0 \\ A(\kappa_-) \end{pmatrix} \xi_1(\kappa_-)e^{\kappa_-x}$ 4) $\begin{pmatrix} \sigma_0 \\ A(-\kappa_-) \end{pmatrix} \xi_1(-\kappa_-)e^{-\kappa_-x}$
III)	1) $\begin{pmatrix} \sigma_0 \\ A(ik_+) \end{pmatrix} \chi_1(k_+)e^{ik_+x}$ 2) $\begin{pmatrix} \sigma_0 \\ A(-ik_+) \end{pmatrix} \chi_1(-k_+)e^{-ik_+x}$ 3) $\begin{pmatrix} \sigma_0 \\ A(\kappa_+) \end{pmatrix} \xi_2(\kappa_+)e^{\kappa_+x}$ 4) $\begin{pmatrix} \sigma_0 \\ A(-\kappa_+) \end{pmatrix} \xi_2(-\kappa_+)e^{-\kappa_+x}$	1) $\begin{pmatrix} \sigma_0 \\ A(ik_+) \end{pmatrix} \chi_1(k_+)e^{ik_+x}$ 2) $\begin{pmatrix} \sigma_0 \\ A(-ik_+) \end{pmatrix} \chi_1(-k_+)e^{-ik_+x}$ 3) $\begin{pmatrix} \sigma_0 \\ A(\kappa_+) \end{pmatrix} \xi_2(\kappa_+)e^{\kappa_+x}$ 4) $\begin{pmatrix} \sigma_0 \\ A(-\kappa_+) \end{pmatrix} \xi_2(-\kappa_+)e^{-\kappa_+x}$	1) $\begin{pmatrix} \sigma_0 \\ A(ik_+) \end{pmatrix} \chi_1(k_+)e^{ik_+x}$ 2) $\begin{pmatrix} \sigma_0 \\ A(-ik_+) \end{pmatrix} \chi_1(-k_+)e^{-ik_+x}$ 3) $\begin{pmatrix} \sigma_0 \\ A(\kappa_+) \end{pmatrix} \xi_1(\kappa_+)e^{\kappa_+x}$ 4) $\begin{pmatrix} \sigma_0 \\ A(-\kappa_+) \end{pmatrix} \xi_1(-\kappa_+)e^{-\kappa_+x}$
IV)	1) $\begin{pmatrix} \sigma_0 \\ A(ik_+) \end{pmatrix} \chi_1(k_+)e^{ik_+x}$ 2) $\begin{pmatrix} \sigma_0 \\ A(-ik_+) \end{pmatrix} \chi_1(-k_+)e^{-ik_+x}$ 3) $\begin{pmatrix} \sigma_0 \\ A(ik_-) \end{pmatrix} \chi_2(k_-)e^{ik_-x}$ 4) $\begin{pmatrix} \sigma_0 \\ A(-ik_-) \end{pmatrix} \chi_2(-k_-)e^{-ik_-x}$	1) $\begin{pmatrix} \sigma_0 \\ A(ik_+) \end{pmatrix} \chi_1(k_+)e^{ik_+x}$ 2) $\begin{pmatrix} \sigma_0 \\ A(-ik_+) \end{pmatrix} \chi_1(-k_+)e^{-ik_+x}$ 3) $\begin{pmatrix} \sigma_0 \\ A(ik_-) \end{pmatrix} \chi_2(k_-)e^{ik_-x}$ 4) $\begin{pmatrix} \sigma_0 \\ A(-ik_-) \end{pmatrix} \chi_2(-k_-)e^{-ik_-x}$	1) $\begin{pmatrix} \sigma_0 \\ A(ik_+) \end{pmatrix} \chi_1(k_+)e^{ik_+x}$ 2) $\begin{pmatrix} \sigma_0 \\ A(-ik_+) \end{pmatrix} \chi_1(-k_+)e^{-ik_+x}$ 3) $\begin{pmatrix} \sigma_0 \\ A(ik_-) \end{pmatrix} \chi_2(k_-)e^{ik_-x}$ 4) $\begin{pmatrix} \sigma_0 \\ A(-ik_-) \end{pmatrix} \chi_2(-k_-)e^{-ik_-x}$

Table C.1: All the column of the transfer matrix $\left(M^{(j)}(x) \right)_m$ where the number in each cell is the column number m and the energy ranges I), II), III), IV) are given by equations (C.2-C.5) for Rashba dominated regime and weak Zeeman regime and by equation (C.6-C.9) for Strong Zeeman regime

List of Figures

1.1	Band structure in the vicinity of the Γ -point. Conducting states correspond to the Γ_6 symmetry while valence to the Γ_7, Γ_8 symmetry. E_0 is the semiconductor energy gap and Δ_0 is splitting introduced by SOC term. Light holes Γ_8^l are associated with states $m_J = \pm 1/2$ and heavy holes Γ_8^h with $m_J = \pm 3/2$. [8]	23
1.2	Qualitative diagram of the heterojunction band structure in the case of linear external potential $V_{ext}(z) = E_{ext} z$. [30]	29
1.3	Orange line $E_{\uparrow}(k_x)$, Blue line $E_{\downarrow}(k_x)$	35
1.4	Datta-Das spin-FET structure. The iron contact are x -polarized ferromagnets that are responsible for injection and detection of spin current. The central region is composed by narrow gap semiconductor in which the Rashba spin orbit coupling is dominant and is controlled by gate potential V_G . Figure taken from Ref.[12]	37
1.5	Experimental measurements of output voltage ΔV measured by [39]. The panel (a) the output voltage at fixed temperature as function of gate voltage V_G and different length of central nano wire $L = 1.65\mu m, L = 1.25\mu m$. The panel (b) measurements for different temperatures. Reference [39]	40
2.1	Measurements framework.	43
2.2	The dispersion relation of the leads (2.13) with 3 open channels $N(E) = 3$. For each fixed energy E can be found the correspondent modes $\pm k_n(E)$ with $n = 1, 2, 3$	48
2.3	Black box model in the case of two conducting channels; Red lines represent incoming modes, blue lines are outgoing modes	50
3.1	Schematic of the Rashba NW on the substrate. The external electric field \mathbf{E}_{SIA} , caused by SIA at the interface between the NW and substrate, gives rise to the RSOC. The spin quantization axis \vec{n} lies in x - z substrate plane, and is determined by both the Rashba effective "magnetic field" and the actual Zeeman magnetic field \mathbf{B}	63
3.2	Dispersion relation in Rashba and Zeeman dominated regimes.	65

3.3	Spin-momentum locking in the case of deep Rashba dominated regime $E_Z \ll 2E_{SO}$. The green and red lines represent massless Dirac-like modes and correspond respectively to the spin-down and spin-up branches. The yellow lines are massive Dirac-like modes.	69
3.4	Set up of the gate controlled Rashba SOC.	73
3.5	A piecewise constant profile of SOC $\alpha(x)$	74
3.6	The NW propagating modes. Panel (a) for Rashba dominated regime, panel (b) for the Zeeman dominated regimes. Red and green curves describe modes propagating rightwards and leftwards, respectively. Alongside is represented the wave vector that is associated to the corresponding band in each energy range.	76
3.7	Evanescent mode inversion. Panel (a) is Rashba dominated regime $E_Z < E_{SO}$, panel (b) is a weak Zeeman dominated regime with $2E_{so} < E_Z < 4E_{so}$ and panel (c) is a strong Zeeman dominated regime $4E_{SO} < E_Z$. The thin lines correspond to $\pm\kappa_+(E)$ while the bold lines to $\pm\kappa_-(E)$. A orange line represent the energy band $E_1(\kappa)$ and blue line is $E_2(\kappa)$ energy band.	77
3.8	Incoming/outgoing modes mapping in the $ E > E_Z$ energy range	83
3.9	The conductance of the single interface $E_{SO}^{(L)} E_{SO}^{(R)}$ in units of conductance quantum $G_0 = e^2/h$ as a function of the energy E/E_Z for fixed spin-orbit energy on the right $2E_{SO}^{(R)}/E_Z = 0.5$ (Zeeman dominated regime) and for various values of spin-orbit energy on the left side: strong Zeeman regime (blue curve), weak Zeeman regime (orange curve), Rashba dominated regime (green curve)	86
3.10	The conductance of the single interface $E_{SO}^{(L)} E_{SO}^{(R)}$ in units of the conductance quantum $G_0 = e^2/h$ is plotted as function of the energy $E/E_{SO}^{(R)}$ for fixed $E_{SO}^{(L)}/E_{SO}^{(R)}$ and for different values of the ratio $E_Z/E_{SO,R}$. (a) the case where the RSO takes the same sign on both interface sides. The transmission is perfect and the Zeeman energy E_Z only controls the number of propagating channels (0, 1 or 2). (b) the RSO has opposite signs across the interface. In this case the Zeeman energy also determines the magnitude of conductance over the entire energy range. Note that, when both sides are in the Rashba-dominated regime (blue curves) a peak of $2G_0$ conductance is present for $E_{min} < E < -E_Z$, i.e. for $-0.878 < E/E_{SO}^{(R)} < -0.5$, due to the presence of two propagating channels below the magnetic gap energy (see Fig.3.6(a)).	87
3.11	The spatial profile of the wavefunction $\Psi(x)$ for $E = 0$, $2E_{SO}^{(R)}/E_Z = 0.5$ and interface at $x = 0$, the upper panel of each plot represent a spin up component Ψ_\uparrow while the lower panel a spin down component Ψ_\downarrow . Notably in the case of Zeeman dominated regime,(plot (a) and right hand side of the interface of plot (b)) the propagating states(oscillating lines) are characterized by both spin-up and -down components. On the other hand in Rashba dominated regime the spin-up component is dominant(left hand side of the interface on plot (b)). Blue and orange lines are respectively real and imaginary part of the wavefunction; Green and red lines are respectively real and imaginary part of evanescent mode.	89
3.12	Generalization of the transfer matrix to multiple interfaces.	90
3.13	Metallic lead model $0 \alpha 0$	91

3.14	The conductance of the lead Model $0 E_{SO} 0$ in units of $G_0 = e^2/h$ is plotted as function of the energy E/E_Z , for different values of the spin-orbit energy of the central region, which is in the strongly Zeeman dominated regime for $E_{SO} = 0.1E_Z$ (blue curve), in the weakly dominated Zeeman regime for $E_{SO} = 0.4E_Z$ (orange curve), and in the Rashba dominated regime for $E_{SO} = 10E_Z$ (green curve). The three panels refer to three different values of the NW length d , in units of the spin-orbit length k_{SO}^{-1}	92
3.15	Configuration with different gates.	93
3.16	The conductance of the magnetic barrier $E_{SO}^{(L)} 0 E_{SO}^{(R)}$ in units of conductance quantum $G_0 = e^2/h$ as function of the energy E/E_Z , for a fixed NW length d . The right region is assumed to be in the Rashba-dominated regime ($E_{SO}^{(R)} = 3E_Z$). The various curves refer to different values of RSOC of the left region. Orange line $E_{SO}^{(L)} = 0.5E_{SO}^{(R)}$, blue line $E_{SO}^{(L)} = -0.5E_{SO}^{(R)}$	95
4.1	Illustration of the Dirac paradox. On each interface side the blue line represents the spin- \uparrow branch of the massless dispersion relation, while red line the spin- \downarrow branch. On the left side of the interface the right-moving states are associated with spin- \uparrow and left-moving states with spin- \downarrow , while the opposite occurs on the right side of the interface: the two interface sides are characterized by an opposite helicity. A spin- \uparrow incoming from the left can seemingly be neither transmitted nor reflected, due to spin conservation.	100
4.2	The band structure of the massless+massive Dirac model implementing the Dirac paradox. In analogy with the Fig.4.1 red and blue lines represent the massless modes, while green curves represent massive bands with gap 2Δ at $k = 0$	104
4.3	The left-hand side of each panel depicts the scattering state wavefunction of a particle injected from the left. The blue and red colors correspond to the spin- \uparrow and spin- \downarrow components of the spinor eigenstate, respectively. Wavy lines are associated with propagating states, in particular the incoming modes are always characterized by spin- \uparrow while outgoing modes by spin- \downarrow . The solid green lines corresponds the evanescent wave of the massive mode. The right side of each panel illustrates the transmission process described correspondingly with Eq.(4.58)-(4.59). The black lines are associated with entries of the transfer matrix that connect non vanishing contribution to the scattering state. Panel (a) refers to the case $\beta_\uparrow = 0$: The evanescent mode appears only on the right side of the interface. Here $M_{31} = 1$, $M_{42} = 1 + i\beta_\downarrow$ and $M_{22} = i\beta_\downarrow$. Panel (b) describes the case $\beta_\downarrow = 0$: The evanescent modes arise on both sides of the junction. Here $M_{31} = 1 + i\beta_\uparrow$, $M_{33} = -i\beta_\uparrow$ and $M_{24} = M_{42} = 1$. In this way, although the transfer matrix presents the direct connection only between the states with the same spin, the evanescent modes of the massive field indirectly allow a spin-flip transmission between the propagating modes.	111
4.4	The transmission coefficient (4.77), plotted as a function of $k_{SO}d$, covers the entire range $T_0 \in [0,1]$	115

4.5 The Dirac paradox configuration realized with a InSb NW setup where two outer gated regions are characterized by opposite RSOC and the central region has a width $d = 100$ nm. The midgap conductance G , obtained from the numerically exact solution with the profile (4.61), is plotted in units of the conductance quantum G_0 as a function of the spin orbit energy, for different values of the external magnetic field E_Z (solid curves). At each value of E_Z , when the Rashba-dominated regime ($2E_{SO} \gg E_Z$) is reached, the various solid curves all tend to the dashed curve describing the result Eq.(4.77), obtained in the low energy limit from the effective massless+massive Dirac model. Panel (b) is a zoom of panel (a) in the regime of spin-orbit values that are realistic with present gating techniques. 117

List of Tables

3.1	Eigenstates of the NW in the Rashba dominated regime. The wavevectors k_{\pm} and κ_{\pm} are given by Eqs.(3.74) and (3.79). The spinors $\chi_{1,2}$ and the velocities of the propagating modes are given in Eq.(3.76) and Eq.(3.75), respectively, while the spinors ξ for the evanescent modes are given in Eqs.(3.80, 3.81).	76
3.2	Eigenstates of the NW in the weak Zeeman dominated regime. The wavevectors k_{\pm} and κ_{\pm} are given by Eqs.(3.74) and (3.79). The spinors $\chi_{1,2}$ and the velocities of the propagating modes are given in Eq.(3.76) and Eq.(3.75), respectively, while the spinors ξ for the evanescent modes are given in Eqs.(3.80, 3.81).	78
3.3	Eigenstates of the NW in the strong Zeeman dominated regime. The wavevectors k_{\pm} and κ_{\pm} are given by Eqs.(3.74) and (3.79). The spinors $\chi_{1,2}$ and the velocities of the propagating modes are given in Eq.(3.76) and Eq.(3.75), respectively, while the spinors ξ for the evanescent modes are given in Eqs.(3.80, 3.81).	79
A.1	Real solutions of $k_{\pm}(E)$ for each energy range in Rashba dominated and Zeeman dominated regimes.	125
A.2	The real solutions of $k_{\pm}(E)$ and their corresponding energy bands	125
A.3	Real solutions of $\kappa_{\pm}(E)$ for each energy range and Regime.	127
A.4	The real solutions of $\kappa_{\pm}(E)$ and their corresponding spinor part of the wavefunction	128
C.1	All the column of the transfer matrix $\left(M^{(j)}(x)\right)_m$ where the number in each cell is the column number m and the energy ranges I), II), III), IV) are given by equations (C.2-C.5) for Rashba dominated regime and weak Zeeman regime and by equation (C.6-C.9) for Strong Zeeman regime . . .	134

Bibliography

- [1] G. Dresselhaus. «Spin-Orbit Coupling Effects in Zinc Blende Structures». In: *Phys. Rev.* 100 (2 1955), pp. 580–586. DOI: [10.1103/PhysRev.100.580](https://doi.org/10.1103/PhysRev.100.580). URL: <https://link.aps.org/doi/10.1103/PhysRev.100.580>.
- [2] E.O. Kane. «Energy band structure in p-type germanium and silicon». In: *Journal of Physics and Chemistry of Solids* 1.1 (1956), pp. 82–99. ISSN: 0022-3697. DOI: [https://doi.org/10.1016/0022-3697\(56\)90014-2](https://doi.org/10.1016/0022-3697(56)90014-2). URL: <https://www.sciencedirect.com/science/article/pii/0022369756900142>.
- [3] Evan O. Kane. «Band structure of indium antimonide». In: *Journal of Physics and Chemistry of Solids* 1.4 (1957), pp. 249–261. ISSN: 0022-3697. DOI: [https://doi.org/10.1016/0022-3697\(57\)90013-6](https://doi.org/10.1016/0022-3697(57)90013-6). URL: <https://www.sciencedirect.com/science/article/pii/0022369757900136>.
- [4] E. O. Kane. «Band structure of narrow gap semiconductors». In: *Narrow Gap Semiconductors Physics and Applications*. Ed. by Wlodek Zawadzki. Berlin, Heidelberg: Springer Berlin Heidelberg, 1980, pp. 13–31. ISBN: 978-3-540-38382-6.
- [5] Yu A Bychkov and E I Rashba. «Oscillatory effects and the magnetic susceptibility of carriers in inversion layers». In: *Journal of Physics C: Solid State Physics* 17.33 (1984), pp. 6039–6045. DOI: [10.1088/0022-3719/17/33/015](https://doi.org/10.1088/0022-3719/17/33/015). URL: <https://doi.org/10.1088/0022-3719/17/33/015>.
- [6] R. Landauer and M. Büttiker. «Resistance of Small Metallic Loops». In: *Phys. Rev. Lett.* 54 (18 1985), pp. 2049–2052. DOI: [10.1103/PhysRevLett.54.2049](https://doi.org/10.1103/PhysRevLett.54.2049). URL: <https://link.aps.org/doi/10.1103/PhysRevLett.54.2049>.
- [7] R. Landauer. «Electrical transport in open and closed systems». In: *Zeitschrift für Physik B Condensed Matter* 68.2 (1987), pp. 217–228. DOI: [10.1007/BF01304229](https://doi.org/10.1007/BF01304229). URL: <https://doi.org/10.1007/BF01304229>.
- [8] G. Bastard and J. Schulman. «Wave Mechanics Applied to Semiconductor Heterostructures». In: 1988.
- [9] B. J. van Wees et al. «Quantized conductance of point contacts in a two-dimensional electron gas». In: *Phys. Rev. Lett.* 60 (9 1988), pp. 848–850. DOI: [10.1103/PhysRevLett.60.848](https://doi.org/10.1103/PhysRevLett.60.848). URL: <https://link.aps.org/doi/10.1103/PhysRevLett.60.848>.
- [10] P N Butcher. «Thermal and electrical transport formalism for electronic microstructures with many terminals». In: 2.22 (1990), pp. 4869–4878. DOI: [10.1088/0953-8984/2/22/008](https://doi.org/10.1088/0953-8984/2/22/008). URL: <https://doi.org/10.1088/0953-8984/2/22/008>.

-
- [11] M. Büttiker. «Quantized transmission of a saddle-point constriction». In: *Phys. Rev. B* 41 (11 1990), pp. 7906–7909. DOI: [10.1103/PhysRevB.41.7906](https://doi.org/10.1103/PhysRevB.41.7906). URL: <https://link.aps.org/doi/10.1103/PhysRevB.41.7906>.
- [12] Supriyo Datta and Biswajit Das. «Electronic analog of the electro-optic modulator». In: *Applied Physics Letters* 56.7 (Feb. 1990), pp. 665–667. DOI: [10.1063/1.102730](https://doi.org/10.1063/1.102730).
- [13] B. J. van Wees et al. «Quantum ballistic and adiabatic electron transport studied with quantum point contacts». In: *Phys. Rev. B* 43 (15 1991), pp. 12431–12453. DOI: [10.1103/PhysRevB.43.12431](https://doi.org/10.1103/PhysRevB.43.12431). URL: <https://link.aps.org/doi/10.1103/PhysRevB.43.12431>.
- [14] M. Büttiker. «Scattering theory of current and intensity noise correlations in conductors and wave guides». In: *prb* 46.19 (Nov. 1992), pp. 12485–12507. DOI: [10.1103/PhysRevB.46.12485](https://doi.org/10.1103/PhysRevB.46.12485).
- [15] Supriyo Datta. *Electronic Transport in Mesoscopic Systems*. Cambridge Studies in Semiconductor Physics and Microelectronic Engineering. Cambridge University Press, 1995. DOI: [10.1017/CB09780511805776](https://doi.org/10.1017/CB09780511805776).
- [16] M. Büttiker. «Dynamic conductance and quantum noise in mesoscopic conductors». In: *Journal of Mathematical Physics* 37.10 (Oct. 1996), pp. 4793–4815. DOI: [10.1063/1.531670](https://doi.org/10.1063/1.531670).
- [17] Ya.M. Blanter and M. Büttiker. «Shot noise in mesoscopic conductors». In: *Physics Reports* 336.1 (2000), pp. 1–166. ISSN: 0370-1573. DOI: [https://doi.org/10.1016/S0370-1573\(99\)00123-4](https://doi.org/10.1016/S0370-1573(99)00123-4). URL: <https://www.sciencedirect.com/science/article/pii/S0370157399001234>.
- [18] M. Born, E. Wolf, and A.B. Bhatia. *Principles of Optics: Electromagnetic Theory of Propagation, Interference and Diffraction of Light*. Cambridge University Press, 2000. ISBN: 9780521784498. URL: <https://books.google.it/books?id=oV80AAAAIAAJ>.
- [19] L. Petersen and P. Hedegård. «A simple tight-binding model of spin-orbit splitting of sp-derived surface states». In: *Surface Science* 459.1 (2000), pp. 49–56. ISSN: 0039-6028. DOI: [https://doi.org/10.1016/S0039-6028\(00\)00441-6](https://doi.org/10.1016/S0039-6028(00)00441-6). URL: <https://www.sciencedirect.com/science/article/pii/S0039602800004416>.
- [20] Francisco Mireles and George Kirczenow. «Ballistic spin-polarized transport and Rashba spin precession in semiconductor nanowires». In: *Phys. Rev. B* 64 (2 2001), p. 024426. DOI: [10.1103/PhysRevB.64.024426](https://doi.org/10.1103/PhysRevB.64.024426). URL: <https://link.aps.org/doi/10.1103/PhysRevB.64.024426>.
- [21] S. A. Wolf et al. «Spintronics: A Spin-Based Electronics Vision for the Future». In: *Science* 294.5546 (2001), pp. 1488–1495. DOI: [10.1126/science.1065389](https://doi.org/10.1126/science.1065389). URL: <https://www.science.org/doi/abs/10.1126/science.1065389>.
- [22] David D. Awschalom, Michael E. Flatté, and Nitin Samarth. «SPINTRONICS». In: *Scientific American* 286.6 (2002), pp. 66–73. ISSN: 00368733, 19467087. URL: <http://www.jstor.org/stable/26059724>.

-
- [23] G. Feve et al. «Rashba effect within the coherent scattering formalism». In: *Phys. Rev. B* 66 (15 2002), p. 155328. DOI: [10.1103/PhysRevB.66.155328](https://doi.org/10.1103/PhysRevB.66.155328). URL: <https://link.aps.org/doi/10.1103/PhysRevB.66.155328>.
- [24] B.H. Bransden and C.J. Joachain. *Physics of Atoms and Molecules*. Prentice Hall, 2003. ISBN: 9780582356924. URL: <https://books.google.it/books?id=i5IPWxDQlCIC>.
- [25] R. Winkler. *Spin-orbit Coupling Effects in Two-Dimensional Electron and Hole Systems*. Springer Tracts in Modern Physics. Springer Berlin Heidelberg, 2003. ISBN: 9783540011873. URL: <https://books.google.it/books?id=LQhcSCuzC3IC>.
- [26] Igor Zutic, Jaroslav Fabian, and S. Das Sarma. «Spintronics: Fundamentals and applications». In: *Rev. Mod. Phys.* 76 (2 2004), pp. 323–410. DOI: [10.1103/RevModPhys.76.323](https://doi.org/10.1103/RevModPhys.76.323). URL: <https://link.aps.org/doi/10.1103/RevModPhys.76.323>.
- [27] O. Krupin et al. «Rashba effect at magnetic metal surfaces». In: *Phys. Rev. B* 71 (20 2005), p. 201403. DOI: [10.1103/PhysRevB.71.201403](https://doi.org/10.1103/PhysRevB.71.201403). URL: <https://link.aps.org/doi/10.1103/PhysRevB.71.201403>.
- [28] B. Andrei Bernevig, Taylor L. Hughes, and Shou-Cheng Zhang. «Quantum Spin Hall Effect and Topological Phase Transition in HgTe Quantum Wells». In: *Science* 314.5806 (2006), pp. 1757–1761. DOI: [10.1126/science.1133734](https://doi.org/10.1126/science.1133734). eprint: <https://www.science.org/doi/pdf/10.1126/science.1133734>. URL: <https://www.science.org/doi/abs/10.1126/science.1133734>.
- [29] J.J. Sakurai. *Advanced Quantum Mechanics*. Always learning. Pearson Education, Incorporated, 2006. ISBN: 9788177589160. URL: <https://books.google.it/books?id=lvmSZkzDFt0C>.
- [30] Jaroslav Fabian et al. «Semiconductor spintronics». In: *Acta Physica Slovaca. Reviews and Tutorials* 57.4-5 (2007). ISSN: 0323-0465. DOI: [10.2478/v10155-010-0086-8](https://doi.org/10.2478/v10155-010-0086-8). URL: <http://dx.doi.org/10.2478/v10155-010-0086-8>.
- [31] A K Geim and K S Novoselov. «The rise of graphene.» eng. In: *Nat Mater* 6.3 (2007), pp. 183–191. ISSN: 1476-1122 (Print); 1476-1122 (Linking). DOI: [10.1038/nmat1849](https://doi.org/10.1038/nmat1849).
- [32] Markus König et al. «Quantum Spin Hall Insulator State in HgTe Quantum Wells». In: *Science* 318.5851 (2007), pp. 766–770. DOI: [10.1126/science.1148047](https://doi.org/10.1126/science.1148047). eprint: <https://www.science.org/doi/pdf/10.1126/science.1148047>. URL: <https://www.science.org/doi/abs/10.1126/science.1148047>.
- [33] C A Perroni et al. «Rashba quantum wire: exact solution and ballistic transport». In: *Journal of Physics: Condensed Matter* 19.18 (2007), p. 186227. DOI: [10.1088/0953-8984/19/18/186227](https://doi.org/10.1088/0953-8984/19/18/186227). URL: <https://doi.org/10.1088/0953-8984/19/18/186227>.
- [34] Markus König et al. «The Quantum Spin Hall Effect: Theory and Experiment». In: *Journal of the Physical Society of Japan* 77.3 (2008), p. 031007. DOI: [10.1143/JPSJ.77.031007](https://doi.org/10.1143/JPSJ.77.031007). eprint: <https://doi.org/10.1143/JPSJ.77.031007>. URL: <https://doi.org/10.1143/JPSJ.77.031007>.
- [35] Chaoxing Liu et al. «Quantum Spin Hall Effect in Inverted Type-II Semiconductors». In: *Phys. Rev. Lett.* 100 (23 2008), p. 236601. DOI: [10.1103/PhysRevLett.100.236601](https://doi.org/10.1103/PhysRevLett.100.236601). URL: <https://link.aps.org/doi/10.1103/PhysRevLett.100.236601>.

- [36] Peter Markoš and Costas M. Soukoulis. *Wave Propagation: From Electrons to Photonic Crystals and Left-Handed Materials*. STU - Student edition. Princeton University Press, 2008. ISBN: 9780691130033. URL: <http://www.jstor.org/stable/j.ctt7s2wj>.
- [37] F. Schwabl, R. Hilton, and A. Lahee. *Advanced Quantum Mechanics*. 2008 Springer E-Books. Springer Berlin Heidelberg, 2008. ISBN: 9783540850618. URL: <https://books.google.it/books?id=o-upPFoJEyKC>.
- [38] A. H. Castro Neto et al. «The electronic properties of graphene». In: *Rev. Mod. Phys.* 81 (1 2009), pp. 109–162. DOI: [10.1103/RevModPhys.81.109](https://doi.org/10.1103/RevModPhys.81.109). URL: <https://link.aps.org/doi/10.1103/RevModPhys.81.109>.
- [39] Hyun Cheol Koo et al. «Control of Spin Precession in a Spin-Injected Field Effect Transistor». In: *Science* 325.5947 (2009), pp. 1515–1518. DOI: [10.1126/science.1173667](https://doi.org/10.1126/science.1173667). eprint: <https://www.science.org/doi/pdf/10.1126/science.1173667>.
- [40] Henrik A. Nilsson et al. «Giant, Level-Dependent g Factors in InSb Nanowire Quantum Dots». In: *Nano Letters* 9.9 (2009). PMID: 19736971, pp. 3151–3156. DOI: [10.1021/nl901333a](https://doi.org/10.1021/nl901333a). eprint: <https://doi.org/10.1021/nl901333a>. URL: <https://doi.org/10.1021/nl901333a>.
- [41] N M R Peres. «Scattering in one-dimensional heterostructures described by the Dirac equation.» eng. In: *J Phys Condens Matter* 21.9 (2009), p. 095501. ISSN: 0953-8984 (Print); 0953-8984 (Linking). DOI: [10.1088/0953-8984/21/9/095501](https://doi.org/10.1088/0953-8984/21/9/095501).
- [42] Andreas Roth et al. «Nonlocal Transport in the Quantum Spin Hall State». In: *Science* 325.5938 (2009), pp. 294–297. DOI: [10.1126/science.1174736](https://doi.org/10.1126/science.1174736). eprint: <https://www.science.org/doi/pdf/10.1126/science.1174736>. URL: <https://www.science.org/doi/abs/10.1126/science.1174736>.
- [43] M. Z. Hasan and C. L. Kane. «Colloquium: Topological insulators». In: *Rev. Mod. Phys.* 82 (4 2010), pp. 3045–3067. DOI: [10.1103/RevModPhys.82.3045](https://doi.org/10.1103/RevModPhys.82.3045). URL: <https://link.aps.org/doi/10.1103/RevModPhys.82.3045>.
- [44] C. H. L. Quay et al. «Observation of a one-dimensional spin-orbit gap in a quantum wire». In: *Nature Physics* 6.5 (2010), pp. 336–339. DOI: [10.1038/nphys1626](https://doi.org/10.1038/nphys1626). URL: <https://doi.org/10.1038/nphys1626>.
- [45] P. Roulleau et al. «Suppression of weak antilocalization in InAs nanowires». In: *Phys. Rev. B* 81 (15 2010), p. 155449. DOI: [10.1103/PhysRevB.81.155449](https://doi.org/10.1103/PhysRevB.81.155449). URL: <https://link.aps.org/doi/10.1103/PhysRevB.81.155449>.
- [46] P. YU and M. Cardona. *Fundamentals of Semiconductors: Physics and Materials Properties*. Graduate Texts in Physics. Springer Berlin Heidelberg, 2010. ISBN: 9783642007101. URL: https://books.google.it/books?id=5aBuKYBT_hsC.
- [47] V. Zelevinsky. *Quantum Physics: Volume 1 - From Basics to Symmetries and Perturbations*. Physics textbook. Wiley, 2010. ISBN: 9783527409792. URL: <https://books.google.it/books?id=ayonWg9UjAAC>.

-
- [48] N.W. Ashcroft and N.D. Mermin. *Solid State Physics*. Cengage Learning, 2011. ISBN: 9788131500521. URL: https://books.google.it/books?id=x_s_YAAACAAJ.
- [49] S. Das Sarma et al. «Electronic transport in two-dimensional graphene». In: *Rev. Mod. Phys.* 83 (2 2011), pp. 407–470. DOI: [10.1103/RevModPhys.83.407](https://doi.org/10.1103/RevModPhys.83.407). URL: <https://link.aps.org/doi/10.1103/RevModPhys.83.407>.
- [50] Ivan Knez, Rui-Rui Du, and Gerard Sullivan. «Evidence for Helical Edge Modes in Inverted InAs/GaSb Quantum Wells». In: *Phys. Rev. Lett.* 107 (13 2011), p. 136603. DOI: [10.1103/PhysRevLett.107.136603](https://doi.org/10.1103/PhysRevLett.107.136603). URL: <https://link.aps.org/doi/10.1103/PhysRevLett.107.136603>.
- [51] Xiao-Liang Qi and Shou-Cheng Zhang. «Topological insulators and superconductors». In: *Rev. Mod. Phys.* 83 (4 2011), pp. 1057–1110. DOI: [10.1103/RevModPhys.83.1057](https://doi.org/10.1103/RevModPhys.83.1057). URL: <https://link.aps.org/doi/10.1103/RevModPhys.83.1057>.
- [52] Ryuji Takahashi and Shuichi Murakami. «Gapless interface states between topological insulators with opposite Dirac velocities.» eng. In: *Phys Rev Lett* 107.16 (2011), p. 166805. ISSN: 1079-7114 (Electronic); 0031-9007 (Linking). DOI: [10.1103/PhysRevLett.107.166805](https://doi.org/10.1103/PhysRevLett.107.166805).
- [53] Christoph Brüne et al. «Spin polarization of the quantum spin Hall edge states». In: *Nature Physics* 8.6 (2012), pp. 485–490. DOI: [10.1038/nphys2322](https://doi.org/10.1038/nphys2322). URL: <https://doi.org/10.1038/nphys2322>.
- [54] Anindya Das et al. «Zero-bias peaks and splitting in an Al–InAs nanowire topological superconductor as a signature of Majorana fermions». In: *Nature Physics* 8.12 (2012), pp. 887–895. DOI: [10.1038/nphys2479](https://doi.org/10.1038/nphys2479). URL: <https://doi.org/10.1038/nphys2479>.
- [55] M. T. Deng et al. «Anomalous Zero-Bias Conductance Peak in a Nb–InSb Nanowire–Nb Hybrid Device». In: *Nano Letters* 12.12 (Dec. 2012), pp. 6414–6419. DOI: [10.1021/nl303758w](https://doi.org/10.1021/nl303758w). URL: <https://doi.org/10.1021/nl303758w>.
- [56] Dong Liang and Xuan P.A. Gao. «Strong Tuning of Rashba Spin–Orbit Interaction in Single InAs Nanowires». In: *Nano Letters* 12.6 (2012). PMID: 22545669, pp. 3263–3267. DOI: [10.1021/nl301325h](https://doi.org/10.1021/nl301325h). eprint: <https://doi.org/10.1021/nl301325h>. URL: <https://doi.org/10.1021/nl301325h>.
- [57] S. Nadj-Perge et al. «Spectroscopy of Spin-Orbit Quantum Bits in Indium Antimonide Nanowires». In: *Physical Review Letters* 108.16 (2012). ISSN: 1079-7114. DOI: [10.1103/PhysRevLett.108.166801](https://doi.org/10.1103/PhysRevLett.108.166801). URL: <http://dx.doi.org/10.1103/PhysRevLett.108.166801>.
- [58] Leonid P. Rokhinson, Xinyu Liu, and Jacek K. Furdyna. «The fractional a.c. Josephson effect in a semiconductor–superconductor nanowire as a signature of Majorana particles». In: *Nature Physics* 8.11 (2012), pp. 795–799. DOI: [10.1038/nphys2429](https://doi.org/10.1038/nphys2429). URL: <https://doi.org/10.1038/nphys2429>.
- [59] Christophe De Beule and Bart Partoens. «Gapless interface states at the junction between two topological insulators». In: *Phys. Rev. B* 87 (11 2013), p. 115113. DOI: [10.1103/PhysRevB.87.115113](https://doi.org/10.1103/PhysRevB.87.115113). URL: <https://link.aps.org/doi/10.1103/PhysRevB.87.115113>.

- [60] Tetsuro Habe and Yasuhiro Asano. «Robustness of gapless interface states in a junction of two topological insulators». In: *Phys. Rev. B* 88 (15 2013), p. 155442. DOI: [10.1103/PhysRevB.88.155442](https://doi.org/10.1103/PhysRevB.88.155442). URL: <https://link.aps.org/doi/10.1103/PhysRevB.88.155442>.
- [61] Hannah J Joyce et al. «Electronic properties of GaAs, InAs and InP nanowires studied by terahertz spectroscopy». In: *Nanotechnology* 24.21 (2013), p. 214006. DOI: [10.1088/0957-4484/24/21/214006](https://doi.org/10.1088/0957-4484/24/21/214006). URL: <https://doi.org/10.1088/0957-4484/24/21/214006>.
- [62] David Sánchez and Rosa López. «Scattering Theory of Nonlinear Thermoelectric Transport». In: *Phys. Rev. Lett.* 110 (2 2013), p. 026804. DOI: [10.1103/PhysRevLett.110.026804](https://doi.org/10.1103/PhysRevLett.110.026804). URL: <https://link.aps.org/doi/10.1103/PhysRevLett.110.026804>.
- [63] Satoshi Sasaki et al. «Encapsulated gate-all-around InAs nanowire field-effect transistors». In: *Applied Physics Letters* 103.21 (2013), p. 213502. DOI: [10.1063/1.4832058](https://doi.org/10.1063/1.4832058). eprint: <https://doi.org/10.1063/1.4832058>. URL: <https://doi.org/10.1063/1.4832058>.
- [64] Bartosz Slomski et al. «Interband spin-orbit coupling between anti-parallel spin states in Pb quantum well states». In: *New Journal of Physics* 15.12 (2013), p. 125031. DOI: [10.1088/1367-2630/15/12/125031](https://doi.org/10.1088/1367-2630/15/12/125031). URL: <https://doi.org/10.1088/1367-2630/15/12/125031>.
- [65] Ilse van Weperen et al. «Quantized Conductance in an InSb Nanowire». In: *Nano Letters* 13.2 (Feb. 2013), pp. 387–391. DOI: [10.1021/nl3035256](https://doi.org/10.1021/nl3035256). URL: <https://doi.org/10.1021/nl3035256>.
- [66] Eduardo J. H. Lee et al. «Spin-resolved Andreev levels and parity crossings in hybrid superconductor–semiconductor nanostructures». In: *Nature Nanotechnology* 9.1 (2014), pp. 79–84. DOI: [10.1038/nnano.2013.267](https://doi.org/10.1038/nnano.2013.267). URL: <https://doi.org/10.1038/nnano.2013.267>.
- [67] Dario Bercioux and Procolo Lucignano. «Quantum transport in Rashba spin-orbit materials: a review». In: *Reports on Progress in Physics* 78.10 (2015), p. 106001. DOI: [10.1088/0034-4885/78/10/106001](https://doi.org/10.1088/0034-4885/78/10/106001). URL: <https://doi.org/10.1088/0034-4885/78/10/106001>.
- [68] A. M. Burke et al. «InAs Nanowire Transistors with Multiple, Independent Wrap-Gate Segments». In: *Nano Letters* 15.5 (2015). PMID: 25879492, pp. 2836–2843. DOI: [10.1021/nl5043243](https://doi.org/10.1021/nl5043243). eprint: <https://doi.org/10.1021/nl5043243>. URL: <https://doi.org/10.1021/nl5043243>.
- [69] Lingjie Du et al. «Robust Helical Edge Transport in Gated InAs/GaSb Bilayers». In: *Phys. Rev. Lett.* 114 (9 2015), p. 096802. DOI: [10.1103/PhysRevLett.114.096802](https://doi.org/10.1103/PhysRevLett.114.096802). URL: <https://link.aps.org/doi/10.1103/PhysRevLett.114.096802>.
- [70] I. van Weperen et al. «Spin-orbit interaction in InSb nanowires». In: *Phys. Rev. B* 91 (20 2015), p. 201413. DOI: [10.1103/PhysRevB.91.201413](https://doi.org/10.1103/PhysRevB.91.201413). URL: <https://link.aps.org/doi/10.1103/PhysRevB.91.201413>.

- [71] Kaoru Yamamoto. *Thermodynamics of Mesoscopic Quantum Systems*. 2015. arXiv: [1504.05493](https://arxiv.org/abs/1504.05493) [[cond-mat.stat-mech](#)].
- [72] S. M. Albrecht et al. «Exponential protection of zero modes in Majorana islands». In: *Nature* 531.7593 (2016), pp. 206–209. DOI: [10.1038/nature17162](https://doi.org/10.1038/nature17162). URL: <https://doi.org/10.1038/nature17162>.
- [73] Jan Raphael Bindel et al. «Probing variations of the Rashba spin–orbit coupling at the nanometre scale». In: *Nature Physics* 12.10 (2016), pp. 920–925. DOI: [10.1038/nphys3774](https://doi.org/10.1038/nphys3774). URL: <https://doi.org/10.1038/nphys3774>.
- [74] Costas Christodoulides. «Electromagnetism». In: *The Special Theory of Relativity: Foundations, Theory, Verification, Applications*. Cham: Springer International Publishing, 2016, pp. 273–295. ISBN: 978-3-319-25274-2. DOI: [10.1007/978-3-319-25274-2_9](https://doi.org/10.1007/978-3-319-25274-2_9). URL: https://doi.org/10.1007/978-3-319-25274-2_9.
- [75] M. T. Deng et al. «Majorana bound state in a coupled quantum-dot hybrid-nanowire system». In: *Science* 354.6319 (2016), pp. 1557–1562. DOI: [10.1126/science.aaf3961](https://doi.org/10.1126/science.aaf3961). eprint: <https://www.science.org/doi/pdf/10.1126/science.aaf3961>. URL: <https://www.science.org/doi/abs/10.1126/science.aaf3961>.
- [76] G. Dolcetto, M. Sasseti, and T. L. Schmidt. «Edge physics in two-dimensional topological insulators». In: *La Rivista del Nuovo Cimento* 39.3 (2016), pp. 113–154. DOI: [10.1393/ncr/i2016-10121-7](https://doi.org/10.1393/ncr/i2016-10121-7). URL: <https://doi.org/10.1393/ncr/i2016-10121-7>.
- [77] Shuang Jia, Su-Yang Xu, and M. Zahid Hasan. «Weyl semimetals, Fermi arcs and chiral anomalies». In: *Nature Materials* 15.11 (2016), pp. 1140–1144. DOI: [10.1038/nmat4787](https://doi.org/10.1038/nmat4787). URL: <https://doi.org/10.1038/nmat4787>.
- [78] Jian-Hua Jiang and Yoseph Imry. «Linear and nonlinear mesoscopic thermoelectric transport with coupling with heat baths». In: *Comptes Rendus Physique* 17.10 (2016). Mesoscopic thermoelectric phenomena / Phénomènes thermoélectriques mésoscopiques, pp. 1047–1059. ISSN: 1631-0705. DOI: <https://doi.org/10.1016/j.crhy.2016.08.006>. URL: <https://www.sciencedirect.com/science/article/pii/S1631070516300858>.
- [79] Zoltán Scherübl et al. «Electrical tuning of Rashba spin-orbit interaction in multi-gated InAs nanowires». In: *Phys. Rev. B* 94 (3 2016), p. 035444. DOI: [10.1103/PhysRevB.94.035444](https://doi.org/10.1103/PhysRevB.94.035444). URL: <https://link.aps.org/doi/10.1103/PhysRevB.94.035444>.
- [80] Shengyuan A. Yang. «Dirac and Weyl Materials: Fundamental Aspects and Some Spintronics Applications». In: *SPIN* 06.02 (2016), p. 1640003. DOI: [10.1142/S2010324716400038](https://doi.org/10.1142/S2010324716400038). eprint: <https://doi.org/10.1142/S2010324716400038>. URL: <https://doi.org/10.1142/S2010324716400038>.
- [81] J. Kammhuber et al. «Conductance through a helical state in an Indium antimonide nanowire». In: *Nature Communications* 8.1 (2017), p. 478. DOI: [10.1038/s41467-017-00315-y](https://doi.org/10.1038/s41467-017-00315-y). URL: <https://doi.org/10.1038/s41467-017-00315-y>.

- [82] J. Kammhuber et al. «Conductance through a helical state in an Indium antimonide nanowire». In: *Nature Communications* 8.1 (2017), p. 478. DOI: [10.1038/s41467-017-00315-y](https://doi.org/10.1038/s41467-017-00315-y). URL: <https://doi.org/10.1038/s41467-017-00315-y>.
- [83] K. Takase et al. «Highly gate-tuneable Rashba spin-orbit interaction in a gate-all-around InAs nanowire metal-oxide-semiconductor field-effect transistor». In: *Scientific Reports* 7.1 (2017), p. 930. DOI: [10.1038/s41598-017-01080-0](https://doi.org/10.1038/s41598-017-01080-0). URL: <https://doi.org/10.1038/s41598-017-01080-0>.
- [84] Fabrizio Dolcini and Fausto Rossi. «Magnetic field effects on a nanowire with inhomogeneous Rashba spin-orbit coupling: Spin properties at equilibrium». In: *Phys. Rev. B* 98 (4 2018), p. 045436. DOI: [10.1103/PhysRevB.98.045436](https://doi.org/10.1103/PhysRevB.98.045436). URL: <https://link.aps.org/doi/10.1103/PhysRevB.98.045436>.
- [85] Önder Gül et al. «Ballistic Majorana nanowire devices». In: *Nature Nanotechnology* 13.3 (2018), pp. 192–197. DOI: [10.1038/s41565-017-0032-8](https://doi.org/10.1038/s41565-017-0032-8). URL: <https://doi.org/10.1038/s41565-017-0032-8>.
- [86] Hanshen Tsai et al. «Clear variation of spin splitting by changing electron distribution at non-magnetic metal/Bi2O3 interfaces». In: *Scientific Reports* 8.1 (2018), p. 5564. DOI: [10.1038/s41598-018-23787-4](https://doi.org/10.1038/s41598-018-23787-4). URL: <https://doi.org/10.1038/s41598-018-23787-4>.
- [87] Kasun Premasiri and Xuan P A Gao. «Tuning spin-orbit coupling in 2D materials for spintronics: a topical review». In: *Journal of Physics: Condensed Matter* 31.19 (2019), p. 193001. DOI: [10.1088/1361-648x/ab04c7](https://doi.org/10.1088/1361-648x/ab04c7). URL: <https://doi.org/10.1088/1361-648x/ab04c7>.
- [88] Atsufumi Hirohata et al. «Review on spintronics: Principles and device applications». In: *Journal of Magnetism and Magnetic Materials* 509 (2020), p. 166711. ISSN: 0304-8853. DOI: <https://doi.org/10.1016/j.jmmm.2020.166711>. URL: <https://www.sciencedirect.com/science/article/pii/S0304885320302353>.
- [89] Hyun Cheol Koo et al. «Rashba Effect in Functional Spintronic Devices». In: *Advanced Materials* 32.51 (2020), p. 2002117. DOI: <https://doi.org/10.1002/adma.202002117>. eprint: <https://onlinelibrary.wiley.com/doi/pdf/10.1002/adma.202002117>. URL: <https://onlinelibrary.wiley.com/doi/abs/10.1002/adma.202002117>.
- [90] Lorenzo Rossi, Fabrizio Dolcini, and Fausto Rossi. «Majorana-like localized spin density without bound states in topologically trivial spin-orbit coupled nanowires». In: *Physical Review B* 101.19 (2020). ISSN: 2469-9969. DOI: [10.1103/PhysRevB.101.195421](https://doi.org/10.1103/PhysRevB.101.195421). URL: <http://dx.doi.org/10.1103/PhysRevB.101.195421>.
- [91] Dmitry Shcherbakov et al. «Layer- and gate-tunable spin-orbit coupling in a high-mobility few-layer semiconductor». In: *Science Advances* 7.5 (2021), eabe2892. DOI: [10.1126/sciadv.abe2892](https://doi.org/10.1126/sciadv.abe2892). eprint: <https://www.science.org/doi/pdf/10.1126/sciadv.abe2892>. URL: <https://www.science.org/doi/abs/10.1126/sciadv.abe2892>.

- [92] Keiko Takase, Kouta Tateno, and Satoshi Sasaki. «Electrical tuning of the spin–orbit interaction in nanowire by transparent ZnO gate grown by atomic layer deposition». In: *Applied Physics Letters* 119.1 (2021), p. 013102. DOI: [10.1063/5.0051281](https://doi.org/10.1063/5.0051281). eprint: <https://doi.org/10.1063/5.0051281>. URL: <https://doi.org/10.1063/5.0051281>.